THE UNIVERSITY OF SYDNEY

DOCTORAL THESIS

Distributed On-chip Brillouin Sensing: Toward Sub-mm Spatial Resolution

Atiyeh ZARIFI

A thesis submitted in fulfillment of the requirements for the degree of

Doctor of Philosophy

in

School of Physics
The University of Sydney

Declaration of Authorship

I, Atiyeh ZARIFI, declare that this thesis titled, "Distributed On-chip Brillouin Sensing: Toward Sub-mm Spatial Resolution" and the work presented in it are my own. To the best of my knowledge, this thesis contains no copy or paraphrase of work published by another person, except where duly acknowledged in the text. This thesis contains no material that has been previously presented for a degree at the University of Sydney or any other university.

Chapter 5 of this thesis is published as [1]. I designed and performed the experiment, analysed the data and wrote the drafts of the manuscript. Chapter 6 of this thesis is published as [2] and [3]. I designed and performed the experiment, analysed the data and wrote the drafts of the manuscripts. This thesis contains material published in [4] including sections 1.4 and 1.5 of chapter 2, in which I provided a review of the literature in the field of Brillouin distributed sensing and wrote the draft of the manuscript. Chapter 4 contains material published in [5], where I performed the experiment, wrote the draft and presented the result in the conference. Section 4.4 of chapter 4 is based on the result published in [6]. I made initial nonlinear loss measurements in hybrid waveguides, which confirmed the feasibility of silicon-chalcogenide hybridisation technique.

In addition to the statements above, in cases where I am not the corresponding author of a published item, permission to include the published material has been granted by the corresponding author.

24-June-2019

Abstract

Stimulated Brillouin scattering (SBS) involves nonlinear interaction of an optical wave with material, which under the phase-matching condition results in generation of an acoustic wave. In turns, part of the optical wave is scattered by the acoustic wave through an inelastic scattering process. SBS enables unique applications in optical fibers and more recently in on-chip photonic waveguides, ranging from RF-signal processing to lasing, frequency combs, RF sources, and light storage. Harnessing on-chip SBS paves the way to photonic integration by enabling powerful functionalities in an integrated, scalable, energy-efficient and potentially CMOS-compatible platform. In this thesis, we explore the possibility of enabling SBS in a silicon-based platform by designing, fabricating and characterizing a hybrid silicon-chalcogenide waveguide, which shows significant improvement in terms of nonlinear losses and SBS gain compared to a standard silicon waveguide. The SBS response in photonic waveguides including the silicon-chalcogenide platform is subject to spectral broadening which influences the quality of the devices whose performance are relying on the narrow linewidth of SBS. The spectral broadening is mainly due to structural non-uniformities along the waveguides which affect the local SBS response and consequently deteriorates the strength of the integrated SBS response. Therefore, characterizing those waveguides is of great importance. To address this issue, we employed the principle of distributed SBS sensing to monitor on-chip waveguides. However, since the waveguides length is on the order of cm and mm, the spatial resolution of the distributed technique needs to be very high, preferably in the sub-mm regime, which is the main goal of this thesis.

List of Publications

This thesis by publication is based on the following articles and conference papers:

Journal Papers

A. Zarifi, B. Stiller, M. Merklein, N. Li, K. Vu, D.-Y. Choi, P. Ma,S. J. Madden, and B. J. Eggleton, “Highly localized distributed Bril-louin scattering response in a photonic integrated circuit,”APL Photonics, vol. 3, p. 036101 (2018).

A. Zarifi, B. Stiller, M. Merklein, Y. Liu, B. Morrison, A. Casas-Bedoya, G. Ren, T. G. Nguyen, K. Vu, D.-Y. Choi, A. Mitchell,S. J. Madden, and B. J. Eggleton, “Brillouin spectroscopy of a hybrid silicon-chalcogenide waveguide with geometrical variations,”Optics Letters, vol. 43, p. 3493 (2018).

A. Zarifi, B. Stiller, M. Merklein, Y. Liu, B. Morrison, A. Casas-Bedoya, G. Ren,T. G. Nguyen, K. Vu, D.-Y. Choi, A. Mitchell, S. J. Madden, and B. J. Eggleton,“On-chip correlation-based Brillouin sensing: design, experiment, and simulation,”Journal of the Optical Society of America B, vol. 36, p. 146 (2019).

A. Zarifi, B. Stiller, M. Merklein, and B. Eggleton, “High Resolution Brillouin Sensing of Micro-Scale Structures,”Applied Sciences, vol. 8, p. 2572, (2018).

B. Morrison, A. Casas-Bedoya, G. Ren, K. Vu, Y. Liu, A. Zarifi, T. G. Nguyen, D.-Y. Choi, D. Marpaung, S. J. Madden, A. Mitchell, and B. J. Eggleton, "Compact Brillouin devices through hybrid integration on silicon," Optica, vol. 4, p. 847-854 (2017)

Conference Papers

A. Zarifi, B. Stiller, M. Merklein, Y. Liu, B. Morrison, A. Casas-Bedoya, G. Ren, A. Mitchell, K. Vu, S. J. Madden, and B. J. Eggleton, "Distributed SBS Sensing in a Silicon-Chalcogenide Platform," in 26th International Conference on Optical Fiber Sensors (2018), paper TuD4.

A. Zarifi, B. Stiller and B. J. Eggleton, "Advanced Functions for Signal Processing and Sensing Harnessing On-Chip SBS," IEEE 7th International Conference on Photonics (ICP) (2018), pp. 1-2.

A. Zarifi, B. Stiller, M. Merklein, K. Vu, S. J. Madden and B. J. Eggleton, "Localized high resolution Brillouin spectrum measurement of a photonic integrated circuit," 2017 Conference on Lasers and Electro-Optics Europe European Quantum Electronics Conference (CLEO/Europe-EQEC) (2017), pp. 1-1.

A. Zarifi, B. Stiller, M. Merklein, K. Vu, S. J. Madden, and B. J. Eggleton, "Distributed Brillouin Scattering Measurement with Sub-mm Spatial Resolution," in Frontiers in Optics (2017), paper FTu4A.5.

A. Zarifi, A. C. Bedoya, B. Morrison, Y. Zhang, G. Ren, T. Nguyen, S. Madden, K. Vu, A. Mitchell, C. Wolff, D. Marpaung, and B. J. Eggleton, "Nonlinear Loss Engineering in a Silicon-Chalcogenide Hybrid Optical Waveguide," in Photonics and Fiber Technology (ACOFT, BGPP, NP) (2016) , paper NM4A.6.

Acknowledgements

First, I would like to thank my principal supervisor, Professor Ben Eggleton for providing me with such unique opportunity to work in his research group. The time that I spent in CUDOS, at the school of physics taught me so many valuable lessons that I forever benefit from them. Thank you Ben for being so supportive and creating a great environment for research, networking, outreach and professional development. Many of these opportunities, with no doubt, were provided through the funding from ARC centre of excellence, CUDOS, which I would like to acknowledge here. I also would like to acknowledge University of Sydney Nano Institute for providing a top-up scholarship during my PhD.

I would like to thank my co-supervisor, Dr. Birgit Stiller for initiating the Brillouin sensing project and the insight she brought to this project. Thank you Birgit for staying so strong, positive and supportive and for believing in me all the time. I am thankful for all the experimental and research skills I learned from you. And, I thank you for always encouraging me to take bigger steps.

I also thank Dr. Alvaro Casas-Bedoya and Dr. David Marpaung who supervised me during the first year of my PhD. Thank you Alvaro for all the experimental tips and guidance that made me confident working with photonic waveguides and thank you for your continues support over the entire PhD. And, thank you David for great discussions we had and for your helpful advice.

A special thanks to Dr. Moritz Merklein, an ex-PhD office-mate and currently a post-doc in the school of Physics. Moritz, you are an example of a real scientist; precise, critical and extremely talented. I thank you for your great contribution to the Brillouin sensing project, for the time you spent discussing and performing experiments with me and for your valuable comments and inputs throughout the project and my thesis.

Furthermore, I thank all the CUDOS admin team, who were extremely supportive and organized many amazing events such as outreach and annual workshops which I attended and benefited from them. I also Thank our amazing lab manager, Dr. Eric Magi, who provided many technical supports required in the lab during the experiment. Thank you Eric for being so responsible and providing a safe lab environment.

I would like to thank all the collaborators who contributed in the fabrication of the waveguides used in these thesis; A/Prof. Steven Madden, Dr. Khu Vu and Dr. Duk-Yong Choi from Australian National University (ANU) and Prof. Arnan Mitchell, Dr. Guanghui Ren and Dr. Thach G. Nguyen from RMIT university.

I would like to thank all the amazing post-docs that I learned from them throughout my research, specially Andrea, Amol, Tomonori and Darren. I also thank Neuton Li, the summer student, who worked with me in the lab for sensing experiment during a summer break. Furthermore, I would like to acknowledge and thank *Max Planck Institute for the science of light* in Erlangen, Germany for supporting my stay during my visit to this institute and the great team I worked with during this period; Professor Gerd Leuchs, Dr. Christoph Marquardt, Dr. Florian Sedlmeir and post-grad student Alexandra Popp.

A very special and big thank you to my fellow office-mates, you were the most amazing aspect of this PhD! Loris, your enthusiasm and energy is exemplary. Blair, thank you for all the efforts you put into teaching me lots of exciting stuff, which most of the time were very useful and thank you for the amazing coffee breaks every

now and then. Yang, thank you for being there after everyone else graduated! You were such a great thesis buddy and the most patient person I ever seen. I also thank all the other students who made the office such a vibrant and active environment, most of them graduated already; Victor, Jane, Bruce, Björn, Neetesh, Scot, Iman, Caitlin, Young, Mattia, El-Abed, Fernando, Kevin, Jiakun and Luke.

Finally, I thank my family for their kind and endless supports which made this journey possible. This and any other achievements I made in my life would have not been possible without your unconditional love and support.

Contents

To my guardian angels; Akram and Mehrdad

1 Introduction

"A journey of a thousand miles begins with a single step."

Tao Te Ching by Laozi

Photonics is an established and ever-growing field which similar to its electronic counter-part plays an undeniable role in cutting-edge research and technological advancements. Photonics bridges the technological gap that is difficult to address by electronics e.g. the bandwidth and power density in short interconnects [7], [8]. In *linear optics*, electromagnetic waves do not interact with each other or the medium they are traveling through. As a result, linear optics provides an ideal solution for transmission lines in telecommunication systems; i.e. silica optical fibers which are insensitive to electromagnetic interference and cross-talk and therefore gives access to a wide bandwidth capacity [9]. In addition, optical fibers exhibit very low loss (typically $0.2\,\mathrm{dB/km}$) at telecommunication wavelengths [9].

In *nonlinear optics*, when the polarizability not only has a linear but also a nonlinear component, electromagnetic waves interact with the medium and change its properties. Via this nonlinear interaction, new electromagnetic waves with new frequencies are generated [10]. Therefore, nonlinear optics has found applications in the generation [11]–[16], processing [17]–[21] and storing [22]–[26] of optical signals, which are some basic elements for realizing all-optical systems. Integrated photonics is an attempt to combine these functionalities on a single platform to provide scalability, low cost, energy efficiency and potentially integration with electronics.

Silicon, due to its compatibility with complementary metal-oxide-semiconductor (CMOS) technology and its relatively low cost [27] is an excellent candidate for photonic integration. However, as a nonlinear optical signal processing platform, silicon is disadvantaged by high nonlinear losses due to two-photon absorption (TPA) [28]. Different approaches to overcome this limitation include TPA-free alternative platforms such as silicon nitride and high index silica (Hydex) [27] - although with lower nonlinearity than silicon - or heterogeneous integration of silicon on insulator (SOI) waveguides with a low nonlinear loss material such as a nonlinear polymers [29]–[31].

In this thesis, we propose and design a novel hybrid waveguide by combining chalcogenide glass with silicon. This approach leads to a significant improvement in nonlinear loss compared to a standard silicon waveguide. Furthermore, this platform can be utilized to enable on-chip functionalities such as narrow-linewidth lasers [32]–[34], all-optical signal processing [18], [35], frequency combs [36], [37], photonic memories [22]–[24] and sensing [38]–[40]. As an example, an on-chip ring resonator is demonstrated in the hybrid silicon-chalcogenide structure as will be described in chapter 4 of this thesis. The underlying nonlinear effect that enables the above-mentioned applications is stimulated Brillouin scattering (SBS).

SBS is an inelastic scattering resulting from the interaction of an optical wave with an acoustic wave in a nonlinear medium. The result of this interaction is the generation or amplification of a second optical wave, known as Stokes wave, whose linewidth is dependent upon the acoustic lifetime in the medium. SBS functionalities mentioned earlier are highly dependent on its *narrow linewidth* response and any non-uniformities in the waveguide deteriorates the SBS efficiency by broadening its linewidth [41]. For the waveguides used in this thesis, including the silicon-chalcogenide waveguide, this Brillouin linewidth is very narrow and on the order of $30\,\mathrm{MHz}$. Another critical consideration for inducing SBS in a waveguide is the simultaneous generation of optical and acoustic modes, which have to spatially overlap with each other [42]. This becomes particularly challenging when dealing with SOI waveguides. In a standard silicon waveguide, the acoustic velocity in the silicon core is higher than that in the silica substrate resulting in the acoustic mode leakage into the silica substrate [43]. Therefore, in order to achieve an SBS interaction in an SOI platform, complex design solutions have been proposed and demonstrated. These approaches include under-etched silicon waveguides [44], silicon membranes [45] and hybrid silicon-chalcogenide waveguide proposed and demonstrated by our research group [6].

The narrow linewidth required in SBS applications and the complex design and fabrication of on-chip SBS waveguides require a monitoring tool to ensure the fabrication consistency and consequently the narrow-linewidth response, which is the main motivation of this thesis. Interestingly, SBS itself can be utilized to monitor such variations in geometry as we will explain next.

SBS has long been known as a sensing mechanism in optical fibers, since any change in temperature and strain influences the opto-acoustic properties of the material and consequently the Brillouin frequency shift [46]. SBS is also sensitive to geometrical changes in optical fibers or on-chip waveguides, because those changes affect the effective refractive index, and can be used to monitor waveguides uniformity [47]–[49]. For this purpose, SBS response needs to be localized within a certain length in the medium, which takes us to the field of distributed Brillouin sensing. Different approaches have been proposed for distributed Brillouin temperature and strain sensing in optical fibers with spatial resolution ranging from $100\,\mathrm{m}$ [50] to $1\,\mathrm{cm}$ [51]. SBS strength scales exponentially with the interaction length [10], therefore SBS can easily be observed in long optical fibers. However, when it comes to on-chip photonic waveguides, the very short length of these devices, which is often on the order of cm- and mm-scale, requires spatial resolutions on the order of mm and even sub-mm. This spatial resolution is even more challenging to achieve given the weak SBS response over such short lengths.

This thesis aims to address two main questions regarding on-chip SBS functionalities in a photonic integrated platform. First, to investigate a new platform which is capable of photonic integration, has an improved nonlinear loss compared to silicon nanowires and provides an active SBS gain medium. Second, to evaluate and characterize the quality of local opto-acoustic interactions in this platform based on a high spatial resolution SBS measurement technique, which offers a state-of-the-art spatial resolution.

The second chapter provides a review of the literature of SBS from the historical point of view when it first was observed in optical fiber to today's state-of-the-art on-chip SBS devices. Then we discuss distributed Brillouin measurement techniques, which are conventionally used for distributed temperature and strain sensing. Next,

we explain how the performance of these techniques evolved over time and their functionality shifted from a distributed sensor in optical fibers to a characterization tool in on-chip waveguides.

In chapter three, we provide the theory necessary to understand nonlinear effects, specifically third-order nonlinearities which are the dominant effects in optical fibers, silicon and silicon-chalcogenide photonic waveguides. We show how the Maxwell's equations can be adapted to describe the propagation of optical waves in a nonlinear medium. The second part of this chapter discusses the physics of the SBS interaction by solving the coupled wave equations for SBS. We then introduce two main platforms for SBS which are used in this thesis. The third part of this chapter explains the principle of distributed Brillouin measurement techniques, including the one we used for demonstrating distributed on-chip sensing.

Chapter four describes the design of the silicon-chalcogenide hybrid platform and the experimental setup for investigating its third-order nonlinear performance. This experiment provides a measurement of self-phase modulation (SPM) and nonlinear loss of silicon and hybrid waveguides. We then provide a model for optical wave propagation through the hybrid waveguide to numerically evaluate its performance. The experimental data and the numerical simulation are compared to a conventional silicon waveguide, which shows two orders of magnitude improvement in terms of the nonlinear loss. The hybrid device is then further modified to accommodate acoustic modes as well as the optical mode for harnessing SBS. It is shown that by optimizing the design we can achieve significant SBS gain in the hybrid waveguide.

Chapter five demonstrates an experimental realization of distributed SBS measurement based on Brillouin optical correlation domain analysis (BOCDA) technique to characterize an on-chip photonic waveguide on a chalcogenide platform. We explain how this technique achieves sub-mm spatial resolution for the first time as a result of high signal to noise ratio (SNR) and high SBS gain.

In chapter six, we use the proof-of-principle experiment introduced in previous chapter to demonstrate a) a distributed Brillouin measurement of the hybrid silicon-chalcogenide platform, and b) a record spatial resolution of $500\,\mu\mathrm{m}$ capable of detecting a $200\,\mu\mathrm{m}$ longitudinal feature in the waveguide.

Finally, we conclude the thesis by providing a summary and an outlook for future works based on this study. These are including further improving the spatial resolution and discovering new pathways for forward Brillouin distributed sensing, which could be of great benefit for monitoring SBS waveguide in silicon platforms.

2 Stimulated Brillouin scattering for sensing: overview and state-of-the-art

In this chapter, we first provide a historical background on SBS in optical fibers in section 2.1 and in micro-scale structures in section 2.2. We then explain how Brillouin scattering is utilized for sensing in section 2.3. Different distributed Brillouin measurement techniques with an emphasis on spatial resolution evolution are discussed in section 2.4. In section 2.5, we discuss Brillouin-based sensing in micro-scale structures and short-length scale devices.

This chapter is mainly based on our published work in the Journal of Applied Sciences [4], with some extensions and modifications in order to adapt to this thesis.

2.1 A historical background on SBS

SBS is a nonlinear interaction between optical and acoustic waves. This interaction is facilitated through an optical force called *electrostriction* and its interaction process called *photoelasticity* [52]. Electrostriction is the tendency of the material to compress in the presence of intense optical fields. Photoelasticity is the change in electric permittivity as a result of a change in material density [43], [52], [53].

The basic SBS process is shown in figure 2.1 and is described as follows; two counter-propagating optical waves (pump and probe) with frequencies ω_p and ω_s travel through the medium. The frequency difference between the two optical waves creates a moving beat pattern with regions of low and high intensity, which in turns modulates the density of the medium through electrostriction. The speed of the beat pattern is equal to $v = \Omega/\Delta k$, where Δk is the difference between the pump and probe waves propagation constants and $\Omega = \omega_p - \omega_s$ is their frequency difference. If the speed of the beat pattern equals the sound velocity in the medium ($v = v_a$), then the acoustic wave in the medium is resonantly excited and is amplified. Under this condition, the frequency difference between the pump and probe waves is called Brillouin frequency shift (BFS). The amplified acoustic wave in turns creates moving index grating using photoelastic effect [43], [53]. The pump wave will reflect back from this moving grating with a Doppler shift in frequency due to the moving nature of the grating. This Doppler shifted pump matches the probe frequency and therefore adds to the strength of the probe wave. The amplified probe (called Stokes wave) further reinforces the acoustic wave and the acoustic wave amplifies the Stokes wave, which forms a positive feedback loop [53]. Brillouin scattering can be observed as backward or forward scattering involving longitudinal and transverse acoustic waves, respectively. Transverse acoustic waves mean that their propagation is mostly in the transverse direction to the propagation of the optical waves

in the waveguide. It should be noted that the term *SBS* used in this thesis refers to stimulated backward Brillouin scattering. Different terminologies are used in the literature for forward scattering such as forward Brillouin scattering (FBS), guided acoustic wave Brillouin scattering (GAWBS) or Raman-like scattering.

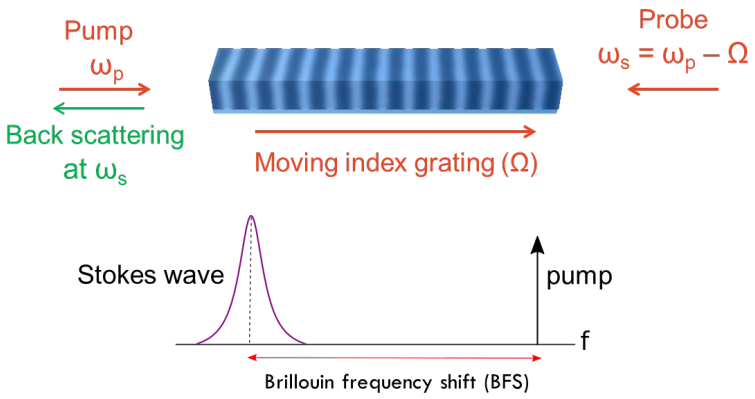

FIGURE 2.1: Schematic of the SBS process in a waveguide.

Brillouin scattering was first predicted by Leon Brillouin in 1922 [54] when he described theoretically the scattering of light waves from thermally excited acoustic waves which is accompanied by a frequency shift. At the same time (1926) Mandelstam studied Brillouin scattering in Russia [55]. However, it was not until the invention of the laser by Maiman in 1960 [56] that *stimulated* Brillouin scattering could be examined. The first experimental observation of SBS in crystals was reported by Chiao et al. in 1964 [57] followed by SBS observation in liquid [57]–[59] and gases [60]. A theoretical model for SBS based on the three coupled waves equations was proposed by Tang et al. [61] describing accurately the amplification of the Stokes wave during the SBS process.

The first observation of SBS in optical fiber was reported by Ippen et al. in 1972 [62]. In his paper, Ippen concluded that *"SBS limits the amount of narrow-band power which one can transmit through a fiber"*. This indicates that SBS from early stage was considered as a nuisance in optical communication systems since even moderate continuous wave (CW) pump powers could result in light interacting with thermal phonons and contributing to the backward SBS process by stimulating even more phonons. At the same time, Smith studied the Brillouin threshold in optical fibers for the backward scattering process to calculate the critical power below which stimulated Brillouin effect may be neglected [63]. This critical power depends upon the effective core area, the propagation loss of the fiber and the gain coefficient of the SBS process in silica fiber. In a different study Boyd et al. [64] derived the theoretical model for the case of the SBS generator that is when SBS is initiated from thermally excited acoustic phonons and showed how the Stokes linewidth and intensity depend upon the physical properties of SBS medium.

The low threshold power of SBS process was soon utilized to demonstrate the first semiconductor laser pumped Brillouin fiber amplifier in 1987 by Olsson et al. [65]. They demonstrated a broad bandwidth Brillouin fiber amplification by applying a frequency modulation (FM) to the pump laser. Shortly after that, Lichtman et al. studied the effect of modulated pump on the SBS threshold and gain [66]. In 1992, Gaeta et al. studied theoretically and experimentally the threshold required

to start a Brillouin oscillation in a cavity and demonstrated the Stokes linewidth narrowing above the threshold for Brillouin oscillation [67].

From an early stage, SBS was used as a characterization tool for optical fibers. This is due to the fact that opto-acoustic properties of the medium and consequently BFS changes with temperature and strain. In 1989, Culverhouse et al. predicted that Stokes frequency shift can be used as a means for distributed temperature sensing [68]. In 1990, Kurashima et al. demonstrated, for the first time, a distributed temperature measurement with spatial resolution of $100\,\mathrm{m}$ by monitoring BFS along the optical fiber [50]. This work followed by Bao et al. [69] and Nikles et al. [70] reporting improvements in spatial resolution. The development of distributed SBS measurement techniques will be discussed in detail in section 2.4.

2.2 SBS in micro-scale waveguides

In recent years, thanks to advanced fabrication methods, more complex forms of waveguides such as photonic crystal fibers (PCF), microfibers and on-chip waveguides have been introduced, which offer enhanced nonlinearity due to their small core dimensions and allow for group velocity dispersion tailoring [71]. If designed properly, these waveguides can support and confine both optical and acoustic modes, which due to their efficient overlap [44], [45], [52], [71]–[74] enable strong SBS effect. The first demonstration of SBS in such waveguides was reported by Dainese et al. [75] showing backward Brillouin scattering in a PCF, followed by SBS observation in microfibers [72] and on-chip waveguides [44], [45], [74]. SBS in micro-scale waveguides enable applications ranging from sensing in micro-structures [76]–[79] to RF signal processing [17], [18], RF sources [11], [12], narrow-linewidth lasers [6], [32], [33], [80], [81], frequency combs [36], and light storage [23], [82]. Examples of Brillouin scattering in micro-scale waveguides are shown in figure 2.2.

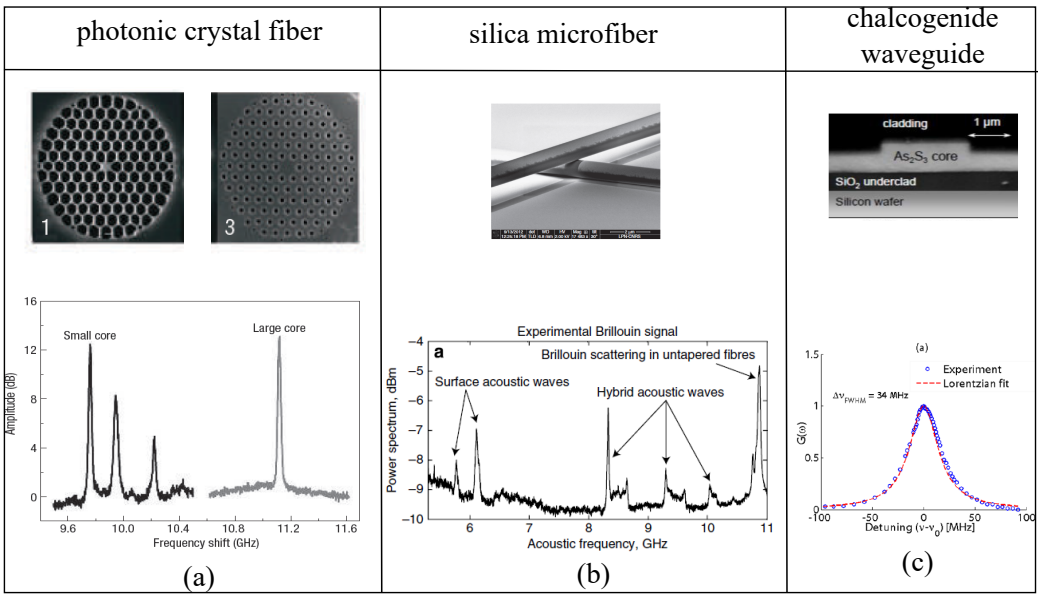

FIGURE 2.2: Examples of Brillouin scattering in a) PCF [75], b) silica microfiber [72] and c) chalcogenide waveguide [74].

The performance of optical waveguides in terms of gain and linewidth is influenced by the geometrical variation along the structure [42], [83], [84]. For example, in microfibers, the effect of Brillouin scattering can be suppressed by controlling the core diameter [52]. The diameter of the core also becomes important when coupling in and out of photonic circuits [85]. It was shown that structural irregularities in a PCF lead to a different Brillouin response compared a perfectly structured PCF [86]. Therefore, a detection technique is required to monitor and characterize opto-acoustic interactions in these structures. In this chapter, we will review Brillouin-based sensing techniques for monitoring and characterizing such structures. In chapter 4 we will explain the fabrication process and nonlinear performance of an on-chip waveguide which is specifically designed for harnessing SBS. In chapters 5 and 6, we demonstrate on-chip distributed sensing based on these waveguides.

2.3 SBS for sensing

Two main properties of the Brillouin gain spectrum are its linewidth and the frequency shift relative to the pump (BFS), which are employed for sensing purposes. The linewidth of the Brillouin gain spectrum is determined by to phonon lifetime or acoustic resonances and the BFS is determined by opto-acoustic properties of the medium. Therefore, any change in the environmental parameters such as temperature and strain or geometrical variations in the waveguide will affect these properties and can be detected by monitoring them.

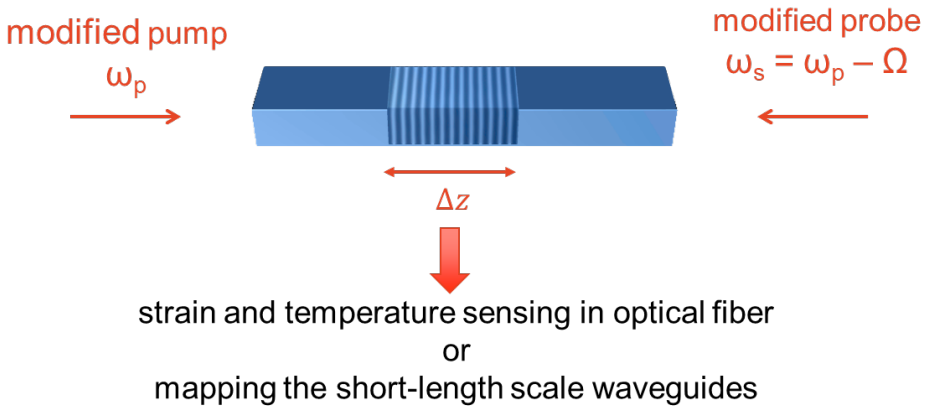

FIGURE 2.3: Schematic of the localized SBS process in a waveguide.

A conventional SBS measurement involves CW pump and signal waves which interfere along the entire length of the medium, and therefore, the measured backscattered signal is an integrated opto-acoustic response. In contrast, a distributed SBS response can be achieved by modifying the intensity or the phase of the pump and signal waves such that the SBS interaction is limited to a specific length in the medium and is suppressed elsewhere as schematically shown in figure 2.3. The most conventional distributed Brillouin measurement technique, which is called Brillouin optical time domain analysis (BOTDA), is based on a pulsed pump and

a CW probe [50], [69], [70], where the pulse duration determines the spatial resolution of the measurement [87]. The pulse duration in this technique is limited by the phonon lifetime, which sets a limit on the spatial resolution. In the following we introduce some of the distributed Brillouin measurement techniques, which are built on the principle of BOTDA or are based on a totally different approach, to advance the sensing capabilities such as spatial resolution and measurement range in optical waveguides.

2.4 Distributed Brillouin sensing techniques

In this section we provide a brief overview of various Brillouin distributed sensing techniques, all of which except the last one are based on backward Brillouin scattering.

2.4.1 Brillouin optical time domain analysis (BOTDA)

Brillouin optical time domain analysis (BOTDA) employs a pulsed pump and a CW probe which limits the SBS interaction length to the pump pulse duration. The first BOTDA demonstration in optical fiber was reported by Horiguchi et al. [88]. Compared to the previously demonstrated Brillouin time domain reflectometry (BOTDR) method [89], which was based on spontaneous Brillouin scattering, this approach has showed improvement in signal to noise ratio (SNR) and sensitivity. The first distributed temperature measurement using BOTDA was reported by Kurashima et al. [50] showing the temperature distribution along a silica single mode optical fiber with a spatial resolution of $100\,\mathrm{m}$ (figure 2.4 (a)). This demonstration was followed by the work of Bao et al. [69] reporting a distributed temperature measurement in an optical fiber with $5\,\mathrm{m}$ spatial resolution (figure 2.4 (b)). In 1996, Nikles et al. [70] showed for the first time a distributed strain and temperature measurement using a *single laser source* and an intensity modulator. The advantage of this approach is the high stability and reliability of the measurement compared to the previous approaches which either used two lasers for the pump and probe [90] or used one laser in the expense of a complex setup [91].

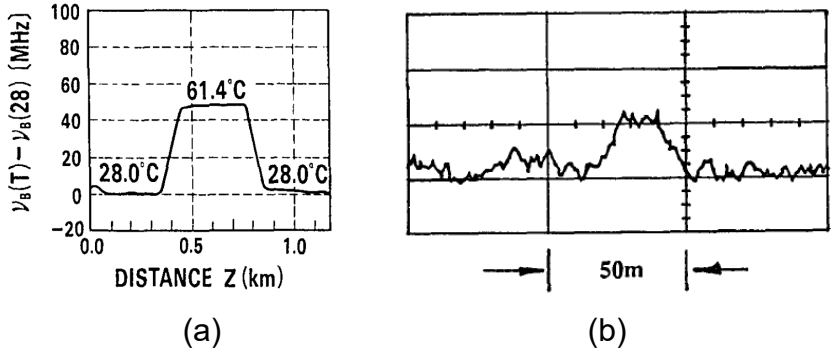

FIGURE 2.4: a) The first distributed temperature measurement using BOTDA with $100\,\mathrm{m}$ spatial resolution [50], b) $5\,\mathrm{m}$ hot spot in an optical fiber detected by BOTDA [69], the vertical axis in (b) is the intensity of back-scattered signal.

The spatial resolution of the BOTDA technique, however, is limited to $1\,\mathrm{m}$. This is due to the fact that for pump pulses shorter than the the phonon lifetime (approximately $10\,\mathrm{ns}$ in silica fiber), the Brillouin spectrum experiences a broadening, which makes the measurement inaccurate [87]. The impact of short pulse duration on SBS gain spectrum in this technique is discussed in chapter 3.

2.4.2 Brillouin echo distributed sensing (BEDS)

BEDS offers a solution to overcome the spatial resolution limit in BOTDA [92]–[94]. This technique, which is also a time-domain technique is based on the initial work of Bao et al. [95], [96]. In BEDS, a sudden change in the phase [39] (phase pulse) or amplitude (bright or dark pulse) of the pump pulse [39], [97] is utilised to localise Brillouin response beyond the phonon lifetime. Since the change in the pump pulse is sudden and much faster than phonon lifetime, the acoustic field experiences only a slight decay but still reflects the pump wave [39]. The bright pulse effect occurs when the background amplitude of the pump stimulates the acoustic wave. An additional increase in the pump appears as an additional amplification in the back-scattered signal, which was reported in [69]. The dark pulse occurs when the pump is normally on and it is switched off for a short time. This effect appears as a sudden drop in the SBS gain [97]. The phase pulse is a π phase shift change applied on the pump for a short time. During this time the pump and probe destructively interfere, and therefore, no SBS gain can be observed [98]. These effects are schematically shown in figure 2.5 [39].

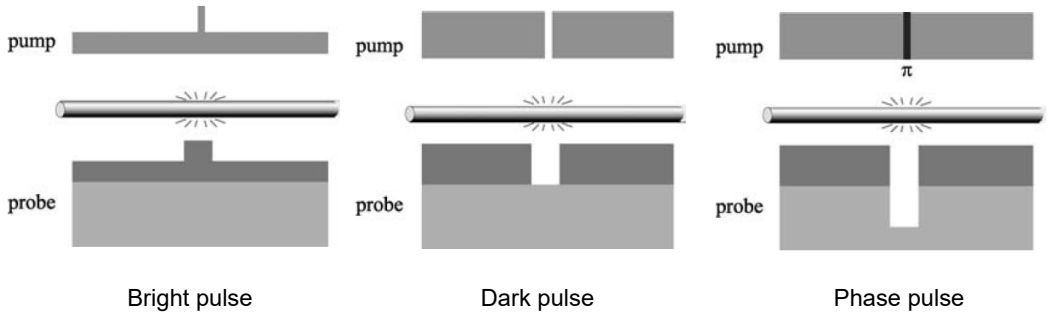

FIGURE 2.5: Schematic presentation of BEDS in bright pulse, dark pulse and phase pulse configurations. Figure is adapted from [39].

Spatial resolutions of $5\,\mathrm{cm}$ and $2\,\mathrm{cm}$ were reported using phase pulse [98] and dark pulse [97] techniques, respectively. Another similar technique is called pre-pump Brillouin optical time domain analysis (PPP-BOTDA). This technique is based on long pump pulses to excite the acoustic wave followed rapidly by a short pump pulse that enables high spatial resolution, while the probe is in the form of a CW signal counter propagating the pump [46], [99]–[101]. Spatial resolution of $2\,\mathrm{cm}$ was demonstrated using this technique [100].

2.4.3 Brillouin optical frequency domain analysis (BOFDA)

In addition to time domain techniques, frequency domain was also utilized to localize the SBS response. BOFDA first introduced by Garus et al. [102]. In this

technique, the pump and the amplified probe signals are transformed into the frequency domain by applying an intensity modulation to either probe [102] or pump [103] signal and then sweeping the modulation frequency to create the frequency response of the system. By dividing the output signal (amplified probe) by the input signal (pump) a transfer function of the system is obtained, which is basically the SBS response [102], [103]. By taking the inverse Fourier transform of this response, Brillouin response as a function of time (or position) is obtained.

Spatial resolution in this technique is given by: $\Delta z = \frac{c}{2n}\frac{1}{f_{m,max}-f_{m,min}}$, where $f_{m,max}$ and $f_{m,min}$ are maximum and minimum modulation frequencies, respectively [102]. Detection of a $20\,\mathrm{m}$ hot spot with a theoretical spatial resolution of $10\,\mathrm{m}$ was reported in [102] (figure 2.6 (a)) and an improved spatial resolution of $3\,\mathrm{cm}$ was demonstrated by [103] (figure 2.6 (b)). This technique requires post-processing (inverse Fourier transform) to recover the Brillouin gain spectrum with respect to the position and therefore, the measurement time is relatively long for cm-long spatial resolutions [103].

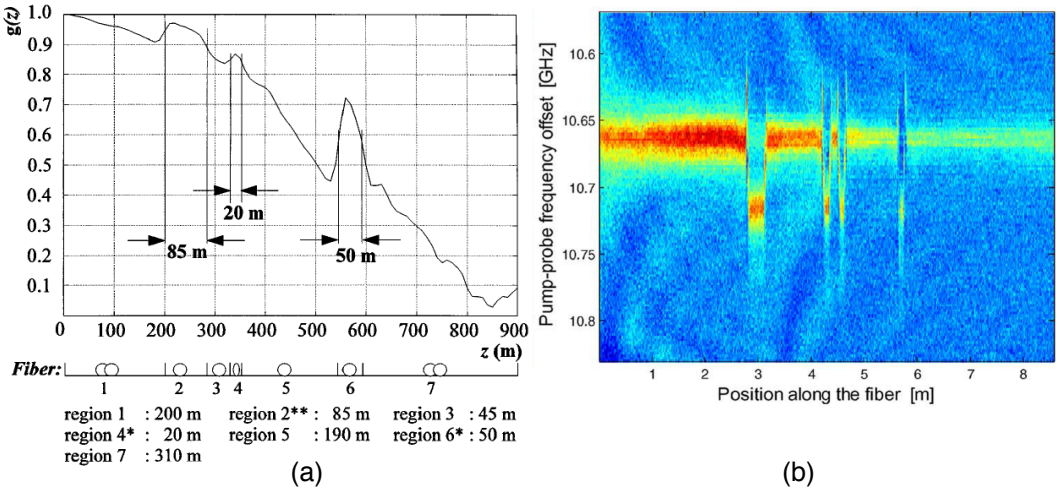

FIGURE 2.6: Distributed measurement based on BOFDA technique with spatial resolution of a) $10\,\mathrm{m}$ (figure is adopted from [102]) and b) $3\,\mathrm{cm}$ (figure is adopted from [103]).

2.4.4 Brillouin dynamic gratings (BDG)

The moving index grating generated by an optical pump and probe in the SBS process can play the role of a moving Bragg reflector for another optical wave under the right phase-matching condition [104]. This function is called BDG, which has a unique reflection spectrum sensitive to environmental variables such as temperature and strain [104], therefore can be used for sensing purposes. BDG employs the refractive index grating generated by SBS process in one polarization to Bragg reflect the pump wave in the orthogonal polarization [105]. For this purpose, two optical pump waves counter-propagate through the same polarization axis in a birefringent waveguide. The frequency difference between the two pumps is equal to the BFS of the medium, therefore a moving index grating (Brillouin dynamic grating) is created in one polarization axis. The probe is launched into the waveguide in an orthogonal polarization axis and is scattered back by the Brillouin dynamic grating formed

in the other axis. In this process, the probe does not interact with the pump wave through SBS directly but is affected by the dynamic grating created by the pump through SBS [104]. Figure 2.7 shows the basic principle of BDG in a birefringent material.

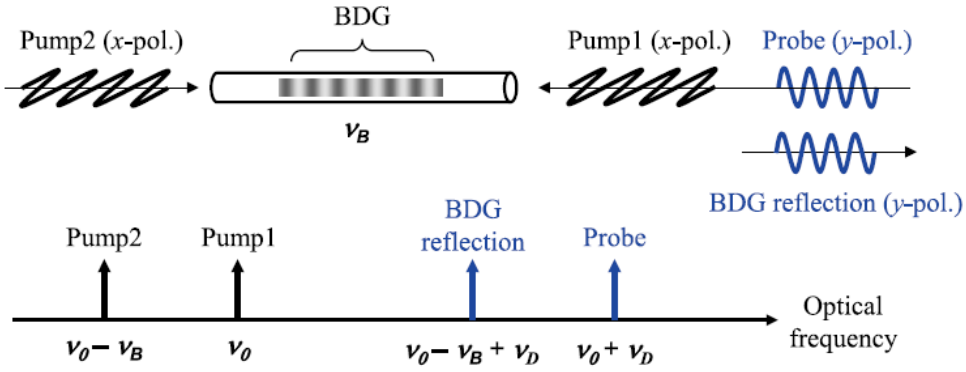

FIGURE 2.7: Schematic principle of BDG in a birefringent medium . Here ν_B and ν_D refer to BFS and BDG frequency, respectively (figure is adapted from [104]).

BDGs have been demonstrated in different platforms such as single mode fibers (SMF) [106] and polarisation maintaining fibers (PMF) [105] by carefully controlling the polarization of the pump and probe waves, photonic chips [107] and few-mode optical fibers (FMFs) [108]. The sensitivity of BDG spectrum has been utilized in time-domain [109] and correlation-domain [109] distributed measurements and has shown to improve the spatial resolution in BOTDA measurement [104], [110].

This technique can achieve sub-cm spatial resolution ($5.5\,\mathrm{mm}$) [110], however, it requires more than one pump laser to realize SBS in two orthogonal polarisation.

2.4.5 Brillouin optical correlation domain analysis (BOCDA)

BOCDA was first introduced by Hotate et al. [111], [112] and offers the highest spatial resolution among the Brillouin distributed sensing techniques. BOCDA is based on the correlation between the counter-propagating pump and probe waves and therefore unlike time domain technique is not limited by phonon lifetime. The pump and probe waves are driven from a low coherence source so that their interference in time is only partially correlated. The length of the correlation peak determines the spatial resolution in this technique. Low-coherence sources involved in BOCDA include frequency-modulated [112] or random-phase-modulated laser sources [51], amplified spontaneous emission (ASE) sources [113], and random lasers [114]. As illustrated in figure 2.8, all these techniques involve a source whose spectral bandwidth is defined either by frequency and phase modulation or a random process. The source is then split into counter propagating pump and probe signals, which are frequency shifted relative to each other by the BFS. The pump and probe signals have a constructive interference at the position of correlation peak, and destructive interference at all the other points due to their randomness, as schematically illustrated in figure 2.8. Different BOCDA approaches are discussed in the following.

The first demonstration of BOCDA was based on frequency modulation (with modulation amplitude or bandwidth of ΔF and modulation frequency f_m) of pump

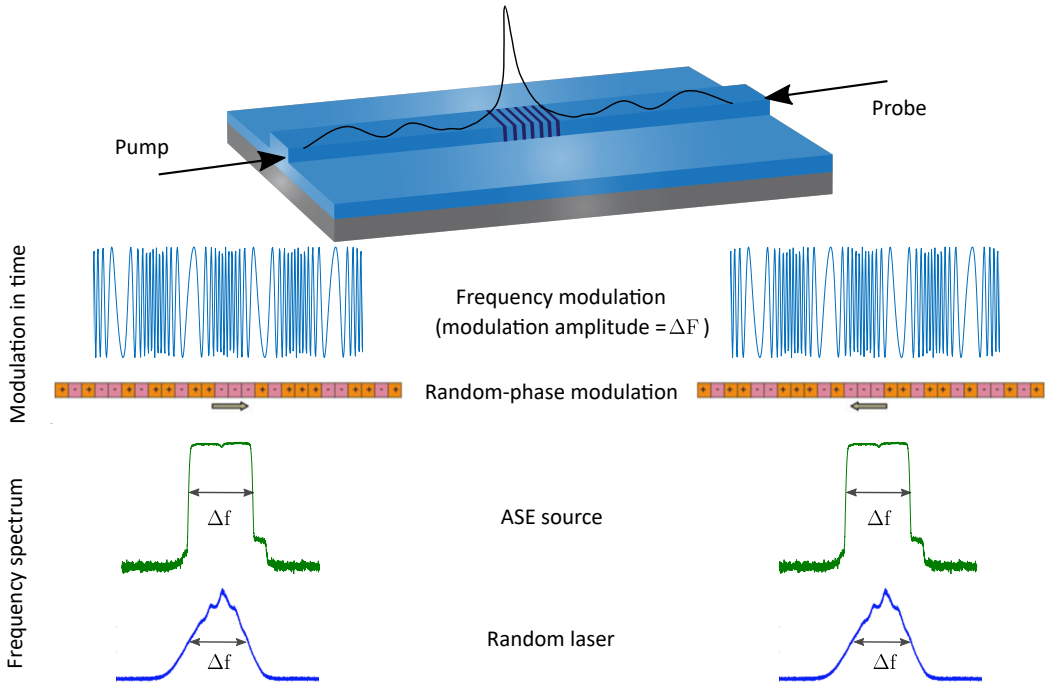

FIGURE 2.8: Schematic of various sources for BOCDA measurement from the top to the bottom: a frequency-modulated laser source with a modulation amplitude of ΔF [115], random phase coded laser source (adopted from [51]), amplified spontaneous emission (ASE) source with spectral width of Δf [1], [113] (adapted from [1], and a random laser based on a distributed feedback laser diode in an external feedback cavity [116] with a spectral width of Δf (adapted from [116].).

and probe waves [112]. The reported spatial resolution was $40\,\mathrm{cm}$ as shown in figure 2.10 (a). The spatial resolution is determined by the modulation amplitude ΔF. Wider modulation amplitude results in the higher spatial resolution. However, if the modulation amplitude is larger than BFS, it raises the problem of spectral overlap between the residual pump back-reflection (due to Rayleigh scattering) and the amplified probe, which cannot be separated using an optical filter. Therefore, the detected signal always has a background noise from this pump back-reflection and consequently a lower SNR. This issue was addressed by introducing two lock-in amplifiers (LIA) in the detection stage to electronically distinguish between the slow intensity-modulated back-reflected pump and the amplified probe [117]. In this technique, both pump and probe go through an extra intensity modulation with modulation frequencies of f_1 and f_2, respectively. As a result, when the two waves are constructively interfere, that is when the probe is amplified by the pump pulses due to Brillouin scattering, a difference frequency component ($f_2 - f_1$) is generated. By locking the LIA into this difference frequency, it is guaranteed that only the amplified probe is detected. A distributed strain measurement with a spatial resolution of $1.6\,\mathrm{mm}$ based on this technique was demonstrated by Song et al. [117]. Figure 2.9 (a)-(b) [38] shows a schematic of BOCDA measurement concept and the double lock-in amplifier scheme incorporated in it.

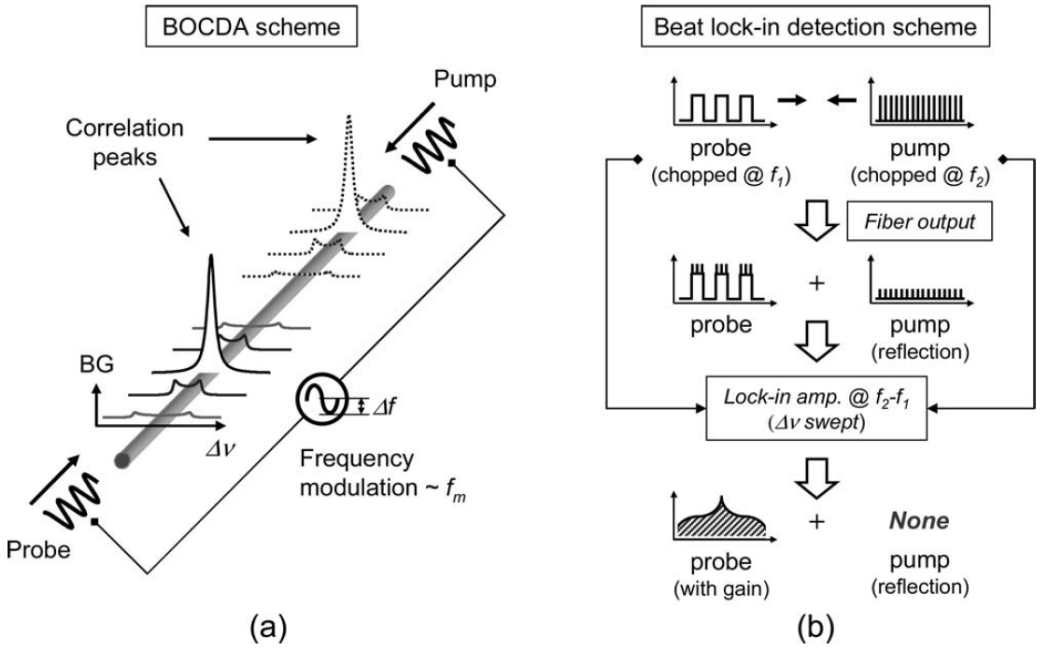

FIGURE 2.9: a) Frequency modulated BOCDA scheme in optical fiber (the modulation amplitude in this figure is expressed by Δf) , b) double lock-in amplifier detection concept (figure is adapted from [38]).

In this technique there is a trade-off between the measurement range and the spatial resolution, because they are both inversely related to the modulation frequency f_m. Therefore by increasing the spatial resolution, the measurement range decreases. This is due to the fact that frequency modulation of the pump and probe results in the generation of *periodic* correlation peaks, which in turns limits the measurement range. The technique introduced in the next paragraph addresses this issue to a great extent.

BOCDA measurements based on random phase-coded pump and probe waves introduced by Zadok et al. [51] significantly extended the measurement range while achieving high spatial resolution. In this technique, the pump and the probe are coded by a binary pseudo-random bit sequence (PRBS) with a symbol duration of T, where the spatial resolution is inversely related to T. The measurement range - defined by the separation between two adjacent correlation peaks - is determined by the length of the PRBS stream, which can be chosen to be considerably long to increase the measurement range [51]. This technique achieved a high spatial resolution of $1\,\mathrm{cm}$, as shown in figure 2.10 (b), with a theoretical measurement range of $1\,\mathrm{km}$ and experimental measurement range of $200\,\mathrm{m}$.

The SNR in this measurement was relatively low due to the existence of off-peak scattering, which scales with the measurement length. By introducing Golomb-coded pump and probe and comparing it with the PRBS coding, Antman et al. showed that a higher SNR and lower off-peak reflectivity can be achieved [118]. This technique was later combined with a time gating approach to demonstrate a distributed measurement with a spatial resolution of $2\,\mathrm{cm}$ and a measurement range of $400\,\mathrm{m}$ [119]. Combining BOCDA with the time gating technique has improved the SNR and the measurement range by eliminating the noise attributed to the locations outside the correlation peak [119]–[121].

A novel adaptation of BOCDA, introduced by Cohen et al. [113] is based on the ASE of an erbium-doped fiber. In this technique, a single correlation peak is generated whose spatial resolution relies on the bandwidth of the ASE source Δf. Unlike the frequency modulation technique, where high speed modulators are required, this approach offers a simple and less expensive solution based on an ASE source to obtain mm-order spatial resolution in optical fibers. Using this technique, a 4 mm hot spot was detected in an optical fiber [113]. The SNR in this approach is affected by the stochastic nature of the ASE source, which introduces an amplitude fluctuation to the SBS response. A medium with stronger SBS interaction such as on-chip photonic waveguides can improve the SNR. One of the main results of this thesis presented in chapter 5 is demonstrating an ASE-based BOCDA measurement of on-chip chalcogenide photonic waveguides, which leads to a higher SNR and a record spatial resolution of 800 µm [1]. Figure 2.10 (c) shows the detection of the waveguide facet with an 800µm spatial resolution using this technique.

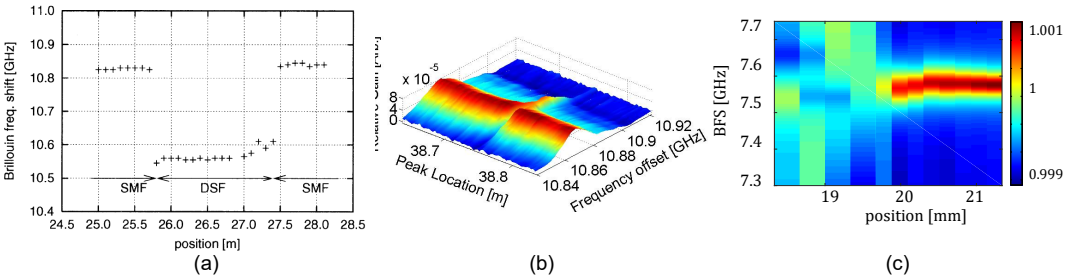

FIGURE 2.10: BOCDA techniques based on a) frequency modulation [112] (figure adopted from [112]), b) phase-coding (figure is adopted from [51]), and c) ASE (figure is adopted from [1]).

The practical spatial resolution in this technique is limited due to two main reasons. First, the probe amplification scales exponentially with the effective opto-acoustic interaction length; therefore, reduction in the effective opto-acoustic length as a result of increasing the spatial resolution leads to a lower SNR. Second, to achieve sub-mm spatial resolutions the ASE bandwidth exceeds the BFS, which results in a spectral overlap between the amplified probe and the back-reflected pump (Rayleigh scattering) and cannot be optically filtered. In the case of on-chip waveguides, this back-reflection is much stronger compared to the optical fiber due to the strong reflection from the waveguide facets, which sets a limit on the spatial resolution of on-chip sensing experiments [1]–[3].

In addition to the above techniques, a low-coherence chaotic laser has also been employed to detect a 5-cm hot spot in an optical fiber based on BOCDA principle [114]. In this method, the coherence of the random laser source is controlled by the feedback loop to the laser, which in turns determines the spatial resolution of the measurement.

Table 4.1 provides a summary of BOCDA distributed sensing techniques on different platforms with an emphasis on mm- and sub-mm spatial resolutions. Noticeable from this table is the change of platforms from optical fibers to on-chip waveguides as we move from cm-scale to mm and sub-mm spatial resolutions.

TABLE 2.1: Spatial resolution achievements in BOCDA techniques with a focus on mm- and sub-mm-scale resolutions.

Spatial Resolution	Technique	Ref.	Platform
40 cm	FM	[111]	optical fiber
10 cm	FM	[122]	optical fiber
5 cm	Random laser	[114]	optical fiber
3 cm	Random-phase code	[123]	microwire
1 cm	FM	[124]	optical fiber
1 cm	Random-phase code	[49], [51]	optical fiber, microwire
6 mm	FM	[47]	silica planar waveguide
4 mm	ASE	[113]	optical fiber
2 mm	FM	[125]	optical fiber
1.6 mm	FM	[38]	optical fiber
800 µm	ASE	[1]	on-chip waveguide
500 µm	ASE	[3]	on-chip waveguide

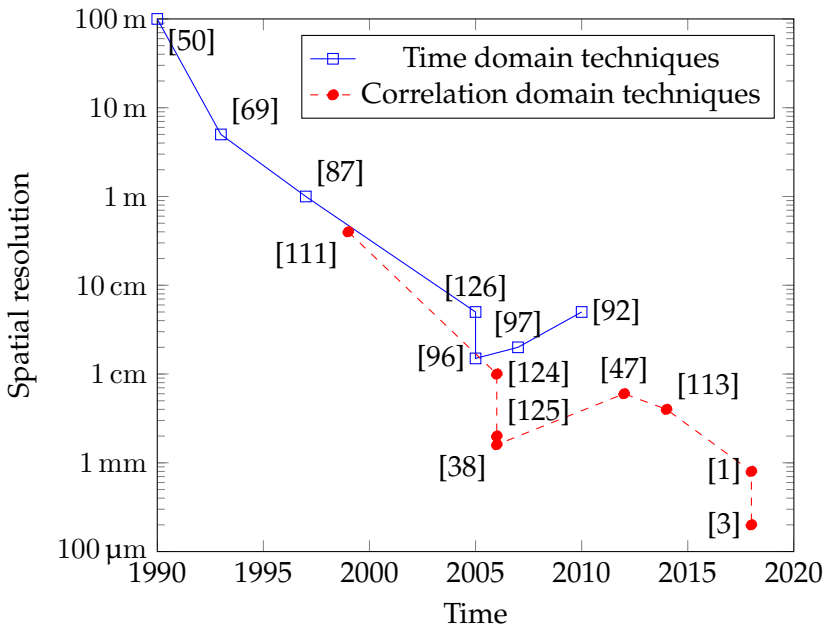

FIGURE 2.11: Overview of the spatial resolution evolution of time domain and correlation domain techniques.

Figure 2.11 compares the spatial resolution evolution of time domain techniques versus correlation domain techniques. The solid blue line in the plot shows the overall trend of the spatial resolution in time domain techniques, which has improved from 100 m to a few cm. The dashed red line indicates the progress in the spatial resolution of correlation domain techniques since their introduction in 1999. It becomes clear from this plot that the highest spatial resolutions so far belong to this technique. It should be noted that this plot does not include all the works published in the field of distributed Brillouin sensing, but only gives an indication of the progress in time domain and correlation domain Brillouin distributed sensing techniques in terms of the spatial resolution capabilities.

It can be seen in plot 2.11 that the introduction and evolution of BOCDA technique has increased the detection capabilities of Brillouin distributed sensing and put more emphasis on applications such as mapping opto-acoustic responses along waveguides [1], [47]. We discuss Brillouin sensing in micro-scale structures in section 2.5.

2.4.6 Distributed forward Brillouin scattering

In techniques we discussed so far, which were based on distributed backward Brillouin scattering, the change in temperature and strain is detected by the effect they impose on the opto-acoustic properties of the core material in optical fibers. Similarly, for applications such as chemical sensing using backward scattering, the substance under test needs to overlap with the core. This requires structural modification of standard fibers [127]–[130] or using special fibers such as PCFs [77]–[79] and microfibers [131]. Utilizing forward Brillouin scattering, however, allows for chemical detection using standard optical fiber without further modifications. This is because acoustic waves in forward scattering resonate across the fiber cross-section between the core and the cladding and can reach the surrounding material [132]. A demonstration of chemical sensing outside the cladding was made by Antman et al. [133] based on this technique.

A distributed measurement of Brillouin forward scattering, however, is very challenging. This is because unlike backward Brillouin scattering, where acoustic waves propagates longitudinally in the medium, in forward Brillouin scattering acoustic waves resonate transversally within the medium [132]. Therefore, a distributed measurement based on time-of-flight, which is the case in backward scattering, cannot be made in this case [134]. Two recent demonstrations of distributed forward Brillouin measurements in optical fibers which are reported in [134] and [132] will be discussed here. In these techniques the transverse acoustic modes resonating between the core and the cladding boundaries are affected by the properties of the surrounding media around the cladding and is detected by monitoring the linewidth of acoustic resonances [134].

The first approach reported by Bashan et al. [134] is called "opto-mechanical time domain reflectometry" and relies on the detection of Rayleigh back-scattering of the two optical waves involved in the stimulated FBS process, as shown in figure 2.12. In this technique, the optical pump and signal waves with a frequency difference equal to the target acoustic resonance frequency are sent to the fiber to stimulate the acoustic wave generation. The time trace of the Rayleigh back-scattering is then collected and the local information of the acoustic resonance is obtained from this time trace. This technique relies on the fact that the power level of the optical waves involved in stimulated FBS at each position is related to a nonlinear opto-mechanical coefficient, which can be used to extract the linewidth of the acoustic resonance. Using this technique, a spatial resolution of $100\,\mathrm{m}$ over $3\,\mathrm{km}$ of optical fibers is reported.

The second approach reported by Chow et al. [132] is based on the detection of backward SBS which contains information about local transverse acoustic modes. In this technique, a long optical pulse modulated by the transverse acoustic frequency is sent to the fiber to stimulate the transverse acoustic waves. It is followed by short pulses at a different frequency such that the short pulse experiences phase modulation as a result of transverse acoustic wave oscillations. By local recovery of the phase change of the second pulse, the properties of the acoustic wave (linewidth)

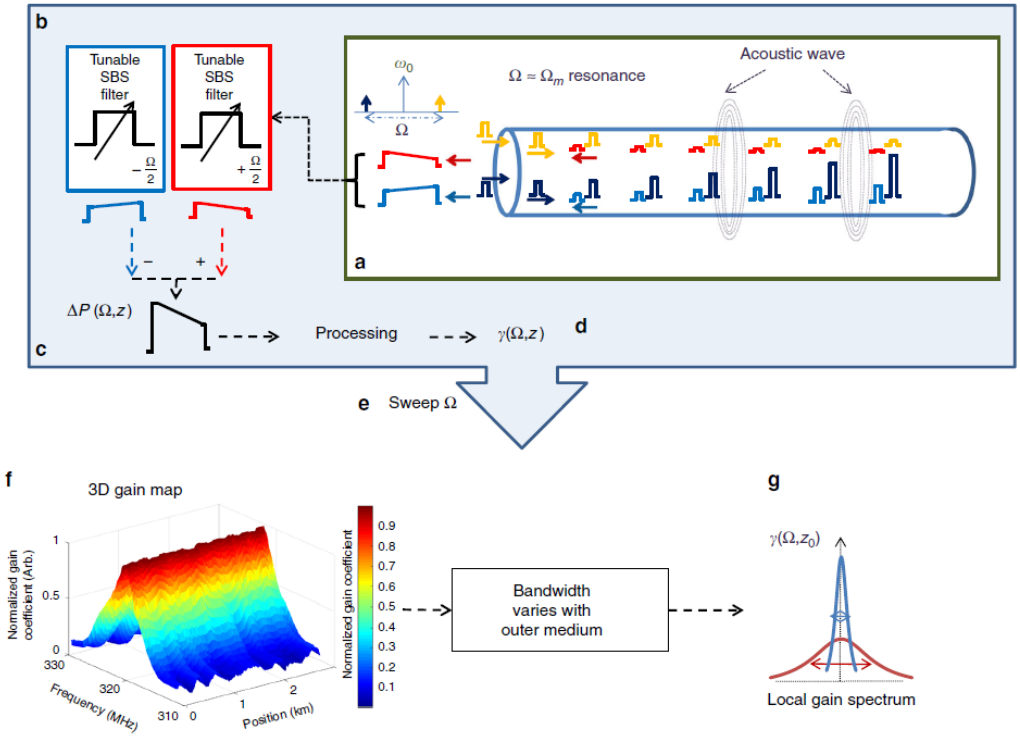

FIGURE 2.12: The principle of opto-mechanical time domain reflectometry based on Rayleigh back-scattering (figure is adapted from [134]).

is determined. This concept is shown in figure 2.13. The local measurement of the phase is performed using BOTDA technique. This means that the optical pulse containing the phase information counter-propagates a CW probe with a frequency difference equal to the BFS. The collected back-scattered wave as a function of time can be used to detect the intensity of a certain acoustic mode locally, which is selected by tuning the pump and probe center frequency. The intensity information is then used to retrieve the linewidth of the acoustic mode. Using this technique a spatial resolution of $15\,\mathrm{m}$ over a $730\,\mathrm{m}$ measurement range was reported.

These experiments open up new opportunities for characterizing on-chip silicon devices in the future, which has not been possible using backward Brillouin distributed measurement. This is mainly due to the fact that silicon exhibits strong forward Brillouin scattering which has found applications in lasers [81], non-reciprocal modulators [135] and RF photonic filters [135] and therefore, opto-acoustic characterization of such devices is of great interest in this field. While the spatial resolution demonstrated by these techniques are not sufficient for monitoring cm- and mm-scale waveguides, there is room for spatial resolution improvement as suggested by the authors.

So far, we mainly reviewed distributed Brillouin measurement techniques and their applications in optical fibers. In the following section, we focus on Brillouin sensing of micro-scale structures as a whole or locally based on the techniques we introduced in this section.

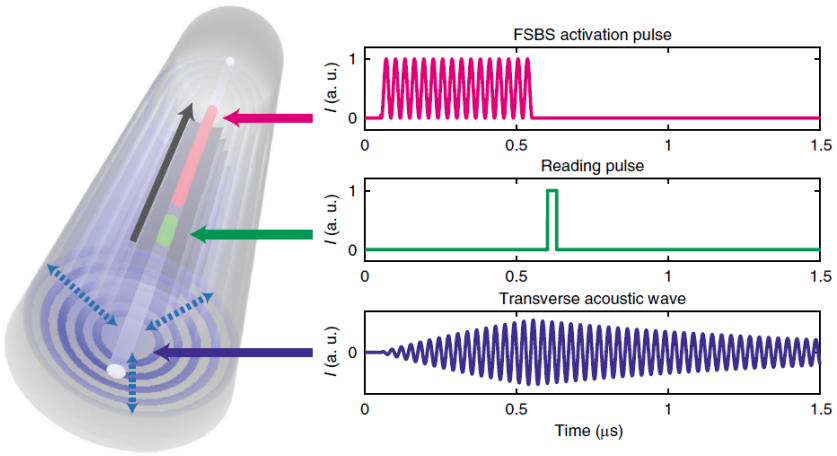

FIGURE 2.13: Concept of the local light phase-recovery based on SBS (figure is adapted from [132]).

2.5 Brillouin sensing of micro-scale structures

Brillouin scattering has been employed to detect geometrical variations such as waveguide diameter in *micro-scale waveguides* including PCFs, microfibers, and on-chip waveguides. In this section, we explain how Brillouin scattering in micro-scale waveguides is affected by their geometries. Then, we discuss detection of transverse and longitudinal variations along the waveguide utilizing forward and backward Brillouin scattering, respectively.

2.5.1 Integrated backward Brillouin measurement

The dependence of Brillouin backward scattering on the waveguide geometry in micro-scale structures is evident in the work of Dainese et al. [75], where it is shown that the spectrum of spontaneous Brillouin scattering in a small-core diameter PCF is significantly different from that in a large-core diameter PCF, as shown in figure 2.14. The large-core PCF shows a single peak at frequency 11.2 GHz, corresponding to the dominant longitudinal acoustic mode in the bulk silica, while the small core PCF shows a family of peaks due to the existence of hybrid shear and longitudinal acoustic modes in the sub-wavelength core structure.

A form of acoustic wave observed in sub-wavelength waveguides is called surface acoustic wave (SAW). Unlike the conventional silica fiber, where the acoustic modes are in the form of pure longitudinal or shear modes, in the sub-wavelength regime, the acoustic wave could take the form of a surface acoustic wave or a hybrid acoustic wave (HAW), consisting of both longitudinal and shear components [42], [75]. SAWs propagate in the direction of the pump, on the surface of the microstructure with a velocity lower than a pure longitudinal wave and scatter the light wave. Figure 2.15 (a) shows SAW spectrum in a microfiber, which was first observed by Beugnot et al. [72]. Tchahame et al. reported the first observation of SAWs in a PCF and experimentally demonstrated that the SAW spectrum is highly dependent on the structure of the PCF, as well as surface irregularities [73]. The two spectra shown in figure 2.15 (b) belong to PCFs with different core diameters. The shift in the Brillouin peak between the two spectra is due to the core diameter difference,

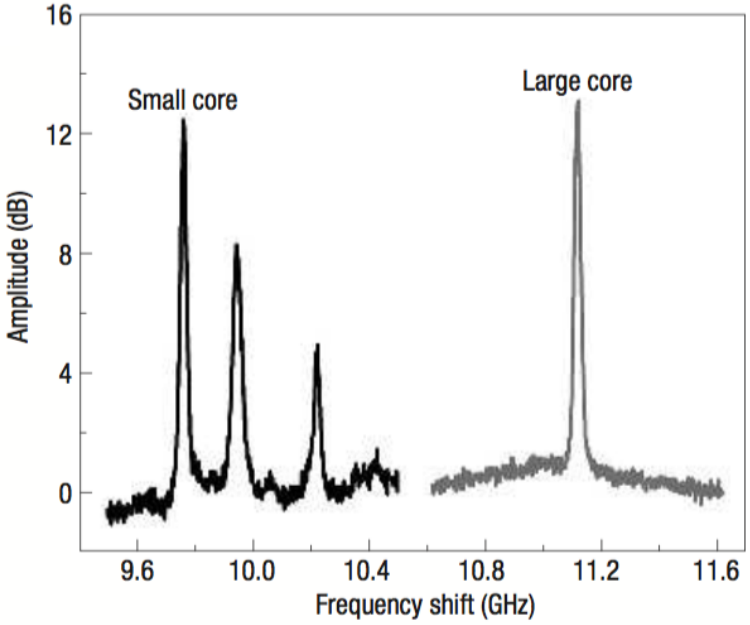

FIGURE 2.14: Comparison of the Brillouin spectrum in a large core diameter photonic crystal fiber (PCF) and a small core diameter PCF (figure is adopted from [75]).

while the difference between the amplitudes is linked to the micro-structure irregularities [73].

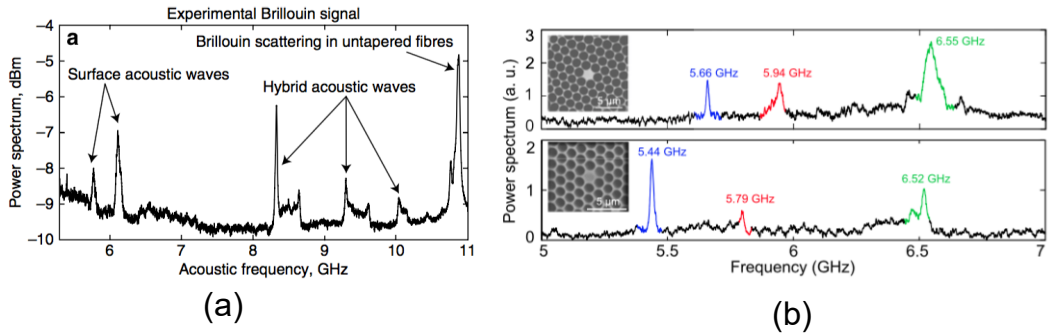

FIGURE 2.15: Spectrum of surface acoustic wave (SAW) in a) a microfiber (figure is adopted from [72]) and b) two PCFs with different core diameters (figure is adopted from [73]).

The backward Brillouin spectrum was utilized to estimate the core diameter of microfibers. Godet et al. [136] demonstrated an in situ measurement of microfiber core diameter with a sensitivity of a few nm based on backward SAW and HAW measurement. After collecting the Brillouin spectrum, it was compared with a numerically-calculated map of the surface, longitudinal and shear acoustic waves at different core diameters (refer to figure 2.16) to estimate the diameter of the core. Florez et al. [52] demonstrated the so called Brillouin self-cancellation effect based on the dependence of the backward Brillouin scattering on the microfiber core diameter. In this work, it was shown that the opposite effects of moving boundaries and photo-elasticity in sub-wavelength regimes could reduce Brillouin back-scattered signal and even

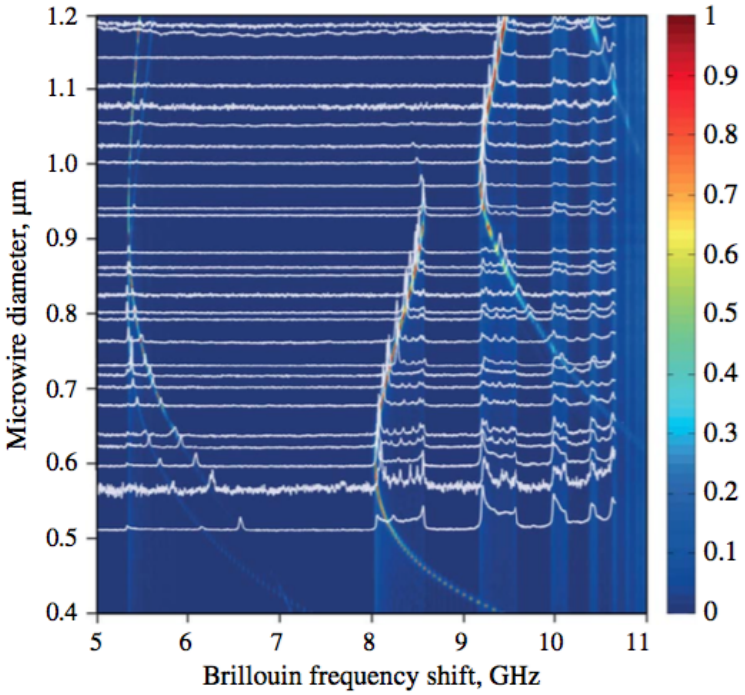

FIGURE 2.16: Mapping of the experimental surface Brillouin spectrum with the numerically-calculated responses to detect the core diameter of the microfiber under fabrication (figure is adopted from [136]).

cancel it at certain core diameters. This experiment suggests that the spectrum of the backward Brillouin scattering could be less sensitive to the core diameter than forward Brillouin scattering, which will be discussed in the next section.

2.5.2 Integrated forward Brillouin measurement

Forward Brillouin scattering has been exploited to measure the core diameter [137]. In addition, the effect of geometry on transverse opto-acoustic responses in micro-scale waveguides has been studied in different platforms; Beugnot et al. [138] showed that the existence of air hole areas in a PCF enhances some transverse acoustic modes while suppressing the others by introducing additional boundary conditions over which phonons are spatially distributed, a behaviour that is different from a conventional dispersion-compensation fiber (DCF). Kang et al. in [71] showed that unlike the conventional silica fiber, which has a weak forward Brillouin interaction, a sub-wavelength PCF provides a strong interaction between the incident pump light and the transverse acoustic modes by tightly trapping them together within the small core of the PCF. The effect of boundary forces namely radiation pressure on opto-acoustic responses of an on-chip silicon nano-structure has been experimentally demonstrated by Van Laer et al. [44], where a pillar-shaped silicon waveguide exhibited significant Brillouin gain by trapping the acoustic mode in the under-etched silicon waveguide and its strong overlap with the transverse optical mode.

In a different study, Kittlaus et al. [45] demonstrated an enhancement on the Brillouin amplification in an on-chip silicon waveguide by designing a suspended silicon membrane, which guides optical and acoustic modes separately and ensures strong opto-acoustic coupling between them.

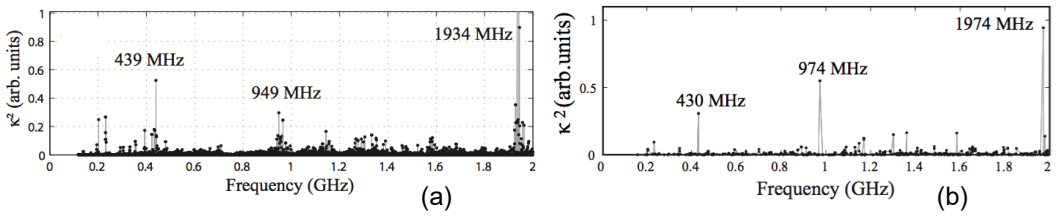

FIGURE 2.17: Finite element model (FEM)-based numerical simulation of a) the elasto-optic coefficient of the PCF under test (figure is adopted from [86]) and b) the elasto-optic coefficient of the perfect PCF (figure is adopted from [86]).

The mentioned works so far show how to detect geometry-dependent opto-acoustic responses and estimate the core diameter of the entire waveguide with high sensitivity. However, in order to fully characterize the opto-acoustic interactions in micro-scale waveguides, an axial opto-acoustic profile of the waveguide needs to be constructed. This can be explained through the following example; In Ref. [86], it is experimentally demonstrated that the spectral width of Brillouin gain profile in a PCF is affected by structural imperfections. The existence of degenerate acoustic peaks in the elasto-optic coefficient plot shown in figure 2.17 (a) is attributed to the transverse structural irregularities such as defect holes, angles, and pitches. For comparison, figure 2.17 (b) shows the calculated elasto-optic parameter for a perfect PCF with no irregularities. It is also theoretically shown by Wolff et al. [41] that the opto-acoustic strength and the spectral linewidth of the Brillouin response in nano-scale Brillouin waveguides are sensitive to fabrication imperfections. However, such defects cannot be located by an integrated SBS measurement. In order to detect longitudinal variations along the waveguide, a distributed SBS measurement is required, which is discussed in the following section.

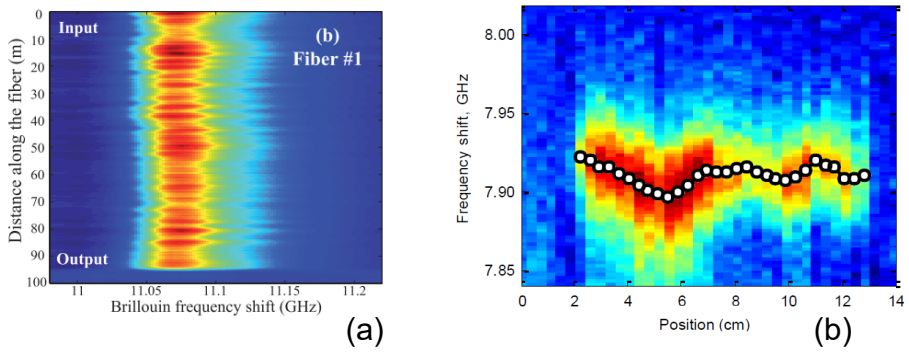

FIGURE 2.18: Longitudinal map of a) a PCF using Brillouin echo distributed sensing (BEDS) techniques with a spatial resolution of 30 cm (figure is adopted from [48]) and b) a microfiber based on phase-coded BOCDA (figure is adopted from [49]).

2.5.3 Distributed backward Brillouin measurement

Characterization of longitudinal opto-acoustic responses in micro-scale waveguides requires a distributed measurement of backward Brillouin spectrum with high spatial resolution. Several studies have utilised distributed Brillouin sensing techniques to characterize micro-scale waveguides, which will be discussed in this section.

The longitudinal map of opto-acoustic responses along a piece of PCF based on BOTDA was reported by Beugnot et al. [139], where the BFS and the full-width half-maximum (FWHM) of the Brillouin spectrum along the PCF was resolved with a spatial resolution of $2\,\mathrm{m}$. Figure 2.18 (a) shows the mapping of the Brillouin responses based on BEDS reported by Stiller et al. [48], where the effect of the strain and the waveguide irregularities on the local backward SBS responses of the PCF with spatial resolution of $30\,\mathrm{cm}$ was studied. Chow et al. [49] mapped the uniformity of a microfiber by capturing the distributed backward SBS responses using phase-coded BOCDA measurement. Figure 2.18 (b) shows the local Brillouin spectrum along the $13\,\mathrm{cm}$-long microwire with spatial resolution of $9\,\mathrm{mm}$. Later, Chow et al. demonstrated a local excitation and capturing of the surface acoustic waves along a microwire [123]. Their setup allows for local excitation and monitoring of the core diameter by analysing surface opto-acoustic responses along the waveguide based on the phase-coded BOCDA technique with a spatial resolution of $5.2\,\mathrm{cm}$. Distinct acoustic resonances along the tapered fiber based on this technique are shown in figure 2.19.

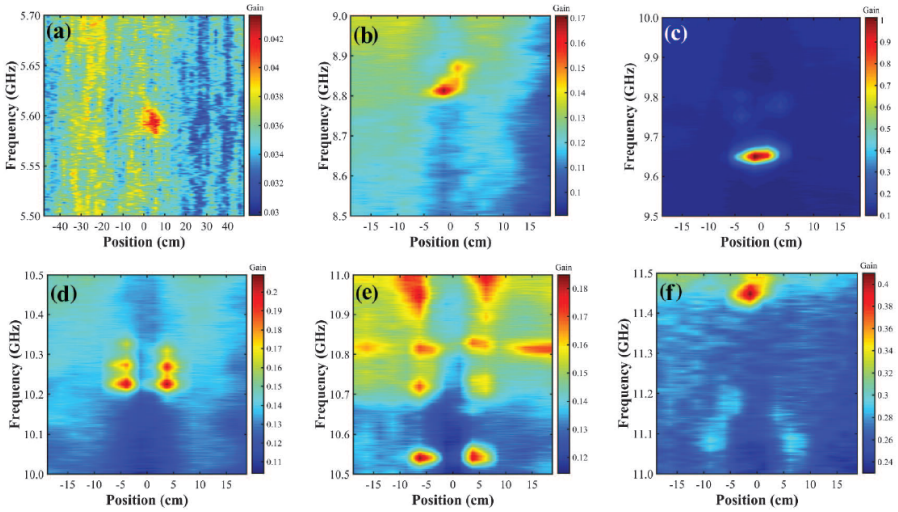

FIGURE 2.19: Brillouin spectrum of the tapered fiber using phase-coded BOCDA measurement at different frequency ranges (a)–(f) (figure is adopted from [123]).

The high spatial resolution offered by BOCDA also enables monitoring of opto-acoustic responses along the cm- and mm-scale on-chip waveguides. Hotate et al. studied the effect of bends on the backward SBS responses in a silica planar waveguide using BOCDA [47]. In this experiment, a frequency-modulated BOCDA measurement with a spatial resolution of $5.9\,\mathrm{mm}$ was demonstrated. In figure 2.20 (a), the oscillations in the BFS along the waveguide determine the positions of the bends

in the waveguide. Following the introduction of the ASE-based BOCDA measurement by [113], which offers simplicity and high spatial resolution, a series of local SBS measurements were conducted on As_2S_3 photonic waveguides which demonstrated waveguide monitoring capability of this technique with sub-mm spatial resolution ($500\,\mu m$) [3]. Chapter 5 and 6 will explain in detail the technique and design, fabrication and experimental steps toward achieving such a high spatial resolution.

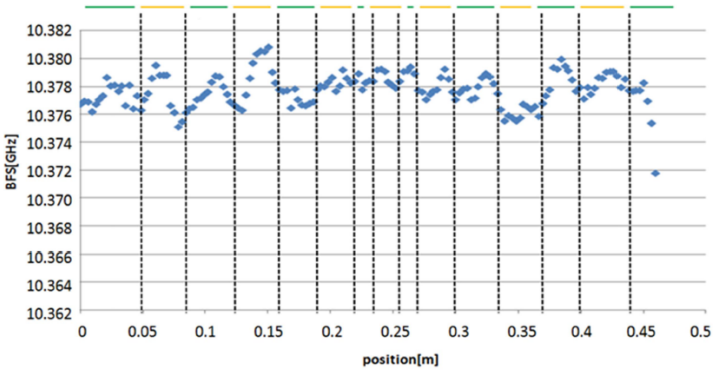

FIGURE 2.20: Mapping of a) a silica planar waveguide with a spatial resolution of $5.9\,mm$ using frequency-modulated BOCDA (figure is adopted from [47]).

3 Nonlinear optics

This chapter explains the origin of nonlinearity in optical materials and gives explanations for two nonlinear effects that are discussed in this thesis namely self-phase modulation (SPM) and SBS. We start with a mathematical description for optical nonlinearity and derive nonlinear wave equation starting from Maxwell equations. Here we distinguish between linear and nonlinear refractive index and loss. Then we solve the nonlinear wave equations to find the evolution of the optical pulse in a nonlinear medium.

The second part of this chapter discusses the origin of Brillouin scattering and its two main manifestations; backward and forward scattering. Then we explain the concept of *stimulated* Brillouin scattering by providing mathematical description for optical and acoustic waves coupling. We find an expression for SBS gain by solving the coupled wave equations for SBS. Finally, SBS in chalcogenide and hybrid waveguide is briefly discussed and SBS interaction in sub-wavelength regimes is explained through an example.

The third part of this chapter deals with distributed SBS response and explains the principle of two main distributed SBS measurement methods namely time- and correlation-domain techniques with a focus on the correlation-domain approach.

3.1 Introduction

Photonics is the science of generating, controlling and detecting photons. Similar to its electronic counterpart, which deals with controlling and manipulating electrons, photonics deals with manipulating photons. However, in contrast to electrons which can interact with each other, photons do not interact with other photons in a linear regime, but interact with other particles such as electrons and phonons [10], [28], [53]. On a microscopic scale (in dielectric materials) the electric field of an optical signal induces an electric dipole moment by displacing the electron orbital from its nucleus as illustrated in figure 3.1 (a). The electric field is represented by $\mathbf{E}(\mathbf{r},t)$ [1] with $\mathbf{r}$ being the position vector and t is the time. On a macroscopic scale, the average dipole moment per unit volume forms a polarization field $\mathbf{P}(\mathbf{r},t)$ as shown in figure 3.1 (b). The induced polarization resonates with the frequency of the incident electric field and radiates an electromagnetic field which interferes with the original electric field. The relation between the induced polarization and the incident electric field in an isotropic material is described by the optical susceptibility in the following form [10]:

$$\mathbf{P}(r,t) = \epsilon_0[\chi^{(1)}\mathbf{E}(r,t) + \chi^{(2)}\mathbf{E}^2(r,t) + \chi^{(3)}\mathbf{E}^3(r,t) + ...], \tag{3.1}$$

[1] Throughout this chapter, bold characters are representing vector variables.

where ϵ_0 is the permittivity of free space, $\chi^{(1)}$ is the linear susceptibility and $\chi^{(2)}$ and $\chi^{(3)}$ are the second-order and third-order nonlinear optical susceptibilities, respectively. In its linear form, this interaction is the origin of the complex linear refractive index n, which can be described by Lorentz $\chi^{(1)}_{\text{Lorentz}}$ and Drude $\chi^{(1)}_{\text{Drude}}$ models [28]:

$$n^2 = 1 + \chi^{(1)}_{\text{Lorentz}} + \chi^{(1)}_{\text{Drude}}, \tag{3.2}$$

The Lorentz model describes the contribution of the bound electrons in semiconductors to the refractive index. The oscillation of a bound electron between a bound state and a virtual level with resonance frequency of the bound electron being ω_0 and a damping constant of γ_L result in a change in susceptibility according to the following equation [28]:

$$\chi^{(1)}_{\text{Lorentz}} = \frac{Nq^2/\epsilon_0 m_e}{\omega_0^2 - \omega^2 + i\gamma_L\omega}, \tag{3.3}$$

where N is the number of dipoles, q is the elementary charge and m_e is the effective mass.

The Drude model describes the contribution of free-carriers to the refractive index, where photons being absorbed by free electrons followed by a nonradiative recombination process result in the change in the susceptibility as follows [28]:

$$\chi^{(1)}_{\text{Drude}} = \frac{Nq^2/\epsilon_0 m_e}{-\omega^2 + i\gamma_D\omega}, \tag{3.4}$$

where γ_D is the Drude damping constant. Free-carrier absorption results in the refractive index change referred to as free-carrier index (FCI) change and the loss mechanism called free-carrier absorption (FCA) [28], [140]. We will explain FCA in section 3.2.2 of this chapter.

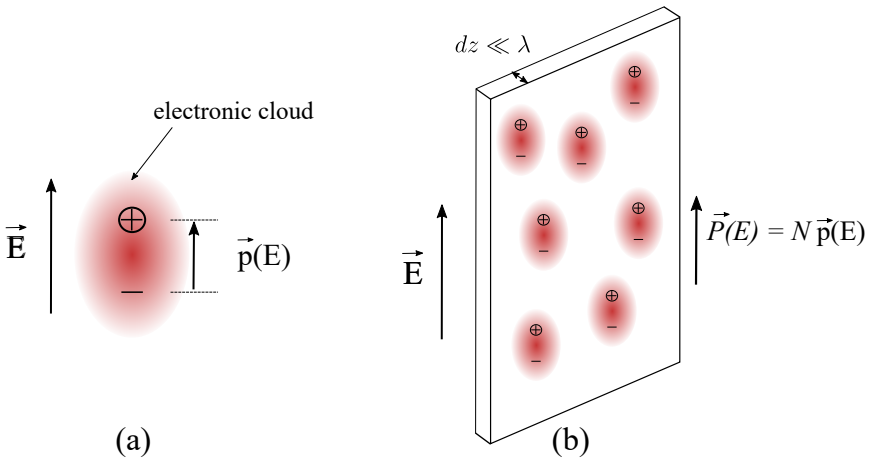

FIGURE 3.1: Induced polarization vector as a result of an incident electric field in dielectric materials: a) microscopic view and b) macroscopic view. In this figure, arrows indicate vector variables.

So far, we looked at the first order susceptibility. What if the induced polarization does not change linearly with the applied electric field? In this case - which happens in the presence of high intensity electric fields - the polarization is expanded in terms of the electric field as described by equation 3.1. In equation 3.1, the electric field

relates to the polarization through nonlinear susceptibility terms resulting in the generation of new frequencies, which is the domain of nonlinear optics.

In this chapter we study two types of optical nonlinearities: first, self induced nonlinearities namely self-phase modulation (SPM) and two-photon absorption (TPA), which stem from the real and imaginary parts of the nonlinear refractive index, respectively. The other nonlinearity studied here is the nonlinear interaction of photons with acoustic phonons known as stimulated Brillouin scattering. Before looking at these nonlinear phenomena, it is necessary to understand the propagation of electric fields through the waveguide, which will be explained using Maxwell's equations.

3.1.1 Maxwell's equations

The interaction of an optical field with a medium is formulated by Maxwell's equations. The optical field is composed of an electric field $\mathbf{E}(\mathbf{r},t)$ and a magnetic field $\mathbf{H}(\mathbf{r},t)$. The propagation of electric and magnetic fields relate to each other through the following equations [10]:

$$\nabla \times \mathbf{E} = -\frac{\partial \mathbf{B}}{\partial t}, \tag{3.5}$$

$$\nabla \times \mathbf{H} = \mathbf{J} + \frac{\partial \mathbf{D}}{\partial t}, \tag{3.6}$$

$$\nabla \cdot \mathbf{D} = \rho, \tag{3.7}$$

$$\nabla \cdot \mathbf{B} = 0, \tag{3.8}$$

where $\mathbf{J}(\mathbf{r},t)$ is the current density vector and ρ is the charge density and $\mathbf{D}(\mathbf{r},t)$ and $\mathbf{B}(\mathbf{r},t)$ are the electric and magnetic flux densities, respectively. The electric and magnetic flux densities are described by the following relations:

$$\mathbf{D} = \epsilon_0 \mathbf{E} + \mathbf{P}, \tag{3.9}$$

$$\mathbf{B} = \mu_0 \mathbf{H} + \mathbf{M}, \tag{3.10}$$

in which $\epsilon_0 = 8.854 \times 10^{-12}$ [F/m] is the vacuum permittivity and $\mu_0 = 4\pi \times 10^{-7}$ [H/m] is the vacuum permeability. $\mathbf{P}(\mathbf{r},t)$ and $\mathbf{M}(\mathbf{r},t)$ are the induced electric and magnetic polarization, respectively. In dielectric materials - which are mainly the type that we study in this thesis - there is no free charge, therefore $\rho(\mathbf{r},t) = 0$. It is also assumed that $\mathbf{J}(\mathbf{r},t) = 0$ and $\mathbf{M}(\mathbf{r},t) = 0$. By taking the curl of equation 3.5 and replacing $\nabla \times \mathbf{B}$ by $\mu_0 \frac{\partial \mathbf{D}}{\partial t}$ from equations 3.6 and 3.10, we obtain:

$$\nabla \times \nabla \times \mathbf{E} = -\mu_0 \frac{\partial^2}{\partial t^2} \mathbf{D}, \tag{3.11}$$

substituting $\mathbf{D}(\mathbf{r},t)$ from equation 3.9 into equation 3.11, we obtain the general wave equation as follows:

$$\nabla \times \nabla \times \mathbf{E} = -\frac{1}{c^2} \frac{\partial^2 \mathbf{E}}{\partial t^2} - \mu_0 \frac{\partial^2 \mathbf{P}}{\partial t^2}, \tag{3.12}$$

where c is the speed of light in vacuum and $\mu_0 \epsilon_0 = \frac{1}{c^2}$. The left hand side of equation 3.12 can be written as:

$$\nabla \times \nabla \times \mathbf{E} \equiv \nabla(\nabla \cdot \mathbf{E}) - \nabla^2 \mathbf{E} \tag{3.13}$$

The term $\nabla \cdot \mathbf{E}$ disappears from the right hand side of equation 3.13 since $\epsilon \nabla \cdot \mathbf{E} = \nabla \cdot \mathbf{D} = \rho = 0$ [10]. Equation 3.13 therefore can be written as:

$$\nabla^2 \mathbf{E} - \frac{1}{c^2} \frac{\partial^2 \mathbf{E}}{\partial t^2} = \mu_0 \frac{\partial^2 \mathbf{P}}{\partial t^2}, \tag{3.14}$$

where the polarization consists of linear ($\mathbf{P}_L$) and nonlinear ($\mathbf{P}_{\mathrm{NL}}$) parts and therefore can be presented in the following from:

$$\nabla^2 \mathbf{E} - \frac{1}{c^2} \frac{\partial^2 \mathbf{E}}{\partial t^2} = \mu_0 \frac{\partial^2 \mathbf{P}_L}{\partial t^2} + \mu_0 \frac{\partial^2 \mathbf{P}_{\mathrm{NL}}}{\partial t^2}, \tag{3.15}$$

In the next section, we look at the optical pulse propagation through the medium using equation 3.15. We study linear and nonlinear behaviour of optical field while propagating in the medium in sections 3.1.2 and 3.2, respectively.

3.1.2 Linear refractive index

As it is shown in equation 3.15, the polarization term consists of linear and nonlinear parts, which are related to the incident electric field according to equation 3.1. In order to find the effect of linear polarization on the optical pulse propagation, we consider an input optical pulse in the following form [10]:

$$\mathbf{E}(\mathbf{r}, t) = \frac{1}{2}[E(\mathbf{r}, t)e^{(-i\omega_0 t)} + c.c.]\hat{x}, \tag{3.16}$$

where $E(\mathbf{r}, t)$ is a slowly varying function of time relative to the optical period and $\hat{x}$ indicates the polarization vector.

Similarly, the linear polarization can be expressed in the following format [10]:

$$\mathbf{P}_L(\mathbf{r}, t) = \frac{1}{2}[P_L(\mathbf{r}, t)e^{(-i\omega_0 t)} + c.c.]\hat{x}, \tag{3.17}$$

while $\mathbf{P}_L$ relates to the electric field through the following relation:

$$\mathbf{P}(\mathbf{r}, t) = \epsilon_0 \chi^{(1)} \mathbf{E}(\mathbf{r}, t). \tag{3.18}$$

To express the relation between linear refractive index and susceptibility, we first consider only the contribution of linear polarization in equation 3.15 by making the assumption that the nonlinear polarization is a small perturbation to the linear polarization [10]. Then, substituting equation 3.18 into the linear form of equation 3.12 results in the following expression:

$$\nabla \times \nabla \times \mathbf{E}(\mathbf{r}, t) = [1 + \chi^{(1)}(\omega)] \frac{1}{c^2} \frac{\partial^2 \mathbf{E}}{\partial t^2}, \tag{3.19}$$

Taking the Fourier transform of equation 3.19 results in the following expression:

$$\nabla \times \nabla \times \mathbf{E}(r, \omega) = [1 + \chi^{(1)}(\omega)] \frac{\omega^2}{c^2} \mathbf{E}(\mathbf{r}, \omega), \tag{3.20}$$

where $\mathbf{E}(\mathbf{r}, \omega)$ is the Fourier transform of $\mathbf{E}(\mathbf{r}, t)$ and is defined as:

$$\mathbf{E}(\mathbf{r}, \omega) = \int_{-\infty}^{\infty} \mathbf{E}(\mathbf{r}, t) e^{(i\omega t)} dt, \tag{3.21}$$

The term $1 + \chi^{(1)}(\omega)$ in equation 3.20 is the frequency dependent dielectric constant $\epsilon(\omega)$, which is a complex number and its real and imaginary parts are related to the real and imaginary parts of the refractive index through the following equation [10]:

$$\epsilon(\omega) = [n(\omega) + i\frac{\alpha(\omega)}{2k_0}]^2, \tag{3.22}$$

where the imaginary part of refractive index is expressed based on the absorption coefficient $\alpha(\omega)$ and the wave number of the incident optical filed $k_0 = \frac{\omega}{c}$. From equation 3.22, the *linear* refractive index and absorption coefficient relate to the susceptibility as follows [10]:

$$n(\omega) = 1 + \frac{1}{2}\mathrm{Re}(\chi^{(1)}(\omega)), \tag{3.23}$$

$$\alpha(\omega) = \frac{\omega}{nc}\mathrm{Im}(\chi^{(1)}(\omega)). \tag{3.24}$$

So far, we have studied the relation between the linear susceptibility and the linear refractive index, however, in order to find the the relation between the nonlinear susceptibility and the nonlinear refractive index, nonlinear polarization term needs to be considered in solving equation 3.15, which will be discussed in the following section.

3.2 Nonlinear refractive index (Kerr nonlinearity)

In equation 3.1, the linear susceptibility is the strongest term which represent the linear light-matter interactions such as linear absorption and dispersion. Higher order susceptibility terms - depending on their orders - require higher optical power in order to be effective, which sets a threshold on the required power to start a nonlinear effect. Therefore, second-order nonlinear effects such as second harmonic generation and electro-optic effects and third-order nonlinearities such as self-phase modulation (SPM), cross-phase modulation (XPM) and four-wave mixing (FWM) are among the strongest nonlinear effects. However, it should be noted that not all materials exhibit second-order nonlinearities. In fact, centrosymmetric materials lack $\chi^{(2)}$ nonlinearity and they only show odd-order nonlinear effects. Therefore, in such materials, examples of which include silica, silicon and chalcogenide, the strongest nonlinear term is $\chi^{(3)}$, which is what we are going to discuss in this section. In the following, we will explain how third-order nonlinearity leads to the so called *nonlinear refractive index* (Kerr nonlinearity), which is the origin of self-induced effects namely SPM as well as a nonlinear absorption process known as two-photon absorption (TPA).

In order to study the effect of third-order nonlinearity in the optical wave equation, one needs to include the effect of nonlinear polarization in equation 3.15. Before going through the equations, we need to make some assumptions: first, as mentioned before $\mathbf{P}_{\mathrm{NL}}$ is treated as a perturbation to $\mathbf{P}_L$. Second, it is assumed that the polarization is maintained in the waveguide under study and therefore the scalar approach is valid and third, the spectral width of the pulse ($\Delta\omega$) satisfies the condition $\frac{\Delta\omega}{\omega_0} \ll 1$, where ω_0 is the pulse center frequency on the order of $10^{15}\ \mathrm{s}^{-1}$, which makes the last assumption valid for optical pulses as short as $0.1\,\mathrm{ps}$. The electric field

again can be written in the form of a slowly varying variable as shown in equation 3.16. Similarly, the nonlinear polarization can be expressed in the form of equation 3.25 with $\mathrm{P_{NL}}(\mathbf{r},t)$ being the slowly varying variable:

$$\mathbf{P}_{\mathrm{NL}}(\mathbf{r},t) = \frac{1}{2}[\mathrm{P_{NL}}(\mathbf{r},t)e^{(-i\omega_0 t)} + c.c.]\hat{x}, \tag{3.25}$$

The relation between the third-order polarization and the electric field according to equation 3.1 can be written as:

$$\mathbf{P}_{\mathrm{NL}}(\mathbf{r},t) = \epsilon_0 \chi^{(3)} \mathbf{E}^3(\mathbf{r},t), \tag{3.26}$$

replacing $\mathbf{E}(\mathbf{r},t)$ from equation 3.16 and $\mathbf{P}_{\mathrm{NL}}(\mathbf{r},t)$ from equation 3.25, we obtain:

$$\mathrm{P_{NL}}(\mathbf{r},t)e^{(-i\omega_0 t)} = \epsilon_0 \chi^{(3)}[\frac{1}{4}E(\mathbf{r},t)e^{(-i3\omega_0 t)} + \frac{3}{4}E(\mathbf{r},t)^3 e^{(-i\omega_0 t)}]. \tag{3.27}$$

The first term in this equation is referred to as the third harmonic generation, which is very weak and can be neglected. The second term is the dominant nonlinear effect and results in the following expression [10]:

$$\mathrm{P_{NL}}(\mathbf{r},t) \approx \frac{3}{4}\epsilon_0 \chi^{(3)} \left|E(\mathbf{r},t)\right|^2 E(\mathbf{r},t), \tag{3.28}$$

in which the term $\frac{3}{4}\epsilon_0 \chi^{(3)} \left|E(\mathbf{r},t)\right|^2$ is referred to as the nonlinear dielectric constant ϵ_{NL}. By substituting equations 3.16, 3.17 and 3.25 in equation 3.15, the Fourier transform of equation 3.15 is found to be:

$$\nabla^2 E + \epsilon(\omega) k_0^2 E(r, \omega - \omega_0) = 0, \tag{3.29}$$

This equation is in the form of the Helmholtz equation, where $\epsilon(\omega)$ is the dielectric constant in frequency domain consisting of linear (ϵ_{L}) and nonlinear (ϵ_{NL}) parts as follows:

$$\epsilon(\omega) = \underbrace{1 + \chi^{(1)}}_{\text{Linear}} + \underbrace{\frac{3}{4}\chi^{(3)} \left|E(\mathbf{r},t)\right|^2}_{\text{Nonlinear}}. \tag{3.30}$$

The relation between *nonlinear* refractive index n_2 and *nonlinear* absorption coefficient α_2 (also called TPA coefficient) with third-order susceptibility can be expressed as [10]:

$$n_2(\omega) = \frac{3}{8n}\,\mathrm{Re}(\chi^{(3)}), \tag{3.31}$$

$$\alpha_2(\omega) = \frac{3\omega_0}{4nc}\,\mathrm{Im}(\chi^{(3)}) \tag{3.32}$$

The complex refractive index can be expressed based the linear and nonlinear refractive index and absorption as follows [10], [28]:

$$n_T = n + n_2 \left|E\right|^2 - i(\alpha + \alpha_2 \left|E\right|^2), \tag{3.33}$$

where n_2 and α_2 are the intensity-dependant refractive index and absorption, respectively. We explain the role of n_2 in nonlinear phase shift or SPM in section 3.2.1. Then we describe the effect of α_2 on the nonlinear loss process in section 3.2.2.

3.2.1 Nonlinear Schrödinger equation (NLSE)

As described in equation 3.29, the nonlinear wave equation takes the form of the Helmholtz equation, therefore it can be solved using the technique of separation of variables [10]. A solution to equation 3.29 is in the form of [10]:

$$E(\mathbf{r}, \omega - \omega_0) = F(x, y)A(z, \omega - \omega_0)e^{ik_0 z}, \tag{3.34}$$

Assuming that the electric field is polarized along the x axis and is propagating in the z direction, $A(z, \omega - \omega_0)$ represents the slowly varying envelope of the pulse and k_0 is the wave number at frequency ω_0. F(x, y) represents the transverse optical mode distribution inside the waveguide, known as the eigenvalue equation in ref. [10]. The eigenvalue equation and the pulse propagation equation are the solutions of equations 3.29 and therefore can be expressed in the form of the following equations:

$$\frac{\partial^2 F}{\partial x^2} + \frac{\partial^2 F}{\partial y^2} + [\epsilon(\omega)k_0^2 - k^2]F = 0, \tag{3.35}$$

$$2ik_0 \frac{\partial A}{\partial z} + (k^2 - k_0^2)A = 0. \tag{3.36}$$

In equation 3.36, the second derivative $\frac{\partial^2 A}{\partial z^2}$ is neglected since $A(z, \omega)$ is a slowly varying function of z. This approximation is known as *the slowly varying amplitude approximation* and it means that the change in the amplitude occurs over many optical cycles. By approximating the dielectric constant to the first order perturbation, we get:

$$\epsilon = (n + \Delta n)^2 \approx n^2 + 2n\Delta n, \tag{3.37}$$

where $\Delta n = n_2 |E|^2 + \frac{i\alpha}{2k_0}$. Now solving equation 3.35 for n^2 and Δn, leads to a modal distribution $F(x, y)$ and its relevant wave number:

$$k(\omega) = k(\omega) + \Delta k(\omega), \tag{3.38}$$

where $\Delta k(\omega)$ is obtained by including the effect of Δn in equation 3.35, resulting in the following expression [10]:

$$\Delta k(\omega) = \frac{\omega^2 n(\omega)}{c^2 k(\omega)} \frac{\int\int_{-\infty}^{\infty} \Delta n(\omega) |F(x, y)|^2 \, dxdy}{\int\int_{-\infty}^{\infty} |F(x, y)|^2 \, dxdy}. \tag{3.39}$$

Substituting equation 3.38 into equation 3.36 we get:

$$\frac{\partial A}{\partial z} = i[k(\omega) + \Delta k(\omega) - k_0]A. \tag{3.40}$$

In equation 3.40, we expand $k(\omega)$ in a Taylor series around ω_0 considering only the first and second-order terms that is: $k(\omega) = k_0 + (\omega - \omega_0)k_1 + \frac{1}{2}(\omega - \omega_0)^2 k_2$. Here, k_1 and k_2 are related to the group velocity v_g and group velocity dispersion (GVD), respectively. By approximating $\Delta k(\omega) \approx \Delta k_0(\omega)$, we get:

$$\frac{\partial A}{\partial z} = i[(\omega - \omega_0)k_1 + \frac{1}{2}(\omega - \omega_0)^2 k_2 + \Delta k_0(\omega)]A \tag{3.41}$$

taking the inverse Fourier transform of function $A(z, \omega - \omega_0)$ in equation 3.41 and replacing $\omega - \omega_0$ with $i\frac{\partial}{\partial t}$, we receive the following equation for A(z,t):

$$\frac{\partial A}{\partial z} + k_1 \frac{\partial A}{\partial t} + ik_2 \frac{\partial^2 A}{\partial t^2} = i\Delta k_0 A. \tag{3.42}$$

This equation can be further simplified by replacing Δk_0 with equation 3.39 which includes the effect of linear absorption (α) and Kerr nonlinearity (n_2) through the term Δn, and considering $k(\omega) \approx n(\omega)\frac{\omega}{c}$ [10]:

$$\frac{\partial A}{\partial z} + k_1 \frac{\partial A}{\partial t} + ik_2 \frac{\partial^2 A}{\partial t^2} + \frac{\alpha}{2} A = i\gamma(\omega_0) |A|^2 A, \tag{3.43}$$

Here, $\gamma(\omega)$ is the nonlinear parameter defined as [10], [141]:

$$\gamma(\omega) = \gamma'(\omega) + i\gamma"(\omega) = \frac{n_2\omega_0}{cA_{\text{eff}}} + \frac{i\alpha_2}{2A_{\text{eff}}} \tag{3.44}$$

where its real and imaginary parts indicate effective Kerr nonlinearity and effective nonlinear loss of the waveguide, respectively. For media with negligible nonlinear loss, $\gamma" = 0$. In equation 3.44, A_{eff} is the effective nonlinear area, which depends upon the mode distribution and is defined as [10]:

$$A_{\text{eff}} = \frac{(\int\int_{-\infty}^{\infty} |F(x,y)|^2 \, dxdy)^2}{\int\int_{-\infty}^{\infty} |F(x,y)|^4 \, dxdy}. \tag{3.45}$$

Then by making the transformation: $T = t - z/v_g$, and using $k_1 = 1/v_g$, where v_g is the group velocity, we are moving in the time frame of the pulse, therefore the term $k_1\frac{\partial A}{\partial t}$ in equation 3.43 vanishes and this equation is further simplified to [10]:

$$\frac{\partial A}{\partial z} + \frac{\alpha}{2} A + ik_2 \frac{\partial^2 A}{\partial T^2} = i\gamma(\omega_0) |A|^2 A, \tag{3.46}$$

It should be noted that equations 3.43 to 3.45 are valid for isotropic media such as optical fibers. However, care should be taken when dealing with non-isotropic media in which the electric field is not entirely transversal and has components in the direction of propagation. This condition will be discussed in chapter 5 when we apply this equation to a non-isotropic medium.

In order to find a general description for the amplitude and the phase evolution of the optical pulse in an isotropic dielectric waveguide, we consider for now that the effect of second-order dispersion (group velocity dispersion) and linear loss in equation 3.46 are negligible, therefore:

$$\frac{\partial A}{\partial z} = i\gamma(\omega_0) |A|^2 A. \tag{3.47}$$

We also represent the complex amplitude $A(z,t)$ by its amplitude $u(z,t)$ and phase $\phi(z,t)$, $A = u(z,t)\text{exp}(i\phi(z,t))$, and substitute it in equation 3.47 to obtain:

$$\frac{\partial u}{\partial z} + iu\frac{\partial \phi}{\partial z} = i\gamma(\omega_0)u^3 = (i\gamma'(\omega) - \gamma"(\omega))u^3 \tag{3.48}$$

Equating the real and imaginary parts of the left hand side to the right hand side and using equation 3.44 give us two expressions for the evolution of the amplitude

and the phase of the optical pulse as follows:

$$\frac{\partial u}{\partial z} = -\frac{\alpha_2}{2A_{\text{eff}}}u^3, \tag{3.49}$$

$$\frac{\partial \phi}{\partial z} = \frac{n_2\omega_0}{cA_{\text{eff}}}u^2. \tag{3.50}$$

From equation 3.50, it can be seen that the nonlinear refractive index (n_2) affects the phase of the optical pulse, which itself has induced the nonlinear effect in the first place. As mentioned earlier, this effect is called SPM and the nonlinear phase shift caused by this effect can be expressed by:

$$\Delta\phi_{\text{NL}} = \frac{n_2\omega_0}{cA_{\text{eff}}}u^2\Delta z = \frac{\omega_0}{c}(n_2 I)\Delta z, \tag{3.51}$$

where intensity is $\text{I} = u^2/A_{\text{eff}}$. This equation shows that the nonlinear phase shift is proportional to the nonlinear refractive index and changes with the intensity. The time-dependent nature of the optical intensity implies that $\Delta\phi_{\text{NL}}$ is a temporally varying phase shift, which in turns leads to the change in instantaneous frequency across the pulse:

$$\Delta\omega(t) = \frac{\partial\phi_{NL}}{\partial t}. \tag{3.52}$$

This time-dependant instantaneous frequency generates new frequencies across the pulse which is called frequency chirping and leads to spectral broadening or narrowing of the optical pulse depending on the initial chirp of the pulse.

Now back to equation 3.46, which resembles the nonlinear Schrödinger equation (NLSE), where k_2 represent group velocity dispersion, α is the linear absorption and γ is the nonlinear parameter. Pulse propagation in a nonlinear medium is therefore dependent upon these parameters. The propagation distance (L), pulse length (T_0) and pulse peak power (P_0) determine which parameter has the dominant effect on the pulse propagation. The effect of these factors can be studied using the following length scales:

$$L_{\text{eff}} = \frac{1 - exp(-\alpha z)}{\alpha}, \tag{3.53}$$

$$L_D = \frac{T_0^2}{|k_2|}, \tag{3.54}$$

$$L_{\text{NL}} = \frac{1}{\gamma' P_0}. \tag{3.55}$$

The effective length L_{eff} provides a length scale which includes the effect of linear loss. Dispersion length L_D and nonlinear length L_{NL} indicate the length over which dispersion and nonlinearity become significant. Based on theses definitions, we can define four different pulse propagation regimes:

- $L_{\text{eff}} \ll L_{NL}$ and $L_{\text{eff}} \ll L_D$: neither dispersive nor nonlinear effects influence the pulse propagation significantly.
- $L_{\text{eff}} \ll L_{NL}$ and $L_{\text{eff}} \sim L_D$: GVD is the dominant effect in pulse propagation.

- $L_{\text{eff}} \sim L_{NL}$ and $L_{\text{eff}} \ll L_D$: nonlinearity is the dominant effect in pulse propagation.
- $L_{\text{eff}} \sim L_{NL}$ and $L_{\text{eff}} \sim L_D$: GVD and nonlinear effects both influence the pulse propagation.

3.2.2 Nonlinear loss

The intensity-dependant loss known as TPA, which results from the third-order nonlinearity is depicted in figure 3.2. As it is seen in this figure, TPA occurs when two photons are absorbed simultaneously and excite an atom to a higher energy state. While TPA does not occur in silica fiber since its band gap energy is larger than the energy of two photons at wavelength $1550\,\text{nm}$ ($2h\nu_0 = 1.6\,\text{eV}$), it becomes a strong nonlinear absorption mechanism in silicon with band gap energy of $E_g = 1.12\,\text{eV}$. Since in this thesis we study waveguides which are based on silicon, our derivations in this section are based on specific values and coefficients for silicon.

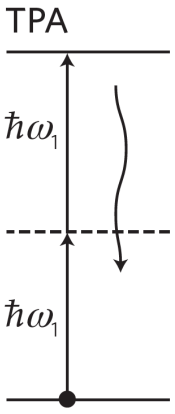

FIGURE 3.2: Schematic of TPA process in silicon. Figure is adapted from ref. [28].

This third-order nonlinear loss mechanism is described by equation 3.49 earlier in this chapter. If we rewrite this equation in terms of intensity we get:

$$\frac{\partial I}{\partial z} = -\alpha_2 I^2, \tag{3.56}$$

As it is seen in equation 3.56, TPA scales quadratically with the input optical intensity, which sets a limit on the maximum input power to the waveguide before the nonlinear absorption becomes too strong. In addition, the absorption of two photons leads to the generation of a free electron in the conduction band. The TPA-induced free electrons result in the process of FCA and therefore add to the total loss of the system. The total optical loss as a result of TPA, FCA and linear absorption can be described by the following equation [142]:

$$\frac{\partial I}{\partial z} = -\alpha_2 I^2 - \alpha_{\text{FCA}} I^3 - \alpha I, \tag{3.57}$$

where α_{FCA} for center frequency of $1550\,\text{nm}$ is expressed by [142]:

$$\alpha_{\text{FCA}} = \sigma(\frac{\lambda}{1.55 \times 10^{-6}})^2 \frac{\alpha_2 \tau_c \lambda}{2hc}. \tag{3.58}$$

In equation 3.58, $\sigma = 1.45 \times 10^{-21}$ is the free-carrier coefficient and $\tau_c \approx 1\,\text{ns}$ is the free-carrier lifetime [143].

Since we will study Kerr nonlinearity in a silicon and silicon-chalcogenide waveguide later in this thesis, we need to develop a model that accounts for TPA and FCA in the optical pulse propagating equation (NLSE). In this section, we look at the effect of TPA and FCA on optical pulse propagation through the NLSE. The effect of nonlinear loss or TPA is included in the imaginary part of the nonlinear parameter (γ") as explained in section 3.2.1. The effect of FCA can be incorporated in the NLSE by solving the rate equations for the TPA-induced free-carrier density (N_c) as follows [141], [144]:

$$\frac{\partial N_c}{\partial t} = (\frac{\alpha_2}{2h\nu_0})I^2 - \frac{N_c}{\tau_c}, \tag{3.59}$$

where $h\nu_0$ is the energy of one photon. In this equation, the first term and the second term on the right hand side refer to the generation rate and recombination rate of free-carriers, respectively [145]. As a result, the NLSE described by equation 3.46 takes the form of the following equation for a silicon-based platform [141], [144]:

$$\frac{\partial A}{\partial z} + i\beta_2 \frac{\partial^2 A}{\partial T^2} + \frac{\alpha}{2} A = (i\gamma' - \gamma") \left|A\right|^2 A - (\sigma/2 + \frac{i2\pi k_c}{\lambda}) N_c A, \tag{3.60}$$

where k_c is the FCD coefficient.

For a more comprehensive study of the amplitude and the phase evolution of an optical pulse in a medium with nonlinear loss, we now represent A(z,T) by its amplitude and phase, but this time we introduce a normalized amplitude relative to the linear loss and optical power (P) such that: $A = \sqrt{P}\text{exp}(\frac{-\alpha z}{2})u$ where the amplitude and the phase of u are $|u| = 1$ and $\angle u = \phi$, respectively. Therefore, we have:

$$A = \sqrt{P}\text{exp}(\frac{-\alpha z}{2} + i\phi). \tag{3.61}$$

By substituting 3.61 in equation 3.60 and solving it for the amplitude and phase, one can obtain information about nonlinear loss and nonlinear phase shift acquired by the pulse as a result of propagating through the medium.

For the purpose of this study, our waveguides meet the condition $L_{\text{eff}} \ll L_D$, since the pulse length is long enough ($10\,\text{ps}$) and the group velocity dispersion parameter for silicon is large ($k_2 = 1\,\text{ps}^2/\text{m}$) [141], therefore the effect of GVD can be ignored in equation 3.60. In addition, in the case of short pulses, the effect of free-carriers absorption is assumed to be negligible since they do not have enough time to recombine over the pulse duration [141]. However, the effect of TPA is still considered in the following equations. As a result, the solution of equation 3.60 is in the form of the following:

$$P(z,T) = \frac{P_0(T) exp(-\alpha z)}{1 + P_0(T) L_{\text{eff}} \gamma"}, \tag{3.62}$$

$$\phi(z,T) = \frac{\gamma'}{\gamma"} ln[1 + \gamma" P_0(T) L_{\text{eff}}], \tag{3.63}$$

where, $P_0(T)$ is the temporal power shape of the input pulse and the effect of nonlinear loss as a result of TPA is included through the term γ". The interplay between SPM and TPA determines the nonlinear phase shift in silicon-based platforms, therefore the nonlinear figure of merit (FOM) of the device can be defined based on these two effects as follows [28]:

$$\text{FOM} = \frac{1}{\lambda}\frac{n_2}{\alpha_2} = \frac{1}{4\pi}\frac{\gamma'}{\gamma"} \tag{3.64}$$

Equation 3.62 to 4.14 will be used in chapter 5 to describe the pulse evolution and the FOM of a silicon and a silicon-chalcogenide waveguide.

3.3 Brillouin scattering

Fluctuations in the optical properties of a material result in the scattering of light. The most common forms of light scattering are Rayleigh, Raman and Brillouin scattering. Rayleigh scattering is the scattering of light from non-propagating density fluctuations, therefore does not lead to any frequency shift [53]. Raman and Brillouin scattering are inelastic scattering, that is in theses processes energy transfers between photons and the medium, resulting in a frequency shift. Raman scattering originates from optical phonons with frequency shift of $\sim 13\,\text{THz}$ and Brillouin scattering originates from acoustic phonons with frequency shift of $\sim 11\,\text{GHz}$ in optical fibers [53].

Brillouin scattering can originate from thermal phonons, which then result in spontaneous scattering of light or could be induced by an optical field, which leads to stimulated scattering. A type of stimulated scattering caused by induced material density variations, is called stimulated Brillouin scattering (SBS). The density variation or in other words, acoustic disturbance, can be due to electrostriction, absorption or radiation pressure. The electrostrictive SBS results from the tendency of materials to become compressed in the presence of an intense optical field, while the absorptive SBS is due to the heat induced by optical absorption in a lossy medium, which expands the material in the areas of high temperature [53]. Radiation pressure is applied by an optical field on the boundaries of the waveguide, which comes into effect when dealing with sub-wavelength waveguides [52]. In this chapter, we describe SBS based on electrostriction, which is valid for isotropic media whose dimensions are much larger than the optical wavelength. But before that, we have a closer look at the spontaneous Brillouin scattering process.

In spontaneous Brillouin scattering, a beam of light is injected into a medium and is scattered by thermally generated acoustic phonons, without modifying the optical properties of the material. The moving acoustic wave generated from the thermal phonons adds a frequency shift to the scattered optical wave due to the Doppler effect. Brillouin scattering, therefore, can result in frequency downshifted (Stokes) or frequency upshifted (anti-Stokes) scattered optical waves depending on the propagation direction of the acoustic wave as illustrated in figure 3.3. In this figure, the incident optical wave with frequency ω_p and wave vectors $\mathbf{k}_p$ is scattered by the acoustic wave of frequency Ω and wave vector $\mathbf{q}$, producing a scattered wave (Stokes or anti-Stokes) with frequency ω_s and ω_{as} and wave vector $\mathbf{k}_s$ and $\mathbf{k}_{as}$ for Stokes and anti-Stokes, respectively.

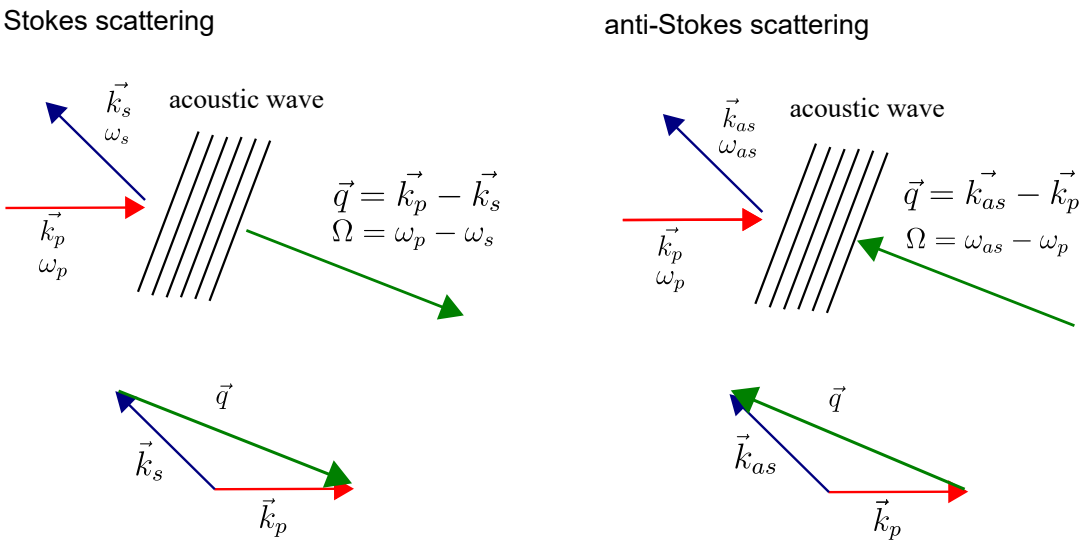

FIGURE 3.3: Phase-matching condition for Stokes and anti-Stokes Brillouin scattering. In this figure, arrows indicate vector variables.

3.3.1 Backward scattering

The scattering of optical waves occurs under the energy and momentum conservation for the three waves involved in this process, therefore for the Stokes wave we have:

$$\Omega = \omega_p - \omega_s, \tag{3.65}$$

and

$$\mathbf{q} = \mathbf{k}_p - \mathbf{k}_s \tag{3.66}$$

The dispersion relation of the optical and acoustic waves can be described by the following relations:

$$\omega_p = |\mathbf{k}_p| \frac{c}{n}, \qquad \omega_s = |\mathbf{k}_s| \frac{c}{n}, \qquad \Omega = |\mathbf{q}| \, v_a, \tag{3.67}$$

where c is the speed of light in vacuum, n is the refractive index of the material and v_a is the acoustic velocity in the medium. If θ is the angle between the scattered and the incident waves, then by substituting equation 3.67 into equation 3.66 and considering that the acoustic frequency (Ω) is much smaller than the optical frequencies (ω_p and ω_s) we can write:

$$|\mathbf{q}| = 2 \, |\mathbf{k}_p| \sin(\frac{\theta}{2}) \tag{3.68}$$

and the acoustic frequency will be:

$$\Omega = \frac{2nv_a}{\lambda_p} \sin(\frac{\theta}{2}) \tag{3.69}$$

where λ_p is the wavelength of the incident optical wave. In optical waveguides, the scattering angle is restricted to either $0°$ or $180°$, therefore, the maximum scattering is achieved in the backward direction with the Brillouin frequency shift (BFS) of:

$$\Omega_B = \frac{2n_{\text{eff}}v_a}{\lambda_p}, \tag{3.70}$$

where n_{eff} is the effective refractive index of the waveguide. The BFS is dependent on material properties [112] and is sensitive to strain and temperature [40], [146], which provides the basis for distributed Brillouin sensing. The change in the BFS as a result of temperature and strain variations is described by the following relations

The relation between the BFS and temperature and strain have been experimentally demonstrated in different platforms such as standard silica fibres [147]–[149], GeO_2-doped fibre [146], dispersion-shifted fibre (DSF) [150], and PCF [151]. Different distributed Brillouin sensing applications relying on this property (BFS) are discussed in chapter 2.

3.3.2 Forward scattering

As mentioned earlier in this chapter, Brillouin scattering originates from a moving acoustic wave is described by equation 3.69, where θ is the angle between the incident wave and the scattered wave. According to this equation the frequency shift in forward direction ($\theta = 0$) in a waveguide is zero. However, such scattering can still be observed with a non-zero frequency shift. It is due to different type of acoustic waves, namely transverse acoustic waves, which have a near zero longitudinal wave vector component. The dispersion plot for forward and backward scattering is shown in figure 3.5. The time-varying nature of transverse acoustic waves applies a phase modulation on the optical pump wave, which can be detected using an interferometry-based technique. Figure 3.4 shows the first demonstration of such detection reported by Shelby et al. [152].

Forward Brillouin scattering has applications in temperature sensing and fiber diameter measurement, which are based on the BFS in the forward direction. As an example, the BFS in the forward Brillouin process for a cylindrical medium such as optical fibre and for a certain acoustic mode (m) is expressed by [153]:

$$\Omega_{GB,m} = \frac{v_{t,m}y_m}{d\pi}, \tag{3.71}$$

where d is the fibre outer diameter, $v_{t,m}$ is the m_{th} transverse mode acoustic velocity, and y_m the m_{th} zero of the Bessel function describing the boundary conditions for the free fibre surface [152]. This forward BFS as described in Equation (3.71) has been utilized to determine the strain coefficient in silica fibre [154] and the temperature coefficient in highly nonlinear fibre [155] and PCF [156], sound velocity in silica fibre [153], and the core diameter of tapered fibre [137].

The intrinsic linewidth of the Brillouin gain spectrum is determined by the phonon lifetime and the structural irregularities of the waveguide. In the forward Brillouin interaction, an extra component contributes to the linewidth of the Brillouin gain spectrum of a given mode due to the transmission losses at the boundaries of the core [133]. These losses are dependent on the acoustic impedance of the surrounding medium and vary from one material to the other. Therefore, the linewidth of the Brillouin gain spectrum has been exploited for chemical sensing purposes in the forward Brillouin scattering process [132]–[134].

With this basic understanding of Brillouin scattering and its importance in Brillouin sensing, we now study the stimulated Brillouin scattering process (SBS).

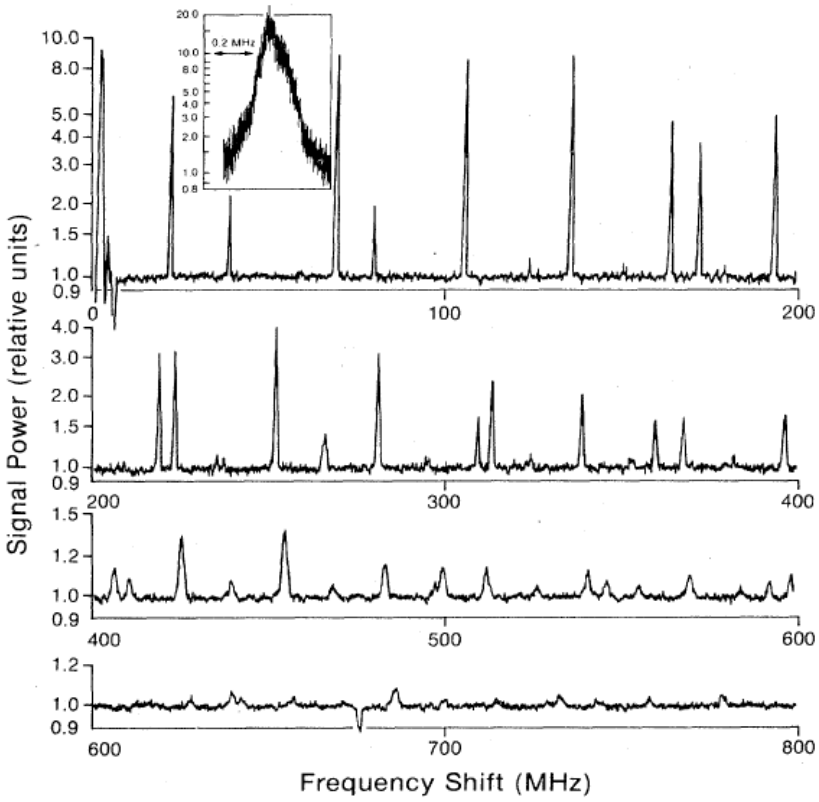

FIGURE 3.4: An example of forward Brillouin scattering in standard single mode fiber detected by an interferometry-based technique [152].

3.3.3 Stimulated Brillouin scattering (SBS)

SBS takes place in a nonlinear medium in two different ways; In the first case, a laser beam with frequency ω_p scatters from density variations initiated from thermal phonons of frequency Ω. The scattered wave, called Stokes wave, is downshifted in frequency to $\omega_s = \omega_p - \Omega$. The interference between the Stokes wave and the laser beam has a component at the difference frequency (Ω), which reinforces the acoustic wave. The interference of the acoustic wave with the laser beam, on the other hand, increases the amplitude of the Stokes wave. In this case, which is also known as SBS generator, The Stokes wave and acoustic wave reinforce each other in a loop.

In another scenario, which is called SBS amplifier, SBS is initiated with the injection of a weak signal wave at the Stokes frequency in the opposite direction of the pump laser to stimulate the density variation in the medium and consequently amplify the Stokes wave. In both scenarios, the positive feedback between the Stokes, pump and acoustic waves under the momentum and energy conservation leads to the amplification of the Stokes wave as shown schematically in figure 3.6. The underlying physical phenomena that enables these interactions is an optical force known as electrostriction which works together with its interaction mechanism photoelasticity. In this section we study electrostriction based on the derivations presented in ref. [53].

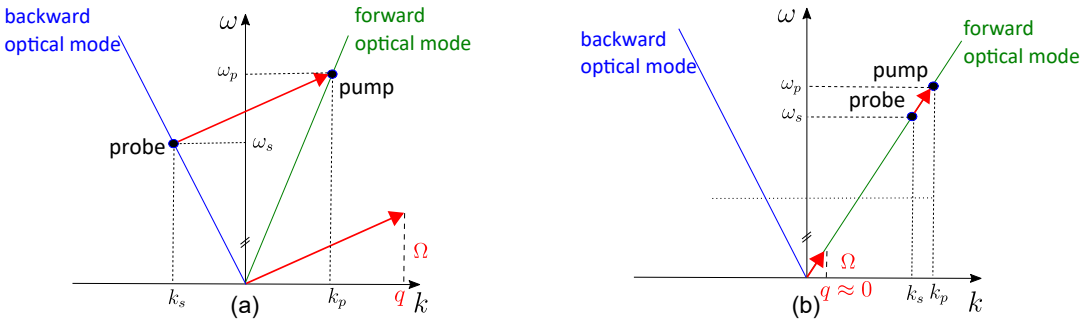

FIGURE 3.5: Optical and acoustic dispersion diagrams showing the phase-matching and energy conservation conditions in: a) backward Brillouin scattering, b) forward Brillouin scattering process. ($\mathbf{k}_p - \mathbf{k}_s = \mathbf{q}$). $\mathbf{k}_p$, $\mathbf{k}_s$, ω_p, ω_s, $\mathbf{q}$ and Ω have different values for the backward and forward Brillouin scattering processes.

Electrostriction

Electrostriction is the tendency of materials to compress in the presence of an electric field [53]. The applied electric field ($\mathbf{E}$) creates dipole moments equal to $\mathbf{P} = \epsilon_0 \alpha \mathbf{E}$ in the material, where α is the molecular polarizability. The energy stored as a result of this polarization is:

$$U = -\frac{1}{2}\epsilon_0 \alpha E^2, \tag{3.72}$$

And the force associated with this change in energy is given by:

$$\mathbf{F} = -\nabla U = \frac{1}{2}\epsilon_0 \alpha \nabla (E^2). \tag{3.73}$$

This force changes the density by $\Delta\rho$ and therefore the dielectric constant of the material is changed by:

$$\Delta\epsilon = (\frac{\partial\epsilon}{\partial\rho})\Delta\rho. \tag{3.74}$$

The potential energy in the material changes as a result of this change in the dielectric constant as follows:

$$\Delta u = \frac{1}{2}\epsilon_0 E^2 \nabla\epsilon. \tag{3.75}$$

The first law of thermodynamic implies that the change in the potential energy must be equal to the work performed to compress the material. This work can be expressed as an applied electrostrictive pressure (p_{st}) that is the pressure due to the applied electric field per unit volume:

$$\Delta w = p_{st}\frac{\Delta V}{V} = -p_{st}\frac{\Delta\rho}{\rho}. \tag{3.76}$$

Now by equating the two expressions for the change in potential energy (equation 3.75) and the work (equation 3.76) $\Delta u = \Delta w$, the electrostrictive pressure can be found to be:

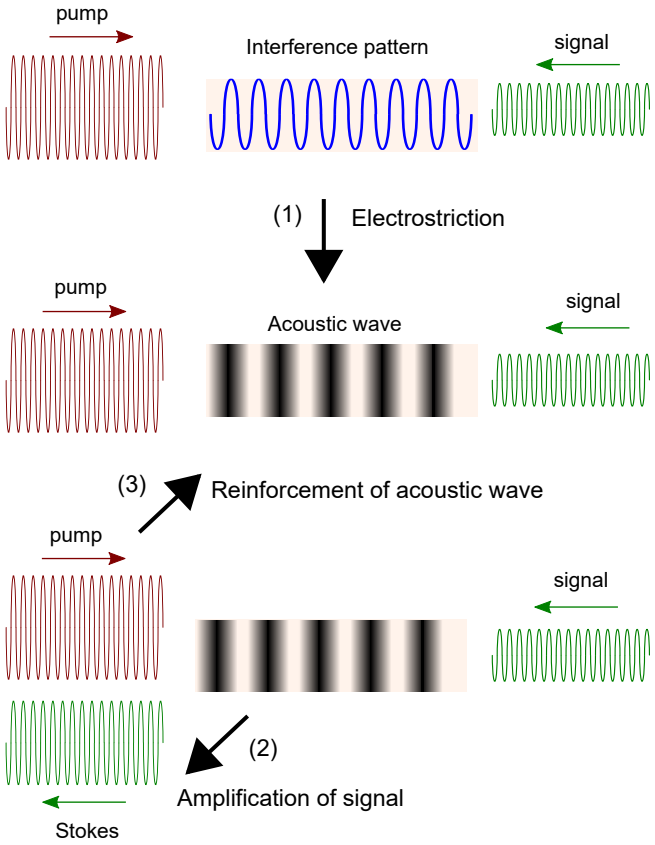

FIGURE 3.6: SBS process through electrostriction.

$$p_{st} = -\frac{1}{2}\epsilon_0\rho(\frac{\partial\epsilon}{\partial\rho}E^2) = -\frac{1}{2}\epsilon_0\gamma_e E^2, \tag{3.77}$$

where $\gamma_e = \rho(\frac{\partial\epsilon}{\partial\rho})$ is known as electrostrictive constant. The change in the density can be calculated based on the electrostrictive pressure as follows:

$$\Delta\rho = -(\frac{\partial\rho}{\partial p})p_{st} = -\rho(\frac{1}{\rho}\frac{\partial\rho}{\partial p})p_{st} = -\rho C p_{st}, \tag{3.78}$$

where $C = \frac{1}{\rho}\frac{\partial\rho}{\partial p}$ is the compressibility. Substituting p_{st} from equation 3.77 to equation 3.78, we obtain:

$$\Delta\rho = \frac{1}{2}\epsilon_0\rho C\gamma_e E^2. \tag{3.79}$$

Equation 3.79 shows how the material density changes as a result of the applied electric field.

3.3.4 Coupled wave equations for SBS

Now that we have an understanding of how the optical and acoustic waves are coupled through electrostriction, we are going to study the evolution of each wave by solving the optical and acoustic wave equations in an isotropic medium simultaneously. The derivations in this section are based on ref. [53].

The optical field in the medium is represented as $E(z,t) = E_p(z,t) + E_s(z,t)$, where E_p and E_s are the electric field for the pump and Stokes waves, respectively and take the form of:

$$E_p(z,t) = A_p(z,t)e^{i(k_p z - \omega_p t)} + c.c. \tag{3.80}$$

and

$$E_s(z,t) = A_s(z,t)e^{i(-k_s z - \omega_s t)} + c.c. \tag{3.81}$$

In equations 3.80 and 3.81, A_p and A_s are the slowly varying envelop of the pump and probe waves, respectively. In a similar way, the acoustic field takes the form of:

$$\tilde{\rho}(z,t) = \rho_0 + [\rho(z,t)e^{i(qz - \Omega t)} + c.c.], \tag{3.82}$$

where $\tilde{\rho}(z,t)$ indicates the rapidly varying field with time whereas $\rho(z,t)$ is the slowly varying amplitude of the acoustic field and ρ_0 is the mean density of the medium. The acoustic wave equation can be written in the following form:

$$\frac{\partial^2 \tilde{\rho}}{\partial t^2} - \Gamma' \nabla^2 \frac{\partial \tilde{\rho}}{\partial t} - v_{ac}^2 \nabla^2 \tilde{\rho} = \nabla \cdot \mathbf{f}, \tag{3.83}$$

In this equation, f is the force per unit volume which is given by: $\mathbf{f} = \nabla p_{st}$ and Γ' is the damping parameter. By substituting equations 3.80 and 3.81 into equation 3.77, we can find an expression for p_{st}, then taking the divergence of the force per unit volume that is $\nabla.\nabla p_{st}$ will result in:

$$\nabla \cdot \nabla p_{st} = \nabla \cdot \mathbf{f} = \epsilon_0 \gamma_e q^2 [A_p A_s^* e^{i(qz - \Omega t)} + c.c.] \tag{3.84}$$

Now substituting equations 3.84 and 3.82 into equation 3.83 and using slowly varying envelop approximation - where the second derivative in equation 3.83 can be ignored - we obtain:

$$-2i\Omega \frac{\partial \rho}{\partial t} + (\Omega_B^2 - \Omega^2 - i\Omega\Gamma_B)\rho - 2iqv_{ac}^2 \frac{\partial \rho}{\partial z} = \epsilon_0 \gamma_e q^2 A_p A_s^*, \tag{3.85}$$

where $\Gamma_B = q^2\Gamma'$ is the Brillouin linewidth which is inversely related to the phonon lifetime: $\Gamma_B = \tau_p^{-1}$. Equation 3.85 can be further simplified by omitting the last term in the left hand side considering that the acoustic wave decays over a very short distance (tens of microns in optical fibers [157]) and therefore the acoustic field can be treated locally. Furthermore, under the steady-state condition the first term on the left hand side also vanishes, which leaves us with the following expression for the acoustic field:

$$\rho(z,t) = \epsilon_0 \gamma_e q^2 \frac{A_p A_s^*}{\Omega_B^2 - \Omega^2 - i\Omega\Gamma_B}. \tag{3.86}$$

Now with the expression for the acoustic wave, we turn to the optical wave equations. The nonlinear wave equations describing the pump and Stokes waves have the form of:

$$\frac{\partial^2 E_i}{\partial z^2} - \frac{1}{(c/n)^2} \frac{\partial^2 E_i}{\partial t^2} = \frac{1}{\epsilon_0 c^2} \frac{\partial^2 P_i}{\partial t^2}, \qquad i = p, s \tag{3.87}$$

The source term in this equation is the nonlinear polarization, which is given by:

$$P = \epsilon_0 \Delta\chi E = \epsilon_0 \Delta\epsilon E = \frac{\epsilon_0}{\rho_0}\gamma_e \rho E, \tag{3.88}$$

where

$$P_i = p_i e^{i(k_i z - w_i t)} + c.c., \qquad i = p, s \tag{3.89}$$

with $p_1 = \frac{\epsilon_0}{\rho_0}\gamma_e \rho A_s$ and $p_2 = \frac{\epsilon_0}{\rho_0}\gamma_e \rho^* A_p$. Substituting equation 3.89, 3.80 and 3.81 into the nonlinear wave equation and using the slowly varying envelope approximation, we obtain:

$$\frac{\partial A_p}{\partial z} + \frac{1}{c/n}\frac{\partial A_p}{\partial t} = \frac{i\omega\gamma_e}{2nc\rho_0}\rho A_s, \tag{3.90}$$

$$-\frac{\partial A_s}{\partial z} + \frac{1}{c/n}\frac{\partial A_s}{\partial t} = \frac{i\omega\gamma_e}{2nc\rho_0}\rho^* A_p, \tag{3.91}$$

where we assumed $\omega_s \approx \omega_p$. Considering steady-state condition that is $\frac{\partial A}{\partial t} = 0$, we obtain the following equations:

$$\frac{\partial A_p}{\partial z} = \frac{i\epsilon_0 \omega q^2 \gamma_e^2}{2nc\rho_0}\frac{|A_s|^2 A_p}{\Omega_B^2 - \Omega^2 - i\Omega\Gamma_B}, \tag{3.92}$$

$$\frac{\partial A_s}{\partial z} = \frac{i\epsilon_0 \omega q^2 \gamma_e^2}{2nc\rho_0}\frac{|A_p|^2 A_2}{\Omega_B^2 - \Omega^2 - i\Omega\Gamma_B}, \tag{3.93}$$

These coupled amplitude equations can be reformulated in terms of the intensity of the two waves as follows:

$$\frac{dI_p}{dz} = -g_B I_p I_s, \tag{3.94}$$

$$\frac{dI_s}{dz} = -g_B I_p I_s, \tag{3.95}$$

where $I_i = 2n\epsilon_0 A_i A_i^*$ and g_B is the SBS gain factor which can be approximated by a Lorentzian profile:

$$g_B = \eta g_0 \left[\frac{(\Gamma_B/2)^2}{(\Omega_B - \Omega)^2 + (\Gamma_B/2)^2}\right], \tag{3.96}$$

where g_0 is the Brillouin gain coefficient defined as:

$$g_0 = \frac{\gamma_e^2 \omega^2}{n v_a c^3 \rho_0 \Gamma_B}. \tag{3.97}$$

In equation 3.96, η represents a normalized overlap integral between optical and acoustic mode(s) in a waveguide and takes a value between 0 and 1.

A final assumption to further simplify the solution of the coupled amplitude equations is to assume that the pump has a much higher power than the Stokes, therefore energy transfer from the signal to the pump does not affect its amplitude so that I_p = constant. Under this condition, which is called *undepleted pump regime*, the evolution of the signal wave intensity from equation 3.95 can be expressed by:

$$\mathrm{I}_s(z) = \mathrm{I}_s(L)\exp(g_B I_p(L-z)), \tag{3.98}$$

As it can be seen in this equation, the signal wave which is injected to the waveguide at z = L amplifies exponentially while propagating through a waveguide. The undepleted pump condition is satisfied throughout this work, therefore we base our calculations on this assumption.

3.3.5 Platforms for SBS

For SBS to take place in a waveguide, both optical and acoustic modes need to be well confined within the waveguide, which depends upon the gain material and waveguide structure. It is evident from equation 3.97 that the Brillouin gain coefficient is related to material properties of the medium such as acoustic velocity, mean density and more importantly refractive index [42]. The importance of the refractive index can be realized by noting that the electrostrictive constant in equation 3.97 scales to the fourth power of refractive index [53]:

$$\gamma_e \approx (n^2-1)(n^2+2)/3. \tag{3.99}$$

Equation 3.97 also suggests that a medium with low acoustic velocity and long phonon lifetime increases the strength of the SBS gain coefficient.

Another factor for optimizing the SBS response is the waveguide structure. As it is seen in equation 3.98, probe amplification scales exponentially with the length of the medium and is inversely related to the waveguide effective area (considering $I = P/A_{\text{eff}}$). Most of the time, a significant reduction of the effective area in short-scale waveguides leads to enhancement in nonlinear effects such as SBS [2] In addition, the overlap integral introduced in equation 3.96 plays a critical role in the performance of SBS waveguides. The quantity of this overlap shows how well the two optical and acoustic modes are confined within the waveguide and overlap with each other. While the optical wave guidance in a waveguide is provided by the refractive index mismatch between the core and the cladding, the acoustic wave guidance is possible through an acoustic impedance mismatch between the two of them [42]. This acoustic mismatch is related to the acoustic velocity of material.

An example of optical and acoustic mode confinement in a chalcogenide rib waveguide is shown in figure 3.7 [74], [158]. In this structure, the core material (chalcogenide) has a higher refractive index and lower acoustic velocity than the silica substrate and cladding, which led to the first demonstration of SBS in an on-chip photonic waveguide [74].

Table 3.1 provides waveguide and opto-acoustic parameters for two main platforms we use in this thesis; chalcogenide rib waveguides and a hybrid silicon-chalcogenide waveguide. Parameter g_B/A_{eff} in table 3.1 includes the effect of waveguide effective area and opto-acoustic overlap integral in the strength of SBS interaction. The longitudinal sound velocity and refractive index of the materials involved in these waveguide structures are shown in table 3.2.

[2] There are occasions, when optical forces in sub-wavelength structures cancel each other and lead to reduction or even cancellation of SBS [52]. This is explained in section 3.3.6 of this chapter.

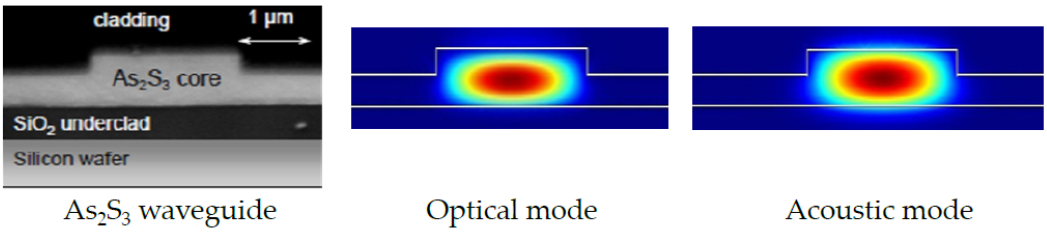

FIGURE 3.7: The cross-section of the chalcogenide rib waveguide and the acoustic and optical mode profile confinement in the waveguide. Figure from ref. [158]

TABLE 3.1: SBS parameters for chalcogenide and hybrid waveguides.

Platform	$\boldsymbol{\Gamma_B}$ [MHz]	$\boldsymbol{\Omega_B}$ [GHz]	$\boldsymbol{A_{\text{eff}}}$ [μm^2]	$\boldsymbol{g_B/A_{\text{eff}}}$ [$\frac{1}{\text{W}\cdot\text{m}}$]
Chalcogenide [159]	34	7.7	2.3	320
Hybrid [6]	~ 40	7.6 *	0.9	750

* This value changes with waveguide width.

3.3.6 SBS in sub-wavelength waveguides

The conventional treatment of SBS in optical fibers considers opto-acoustic coupling as a bulk effect which arises from dispersive, photoelastic and mechanical properties of the material [83], which is described by electrostriction. This is valid under the assumption that the waveguide dimensions are much larger than the acoustic wavelength ($w, h, r \gg \frac{2\pi v_a}{\Omega}$) [42], where w and h stand for the waveguide width and thickness in a square waveguide and r is the waveguide radius in a circular waveguide, respectively. However, in sub-wavelength, high index contrast waveguides such as silicon nanowires, the strength of photon-phonon coupling cannot be fully described by electrostriction alone. This is due to the fact that as the surface to volume ratio in a waveguide increases, that is the waveguide cross-section decreases, the effect of boundary forces becomes more pronounced. Therefore, opto-acoustic coupling in the sub-wavelength regime is a function of both nonlinear material and waveguide geometry. The most well-known boundary effect arises from the pressure applied by the electric field to the surface of the waveguide, known as *radiation pressure*. The effect of this force on the boundaries is called *moving boundary effect*.

Here, we explain the effect of radiation pressure and electrostriction in a sub-wavelength waveguide through a simplified example from Ref. [52]. In this example, we consider a silica nanowire with diameter d, whose boundaries expand out by surface acoustic displacement u_s as a result of an applied electric field. The boundary expansion due to this effect is $\Delta A_1 = \pi d u_s$ and the change in refractive

TABLE 3.2: Refractive index and acoustic velocity of optical materials used in this thesis. These value are from ref. [43].

Material	$\boldsymbol{v_a}$ [m/s]	$\boldsymbol{n}$
Chalcogenide (As_2S_3)	2500	2.45
Silicon	8900	3.5
Silica	5960	1.45

index over the expanded area is $\Delta n_1 = n_{silica} - n_{air}$. The electrostriction acts on the cross-section of the waveguide ($A_2 = \pi d^2/4$) and if we consider only the radial expansion, the radial strain can be calculated as $S_r = 2u_s/d$ and the change in the refractive index will be: $\Delta_{n2} = -1/2 n_{silica}^3 p_{11} S_r$ with $p_{11} = 0.121$ is the silica photoelastic coefficient. The two effects are shown in figure 3.8. The strength of each effect is estimated by the refractive index perturbation across the affected area. Therefore we have: $\eta_1 = \Delta n_1 \Delta A_1$ and $\eta_2 = \Delta n_2 \Delta A_2$ being the strength of radiation pressure and photoelastic effects, respectively. In this particular example, the two effects are comparable and since the sign of η_2 is opposite the η_1, they can cancel each other for specific wire diameter. This example makes it clear that in the sub-wavelength regime, the effect of boundary forces is of significant importance and needs to be taken into account in the opto-acoustic coupling calculation.

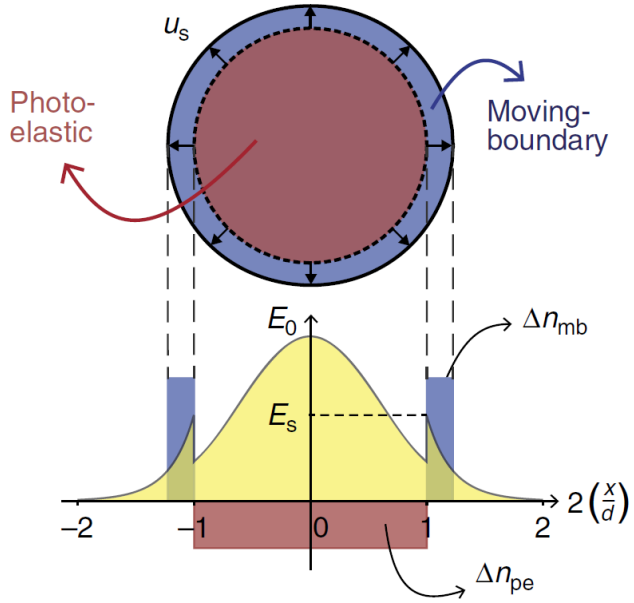

FIGURE 3.8: The figure is taken from Ref. [52] shows the effect of moving boundary and photo-elasticity in the refractive index change and compares the strength of each effect in terms of the product $\Delta n * affectedarea$. Here $\Delta n_{mb} = \Delta n_1$ and $\Delta n_{pe} = \Delta n_2$.

This effect can be included in the calculations by first using a fully vectorial approach to solve the coupled mode equations since in the sub-wavelength regime the electric field has an axial component in addition to the transverse components which needs to be taken into consideration. Furthermore, the effect of radiation pressure and electrostriction can be included using the opto-acoustic overlap integral introduced in equation 3.96 separately for each effect and the total effect will be the superposition of the two effects [83], [84]. The waveguide dimensions in this thesis do not reach sub-wavelength regime and therefore the effect of moving boundaries in the calculation of the SBS coupling is negligible. However, the numerical calculations of the opto-acoustic overlap presented in chapter 6 are based on a fully vectorial approach.

3.4 Distributed Brillouin measurement

Here, we explain two main mechanisms for distributed Brillouin measurements. The first approach is based on a pulsed pump, where the length of the pump pulse determines the SBS interaction length and consequently the spatial resolution of the SBS measurement. This is the main idea behind Brillouin optical time domain analysis (BOTDA) technique. In the other approach, the distributed response is achieved by limiting the coherence of pump and probe waves such that their interference has a limited coherence length over which the SBS interaction can occur. Brillouin optical correlation domain analysis (BOCDA) is based on this principle. We describe four different methods to achieve BOCDA measurements namely frequency modulated, phase-coded, ASE-based and random laser-based BOCDA. In addition, we provide an expression for the local SBS gain within the context of frequency modulated BOCDA.

3.4.1 BOTDA

BOTDA was first proposed by Horiguchi et al. [88], [89]. In this technique, pump pulses of center frequency ω_p counter-propagate with CW probe wave of frequency ω_s, with Ω_B being the BFS in the medium. SBS only occurs at the location of the propagating pump pulse, which can be detected by monitoring the amplification of the back-scattered signal as a function of time. Any irregularity or change in the temperature/strain along the medium that affects the BFS, results in a drop in the amplification of the probe wave. The position of the local effect can be resolved by translating the time over which the change in probe amplification has occurred (dt) using the relation: $dt = \frac{2n_{\text{eff}}dz}{c}$, where n_{eff} is the effective refractive index of the medium. The basic principle of BOTDA is schematically shown in figure 3.9.

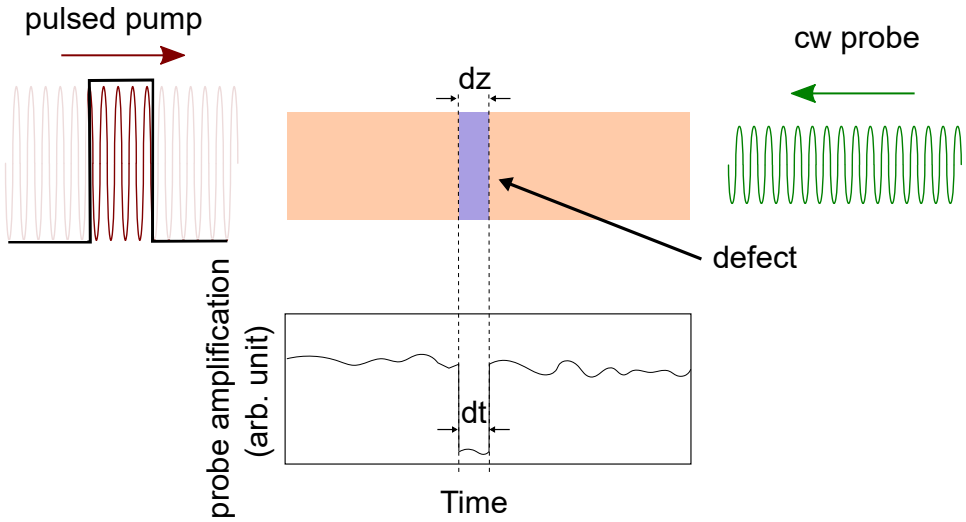

FIGURE 3.9: A time trace showing probe amplification based on BOTDA measurement.

In this technique, the spatial resolution is determined by the duration of the pump pulse. The pulse length is limited by the phonon lifetime in the medium, which is approximately $10\,\text{ns}$ in silica fiber corresponding to approximately $30\,\text{MHz}$ Brillouin spectrum linewidth and $1\,\text{m}$ fiber length) [160]. Figure 3.10 shows how the

Brillouin gain is affected by the pulse length. From this plot, we can see as the pulse length approaches $1\,\mathrm{m}$, the Brillouin gain spectrum broadens and the amplification of the probe wave decreases. This is due to the fact that the acoustic field does not have enough time to build up for pulse duration comparable to or shorter than the phonon lifetime [87], [160]. In addition, equation 3.96 representing the SBS gain factor for CW pump is no longer valid for a short pulsed pump. In the case of a short pulse, the effect of pulse length (L) needs to be considered in equation 3.96 by convoluting the SBS gain factor (g_B) with the spectrum of the pump pulse [87]. As a result, for pulses shorter than the phonon lifetime, the wide spectrum of the pulse broadens the SBS gain spectrum and reduces the SBS amplification [160]. In chapter 2, we reviewed alternative approaches in time domain for improving the spatial resolution beyond $1\,\mathrm{m}$.

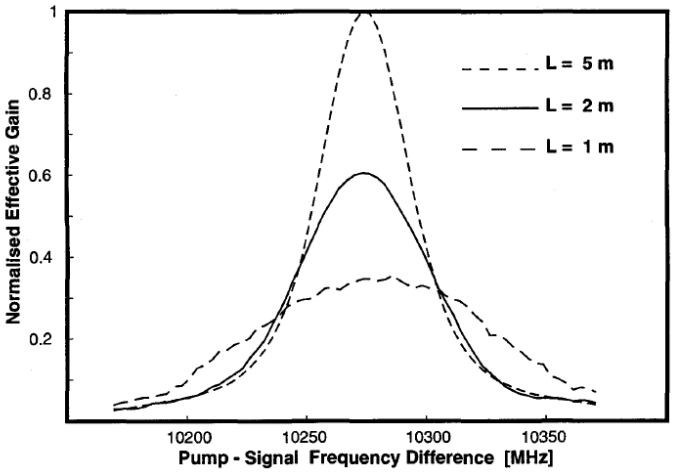

FIGURE 3.10: Reduction in SBS gain and increase in Brillouin gain spectrum as a result of reducing the pump pulse length (L). Figure is adapted from ref. [87].

3.4.2 BOCDA

In BOCDA technique, which is the focus of this thesis, the localization of the SBS response can be achieved through four different approaches as will be explained in the following.

Frequency modulated BOCDA

The first BOCDA technique proposed and demonstrated by Hotate et al. [112] was based on frequency modulation of the pump and the probe waves. In this technique, the frequency of the pump and probe varies with the modulation frequency of f_m and modulation amplitude of ΔF. The electric field of the counter-propagating pump (E_p) and probe (E_z) at position z along the medium with length L can be expressed by the following equations:

$$E_p(z,t) = A_p(z,t)e^{i(k_p z - [\omega_p + 2\pi\Delta f cos(2\pi f_m(t-z/v_g))]t)} + c.c. \tag{3.100}$$

and

$$E_s(z,t) = A_s(z,t)e^{i(-k_s z-[\omega_s+2\pi\Delta f cos(2\pi f_m(t-(L-z)/v_g))]t)} + c.c. \tag{3.101}$$

The interference between the pump and probe results in a time and position-dependant frequency difference as follows [161]:

$$\begin{aligned}\omega(z,t) &= \omega_p - \omega_s + 2\pi\Delta f[cos(2\pi f_m(t-z/v_g)) - cos(2\pi f_m(t-(L-z)/v_g))] \\ &= \omega_p - \omega_s + 2\pi\Delta f\ sin(\pi f_m(L-2z)/v_g) \times\ sin(\pi f_m(2t-L)/v_g).\end{aligned} \tag{3.102}$$

As it is seen in this equation, the frequency difference between the pump and probe only matches the BFS ($\omega_p - \omega_s$) at specific locations along the medium, which can be determined by equating the term $sin(\pi f_m(L-2z)/v_g)$ in equation 3.102 to zero. Therefore, we get:

$$z_k = \frac{1}{2}(L - k\frac{v_g}{f_m}), \quad k = 0, 1, 2, ... \tag{3.103}$$

At these locations, called correlation peaks, SBS occurs efficiently while at any other location along the medium the SBS interaction is not efficient, since the frequency difference between the pump and the probe does not match the BFS. In addition, this equation indicates that correlation peaks occur periodically in the medium with the interval of [38], [112]:

$$d_m = \frac{v_g}{2f_m}, \tag{3.104}$$

which limits the measurement range in this technique. The spatial resolution of this technique is defined by Hotate et al. [115] as the "distance from the correlation peak where the gain falls to half of its value". It is expressed by equation:

$$\Delta z = \frac{v_g\Gamma_B}{2\pi f_m \Delta F}. \tag{3.105}$$

From equations 3.104 and 3.105, it becomes evident that there is a trade-off between the measurement range and the spatial resolution. This issue is addressed in phase-coded BOCDA.

Gain expression for BOCDA

In BOCDA the spectrum of the pump and probe is much broader than the spectral linewidth of SBS. In other words, phase fluctuations of pump and probe waves are much faster than the phonon lifetime. Their effect needs to be considered in calculating the gain (g) that the probe undergoes when traveling through the medium. This can be obtained by convoluting the power spectrum of the pump and probe beat with the SBS gain factor (g_B) for each section of the medium, as expressed in equation 3.106 and as illustrated in figure 3.10 [112].

$$g = \frac{v_g\bar{P}_1}{A_{\text{eff}}\Delta t}\int_{-\infty}^{\infty} d\tau \int_{-\infty}^{\infty} g_B(\tau,\nu)\left|\chi(\tau,\nu)\right|^2 d\nu, \tag{3.106}$$

where v_g is the group velocity of light in the medium, $\bar{P}_1$ is the average pump power, A_{eff} is the waveguide effective area, Δt is the coherence time of the pump and probe

signals and $\chi(\tau,\nu)$ is the Fourier spectrum of the pump and probe beat as a function of the delay (τ) and the frequency shift (ν) between the pump and the probe and is expressed by:

$$\chi(\tau,\nu) = \frac{nc\epsilon_0 A_{\text{eff}}}{2\sqrt{\bar{P}_1\bar{P}_2}} \int_{-\infty}^{\infty} A_p(t)A_s^*(t-\tau)\exp(i2\pi\nu t)dt, \tag{3.107}$$

where n is the refractive index of the medium and $\bar{P}_2$ is the average probe power. It should be noted that equations 3.106 and 3.107 are obtained by taking into account the evolution of the optical and acoustic fields with time in solving SBS coupled equations (equations 3.85, 3.90 and 3.91).

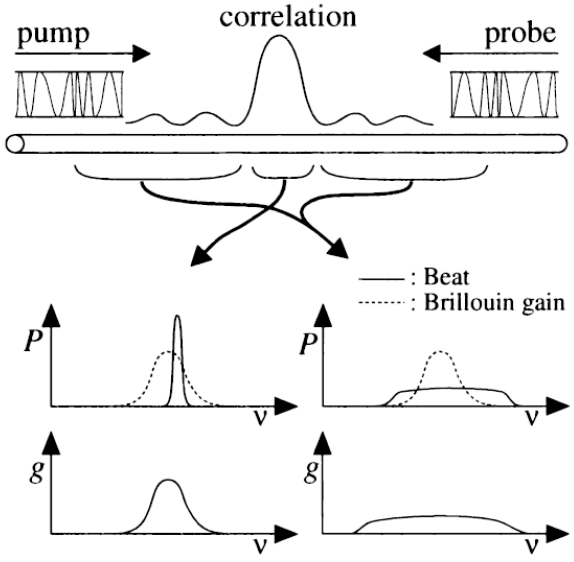

FIGURE 3.11: Construction of the Brillouin gain spectrum (g) inside and outside of the correlation peak [112]; P is the power spectrum of the pump and probe beat.

As it can be seen in figure 3.11, the power spectrum of the pump and probe beat at the correlation peak is quite narrow - since the frequency modulation is canceled out at this position - while it broadens for the positions outside the correlation peak. This means that the SBS response inside the correlation peak reaches the steady state condition after the build up of the acoustic field, while the SBS response outside the correlation peak has to be treated as a transient process [51].

Phase-coded BOCDA

The random phase coded technique was first introduced by Zadok et al. [51]. In this technique, a binary pseudo random bit sequence (PRBS) with bit duration of T (T much smaller than the acoustic lifetime) is applied on the pump and the probe waves complex envelop. In the positions along the medium, where the pump and the probe have the same distance from the point of their entry to the medium, their phase always matches as illustrated in figure 3.12 (correlation peaks). The strength of the acoustic field is determined by the product of the pump wave envelope and the probe complex conjugate envelope as expressed in equation 3.85 earlier. Therefore, at the position of the correlation peak, the acoustic field can build up effectively

and results in the SBS interaction. At any other point in the medium, the acoustic field does not have enough time to build up due to the fast alternation between the phase of the pump and probe complex envelop, therefore the SBS interaction is suppressed in those locations. In [113] Cohen et al. present an expression for the acoustic wave evolution for a time-dependent SBS interaction. This expression is obtained by integration over the acoustic wave equation (equation 3.85) while neglecting $\frac{\partial \rho}{\partial z}$ term [113]:

$$\begin{aligned}\rho(z,t) =& ig_1 \exp(-\Gamma_A t) \int_0^t \exp(\Gamma_A t') A_p(t' - z/v_g) A_s^*(t' - (L-z)/v_g) dt' \\ =& ig_1 \int_0^t \exp(-\Gamma_A (t-t')) A_p(t' - z/v_g) A_s^*(t' - z/v_g + \theta(z)) dt',\end{aligned} \tag{3.108}$$

where

$$\Gamma_A = i\frac{\Omega_B^2 - \Omega^2 - i\Omega\Gamma_B}{2\Omega} \qquad \text{and} \qquad g_1 = \frac{\gamma_e q^2}{8\Omega\pi},$$

and $\theta(z)$ is a position-dependent delay between the pump and the signal wave.

The spatial resolution and the measurement range in this method is determined by the bit duration and the PRBS sequence length (M) as follows [51]:

$$\Delta z = \frac{1}{2} v_g T \qquad \text{and} \qquad d_m = \frac{1}{2} M v_g T \tag{3.109}$$

Here, the spatial resolution is decoupled from the measurement range; M can be chosen to be long, while the spatial resolution remains high [51].

BOCDA based on amplified spontaneous emission (ASE)

Up to this point, the local SBS response in BOCDA is achieved by making the pump and the probe waves uncorrelated using broad-band frequency modulation or long sequence random phase coding. An ASE source can also be used for this purpose, since it is by nature a random noise source. This means it includes radiative spontaneous emissions with random fluctuations in amplitude and phase, which are uncorrelated to one another [157], [162]. The ASE-based BOCDA was first proposed and demonstrated by Cohen et al. [113]. Our investigations in this thesis are based on this method.

ASE refers to the amplification of the spontaneously emitted photons in a gain medium, which happens close to the direction of the amplification medium and can stimulate the emission of more photons [163]. The gain medium in this study is an erbium doped fiber with an ASE spectrum that expands over a bandwidth of $4\,\mathrm{THz}$ covering wavelengths from $1525\,\mathrm{nm}$ to $1570\,\mathrm{nm}$. The coherence time of the ASE (Δt) is determined by its full-width half maximum (FWHM) bandwidth (Δf) and its power spectral density profile [157], [162], [164]. Consequently, the spatial resolution is given by $\frac{1}{2} v_g \Delta t$. Therefore, the power spectral density profile of the ASE can be tailored in terms of shape and bandwidth using a relevant filter shape to provide the required spatial resolution. Table 4.1 lists some of the common power spectral densities and their auto-correlation functions in each case. The last column in this table shows the extinction ratio for the highest sidelobe, which determines

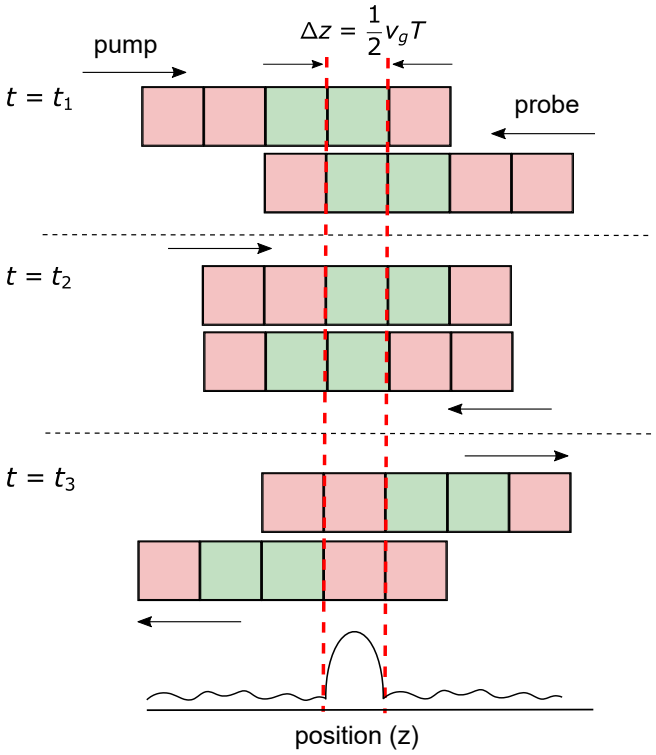

FIGURE 3.12: A schematic of PRBS coded BOCDA technique, where red and green squares show 0 and π phase, respectively. The pump and probe complex envelop at three time frames for a short sequence code is shown, where the signs of the two waves in the middle of the medium is always the same. The bottom plot shows the build up of the acoustic wave in the middle of the waveguide (at the position of correlation peak).

the level of SBS suppression outside the correlation peak. We discuss some technical considerations regarding selection of the best filter shape in chapter 5.

Similar to the random phase-code BOCDA, the position of the correlation peak in ASE-based BOCDA occurs at the point which has the same distance from the pump and probe entry to the medium. Unlike the two other techniques, this technique is not limited by the measurement range. The periodicity in the correlation peak arises from the modulation of the phase or frequency in the previous approaches, however, in the ASE-based technique there is no modulation and we are dealing only with one correlation peak.

Similar to the previous approaches, SBS is suppressed outside the correlation peak due to the rapid fluctuations in phase and amplitude of the pump and probe complex envelopes, which does not allow the acoustic field to build up. Within the correlation peak, however, the acoustic field can build up since the pump and probe complex amplitudes have the same phase at that point. A simulation of the acoustic field build up at the position of the correlation peak based on equation 3.108 is shown in figure 3.13 [113]. In this simulation, the ASE bandwidth is set to $25\,\mathrm{GHz}$ corresponding to $4\,\mathrm{mm}$ spatial resolution in silica fiber and the build-up of acoustic field occurs over approximately $10\,\mathrm{ns}$.

TABLE 3.3: Cross-correlation function and correlation time for rectangular, Lorentzian and Gaussian power density functions [164].

Power density function	Auto-correlation function	Sidelobe extinction
rectangular: $\mathrm{rec}(\frac{f}{\Delta \mathrm{f}})$	$\Delta \mathrm{f}\,\mathrm{sinc}(\Delta \mathrm{f}\,\tau)$	$-13\,\mathrm{dB}$
Triangular: $\mathrm{tri}(\frac{f}{\Delta \mathrm{f}})$	$\Delta \mathrm{f}\,\mathrm{sinc}^2(\Delta \mathrm{f}\,\tau)$	$-26\,\mathrm{dB}$
Gaussian: $\exp(-\pi\,\frac{f^2}{(\Delta \mathrm{f})^2})$	$\frac{\Delta \mathrm{f}}{\sqrt{\pi}}\exp((-\Delta \mathrm{f})^2\tau^2)$	no sidelobe

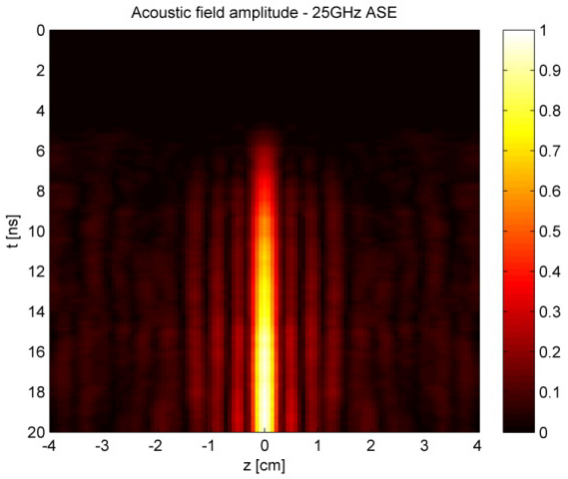

FIGURE 3.13: Simulation of acoustic field in ASE-based BOCDA showing the acoustic build up time of $10\,\mathrm{ns}$ and the spatial resolution of $4\,\mathrm{mm}$. This simulation is from ref. [113].

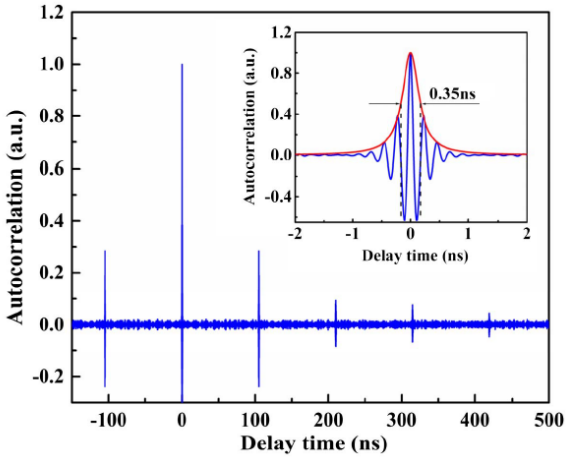

FIGURE 3.14: Auto-correlation function of a random laser with a zoom-in on the correlation peak [114].

BOCDA based on random lasers

Random lasers have also been used for BOCDA measurement [114]. A random laser, unlike a conventional laser, does not rely on a cavity with reflective surfaces or periodic structures. In a random laser, photons are scattered from multiple particles in a disorder gain medium [165]. Therefore, the output of the random laser has low spatial coherence. This means that a random laser can be used to create a correlation peak within a medium in a similar way as the ASE source. The auto-correlation function of a random laser with a bandwidth of $2\,\mathrm{GHz}$ is shown in figure 3.14 [114]. The spatial resolution of the measurement is determined by the width of the correlation peak. Since the underlying BOCDA principle in this case is the same as the previous case, we do not extend this topic any further.

4 Kerr nonlinearity and SBS in silicon-chalcogenide hybrid waveguides

4.1 Introduction

Silicon photonics, which typically deals with silicon on insulator (SOI) platforms, has attracted a considerable attention over the past decades. This is mainly due to its unique features including: high refractive index contrast which provides a high level of optical confinement, transparency in the near mid-infrared (mid-IR) region and compatibility with CMOS technology. Being compatible with mature CMOS technology provides scalability, small feature size, low cost, efficient power consumption and integration of optics with electronics on a single chip [28]. Figure 4.1 schematically shows the integration of several key optical functions including grating couplers, waveguides, modulators, photodetectors and metal-oxide semiconductor field-effect transistors (MOSFETs) on a single chip [166]. Some of these devices are briefly introduced in the next paragraph.

Modulators on SOI devices are driven by the plasma dispersion effect, where the change in the free carrier density changes the refractive index of silicon and modulates the light [166]. Different types of modulators include carrier-depletion mode devices based on a reversed biased PN junction [167], Mach-Zehnder interferometer (MZI) structures [168]–[170], resonant structures [171]–[174] and devices based on hybrid integration of other materials into silicon platforms. The hybrid integration could be in the form of bonding III/V materials into silicon platform [175], epitaxially growing germanium [176], graphene cladding [177] or active electro-optic polymers introduced to slot waveguides [178] and photonic crystal fibers (PCF) [179]. *Photodetectors* can be realized by integrating materials such as germanium, which has a narrower band gap than silicon as a detector in telecom operating wavelengths [180]. In addition, III/V materials can also be used for photodetection [181]. Furthermore, *on-chip light sources* are achieved by either bonding [182], [183] or epitaxial growth of III-V materials on the silicon wafer [184], [185].

These key optical components enable a large number of applications in silicon photonics including data communication [7], [186], [187], bio-sensing [188], [189], gas sensing [190], light detection and ranging (LIDAR) systems [191] and novel light sources [184], [192].

In addition to the linear devices mentioned so far, SOI platforms also enable powerful nonlinear functionalities such as supercontinuum generation [193], [194], Raman and Brillouin lasing [6], [81], [195], [196], slow light effect [197], parametric

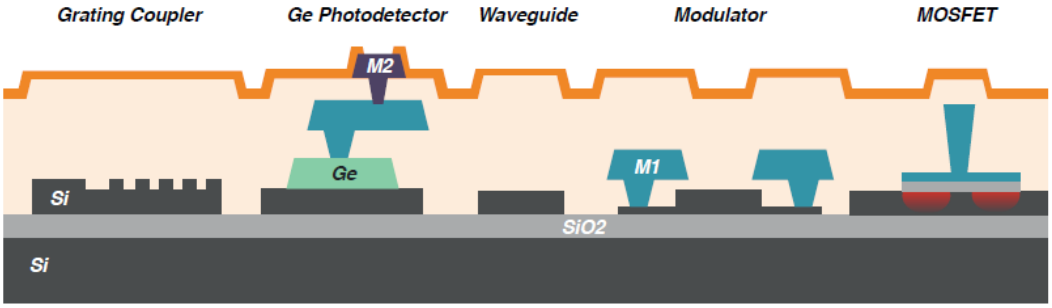

FIGURE 4.1: Several optical functionalities on a SOI platform enabled by CMOS technology. Figure from ref. [166].

amplification based on FWM [198] and wavelength conversion [199], [200] and demultiplexing [30], [201]. However, in nonlinear regime silicon exhibits a large nonlinear absorption due to TPA and FCA (explained in detail in chapter 3) on telecom wavelengths, which puts a limit on the maximum input power [28] and the speed of signal processing in silicon waveguides [30]. Here we discuss different approaches to overcome this challenge and enable such applications in silicon platforms.

One solution is to use a PIN structure, where a silicon waveguide is placed between two regions of p-doped and n-doped silicon. By applying a reverse bias across the silicon waveguide a depletion region is created. Examples of this method are shown in figure 4.2, where the TPA-induced free carriers are constantly swept away from the waveguide [142], [202]–[205]. Alternatively, silicon can be heterogeneously

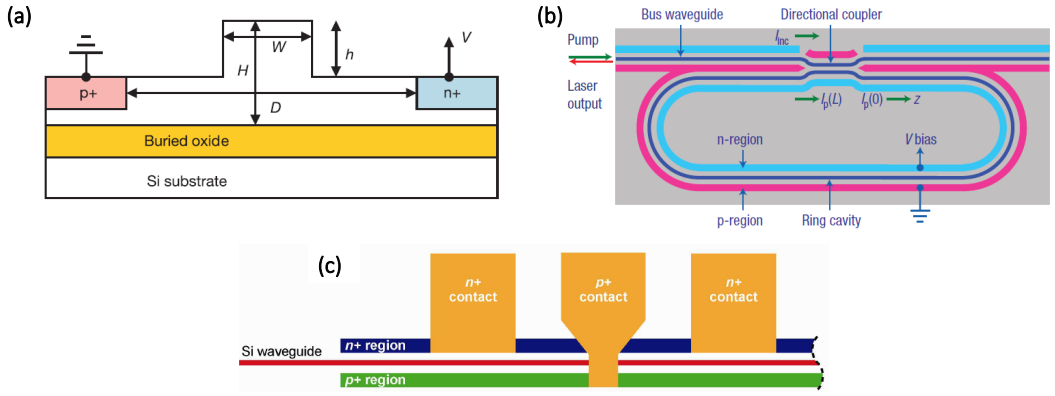

FIGURE 4.2: Reverse biased p-i-n junction to remove the effect of free carriers in siliocn waveguides. a) Ref. [205], b) Ref.[196] and c) Ref. [142].

integrated with another low loss and highly nonlinear material to take advantage of the nonlinearity of the second material while avoiding the nonlinear loss of silicon. The second nonlinear material could be added in the form of a cladding on top of a small core silicon nanowire or deposited in a gap between the two silicon nanowire in a slot waveguide structure. The former approach, also known as cover nonlinearity, pushes the optical field away from the small-core silicon nanowire such that the optical field mostly propagates through the nonlinear cladding material [31]. The nonlinear loss is therefore reduced by preventing the optical field to propagate

through silicon and guiding it through the nonlinear cladding. The trade-off in this approach is the increase in the nonlinear effective area by spreading it out into the cladding, which reduces the power per unite area (intensity) and consequently the waveguide nonlinear parameter (γ').

A slot waveguide consists of two silicon core waveguides with a gap in between, which is filled with a lower refractive index material. The discontinuity of the electric field across the waveguide cross-section results in the enhancement of the electric field component of the quasi-TE mode across the high refractive index boundary of the waveguide. This enhancement is proportional to the second power of refractive index ratio between the silicon and the gap material as shown in figure 4.3 [30], [206]. In this case, the optical mode is mostly confined within the slot area rather than the silicon rails resulting in a small effective mode area and consequently strong nonlinear interaction. Examples of silicon slot waveguides are silicon rails filled with organic material [30], [207], nonlinear polymer [29], chalcogenide glass [208], [209] and nanocrystals [209]–[212].

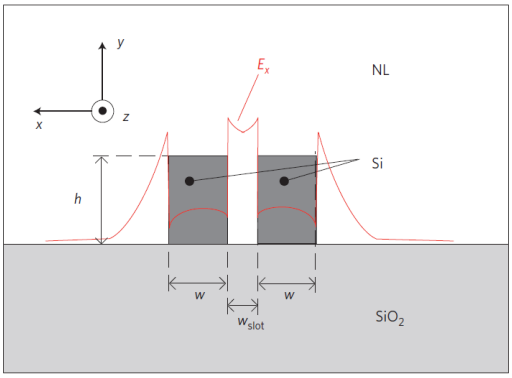

FIGURE 4.3: Discontinuity of the electric field across the waveguide slot waveguide cross-section. Figure is adapted from ref. [30].

Other approaches to avoid TPA-induced free carriers are using CMOS-compatible materials with low nonlinear loss such as high refractive index silica (hydex) and silicon-nitride [27], [213] or shifting the operating wavelength toward mid-IR, where the energy of two photons is smaller than the silicon band gap, therefore TPA and consequently FCA reduces significantly [214], [215].

Our aim in this chapter is to enable stimulated Brillouin scattering (SBS), which is one of the strongest third-order nonlinearities, on an on-chip silicon-based waveguide. As explained in chapter 3, SBS is based on the nonlinear coupling between optical and acoustic modes and requires the two modes to overlap efficiently in a waveguide. As a result, in order to harness SBS on a silicon-based waveguide, we face two main challenges. First is to overcome the nonlinear loss in silicon, and second is to provide both optical and acoustic modes confinement in the waveguide. To address these issues, we propose hybrid integration of silicon with chalcogenide in the form of a cover nonlinearity.

The silicon-chalcogenide hybrid waveguide exhibits a very low nonlinear loss. Chalcogenide has a much lower TPA coefficient compared to silicon therefore, for the same input power the third-order nonlinear loss is much lower in the hybrid waveguide - two orders of magnitude lower nonlinear loss - compared to the SOI

waveguide. Furthermore, chalcogenide has a high Brillouin gain coefficient g_0 (introduced in chapter 3) which can be employed to enable SBS in the hybrid waveguide. In the next paragraph we explain why an intermediate material such as chalcogenide is required to enable SBS in a SOI platform.

Although many on-chip SBS applications have been demonstrated over the past decade [11], [23], [35], [47], [81], [216], [217], only a limited number of them are based on SOI platform. This is mainly due to the fact that, in SOI platforms the higher acoustic velocity in the silicon core compared to the silica (SiO_2) substrate results in the acoustic mode leakage from the silicon core to the substrate [42]. Therefore, alternative solutions such as under-etched pillar shape silicon waveguides [44] and silicon membranes [45] were proposed to demonstrate SBS in silicon waveguides as shown in figure 4.4. The former structure allows for strong opto-acoustic overlap by limiting the leakage of acoustic field to the silica substrate and the latter structure guides optical and acoustic modes independently and allow for a very low propagation loss. Here, we take advantage of the hybrid design and heterogeneously combine silicon with chalcogenide glass (As_2S_3) to provide a strong opto-acoustic coupling necessary for harnessing SBS. This allows us to demonstrate SBS functionalities in an integrable platform while avoiding TPA in silicon.

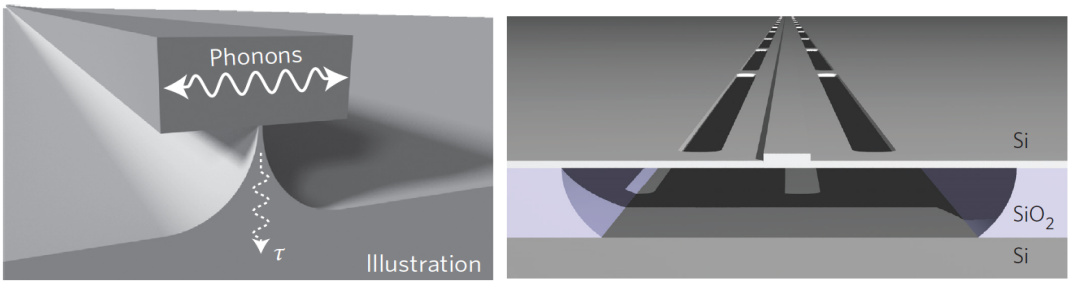

FIGURE 4.4: Illustration of a) under-etched pillar shape silicon waveguide [44], and b) silicon membrane [45] for harnessing SBS in SOI structures.

The structure of this chapter is as follows: In the first part of this chapter - which is mainly based on our publication: *"nonlinear loss engineering in a silicon-chalcogenide hybrid optical waveguide"* [218] - we describe the hybrid silicon-chalcogenide structure. Then we explain the hybrid waveguide performance in terms of Kerr nonlinearity based on the experimental measurement of SPM and nonlinear loss resulting in an expression for nonlinear FOM. The nonlinear FOM is also confirmed by waveguide simulation and solving NLSE for the hybrid waveguide. A comparison between the nonlinear FOM between a conventional silicon nanowire and a hybrid waveguide is provided, which shows the nonlinear loss and FOM improvement in the hybrid waveguide compared to the silicon nanowire. In the second part of this chapter - which is based on the work *"Compact Brillouin devices through hybrid integration on silicon"* [6] - we show that by modifying the hybrid waveguide, SBS gain of $18\,\mathrm{dB}$ can be achieved in this platform. An on-chip Brillouin resonator is demonstrated as in this hybrid waveguide.

4.2 Design and modeling of the hybrid waveguide

A schematic of the hybrid waveguide is shown in figure 4.5. It consists of a $220\,\mathrm{nm}$ thick silicon waveguide on top of a $2\,\mu\mathrm{m}$ silicon oxide substrate The light is coupled in and out of the waveguide using grating couplers. Grating couplers are gradually tapered down to a $150\,\mathrm{nm}$ wide silicon waveguide with the length of $2\,\mathrm{mm}$. The entire SOI structure except the grating couplers is then covered by $700\,\mathrm{nm}$ thick As_2S_3 layer. A layer of SiO_2 cladding is added on top to provide further protection. According to the simulation results, $62\,\%$ of the optical field propagates through the silicon core in the silicon nanowire in the absence of chalcogenide cladding, whereas in the case of hybrid waveguide only $0.4\,\%$ of the optical field resides in the silicon core. Therefore, the overall TPA is reduced considerably in the hybrid waveguide.

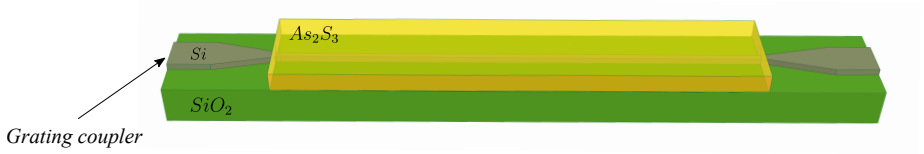

FIGURE 4.5: Schematic of the hybrid waveguide.

Three different lengths of hybrid waveguide (1 mm, 2 mm and 4 mm) were used to determine the propagation loss of 3.1 dB/cm using cut-back method. The coupling loss was measured to be 5.5 dB per grating coupler.

4.2.1 NLSE for sub-wavelength waveguides

The nonlinear parameter (γ) and the effective area (A_{eff}) described in chapter 3 are valid for large core diameter waveguides such as conventional silica fiber where the waveguide is operating in the weak guidance regime, that is the optical mode is purely transverse and has no component in the direction of propagation [219]. However, for the sub-wavelength and inhomogeneous waveguides such as the hybrid silicon-chalcogenide waveguide, this assumption no longer holds [220]. In the hybrid waveguide, the cross-section is no longer homogeneous but rather consists of two different materials over which the optical mode is distributed in a non-uniform manner. In addition, due to the sub-wavelength dimensions of these waveguides, the optical mode is no longer purely transversal but it has a component in the direction of optical wave propagation, therefore the effect of this modal component needs to be considered while dealing with such structures [219].

Different works have been done in this area in order to include the effect of modal component and waveguide inhomogeneity in the calculation of the nonlinear parameter and effective area in the sub-wavelength waveguides [31], [221], [222]. Here we follow the most general approach proposed by Afshar et al. [222], where a full vectorial solution of Maxwell's equations in a single mode nonlinear waveguide leads to a vectorial version of NLSE introduced in chapter 3, as follows:

$$\frac{\partial A}{\partial z} + \beta_1 \frac{\partial A}{\partial t} + i\beta_2 \frac{\partial^2 A}{\partial t^2} = i\gamma^V \left|A^2\right| A, \tag{4.1}$$

in which γ^V is the vectorial nonlinear parameter and is defined as:

$$\gamma^V = \frac{2\pi}{\lambda}\frac{\epsilon_0}{\mu_0}\frac{\int_\infty n^2(x,y)n_2(x,y)[2\left|e^4\right| + \left|e^2\right|^2]dA}{3\left|\int_\infty (e\times h^*).\hat{z}dA\right|^2}. \tag{4.2}$$

In equation 4.2, e and h are the modal distribution of electric and magnetic fields, and n and n_2 are the linear and nonlinear refractive index distribution, respectively. In Ref. [222], Afshar et al. proposed a factorization of γ^V to clarify the contribution of the following three factors on the waveguide nonlinearity: 1) nonlinear refractive index through n_2^{avg}, 2) modal distribution of the electric field within the nonlinear medium through A_{eff} and 3) group velocity of the optical mode through v_g. Each of these terms are defined based on the factorization of equation 4.2 as follows:

$$\gamma^V = \frac{2\pi}{\lambda}(\frac{c}{n_{\text{core}}v_g})^2\frac{n_2^{avg}}{A_{\text{eff}}}, \tag{4.3}$$

$$v_g = \frac{\int_\infty (e\times h^*).\hat{z}dA}{\epsilon_0\int_\infty[2n^2 - (\lambda dn^2/d\lambda)]\left|e\right|^2 dA}, \tag{4.4}$$

$$n_2^{avg} = \frac{n_{\text{core}}^2\int_\infty[n^2 - (\lambda dn^2/d\lambda)]n_2[2\left|e^4\right| + \left|e^2\right|^2]dA}{3\int_\infty n^4\left|e\right|^4 dA}, \tag{4.5}$$

which can be further simplified to:

$$n_2^{avg} = \frac{n_{\text{core}}^2\int_\infty[n^2 - (\lambda dn^2/d\lambda)]n_2\left|e^4\right| dA}{\int_\infty n^4\left|e\right|^4 dA}, \tag{4.6}$$

assuming that $\left|e^4\right| \approx \left|e^2\right|^2$ [222]. And finally the effective area can be written as:

$$A_{\text{eff}} = \frac{(\int_\infty n^2\left|e\right|^2 dA)^2}{\int_\infty n^4\left|e\right|^4 dA}. \tag{4.7}$$

For the rest of this chapter, our calculations are based on these main equations.

4.2.2 Modeling the waveguide nonlinearity

Optical mode distribution in the hybrid waveguide was calculated using a commercial-grade simulator eigenmode solver and propagator - Lumerical mode solution [223] - as shown in figure 4.6 (a). As it is seen in this figure, the optical mode is pushed out of the silicon core and most of the optical power is concentrated on the boarders of the silicon core and chalcogenide cladding. This results in a higher propagation loss in the hybrid waveguide compared to the standard silicon waveguide, since sidewall roughness plays a major role in linear loss of the waveguides [166]. The power distribution of the fundamental mode over a standard silicon waveguide is also shown in figure 4.6 (b) to provide a comparison between the two structures. From this figure, most of the power in the silicon waveguide is concentrated in the core area.

We then exported the numerically calculated electric and magnetic field from Lumerical software to Matlab in order to calculate the nonlinear parameters of the waveguide by solving equations 4.2 to 4.7. The waveguide cross-section is divided to smaller areas as shown in figure 4.7 and the nonlinear parameters are then calculated for sections A_1 to A_5 separately with respect to their refractive index and

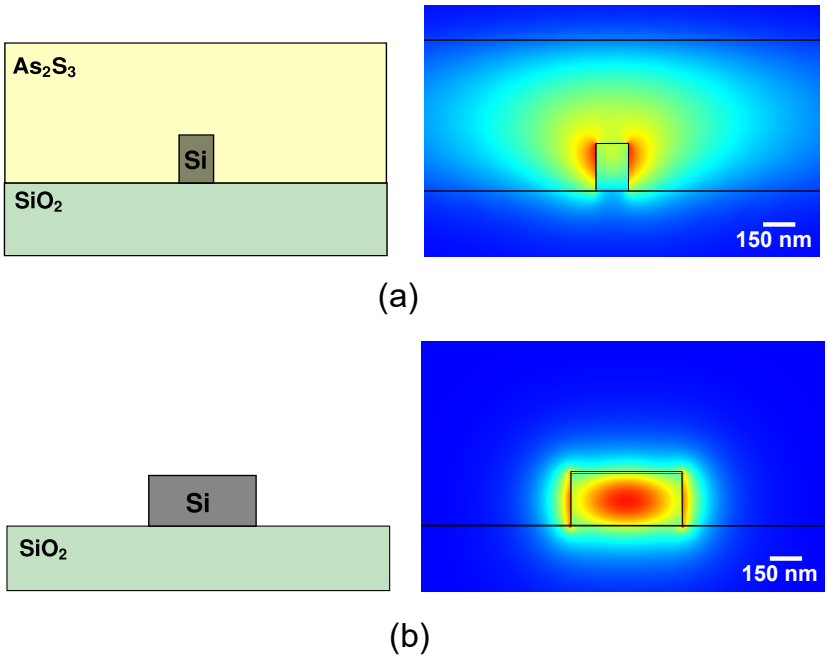

FIGURE 4.6: Waveguide cross-section and optical mode distribution in a) a hybrid waveguide, b) a standard silicon waveguide.

TABLE 4.1: Sellmeier coefficients for different materials in the model after ref.**Nolte2015**

Sellmeier coefficients	Si	SiO_2	As_2S_3
B_1	10.668429	0.6961663	4.24
B_2	0.0030435	0.4079426	
B_3	1.5413341	0.8974794	
C_1	0.3015165	0.0684043	2.5758
C_2	1.13475115	0.1162414	
C_3	1104.0	9.896161	

geometry. The refractive index for each material is calculated either by importing material refractive index obtained from the fabrication process or using Sellmeier model according to:

$$n^2(\lambda) = 1 + \sum_i \frac{B_i \lambda^2}{\lambda^2 - C_i}, \tag{4.8}$$

where B_i and C_i are the Sellmeier coefficients and their value for Si, SiO_2 and As_2S_3 are listed in table 4.1 [224].

Equation 4.6 can be used in its complex form to provide an effective nonlinear absorption coefficient α_2^{avg} in addition to the effective nonlinear refractive index n_2^{avg}. For this purpose, we replace n with $(n - i\alpha)$ and n_2 with $(n_2 - i\alpha_2)$, respectively and repeat the calculation for each region. The real and imaginary part of this equation results in the effective nonlinear refractive index and effective nonlinear absorption coefficient, respectively. The complex nonlinear factor is then calculated using equation 4.1, whose real and imaginary parts can be used to determine the nonlinear

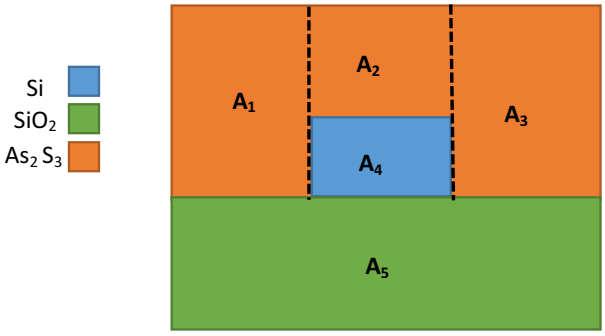

FIGURE 4.7: Inhomogeneous cross-section of the hybrid waveguide and its divisions for waveguide parameters calculations.

FOM similar to what is obtained in chapter 3:

$$\text{FOM} = \frac{1}{\lambda}\frac{n_{2,\text{avg}}}{\alpha_{2,\text{avg}}} = \frac{1}{4\pi}\frac{\text{Re}(\gamma^V)}{\text{Im}(\gamma^V)} \tag{4.9}$$

TABLE 4.2: Calculated waveguide parameters for silicon and chalcogenide platforms.

Platform	v_g	$n_{2,avg}$	$\alpha_{2,avg}$	A_{eff}	γ^V	FOM
Silicon	0.65×10^8	5.76×10^{-18}	9.7×10^{-12}	1.03×10^{-13}	$398 + 83i$	0.38
Hybrid	0.98×10^8	2.82×10^{-18}	8.67×10^{-13}	8.5×10^{-13}	$21 + 0.8i$	2.09

The calculated parameters based on the described method at wavelength $1550\,\text{nm}$ are shown in table 4.2. The script used for these calculations can be found in Appendix A. We repeat the same calculations for a standard silicon waveguide to make a comparison between the two platforms in terms of the Kerr nonlinearity, nonlinear loss and FOM. As it is seen in this table, although the average Kerr nonlinearity (n_2^{avg}) in silicon is higher than the hybrid waveguide, the overall FOM in hybrid is five times higher than the silicon due to the much lower nonlinear absorption in the hybrid waveguide. Furthermore, as explained before, the larger effective nonlinear area in the hybrid waveguide is due to the optical mode distribution which is less confined in the hybrid waveguide compared to the silicon waveguide as shown in figure 4.6.

4.3 Experiment

In order to measure the waveguide nonlinear FOM, we measured the power and the spectrum of $10\,\text{ps}$ TE-polarized pulses with repetition rate of $38\,\text{MHz}$ propagating through the waveguide for different input power levels using the setup shown in figure 4.8. Following the approach explained in chapter 3, the nonlinear loss can be extracted from the input and output power measurement and the Kerr nonlinearity induced by SPM can be obtained from the spectrum broadening of the pulses.

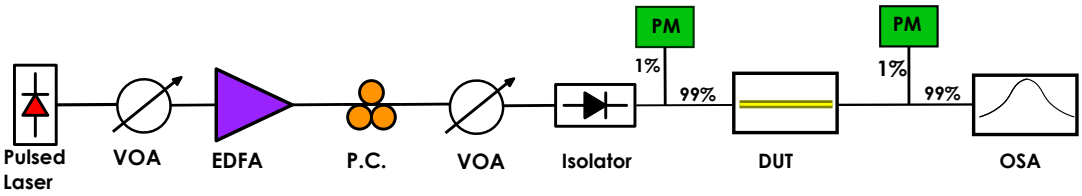

FIGURE 4.8: Experimental setup to measure nonlinear loss and Kerr nonlinearity in silicon and hybrid waveguides.

The pulse length is selected to be short in order to limit the effect of free carriers absorption. Although the free-carriers are not completely eliminated, we approximated our calculations based on the assumption that their contribution is negligible. In addition the length of the silicon and hybrid waveguides are short enough ($L_{\text{eff}} \ll L_D$) to ignore the effect of group velocity dispersion (GVD).

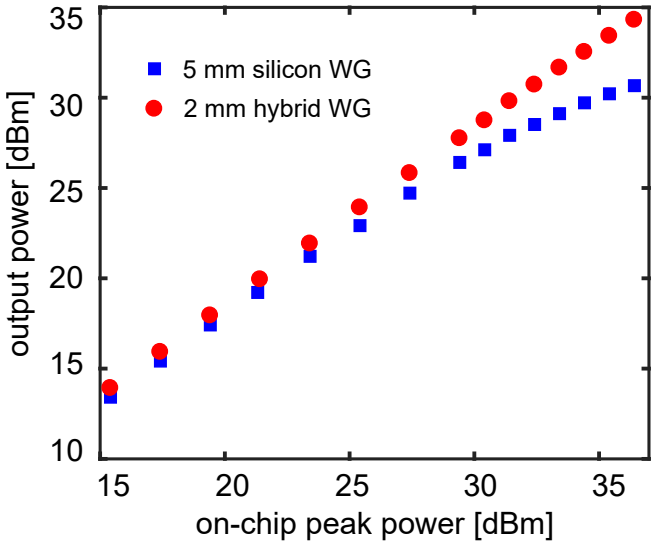

FIGURE 4.9: Output power vs input power in silicon and hybrid waveguides.

The output of the pulsed laser goes through an isolator and is amplified using an erbium-doped fiber amplifier (EDFA) to provide enough peak power for the nonlinear effect. Output power is measured while changing the input power using a variable optical attenuate (VOA) and monitoring the power before and after the waveguide through the $1\,\%$ port of $99/1$ couplers. The coupling in and out of the waveguide is done through grating couplers with coupling loss of approximately $5.5\,\text{dB/facet}$. The devices under test are silicon and hybrid silicon-chalcogenide waveguides. Output vs input power for silicon and hybrid waveguides are plotted in figure 4.9. As it can be seen in this plot, the relation between the input and output power for silicon waveguide is not linear and for input powers above $30\,\text{dBm}$ the output power starts to saturate.

By plugging in $P_{in} = P_0(T)$ and $P_{out} = P(L_{\text{eff}}, T)$ in equation:

$$P(z,T) = \frac{P_0(T)exp(-\alpha z)}{1 + P_0(T)L_{\text{eff}}\gamma"}, \tag{4.10}$$

FIGURE 4.10: P_{in2} and P_{out2} refer to the input and output power of the hybrid waveguide as plotted in figure 4.9.

which is already introduced in chapter 3, the imaginary part of the nonlinear factor for silicon waveguide can be found. However in the case of the hybrid waveguide, the contribution of silicon tapers attached to both ends of the waveguide needs to be removed in order to extract the imaginary part of the nonlinear factor of the hybrid waveguide section. This can be done by solving equation 4.10 for each waveguide section separately and use the output of one section as the initial conditions for the next section (as shown schematically in figure 4.10) to find the contribution of each part to the overall imaginary part of the nonlinear factor.

We then infer the insertion loss from the input and output power by using the relation: $10^{*}\text{Log}(P_{out}/P_{in})$. Figure 4.11 compares the nonlinear loss plot of hybrid waveguide with that of standard silicon nanowire, which confirms much lower nonlinear loss in the case of hybrid waveguide. In this figure, we plot the normalized loss by removing the effect of coupling losses, which is in the form of a vertical offset to provide a better visual comparison. A fit to the nonlinear loss curves is shown with dashed line and is obtained using the NLSE model.

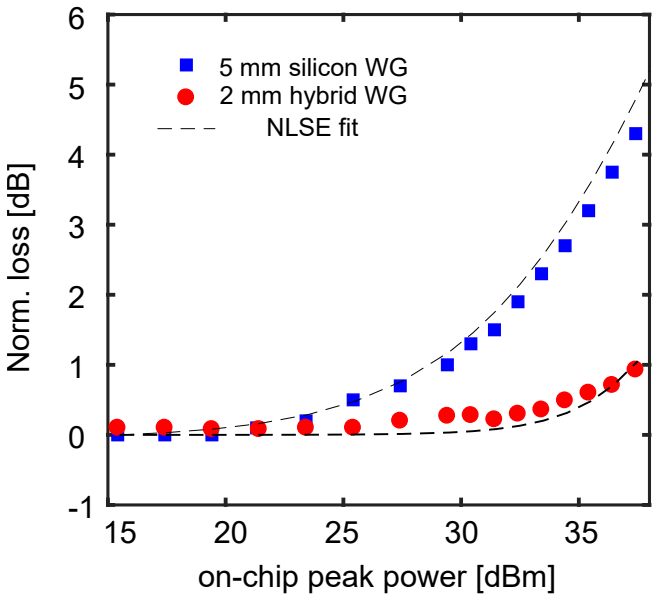

FIGURE 4.11: Nonlinear loss in silicon and chalcogenide waveguides.

Next, we measure the output spectrum of the pulses in silicon and hybrid waveguides as a function of input power level. Figure 4.12 shows the spectral broadening for the two waveguides. As it can be seen from this figure, spectral broadening in the silicon is much higher than the hybrid waveguide for the same input peak power due to the higher nonlinear Kerr coefficient in silicon. The real part of the nonlinear

parameter can be extracted from the spectral broadening. We limit our calculations to the regime where the input power level is low enough so that the effect of FCA is negligible, that is in the regime where input-output power relation is linear. The spectral broadening can be related to the nonlinear phase shift using the following equations from ref. [10].

$$\Delta\omega_{rms}^2 = \left\langle(\omega-\omega_0)^2\right\rangle - \left\langle(\omega-\omega_0)\right\rangle^2, \tag{4.11}$$

where $\Delta\omega_0$ is the initial RMS spectral width and $\left\langle(\omega-\omega_0)^2\right\rangle$ is an average over the spectral broadening induced by SPM ($S(\omega)$), which can be calculated by:

$$\left\langle(\omega-\omega_0)^n\right\rangle = \frac{\int_{-\infty}^{\infty}(\omega-\omega_0)^n S(\omega)d\omega}{\int_{-\infty}^{\infty}S(\omega)d\omega}, \tag{4.12}$$

For a Gaussian pulse, the spectral broadening factor will be:

$$\frac{\Delta\omega_{\text{rms}}}{\Delta\omega_0} = (1+\frac{4}{3\sqrt{3}}\phi_{max}^2)^{1/2}, \tag{4.13}$$

Since we are using a Gaussian pulse shape (measured by Frequency-resolved optical gating (FROG) traces), this relation can be applied to our measured data. By substituting spectral broadening $\Delta\omega_{rms}$ and $\Delta\omega_0$ obtained from the experiment in equation 4.13, the maximum nonlinear phase shift can be found. The nonlinear phase shift obtained here can be plugged into equation:

$$\phi(z,T) = \frac{\gamma'}{\gamma"}ln[1+\gamma" P_0(T)L_{\text{eff}}], \tag{4.14}$$

which is already introduced in chapter 3, to find the real part of γ in the silicon waveguide. In the case of hybrid waveguide, however, we again divide the waveguide into segments of silicon tapers and hybrid waveguide to extract the contribution of the hybrid waveguide section to the real part of the nonlinear parameter as illustrated in figure 4.13.

It is evident from figure 4.12 that, despite the higher nonlinear loss, silicon waveguide exhibits wider spectrum broadening compared to the hybrid waveguide. This may raise the question of what is the advantage of a hybrid waveguide in terms of Kerr nonlinearity. It should be noted that chalcogenide has a lower nonlinear refractive index compared to silicon, and if one cares about Kerr nonlinear applications such as fast optical switching [225], [226], then it is more appropriate to choose a material for hybrid integration that has a nonlinear refractive index comparable or higher than silicon as already presented in the literature [29], [30], [227], [228]. However, in our study we need to consider requirements necessary for harnessing SBS in such platform and chalcogenide due to its high opto-acoustic coefficient is selected for this purpose.

Table 4.3 summarizes the experimental values of real and imaginary parts of the nonlinear factor and the FOM for the hybrid and standard silicon waveguides. This FOM determines the achieved nonlinear gain (nonlinear phase shift) in the expense of nonlinear loss. The hybrid waveguide exhibits 100 times improvement in terms of TPA-induced nonlinear loss and 20 times lower Kerr nonlinearity $\mathrm{Re}(\gamma)$ compared to the silicon nanowire. Therefore, the overall FOM as defined in equation 4.9 is improved by a factor of five. This brings FOM of the hybrid structure to a value

greater than 1, which is required for all-optical signal processing applications [8]. The discrepancy observed between the experiment (reported in table 4.3) and the modeling (reported in table 4.2) is most likely due to the fabrication tolerances and simplifications that are made in the modeling.

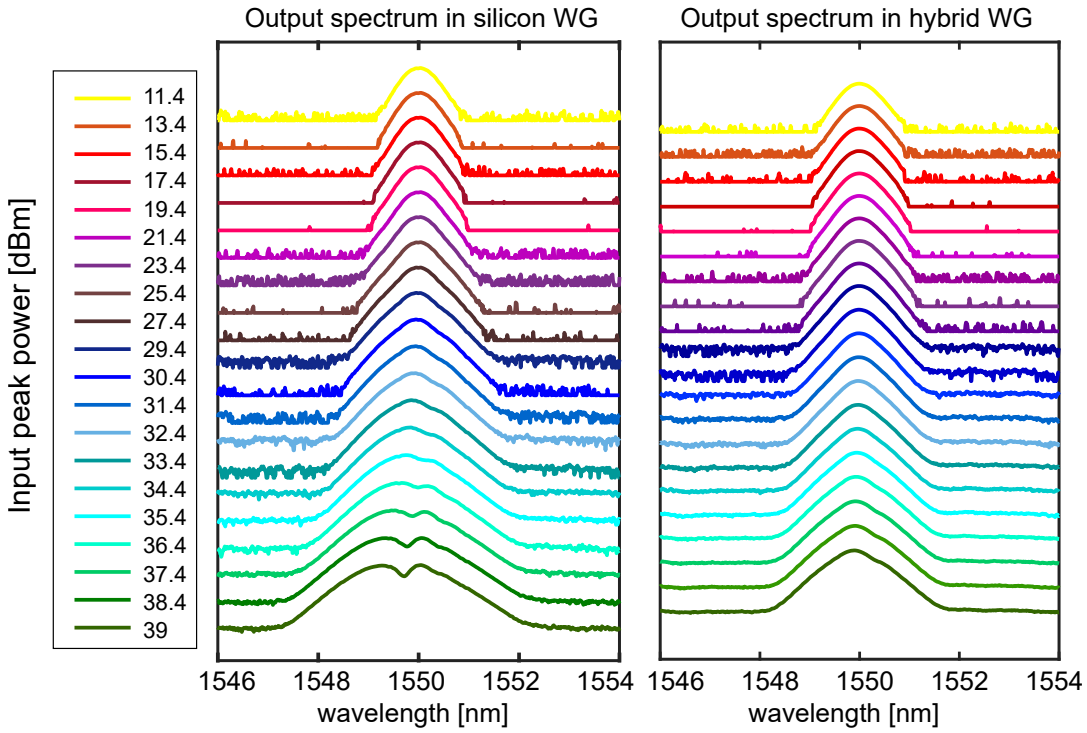

FIGURE 4.12: Spectrum broadening in silicon and hybrid waveguide.

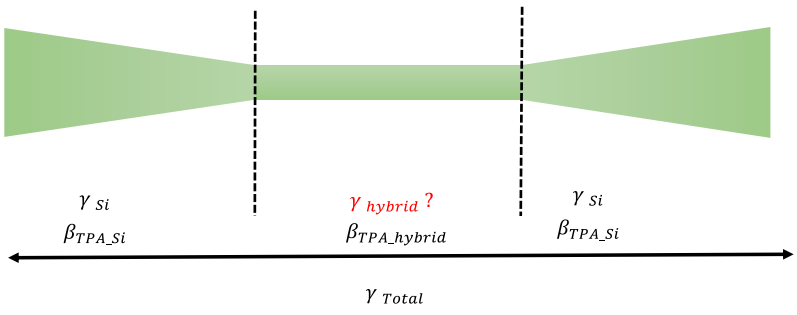

FIGURE 4.13: Extracting $\mathrm{Re}(\gamma)$ for the hybrid waveguide from the overall waveguide response.

TABLE 4.3: Experimental value of waveguide nonlinear parameters for silicon and hybrid platforms.

Platform	**Re(γ)**	**Im(γ)**	**FOM**
Silicon	296	81.5	0.28
Hybrid	13	0.79	1.29

4.4 SBS in silicon-chalcogenide hybrid waveguides

In the previous section, we demonstrated that the hybrid silicon-chalcogenide waveguide in the form of a cover nonlinearity provides two orders of magnitude lower nonlinear loss and a nonlinear FOM higher than 1.

In this section, we discuss how the hybrid waveguide described earlier can be modified to accommodate SBS. Two main design modifications are required to enable SBS in the hybrid waveguide: 1) removing the narrow silicon strip entirely and 2) etching the chalcogenide cladding to form a waveguide that could support the optical and acoustic modes. In this way, light is coupled in and out of the waveguide through silicon grating couplers and SBS interaction occurs in the chalcogenide waveguide. The design of the waveguide is as follows; it starts with a standard SOI platform consisting of silicon grating couplers tapered down to a $450\,\mathrm{nm}$ wide silicon nanowire. The silicon nanowire then further tapers down from $450\,\mathrm{nm}$ to a $150\,\mathrm{nm}$ tip over the length of $100\,\mu\mathrm{m}$, which leads to an open area with no silicon deposition. A $680\,\mathrm{nm}$ thick chalcogenide layer is then deposited on top of the SOI structure, which covers the area between the two grating couplers but leaves the grating couplers uncovered. A $1.9\,\mu\mathrm{m}$ wide waveguide is patterned using electron beam lithography (EBL) technique in the area where chalcogenide is deposited. Finally, a $1\,\mu\mathrm{m}$ layer of silica cladding covers the waveguide for further protection and providing better confinement. A schematic of the etched hybrid structure is shown in figure 4.14 [6].

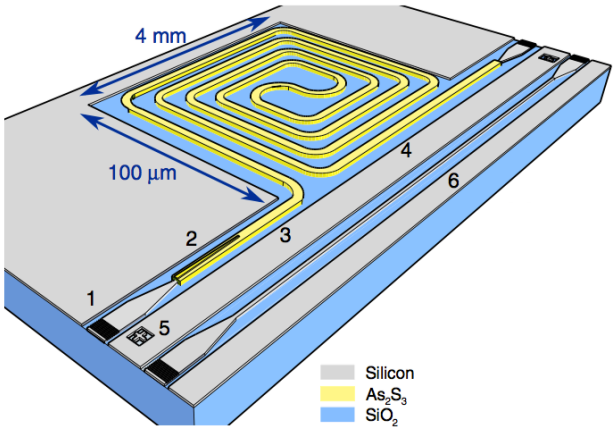

FIGURE 4.14: Structure of the hybrid waveguide for SBS interaction [6].

The silicon taper connecting silicon nanowire to chalcogenide waveguide is long enough to guarantee a smooth optical mode transition. The chalcogenide waveguide is in the form of a spiral consisting of several bends with the physical length of $5.8\,\mathrm{cm}$ and effective length of $3.9\,\mathrm{cm}$ considering the propagation loss of $0.7\,\mathrm{dB/cm}$. The total insertion loss of the waveguide is $4\,\mathrm{dB}$. The waveguide cross-section and the mode profile of fundamental TE mode in the chalcogenide waveguide are shown in figure 4.15 (a) and (b) [6]. The dispersion plot of chalcogenide waveguide shown in figure 4.15 (c) indicates that it can support up to ten optical modes, however a smooth transition from the single mode silicon waveguide to the wider chalcogenide waveguide guarantees that most of the optical power remains in the fundamental

mode while coupling into the chalcogenide waveguide. A transmission loss of $1\,\%$ is calculated through numerical simulation.

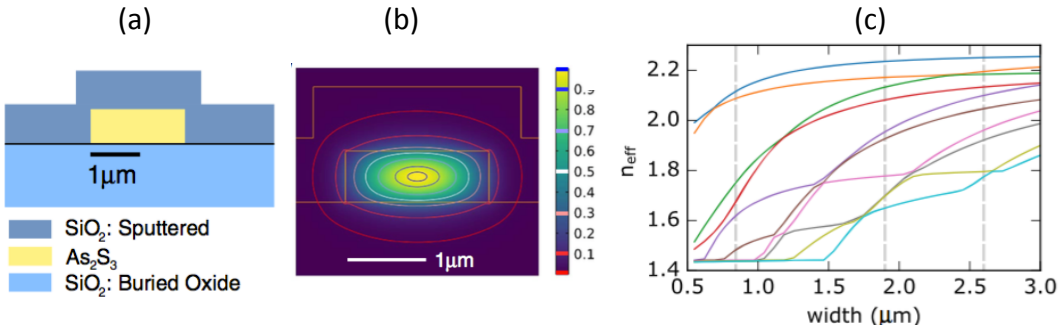

FIGURE 4.15: a) hybrid waveguide cross-section, b) mode profile of fundamental TE mode in hybrid waveguide, c) dispersion plot of the hybrid waveguide; this plot shows effective refractive index calculated for the first ten waveguide modes start from the fundamental mode (TE_0) in blue color up to 10^{st} order mode shown in cyan color. Figure is adopted from ref. [6].

SBS in the hybrid waveguide is measured using the experimental setup shown in figure 4.16. The setup consist of a laser source at frequency ω_c, which divides into pump and probe arms. The pump wave is modulated by an intensity modulator to create an upper-side band shifted by ω_0 from the carrier frequency while the carrier and lower side band are removed by a band-pass filter. The pump is then amplified by an erbium-doped fiber amplifier and is sent into the waveguide through the grating coupler. In the probe arm, the signal is modulated by a single-side band modulator with frequency $\omega_{RF} \approx \omega_0 - \Omega_{SBS}$, where Ω_{SBS} is the Brillouin frequency shift. The upper side band and the carrier then coupled to the waveguide through grating couplers. The probe amplification is collected at port 3 of circulator, where the pump back-reflection is rejected by a band-pass filter. The two remaining frequency components beat together and the amplification of the modulated side band can be measured around the beat frequency ω_{RF} to construct the Brillouin spectrum. The spectrum of the amplified probe for different pump powers are shown in figure 4.16. From this plot, a net Brillouin gain of $18.5\,\mathrm{dB}$ is obtained using the hybrid structure.

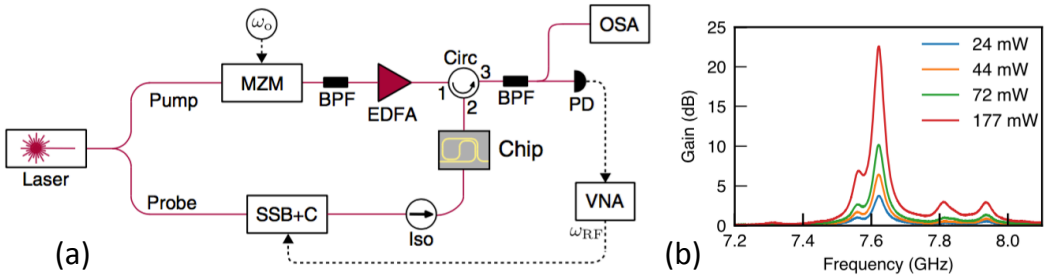

FIGURE 4.16: a) Experimental setup for SBS measurement in hybrid waveguide, b) SBS spectrum at different pump power levels [6].

The Brillouin gain obtained in the hybrid waveguide is further utilized to demonstrate a SBS laser on a silicon-based platform [6]. This is achieved through careful

design of a chalcogenide ring resonator whose free spectral range (FSR) precisely matches the Brillouin frequency shift (BFS) of the waveguide. The detail of the design and experiment can be found in ref. [6].

4.5 Summary

In this chapter, we experimentally demonstrated third-order nonlinearities namely SPM and SBS on a silicon-chalcogenide hybrid waveguide. The first part of this chapter was aimed to demonstrate the nonlinear loss improvement necessary for enabling third-order nonlinear interactions in SOI platforms. A nonlinear FOM was defined to compare the nonlinear performance of a standard silicon waveguide with a silicon-chalcogenide hybrid waveguide. The hybrid waveguide introduced in this chapter is in the form of a cover nonlinearity, however, another possible solution would be the use of a slot waveguide filled with chalcogenide. This approach would result in a much smaller effective area and a higher nonlinear parameter. It is worth mentioning that we also attempted silicon-chalcogenide slot waveguide. However due to the large fabrication tolerances in the thickness of deposited chalcogenide filling and the fact that the slot waveguide operation is sensitive to the thickness of the chalcogenide layer, we were not able to achieve optical transmission in this waveguide.

We also showed how SBS can be achieved in a silicon-chalcogenide hybrid waveguide by properly forming a chalcogenide waveguide, which can confine both optical and acoustic modes. The ability to harness SBS in this waveguide and the flexible design technique allow us to fabricate custom-designed SBS waveguides, which will be used in chapter 5 and 6 to demonstrate our experiments in on-chip SBS distributed sensing.

5 Distributed Brillouin sensing in chalcogenide waveguides: proof-of-concept

As discussed in chapter 2, among different approaches that can be used for a distributed SBS measurement, BOCDA offers the highest spatial resolution. Therefore, we use this technique to measure local SBS responses of photonic waveguides on a chip. Here, an analogy is made to describe the mechanism of BOCDA. BOCDA in many ways can be compared to a radio detection and ranging (radar) systems; both technologies are based on the interference of two electromagnetic waves - one is in the radio frequency (RF) domain and the other is in the optical domain. Also, similar to radar which uses the cross-correlation between the transmitted and the received signals to determine the distance (by measuring the time delay) and the velocity (by measuring frequency difference) of a moving object, BOCDA uses the cross-correlation between the counter-propagating, frequency-shifted pump and probe signals to detect the SBS response at a certain position along the medium as illustrated in figure 5.1 (a) and (c).

In the case of radar, the received signal is compared against copies of the transmitted signal with different delays and frequency shifts. When the delay and the frequency shift of one of the copies matches to that of the received signal, the cross-correlation function between the two signals reaches its maximum value and that way the position and the velocity of the object can be detected. Figure 5.1 (b) shows the cross correlation of the transmitted and the received signals for different delays and at different frequencies through a two-dimensional function called ambiguity function [229], which will be discussed further in the next section. In BOCDA system, the ambiguity function is formed by first varying the frequency shift between the pump and probe waves to find the frequency shift that matches the best to the BFS (here the frequency shift between the two waves is caused by the moving index grating traveling with the acoustic velocity in the medium), and second by scanning the entire length of the waveguide to find the position where the strength of the SBS signal is maximum. Similar to radar, the ambiguity function determines the frequency and spatial resolution of the measurement as shown in figure 5.1 (d).

The following section describes the modeling and experimental steps toward sub-mm spatial resolution measurement of a chalcogenide chip based on ASE-based BOCDA setup.

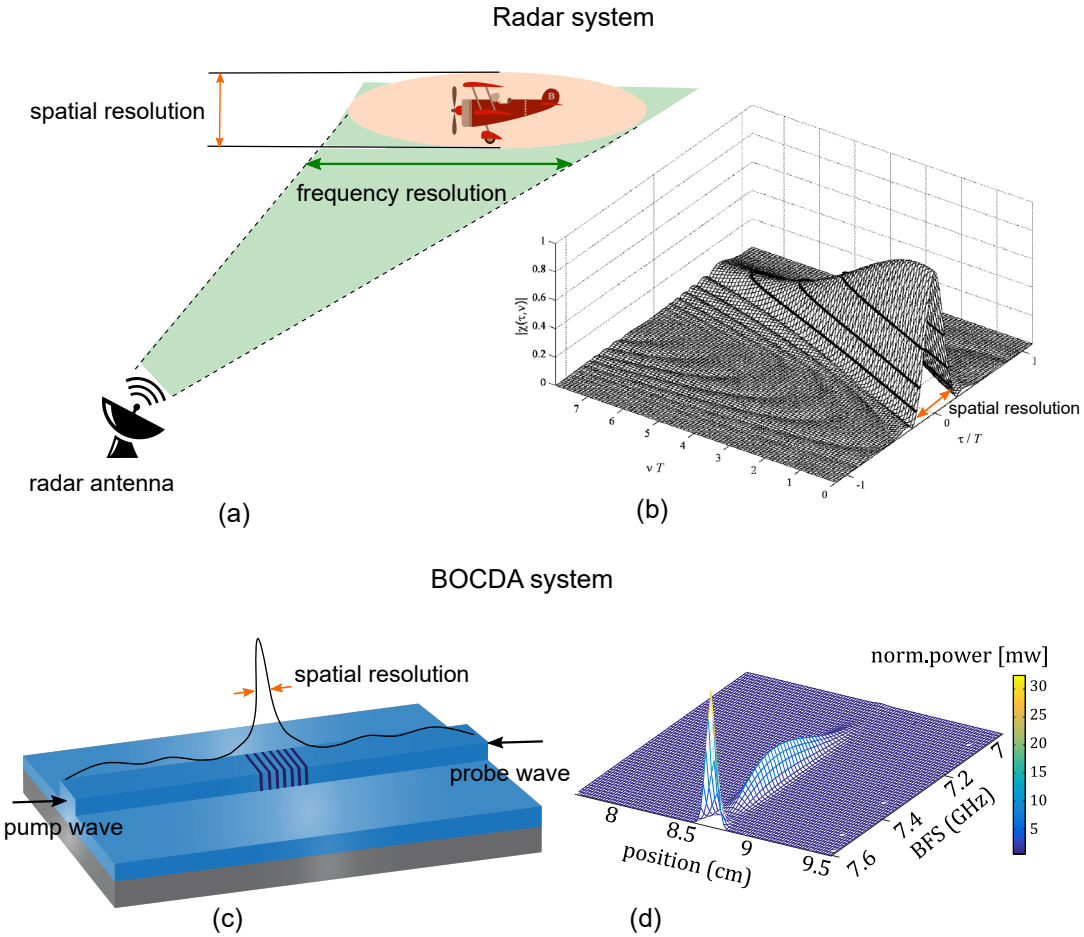

FIGURE 5.1: a) A radar system detecting a moving object with the spatial and frequency resolution determined by the ambiguity function of the transmitted and received signals. b) An example of the ambiguity function for an amplitude-weighted linear-FM pulse [229]. c) BOCDA measurement detecting SBS response in a position along the waveguide using ambiguity function of the pump and the probe signals. d) Ambiguity function of the rectangular-shape ASE pump and probe signals.

5.1 Publication: Highly localized distributed Brillouin scattering response in a photonic integrated circuit

Atiyeh Zarifi, Birgit Stiller, Moritz Merklein, Neuton Li, Khu Vu, Duk-Yong Choi, Pan Ma, Stephen J. Madden, and Benjamin J. Eggleton. "Highly localized distributed Brillouin scattering response in a photonic integrated circuit." *APL Photonics* **3**, *no. 3, page 036101, (2018).*

Abstract

The interaction of optical and acoustic waves via stimulated Brillouin scattering (SBS) has recently reached on-chip platforms, which has opened new fields of applications ranging from integrated microwave photonics and on-chip narrow-linewidth lasers, to phonon-based optical delay and signal processing schemes. Since SBS is

an effect that scales exponentially with interaction length, on-chip implementation on a short length scale is challenging, requiring carefully designed waveguides with optimized opto-acoustic overlap. In this work, we use the principle of Brillouin optical correlation domain analysis (BOCDA) to locally measure the SBS spectrum with high spatial resolution of $800\,\mu\mathrm{m}$ and perform a distributed measurement of the Brillouin spectrum along a spiral waveguide in a photonic integrated circuit (PIC). This approach gives access to local opto-acoustic properties of the waveguides, including the Brillouin frequency shift (BFS) and linewidth, essential information for the further development of high quality photonic-phononic waveguides for SBS applications.

Introduction

Stimulated Brillouin scattering (SBS) is an opto-acoustic interaction, in which the energy of the pump wave transfers into a frequency down-shifted probe wave (Stokes) through an acoustic wave. SBS enables many applications [230] such as narrow linewidth lasers [32]–[34], [80], optical delay lines [22]–[24], temperature [231] and strain sensors [38], [39], [161], [232], microwave generation [11], [12] and signal processing [18], [19], [35]. In particular, the possibility to generate SBS on-chip opens a new paradigm for compact integrated devices in a small-footprint [19], [44], [74], [217]. Harnessing SBS on-chip, however, is challenging since SBS scales exponentially with the interaction length [10]. To achieve strong opto-acoustic coupling, it is necessary to confine the optical and acoustic mode simultaneously in a small cross-section [42]. One possibility is to use soft-glass waveguides sandwiched between a more rigid cladding material [74], however in recent years more complex structures were put forward to generate strong on-chip opto-acoustic overlap, such as under etched silicon waveguides [44], [45], hybrid silicon-silicon nitride membranes [233], fully suspended nanowires [44], band gap engineered soft-glass waveguides [234] or multi-material hybrid circuits [6], [235]. The high complexity of the waveguides that guide optical and acoustic waves, and the sensitivity of these modes to even small variations in geometry [41], [47], [236] requires a technique to probe the opto-acoustic coupling strength on a sub-millimeter length scale. These new insights will help to better understand local parameters effecting the overall SBS gain response, ensuring high performance and high yield of the photonic waveguides. In addition, as part of the design process, it is critical to study and characterise new designs against the simulation results and understand the effect of local design parameters such as tapers, bends and couplers on the overall opto-acoustic response of the waveguide.

Numerous distributed SBS measurement techniques have been developed, including Brillouin optical time domain analysis (BOTDA) [39], [69], [70], Brillouin echo distributed sensing (BEDS) [92], [93] and Brillouin optical correlation domain analysis (BOCDA) [40], [112], [161]. BOTDA has limited spatial resolution, since the pump pulses should not be shorter than the phonon lifetime (corresponding to 1 m spatial resolution in optical fiber). BEDS proposal was put forward to overcome this limitation relying on a short π phase shift applied to the continuous wave (CW) pump instead of a pulsed pump, which improves the spatial resolution down to $1\,\mathrm{cm}$ [39], [92]. BOCDA enables millimeter order spatial resolution through broad spectrum pump and probe whose product in time domain is a spatially localized

correlation peak. The linewidth of this correlation peak defines the spatial resolution of the system.

The first BOCDA technique was based on the broad-spectrum frequency-modulated pump and probe waves [111], [112]. A more advanced setup using the same technique was introduced in [38], where $3\,\mathrm{mm}$ spatial resolution in fiber was experimentally demonstrated. Also, a $5.9\,\mathrm{mm}$ spatial resolution Brillouin frequency shift measurement in PLC was reported in [47]. Following the initial demonstration of BOCDA, different variations of BOCDA have been introduced, including random bit phase-modulated pump and probe [51], Golomb-code modulated pump and probe [237] and noise-based correlation technique [113], [157]. The realization of the broad-spectrum pump and probe through the frequency and phase modulation adds to the complexity of the experiment and limits the measurement range due to multiple correlation peaks, whereas the noise-based correlation technique relies only on the amplified spontaneous emission (ASE) of an Erbium doped fiber [113], which offers simplicity and high spatial resolution. $3\,\mathrm{mm}$ and $4\,\mathrm{mm}$ spatial resolution in fiber were reported in [238] and [113], respectively using the noise-based approach. However, the noise-based approach suffers from limited signal to noise ratio (SNR) mainly due to the stochastic nature of the ASE source.

In this work, we chose the latter approach to characterise chalcogenide photonic waveguides, since this technique offers the highest spatial resolution based on a simple ASE source. We demonstrate a record on-chip spatial resolution using this noise-based BOCDA measurement and a significant improvement in SNR is achieved by adding a lock-in amplifier (LIA) to the setup. We spatially resolve the Brillouin response of a chalcogenide photonic waveguide on a chip with a high spatial resolution of $800\,\mu\mathrm{m}$, which we believe is the the smallest section over which SBS has been observed in a planar waveguide. This setup employs the ASE of an Erbium doped fiber to resolve features such as waveguide thickness and the resultant effective refractive index change of an As_2S_3 photonic waveguide. This work provides the basis for the understanding of a very local interaction of optical and acoustic waves and the design of novel waveguide structures.

Principle of operation

SBS is an inelastic scattering effect, in which two counter-propagating optical pump and probe waves generate a moving index grating in the medium, which travels with the acoustic velocity (v_a). The pump wave is backscattered by the moving index grating, which results in a frequency down-shifted Stokes wave in the backward direction. The frequency difference between the pump and the Stokes is called the Brillouin frequency shift (BFS) Ω_B and is defined as [53], [239]:

$$\Omega_B = \frac{2n_{\mathrm{eff}}\mathrm{v}_a}{\lambda}, \tag{5.1}$$

where n_{eff} is the effective refractive index of the medium and λ is the pump wavelength. The BFS depends upon the optical material as well as the waveguide dimensions and environmental conditions such as temperature and strain, which makes SBS suitable for sensing purposes [40], [161], [231]. In order to employ SBS as a distributed sensing approach, a localize BFS measurement is required. Among the different distributed SBS techniques introduced in the previous section, we select BOCDA since it provides the highest spatial resolution down to mm-scale [38], [113],

which is the preferred method for mapping cm-scale integrated photonic circuits [47].

The key to realize a localized SBS measurement using BOCDA is that unlike the conventional SBS measurement technique, which relies on the coherent pump and probe signals, BOCDA employs a highly non-coherent signal as the pump and the probe [112]. In general, the cross-correlation function between the pump and the probe signals (could also called the auto-correlation function since the pump and the probe signals are driven from the same source) defines the spatial resolution of the local SBS response. For an integrated SBS measurement, the coherent pump and probe signals create a constant cross-correlation function along the medium, therefore the SBS response is the accumulative gain collected from the entire length of the medium. In BOCDA, however, the cross-correlation between the non-coherent pump and probe signals gives rise to a spatially localized correlation peak, which confines the SBS response into a narrow region and suppresses it elsewhere in the medium [112]. This gives access to a localized SBS response and is illustrated in Fig. 5.2(a).

A filtered ASE source with a bandwidth of 80 GHz and its auto-correlation function are shown in Fig.5.2(b) and Fig.5.2(c), respectively. The bandwidth Δf of the ASE spectrum defines its coherence time Δt by: $\Delta t \Delta \mathrm{f} \approx 1$. Therefore, the spatial resolution of the localized response can be adjusted by changing the ASE bandwidth [113].

The overall SBS gain (g) is obtained by adding together the individual local Brillouin gain spectrum g_B, spatially weighted by the cross-correlation function over the entire length of the waveguide using the following equation [112]:

$$g = \frac{v_g \bar{P}_1}{A_{\text{eff}} \Delta t} \int_{-\infty}^{\infty} d\tau \int_{-\infty}^{\infty} g_B(\tau, \nu) \left|\chi(\tau, \nu)\right|^2 d\nu, \tag{5.2}$$

where v_g is the group velocity of light in the medium, $\bar{P}_1$ is the average pump power, A_{eff} is the waveguide effective area, and $\chi(\tau, \nu)$ is a two dimensional function, which defines the cross-correlation between the complex envelope of the pump $u(t)$ and the probe $u(t-\tau)$ as a function of the delay (τ) and the frequency shift (ν) between the pump and the probe. $\chi(\tau, \nu)$ is calculated using the following equation [112], [229]:

$$\chi(\tau, \nu) = \frac{nc\epsilon_0 A_{\text{eff}}}{2\sqrt{\bar{P}_1 \bar{P}_2}} \int_{-\infty}^{\infty} u(t) u^*(t-\tau) \exp(i2\pi\nu t) dt, \tag{5.3}$$

where n is the refractive index of the medium, c is the speed of light in the vacuum, ϵ_0 is the free space permittivity and $\bar{P}_2$ is the average probe power. Equation 5.3 is also known as the ambiguity function [229], since it introduces a degree of ambiguity in the measured Brillouin gain spectrum. A simulation of the ambiguity function for the $80\,\mathrm{GHz}$ ASE spectrum pump and probe is shown in Fig. 5.2(d).

In this simulation, the medium is a $17.5\,\mathrm{cm}$ chalcogenide waveguide with the BFS of $7.6\,\mathrm{GHz}$, and the pump and the probe arm are assumed to have the same length (zero delay between the pump and the probe). The delay between the pump and the probe can be translated into the position in the waveguide using the relation: $x = \frac{1}{2}(v_g \tau + L)$, where v_g is the group velocity in the waveguide and L is the total length of the waveguide. As it can be seen in Fig. 5.2(d), the correlation peak occurs in the middle of the waveguide (plotted in linear scale), and the frequency response is maximum at $7.6\,\mathrm{GHz}$.

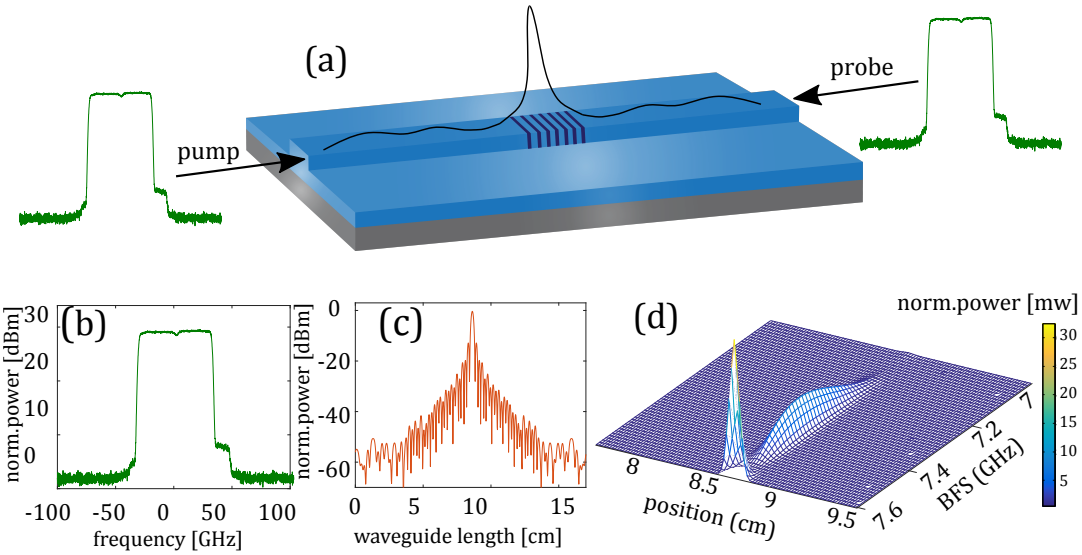

FIGURE 5.2: a) Correlation peak in the waveguide as a result of broad-spectrum pump and probe. b) 80 GHz ASE spectrum and c) its auto-correlation function in dB scale along the waveguide. d) Ambiguity function of an 80 GHz square ASE spectrum in a As_2S_3 waveguide, the colormap is scaled with the normalized linear power of the ambiguity function.

In our experiments, a filtered ASE of an Erbium doped fiber is used as the common source for the pump and the probe. The correlation peak position is moved along the medium using a delay line to change the relative delay between the pump and the probe arms. The integral sum of the local Brillouin gain spectrum multiplied by the local spectrum of the ambiguity function over the length of the medium is measured for each delay step, which is referred to as the local SBS response in this document. This product is maximum at the correlation peak and is suppressed by the shape of the correlation function at any other point. The contribution of these points add to the ambiguity (noise) of the overall Brillouin gain spectrum.

Experiment and discussion

Experimental setup

The experimental setup is shown in Fig. 5.3(a). The ASE spectrum of an Erbium doped fiber passes through a polarization beam splitter (PBS) and is filtered to a square-shape spectrum. The bandwidth of the band-pass filter varies from 25 GHz to 89 GHz depending on the desired spatial resolution. An Erbium doped fiber amplifier (EDFA) is used to pre-amplify the polarized filtered ASE, which is then divided between the pump and the probe arms with a power ratio of 30 % to 70 %, respectively.

The pump signal is modulated by a Mach-Zehnder modulator (MZM) using square pulses of 500 ns width and 5 % duty cycle. The same radio-frequency (RF) source that derives the MZM, triggers the lock-in amplifier (LIA) with the reference frequency of 100 kHz. In the probe arm, a dual-parallel Mach-Zehnder modulator (DPMZM) is used to generate a single sideband (SSB), down-shifted by the BFS (10.8 GHz for SMF and approximately 7.6 GHz for chalcogenide waveguides).

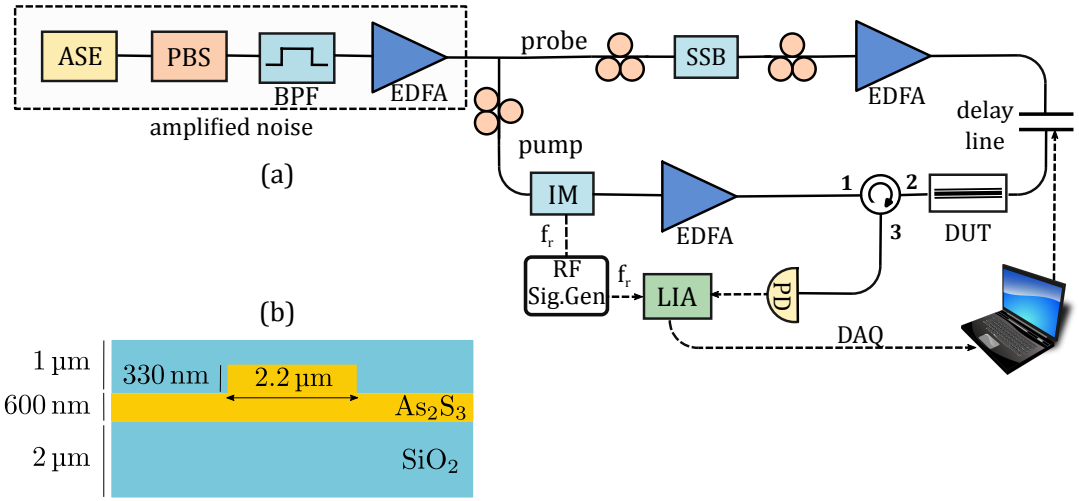

FIGURE 5.3: a) Setup for BOCDA measurement. LIA: lock-in amplifier, BPF: band-pass filter, PBS: polarization beam splitter, IM: intensity modulator, SSB: single side band modulator, PD: photo-detector, DUT: device under test, f_r: reference frequency, RF Sig. Gen.: radio frequency signal generator, DAQ: data acquisition. b) cross-section of the As_2S_3 short waveguide.

This technique results in $25\,\mathrm{dB}$ of side-band and carrier suppression, which is critical to improve the SNR. The SSB is swept over a $350\,\mathrm{MHz}$ frequency span around the BFS using an automated RF signal generator to measure the SBS gain spectrum. The delay line is swept automatically to change the delay between the pump and the probe arms and therefore, changing the position of the correlation peak in the medium. The pump and the probe signals counter-propagate through the medium and the back- scattered signal (Stokes) is collected at port 3 of the circulator. At the LIA, only frequency components which match the frequency of the pump pulses (reference frequency) are detected and amplified and the rest of the ASE spectrum coming from the probe is rejected; this will improve the SNR of the measurement. Also, since SBS is a polarization sensitive process and our waveguide is strongly birefringent, careful consideration was taken during the measurement to align the polarization of the pump and the probe signals to the fundamental TE mode. Once the polarisation is optimised, it remained unchanged during the measurement.

Signal to noise ratio (SNR)

The SNR for this experiment is defined as the ratio of the increment in the expected value of the detector reading due to the SBS amplification (ΔW) to the detector noise (σ_W) as described in reference [113].

$$\mathrm{SNR} = \frac{\Delta W}{\sigma_W}. \tag{5.4}$$

After substituting the terms ΔW and σ_W from reference [238], the SNR can be summarized as follows:

$$\mathrm{SNR} = \frac{g_B P_P}{A_{\mathrm{eff}}} \sqrt{\frac{v_g T \Delta x}{2}}, \tag{5.5}$$

where g_B is the SBS gain coefficient, P_P is the peak pump power, A_{eff} is the effective waveguide area, v_g is the group velocity, T is the LIA integration time and Δx is the spatial resolution. In our devices g_B/A_{eff} is in the order of $400\,\text{m}^{-1}\,\text{W}^{-1}$, the detector integration time is $50\,\text{ms}$ and depending on the peak pump power and the spatial resolution of the measurement, the SNR varies from 36 dB to 38 dB. It should be noted that we calculated the SNR by taking into account the contribution from the LIA, which is not present in the previously reported measurement [238], where instead a large number of averaging was performed to improve the signal detection.

The SNR of this measurement is mainly limited by the stochastic nature of the ASE source [162]. In addition, since this measurement is carried out in a photonic waveguide, we have a strong back reflection component at the reference frequency ($100\,\text{kHz}$) due to the waveguide facets and Rayleigh back scattering. The contribution of the pump back reflection is therefore always present in the measurement and deteriorates the experimental SNR.

Scanning the waveguide

We aim to fully detect and resolve a short As_2S_3 rib waveguide. The waveguide is $2.2\,\mu\text{m}$ wide with slab thickness of $600\,\text{nm}$ and ridge thickness of $330\,\text{nm}$ as shown in Fig. 5.3(b). The light is coupled into and out of the waveguide using lensed fibers with approximate coupling loss of 4.2 $\pm$ 0.2 dB per facet. The propagation loss is about $0.2\,\text{dB}\,\text{cm}^{-1}$ and the total loss of the waveguide is 9 $\pm$ 0.5 dB at the pump peak power of 27 dBm.

The filter bandwidth is set to $25\,\text{GHz}$ corresponding to $2.5\,\text{mm}$ spatial resolution in the waveguide according to:

$$\Delta x \approx \frac{1}{2} v_g \Delta t, \tag{5.6}$$

where $v_g = \frac{c}{n_g}$ and n_g is the group index of the waveguide.

The delay line and the RF signal generator are controlled by a computer program; the delay line takes $1\,\text{mm}$ steps at every $5\,\text{s}$ and the RF signal generator sweeps the probe signal over $350\,\text{MHz}$ span with $2.5\,\text{MHz}$ spectral resolution for each delay step. For every frequency, the back scattered signal is collected at port 3 of the circulator and is measured by the LIA.

By moving the correlation peak through the waveguide using the delay line, a map of local Brillouin responses is created as shown in Fig. 5.4(a). The region over which the local Brillouin responses are detected is approximately $20.8\,\text{mm}$, corresponding to the length of the waveguide.

By fitting the local responses with a Lorentzian profile, a map of BFS over the length of the waveguide is established. The BFS over this region is fairly consistent with a mean value of $7.58\,\text{GHz}$ and standard deviation of $3.2\,\text{MHz}$, which confirms the uniformity of the waveguide. In order to confirm this measurement, the waveguide is scanned in a reverse direction; that is the pump and the probe directions are swapped. This measurement also shows consistent BFS over the waveguide length. The BFS associated with the two measurements are shown in Fig. 5.4(b).

A local Brillouin response at a random position in the waveguide ($1.4\,\text{cm}$ from the waveguide input facet) is shown in Fig. 5.4(c). A Lorentzian profile is fitted to the measured points, which has a linewidth of $41\,\text{MHz}$ and a maximum at $7.58\,\text{GHz}$, corresponding to the linewidth and the BFS of the local SBS gain spectrum. The

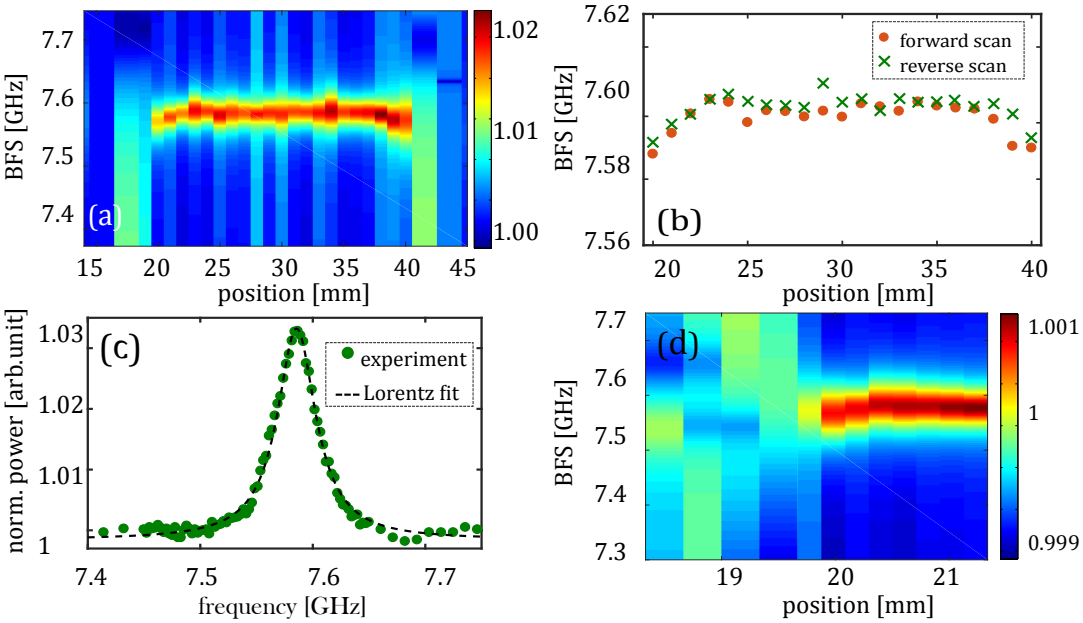

FIGURE 5.4: a) Normalized,Lorentz fit of the BOCDA measurement in a short As_2S_3 waveguide (the colormap plot shows the normalized power in a linear scale). b) BFS of the forward and backward scan. c) A local Brillouin spectrum at $1.4\,\mathrm{cm}$ from the waveguide facet with a Lorentzian fit. d) Scan of the waveguide facet with $800\,\mu\mathrm{m}$ spatial resolution, averaged over four traces (the colormap shows the normalized power in a linear scale).

measured local gain at this position is approximately $0.15\,\mathrm{dB}$, and the SNR according to Equation 5.4 is $25\,\mathrm{dB}$. The discrepancy between the calculated and the measured SNR is mainly due to the strong pump back-reflection coming from the waveguide facets.

The filter bandwidth is then increased to $80\,\mathrm{GHz}$, which corresponds to a spatial resolution of $800\,\mu\mathrm{m}$ in the waveguide. The edge of the waveguide is resolved using this high spatial resolution setting as it is shown in Fig. 5.4(d). Since the SBS interaction length is only $800\,\mu\mathrm{m}$, an averaging over four measurements is required to resolve this region. The delay steps in the delay line are set to 1 mm in free space and the scanning range is over 3 mm length of the waveguide. As the correlation peak travels from the lensed fiber into the chalcogenide waveguide, the optical field experiences different effective refractive indexes. This means that for a fixed delay step in free space ($1\,\mathrm{mm}$), the delay steps outside the waveguide are longer ($0.33\,\mathrm{mm}$) than the delay steps inside the waveguide ($0.2\,\mathrm{mm}$). This feature can be seen in Fig. 5.4(d).

Waveguide characterization

The second experiment aims to look at the uniformity of a long spiral waveguide ($17.5\,\mathrm{cm}$ long), which consists of several $180°$ bends (with bend radius of approximately $200\,\mu\mathrm{m}$) as well as straight regions. The waveguide is in the form of a rib waveguide and is $2.4\,\mu\mathrm{m}$ wide with slab thickness of $600\,\mathrm{nm}$ and ridge thickness of $330\,\mathrm{nm}$.

The filter bandwidth is set to $62.5\,\mathrm{GHz}$ corresponding to $1\,\mathrm{mm}$ spatial resolution in the waveguide. The waveguide insertion loss is 15 ± 1 dB and the pump peak power before coupling is set to 29 dBm. The spectral resolution of the measurement is $2.5\,\mathrm{MHz}$ and each local measurement takes $5\,\mathrm{s}$ to complete. Fig. 5.5(a) shows a map of local Brillouin responses over the first $5\,\mathrm{cm}$ of the waveguide, which is closer to the pump arm. As it is plotted in Fig. 5.5(a), the local BFS gradually changes in an oscillating pattern as we scan through the waveguide. In order to confirm this measurement, the waveguide is scanned in the reverse direction by physically swapping the pump and the probe connections to the waveguide. As it is shown in Fig. 5.5(b) - which is a mirrored image of the first scan, the same variations in the local BFS is observed when the direction of the scan is changed. From Fig. 5.5(b), it can be seen that the SNR of the local responses in the second scan is lower compared to the first scan. This is due to the fact that the two measurements are not symmetric. In the first measurement, we scan the edge of the waveguide (toward the pump) whereas in the second measurement, the pump and probe are swapped and the pump is now located further away from the scanning region. Therefore, the pump signal experiences an additional propagation loss (3.5 dB), which results in a lower SNR.

Fig. 5.5(c) confirms that the local BFS in the forward and the reverse scan match. In addition, a local BFS variation of $22\,\mathrm{MHz}$ is observed in this plot. This suggests that the optical mode experiences varying effective refractive index as it propagates through the waveguide, according to Equation 6.1. By matching the BFS to the waveguide layout as shown in Fig. 5.5(d), it can be seen that as we scan from the edge of the waveguide toward the bends and travels back to the edge, the BFS changes accordingly. This confirms that the waveguide has a lower effective refrative index at the edge and slightly higher effective refractive index at the center. The linewidth of the local SBS responses along the waveguide is shown in Fig. 5.5(e). The standard deviation is $1.53\,\mathrm{MHz}$and $6.03\,\mathrm{MHz}$for the forward and the backward scan, respectively. The local Brillouin response and its Lorentzian fit at position $2\,\mathrm{cm}$ from the edge of the waveguide for the forward measurement are depicted in Fig. 5.5(f). The local response has a linewidth of $42.7\,\mathrm{MHz}$ and a BFS of $7.72\,\mathrm{GHz}$ as shown in Fig. 5.5(f). The local gain at this position is measured to be $0.9\,\mathrm{dB}$, and the SNR according to Equation 5.4 is $26.7\,\mathrm{dB}$.

Simulation and Analysis

In order to confirm the effective refractive index variation, we used the spectroscopic reflectometry technique [240] to obtain the refractive index information of the chalcogenide film across the wafer with a resolution of $1\,\mathrm{cm}^2$. Fig. 5.6(a) shows the reflectometry result where the red box indicates the region which is scanned by the BOCDA setup. The map indicates 0.008 index variation over $20\,\mathrm{mm}$ length of the waveguide. In addition, we investigate the effect of deposition and etching non-uniformity on the effective refractive index by sweeping the ridge and the slab thicknesses over the fabrication variation of $\pm 5\,\%$ using a commercial-grade simulator eigenmode solver and propagator [223]. The result is presented in Fig. 5.6(b). From this figure, a change of $22.8\,\mathrm{MHz}$ in BFS occurs if the ridge and the slab thicknesses increase by $5\,\%$ from the edge of the waveguide toward the center, which agrees well with the BOCDA measurement. Note that this photonic chip, which has

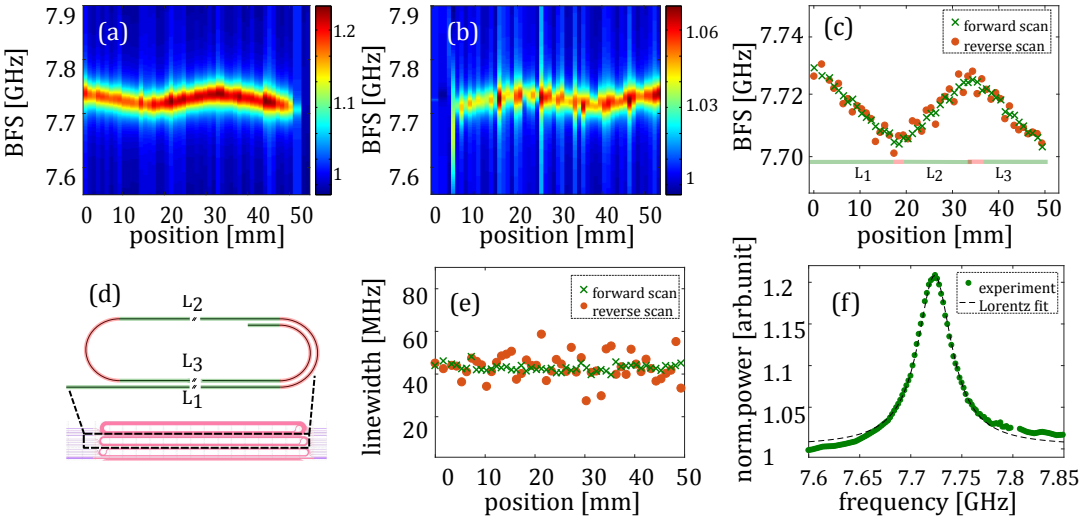

FIGURE 5.5: BOCDA scan of the long waveguide in a) forward direction and b) reverse direction (the colormap shows the normalized power in a linear scale). c) BFS of the forward and the backward scan. d) the mask layout and the schematic of the scanned region in the waveguide. e) Local SBS linewidth of the forward and reverse scan. f) Local SBS response at position 2 cm from the front facet in the forward direction.

extreme variation in its refractive index values (not a typical one), was selected to enable us to track these changes with our BOCDA system.

The effect of the bends on the effective refractive index change and consequently the BFS change is also studied; the numerical simulation indicates 3 MHz BFS change due to the bends for the fundamental TE mode (which is the dominant mode in the waveguide) and 120 MHz change in the BFS as a result of coupling to the higher order mode. Comparing these values with the experimental observation, confirms that the BFS variation is not due to the bends and that the optical mode remains unaffected by the bends.

Spatial Resolution Confirmation

In order to confirm the spatial resolution of the BOCDA setup, detection of a 1 mm long dispersion shifted fiber (DSF) spliced in between the two pieces of single mode fiber (SMF) with slightly different BFS is demonstrated.

The ASE bandwidth is set to 89 GHz, which corresponds to 1.1 mm spatial resolution in silica fiber. The correlation peak is moved by 0.2 mm steps in fiber. As it moves from the SMF into the DSF and back to the SMF again, the BFS of the local Brillouin responses changes from 10.89 GHz to 10.68 GHz and back to 10.89 GHz as shown in Fig. 5.7(a). Fig. 5.7(b) shows the appearance and disappearance of the DSF peak over the short region of 1 mm. As it is observed in Fig. 5.7(b), the SMF peak is present in all the traces since part of the correlation peak always overlap with the SMF. However, the amplitude of the SMF peak is the lowest when the correlation peak is entirely inside the DSF, and has minimum overlap with the SMF. The SNR in this measurement is low because silica fiber has lower SBS gain compared to the

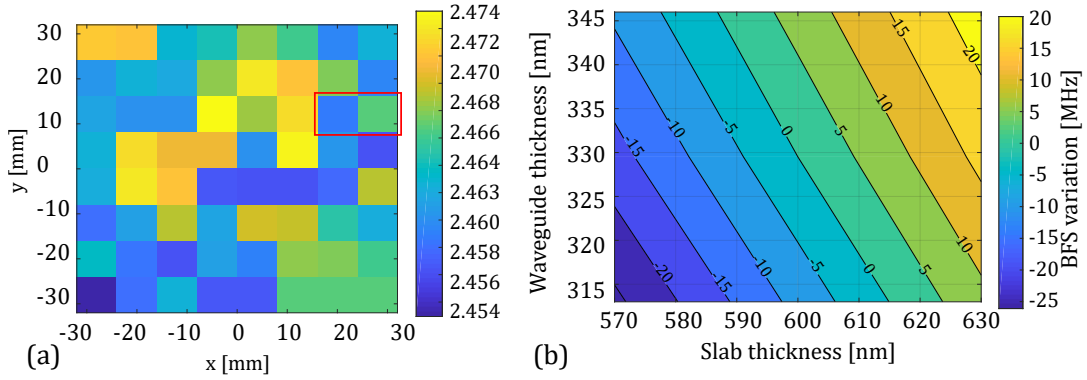

FIGURE 5.6: a) Refractive index map of the wafer taken by a spectroscopic reflectometer (the BOCDA scanned region is indicated by the red box). b) Simulation result of variation in BFS as a function of slab thickness and waveguide thickness.

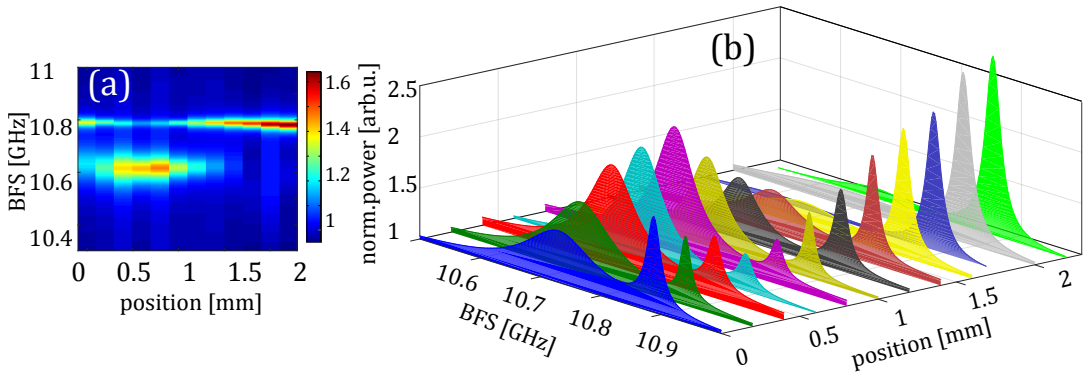

FIGURE 5.7: a) Scan of a 1 mm piece of DSF spliced in between the SMF fiber with 1.1 mm spatial resolution (the colormap shows the linear normalized power). b) Local SBS response at different positions of the sample.

As_2S_3 waveguide. Therefore, we averaged the measurement over four traces to fully recover the DSF piece.

Conclusion

A BOCDA distributed SBS measurement with on-chip spatial resolution of 800 µm and 1.1 mm spatial resolution on fiber is presented. This sub-mm spatial resolution is achieved despite the challenges present in the photonic waveguide measurement including sensitive power handling, strong polarisation sensitivity, additional loss due to the coupling from the fiber to the waveguide and strong back reflection due to the waveguide facets, which are not present in any of the fiber based measurement previously reported. The issue of SNR reported in Ref. [113] was addressed using a LIA detection technique. Using this setup, we demonstrate the degree of uniformity of As_2S_3 waveguide. As a proof of principle demonstration, we resolved 5% variations in waveguide thickness, which is in agreement with expected fabrication tolerances. This demonstration presents the first on-chip SBS response measurement with sub-mm resolution and opens up new opportunities to discover fundamental

opto-acoustic effects locally in SBS integrated platforms, which have not yet been studied closely. In addition, from the design optimization point of view, this setup will enable us to study the local SBS response in any part of the waveguide which is subjected to the geometrical variations such as tapers and bend regions in long spiral waveguides, which is critical for designing new opto-acoustic waveguides.

5.2 Additional measurements

In addition to the published work reported in the previous section, we provide some additional measurement to give the reader a better prospective on the technical aspects of the measurement and the limitations we were facing in the experiment.

The effect of ASE spectrum on the spatial resolution

Here, we experimentally study the effect of the pump and probe spectral profile on the spatial resolution of the BOCDA measurement. From table 1.3 in chapter 3, it is evident that a Gaussian power spectral density profile would be a good choice for this purpose, since its auto-correlation function is also a Gaussian function and does not have any sidelobes [164]. Such spectral shape can be constructed using a specialized filter known as *WaveShaper* by FINISAR [241]. However, the extinction ratio of this filter is not as high as some other rectangular filters (*Yenista XTM-50 [242] and Alnair-BVF-300CL [243]*) which were available to us. The rectangular filters provide approximately $10\,\mathrm{dB}$ higher extinction ratio compared to the WaveShaper. Although the Gaussian profile performed well up to spatial resolution of $1.5\,\mathrm{mm}$, its performance deteriorated for spatial resolutions beyond this point due to the weak SNR. As a result, we proceeded our measurements using the high extinction ratio rectangular filter.

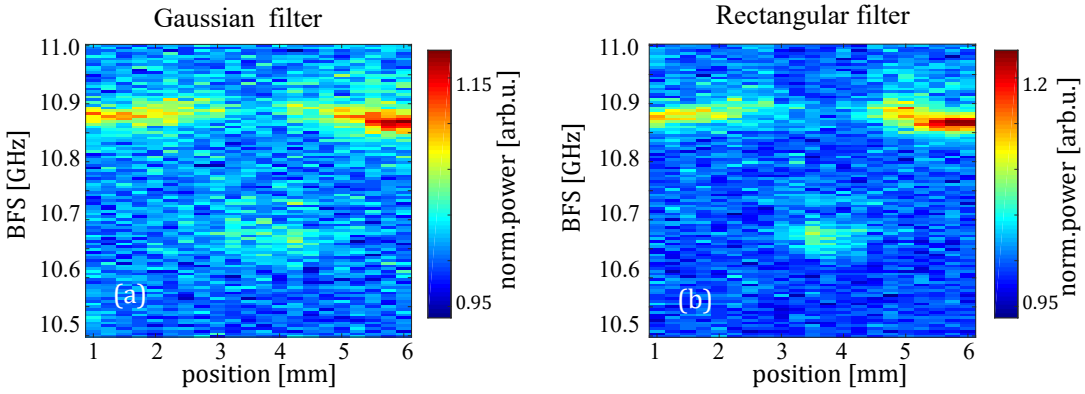

FIGURE 5.8: Measurement of $1\,\mathrm{mm}$ piece of DSF using ASE-based BOCDA technique with a) a Gaussian and b) a rectangular filter.

Figure 5.8(a) represents the measurement of a $1\,\mathrm{mm}$ piece of DSF using a Gaussian filter with $1.5\,\mathrm{mm}$ spatial resolution. We also provided the same measurement using a rectangular filter with spatial resolution of $1\,\mathrm{mm}$ in figure 5.8(b). The step size in both measurement are $0.25\,\mathrm{mm}$. As it can be seen in this figure, the $1\,\mathrm{mm}$ DSF can be detected by both filter shape, however, the SNR in the rectangular filter shape is slightly higher than the one measured with the Gaussian filter. In both measurements, we averaged over four traces to improve the SNR.

In addition to the ASE spectral profile, we also investigated the effect of filter bandwidth on the strength of local SBS responses. Figure 5.9 shows the local SBS response for three different bandwidth at the same point along the DSF. Here we used the rectangular filter and changed the bandwidth from 40 GHz to 100 GHz. As it can be seen in this plot, the amplitude of the local Brillouin gain decreases as the filter bandwidth increases. It is also evident from this figure that the linewidth of SBS response increases as the bandwidth of the filter increase. This is due to the fact that by increasing the ASE bandwidth, we limit the SBS interaction to a shorter length within the medium and therefore, the amplitude and the linewidth of the SBS response deteriorate.

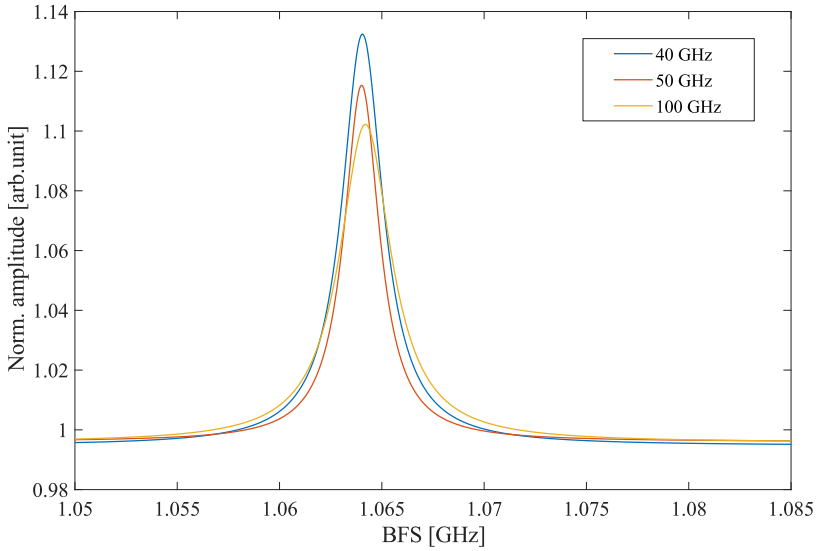

FIGURE 5.9: Normalized local Brillouin gain spectrum for three different ASE bandwidths.

In this chapter,we demonstrated an on-chip SBS measurement on a chalcogenide rib waveguide. We were able to obtain a map of the local BFS along on-chip waveguides by limiting the SBS interaction length to 800 µm and showed the uniformity of these waveguides. In the next chapter, we explain how this technique can be used on a silicon-based platform. We also customize the design of the photonic waveguides on this new platform to confirm on-chip spatial resolution.

6 Distributed Brillouin sensing in customized hybrid waveguides: record spatial resolution

In the previous chapter, we measured the distributed SBS response of a chalcogenide waveguide with on-chip spatial resolution of $800\,\mu\mathrm{m}$. We confirmed the spatial resolution by detecting a $1.1\,\mathrm{mm}$ piece of DSF spliced in between standard SMF. In this chapter, we design and fabricate hybrid silicon-chalcogenide waveguides with controlled longitudinal variations to first demonstrate an on-chip distributed measurement in a silicon-based platform, and second to confirm the on-chip spatial resolution using a controlled defect on chip.

In section 6.1, we elaborate on the design considerations of silicon-chalcogenide waveguides for sensing. Sections 6.2 and 6.3 are published results in ref. [2] and [3], respectively. Section 6.2 of this chapter demonstrates the detection of a $2\,\mathrm{mm}$ longitudinal feature in a hybrid silicon-chalcogenide waveguide, which is the first demonstration of on-chip Brillouin sensing on a silicon-based chip. Section 6.3 demonstrate spatial resolution up to $500\,\mu\mathrm{m}$ with detection capability of $200\,\mu\mathrm{m}$, which was achieved by further optimizing the experimental setup, that is separating the Rayleigh scattered pump from the amplified probe. In this section, we also provide more insight toward opto-acoustic interactions in these hybrid waveguides and explain how SBS response can be used to sense the geometrical variations along the waveguide. In section 6.4 we provide an analysis on the effect of fabrication tolerances on opto-acoustic responses of hybrid waveguides.

6.1 Waveguide design considerations

In order to demonstrate on-chip geometrical variation sensing, we take advantage of the flexible design and fabrication process enabled by IPKISS design work flow and EBL technology, respectively. IPKISS is a design framework for integrated photonic circuits (*IPKISS* from *Luceda photonics*). Part of the mask design for the hybrid structures with variations in width is shown in figure 6.1. The boxes in the middle of the waveguides show the region with different width compared to the rest of the waveguide, providing a platform for on-chip sensing.

In the hybrid silicon-chalcogenide platform, light is coupled in and out of the waveguide through grating couples, which are connected to silicon nanowires. The silicon nanowires then tapered down over a length of $100\,\mu\mathrm{m}$ to a narrow tip of $150\,\mathrm{nm}$. Optical mode enters the chalcogenide waveguide at the end of this tip. One of the design considerations in these waveguides is, therefore, the smooth transition of optical mode from the silicon nanowire to the chalcogenide waveguide through the silicon taper. This adiabatic transition is guaranteed by selecting the taper length

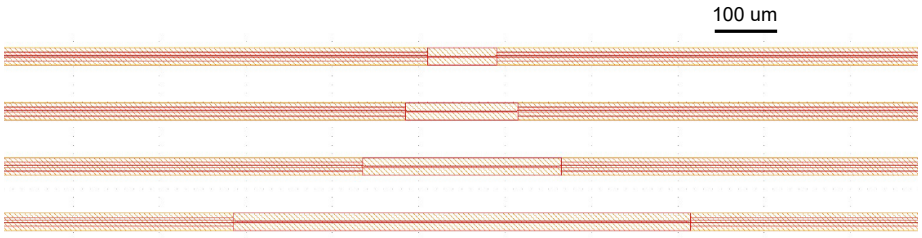

FIGURE 6.1: Part of the chalcogenide waveguides mask layout with the sensing region varying in lengths from $100\,\mu m$ to $1\,mm$.

such that $l \gg \lambda$, where $l = 100\,\mu m$ is the taper length and $\lambda = 1.55\,\mu m$ is the optical wavelength.

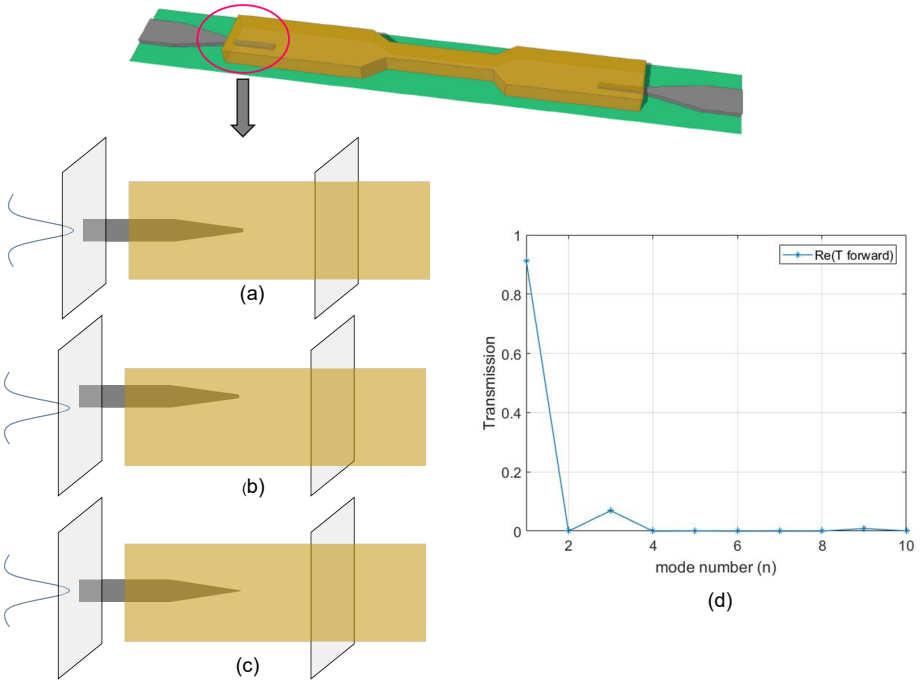

FIGURE 6.2

In order to estimate the effect of fabrication tolerances on the performance of the taper, we performed a 3D Finite Difference Time Domain (FDTD) simulation using Lumerical software [223]. Figure 6.2 summarizes the result of this simulation. The hybrid waveguide is shown at the top of this figure with the zoom-in on the silicon taper. Figure 6.2 (a) shows the ideal case, when the silicon taper is at the center of the chalcogenide waveguide and its tip width is $150\,nm$. Figure 6.2 (b) represents the case when the silicon taper is offset from the center of the chalcogenide waveguide by $200\,nm$ and in figure 6.2 (c) the width of the tip varies from $250\,nm$ to $50\,nm$. Figure 6.2 (d) shows the transmission of the first ten optical modes from the silicon to the chalcogenide waveguide, which is the overlap of the transmission in all three cases. As it can be seen in this plot, the transmission profiles are almost identical despite the variations in the position and geometry of the taper, which shows that the taper design is robust against the fabrication tolerances. It should be noted that

the variations used for the simulation are slightly higher than the reported fabrication tolerances from our collaborators. Another point we can infer from the plot in figure 6.2 (d) is that the majority of the optical power (more than $90\,\%$) is expected to transfer to the fundamental TE mode of the chalcogenide waveguide and only less than $10\,\%$ of it guided into the second order TE mode. This becomes important when performing opto-acoustic simulation in section 6.3 of this chapter.

6.2 Publication I: Brillouin spectroscopy of a hybrid silicon-chalcogenide waveguide with geometrical variations

Atiyeh Zarifi, Birgit Stiller, Moritz Merklein, Yang Liu, Blair Morrison, Alvaro Casas-Bedoya, Guanghui Ren, Thach G. Nguyen, Khu Vu, Duk-Yong Choi, Arnan Mitchell, Steven J. Madden, and Benjamin J. Eggleton, "Brillouin spectroscopy of a hybrid silicon-chalcogenide waveguide with geometrical variations," Opt. Lett. 43, 3493-3496 (2018)

Abstract

Recent advances in design and fabrication of photonic-phononic waveguides have enabled stimulated Brillouin scattering (SBS) in silicon-based platforms, such as under-etched silicon waveguides and hybrid waveguides. Due to the sophisticated design and more importantly high sensitivity of the Brillouin resonances to geometrical variations in micro- and nano-scale structures, it is necessary to have access to the localized opto-acoustic response along those waveguides to monitor their uniformity and maximize their interaction strength. In this work, we design and fabricate photonic-phononic waveguides with a deliberate width variation on a hybrid silicon-chalcogenide photonic chip and confirm the effect of the geometrical variation on the localized Brillouin response using a distributed Brillouin measurement.

Main body

Stimulated Brillouin scattering (SBS) is an inelastic scattering process in which energy of the optical pump wave is coupled to a frequency down-shifted Stokes wave through a moving acoustic wave. SBS enables a range of applications such as microwave signal processing [35], [216], [244] , microwave signal generation [11], [217], light storage [23], [82], [245], [246] and sensing [38], [47], [69], [70], [133], [136], [247]. There has been a strong interest to activate SBS-enabled functionalities in silicon platforms. This is mainly due to the fact that silicon photonics is capable of integrating multiple functions such as modulators and detectors into a single chip using the same facilities as for microelectronics circuits [166]. However, harnessing SBS in silicon-based platforms is challenging. This difficulty is mainly attributed to the acoustic mode leakage in silicon on insulator (SOI) devices which results in a poor opto-acoustic overlap [42]. Moreover, nonlinear loss caused by two photon absorption (TPA) and free carrier absorption (FCA) limits the coupled pump power and hence the nonlinear coupling to acoustic waves [45]. A number of approaches have been demonstrated to harness SBS in silicon, such as under-etched silicon structures, which allows for strong opto-acoustic overlap in SOI platforms [44] and suspended

silicon membranes which allows for independent photonic and phononic design and therefore significantly lower propagation loss [45].

Recently, the hybrid integration of soft glasses on a silicon-based platform has been demonstrated, in which SBS interaction takes place in the soft glass while the coupling into and out of the waveguide is through silicon grating couplers [6]. This approach takes advantage of a large SBS coefficient and negligible nonlinear loss in the soft glass (As_2S_3) while giving access to the rich library of functional silicon devices, which is promising for bringing SBS-functionalities into a silicon integrated photonic platform. Such novel design requires a characterization system to evaluate the opto-acoustic interaction at critical design points such as bends and tapers. This is of critical importance since structural variations along the waveguide results in Brillouin resonance broadening and reduces the Brillouin scattering efficiency [41]. Therefore, an SBS-based distributed measurement technique with high spatial resolution is required to map SBS response against the position in the few-mm long hybrid waveguides.

Brillouin scattering has been widely employed to study the uniformity and acoustic properties of optical fibers and micro-structures. Distributed Brillouin scattering has been employed to map the excited surface acoustic waves in microfibers [123] and to study the effect of diameter and micro-structure fluctuations in photonic crystal fibers [48], [139], [236]. In-situ monitoring of a tapered fiber diameter based on backward Brillouin spectroscopy was reported by [136]. On-chip waveguide characterization was also performed using distributed SBS measurement on a planar lightwave circuit (PLC) [47] and more recently on a chalcogenide photonic waveguide [1]. Forward Brillouin scattering, also called guided acoustic wave Brillouin scattering (GAWBS) was used to characterize the diameter of a tapered fiber [52], [137], [248] and the core diameter of photonic crystal fibers [139].

This work presents a custom-designed photonic waveguide for distributed sensing in order to confirm geometrical variations of the photonic waveguides with a confirmed spatial resolution. Brillouin optical correlation domain analysis (BOCDA) technique based on an amplified spontaneous emission (ASE) of an Erbium doped fiber [1], [113] was employed to characterize the silicon-chalcogenide hybrid waveguide. The hybrid integration approach underpinned by the flexible electron beam

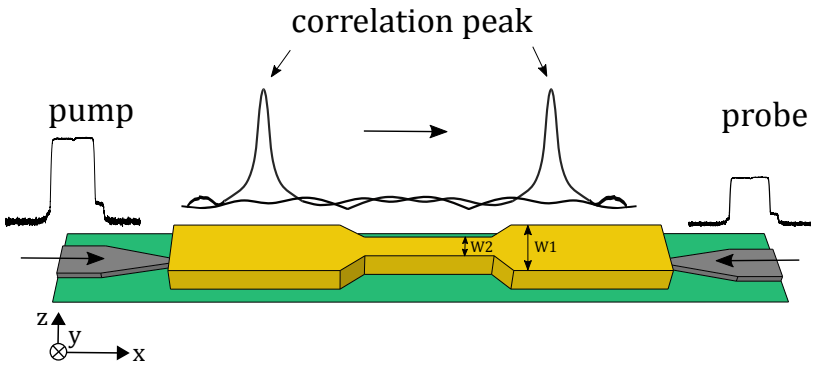

FIGURE 6.3: Schematic of the BOCDA scheme in a hybrid waveguide. The gray region shows the silicon grating couplers tapers into the chalcogenide waveguide which is colored in yellow. w_1 and w_2 are $1.9\,\mu m$ and $1.08\,\mu m$, respectively. The waveguide is scanned by changing the position of the correlation peak along the waveguide.

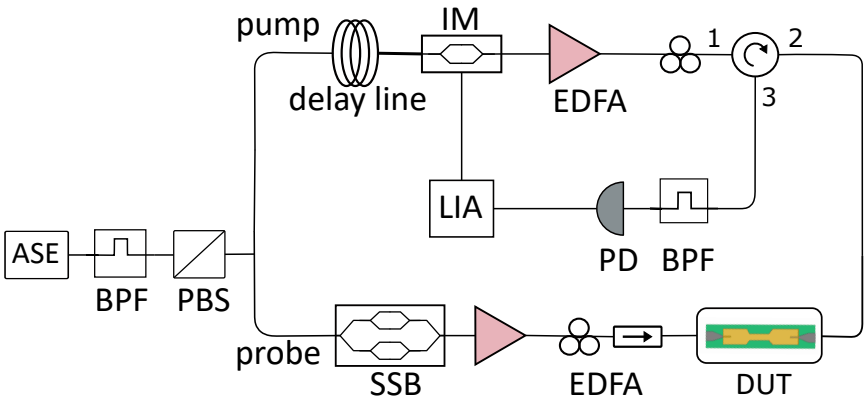

FIGURE 6.4: Schematic of the BOCDA setup. BPF: band pass filter, PBS: polarization beam splitter, SSB: single side-band modulator, IM: intensity modulator, LIA: lock-in amplifier, PD: photo-detector, EDFA: Erbium doped fiber amplifier, DUT: device under test.

lithography (EBL) patterning technique enables us to introduce controlled variations in the waveguide in order to demonstrate and confirm the spatial resolution and the sensing capability of the distributed SBS measurement system.

A schematic of the hybrid waveguide is shown in figure 6.3. The design starts with a SOI platform consisting of silicon grating couplers to couple light into the standard silicon nanowire ($220 \times 450\text{nm}$) which continues for $1\,\text{mm}$. The standard silicon grating coupler is designed to couple only the fundamental TE mode into the silicon nanowire. The width of the silicon nanowire is then adiabatically reduced to a $150\,\text{nm}$ before it interfaces with the $690\,\text{nm}$ thick chalcogenide (As_2S_3) region so that the optical mode can progressively transfers from the silicon to the chalcogenide waveguide. The silicon-chalcogenide transition is optimized to couple the majority of the light in to the fundamental TE mode of the wide chalcogenide waveguide and only less than $10\,\%$ of the light is coupled into the higher order TE mode. The chalcogenide strip waveguide is $1.9\,\mu\text{m}$ wide which is adiabatically reduced to $1.08\,\mu\text{m}$ in the middle for $2\,\text{mm}$. The total length of the chalcogenide waveguide is $6\,\text{mm}$ and the length of the tapers is $15\,\mu\text{m}$.

Since the Brillouin frequency shift (BFS) is sensitive to the waveguide cross-section, the variation in the width can be detected by monitoring the BFS along the waveguide. In the back-scattered SBS process the coupling between the optical pump and the Stokes waves through the traveling acoustic wave is most efficient when the three waves are phase-matched. That is, if the propagation constant of the pump and Stokes waves are $\mathbf{k}_\text{p}$ and $\mathbf{k}_\text{s}$, then the propagation constant of the acoustic wave must be $\mathbf{q} = \mathbf{k}_\text{p} - \mathbf{k}_\text{s}$ [43]. Under this condition, one or more acoustic modes will exist for a given optical mode, whose overlap with the optical mode creates the Brillouin gain profile and determines the BFS. The BFS can be estimated by:

$$\Omega_B = \frac{2n_\text{eff}\text{v}_a}{\lambda}, \tag{6.1}$$

where v_a is the velocity of each acoustic mode in the medium, n_eff is the effective refractive index and λ is the pump wavelength. As a result, any change in waveguide geometry affects the effective refractive index and the acoustic mode resonances [123] and consequently the BFS.

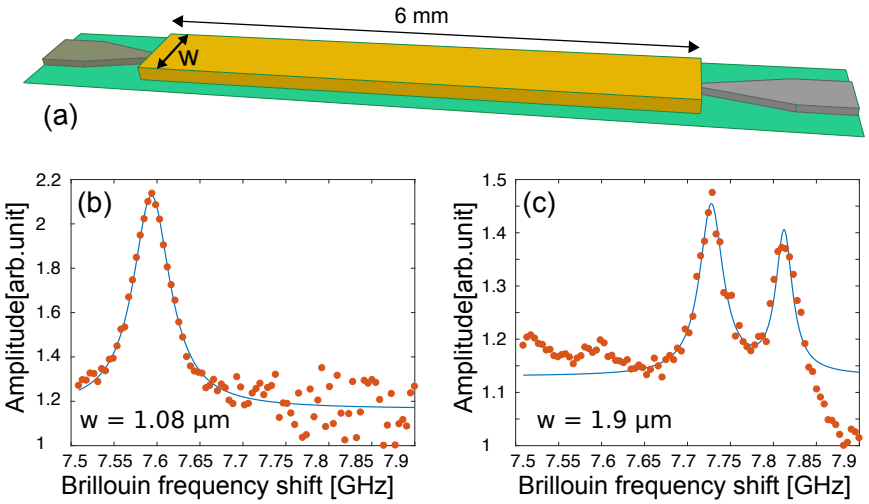

FIGURE 6.5: a) Schematic of the reference silicon-chalcogenide hybrid waveguide with constant width w. b) Integrated SBS response in $1.08\,\mu$m-wide waveguide, and c) in $1.9\,\mu$m-wide waveguide. (The dots show the measured data and the solid blue line shows the Lorentz fit).

The distributed measurement of SBS responses in the waveguide with 2 mm spatial resolution is enabled by the BOCDA technique [38]. In this method, the pump and the probe signals are driven from a random noise source (in this case a filtered ASE source) in such a way that the efficient SBS interaction between the two waves occurs only at the correlation peak. As illustrated in the schematic in figure 6.3, the local SBS responses along the waveguide is obtained by moving the position of the correlation peak. More details about this technique is provided in references [1], [113].

Unlike the time-dependent techniques, where the spatial resolution is limited by the pulse width [87], the spatial resolution in this method is mainly limited by the stochastic nature of the ASE source which limits the signal to noise ratio (SNR) of the measurement. The spatial resolution in the ASE-based BOCDA measurement is given by $\frac{1}{2}V_g\Delta t$, where V_g is the group velocity of the optical mode and Δt is inversely related to the spectral bandwidth of the pump and the probe.

A schematic of the experimental setup is shown in figure 6.4, where an ASE source is sent to a band pass filter and after passing through a polarization beam splitter, is split to the pump and probe signals. In the probe arm, an RF frequency equal to the BFS is applied to the modulator to implement single side-band carrier suppressed (SSB-CS) modulation, generating the probe by downshifting the pump. By sweeping the probe signal using an RF synthesizer, the Brillouin gain spectrum around the BFS is measured. An intensity modulator in the pump arm is used to generate $500\,$ns pump pulses with the period of $10\,\mu$s and the peak pump power of $300\,$mW. The same RF pulse generator that is used in the pump arm, triggers the lock-in amplifier (LIA) in the detection stage. The use of an LIA in the setup improves the SNR.

The distributed measurement along the waveguide is performed by changing the relative delay between the pump and the probe arms using a delay line. The spectral resolution of the distributed measurements is $4.5\,$MHz. After collecting the

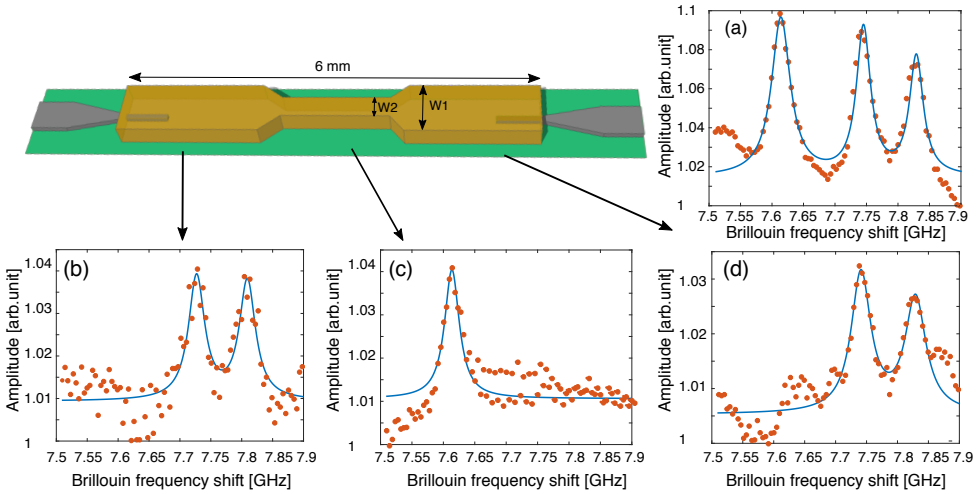

FIGURE 6.6: a) BOCDA measurement of the waveguide with 12 mm spatial resolution. BOCDA measurement with $2\,\mathrm{mm}$ spatial resolution in b) $w_1 = 1.9\,\mu\mathrm{m}$ wide region at the left, c) $w_2 = 1.08\,\mu\mathrm{m}$ wide region in the middle, and d) $w_1 = 1.9\,\mu\mathrm{m}$ wide region at the right side of the waveguide. (The dots show the measured data and the solid blue line shows the Lorentz fit in all the plots).

backscattered signal at port 3 of the circulator, a sharp optical filter is used before the photo-detector in order to remove the pump back reflection as much as possible. The average back reflection from the pump is measured to be $-18\,\mathrm{dB}$. However, filtering at this stage is challenging since the back-reflected pump and the amplified probe have a large spectral overlap. Therefore, it is not possible to filter the pump back reflection without cutting part of the SBS signal.

To confirm the BFS associated with each waveguide geometry, we first measured the integrated SBS response in two hybrid reference waveguides with $1.08\,\mu\mathrm{m}$ and $1.9\,\mu\mathrm{m}$ widths as shown in figure 6.9 (a). The length of each reference waveguide is $6\,\mathrm{mm}$ and the width is constant along the waveguide. Figure. 6.9 (b) and (c) show the integrated SBS response for $1.08\,\mu\mathrm{m}$ wide and $1.9\,\mu\mathrm{m}$ wide waveguides, respectively. As illustrated in figure 6.9, the BFS for the two reference waveguides with different cross-sections happens at different frequencies as expected from equation (6.1). In addition, the Brillouin spectrum of the wider reference waveguides consists of two BFS peaks, while the Brillouin spectrum of the narrower waveguide has only one BFS. According to the simulation results, this is most likely due to the existence of multiple acoustic modes who satisfy the phase matching condition in the wider region of the waveguide and provide large overlaps with the optical mode.

We then changed the device under test to the hybrid waveguide with varying width and performed an integrated SBS measurement to observe the Brillouin spectrum of the entire waveguide. In order to perform this measurement, we set the spatial resolution of the measurement to twice the length of the waveguide ($12\,\mathrm{mm}$) by setting the ASE bandwidth to $5\,\mathrm{GHz}$. The delay line is adjusted in such a way that the pump and the probe arms have exactly the same length so that the correlation peak occurs in the middle of the waveguide and covers the entire structure. figure 6.6(a) illustrates the integrated SBS response of the hybrid waveguide. As seen in figure 6.6(a), the Brillouin spectrum consists of three BFS at distinct frequencies of 7.60, 7.74 and 7.82 GHz.

A higher spatial resolution is required to individually detect BFS peaks at different positions along the waveguide. Therefore, the ASE bandwidth was set to $30\,\mathrm{GHz}$ corresponding to $2\,\mathrm{mm}$ spatial resolution in the waveguide. A distributed measurement was performed by stepping the delay line with $2\,\mathrm{mm}$ steps along the waveguide. The local SBS response at different points of the hybrid waveguide are plotted in figure 6.6(b) to (d). The Brillouin spectrum at $1.9\,\mu\mathrm{m}$ wide section consists of two BFS at 7.74 and 7.82 GHz. However, in the middle section with $1.08\,\mu\mathrm{m}$ width only one BFS peak is observed at $7.60\,\mathrm{GHz}$. The Brillouin spectrum collected from different sections of the waveguide agree with the integrated measurement taken at reference waveguides with similar widths. As seen in figure 6.6(b) to (d), $800\,\mathrm{nm}$ change in the waveguide width results in $140\,\mathrm{MHz}$ change in the BFS for the fundamental mode, in agreement with equation (6.1). However, since the linewidth of the measurement is in the order of $40\,\mathrm{MHz}$, width variation as small as $100\,\mathrm{nm}$(corresponding to $20\,\mathrm{MHz}$ BFS change) is expected to be detected by this system. The narrow linewidth of the integrated measurement also confirms the homogeneity of the reference waveguide along the length. The spatial resolution of the system is confirmed to be $2\,\mathrm{mm}$ since the section in the middle is clearly resolved without detecting the Brillouin response from the other sections of the waveguide.

In conclusion, we reported a distributed SBS measurement based on the BOCDA technique on a silicon-chalcogenide hybrid waveguide. Spatial resolution of $2\,\mathrm{mm}$ has been demonstrated by resolving a $2\,\mathrm{mm}$ feature on the waveguide. This measurement is a proof-of-principle for waveguide characterization in a silicon-based platform with an active SBS gain medium. In addition, this approach provides valuable information about geometry-dependent opto-acoustic responses for further design and fabrication improvement. The spatial resolution of this measurement was mainly limited by the strong pump back reflection from the grating couplers. Optical filtering of the pump back reflection was also limited due to the wide spectral overlap between the pump back reflection and the amplified probe. Further improvement in spatial resolution is therefore possible by improving the SNR and reducing the back reflection from the grating couplers in the fabrication process.

6.3 Publication II: On-chip correlation-based Brillouin sensing: design, experiment and simulation

Atiyeh Zarifi, Birgit Stiller, Moritz Merklein, Yang Liu, Blair Morrison, Alvaro Casas-Bedoya, Guanghui Ren, Thach G. Nguyen, Khu Vu, Duk-Yong Choi, Arnan Mitchell, Steven J. Madden, and Benjamin J. Eggleton, "On-chip correlation-based Brillouin sensing: design, experiment and simulation." J. Opt. Soc. Am. B 36, 146-152 (2019)

Abstract

Wavelength-scale SBS waveguides are enabling novel on-chip functionalities. The micro- and nano-scale SBS structures and the complexity of the SBS waveguides require a characterization technique to monitor the local geometry-dependent SBS responses along the waveguide. In this work, we demonstrate an experimental spatial resolution of $500\,\mu\mathrm{m}$, which can detect feature sizes down to $200\,\mu\mathrm{m}$ on a silicon-chalcogenide photonic waveguide using Brillouin optical correlation domain analysis (BOCDA) technique. We provide extensive simulation and analysis of how multiple acoustic and optical modes associated with geometrical variations influence the Brillouin spectrum.

Introduction

Stimulated Brillouin scattering (SBS) is an inelastic scattering process in which a pump photon interacts with an acoustic phonon and generates a Stokes photon. The generated photon is down-shifted from the pump frequency by the acoustic resonance frequency and its linewidth is dependent upon the acoustic phonon lifetime in the medium [10]. The hypersonic (GHz) frequency shift resulting from the SBS process provides a bridge between electronics and photonics enabling powerful applications such as pure microwave sources [11], [217] and tunable radio frequency (RF) filters [17], [18]. The narrow linewidth of the SBS process makes it suitable for Brillouin-based lasers [6], [32], [33], [80], [81] and frequency comb generation [36], [37]. Furthermore, the difference between the light and sound velocity enables light storage applications in photonic waveguides [12], [24], [82]. Finally, since the SBS frequency shift is an intrinsic characteristic of the medium, SBS has become an ideal sensing mechanism in optical fiber networks [38], [40], [50], [69], [70], [113], [114], [149], [161]. Since the SBS response is sensitive to environmental variables such as temperature and strain, it has been adopted as a distributed sensing mechanism in long optical fibers to monitor critical structures such as buildings and bridges [38], [69], [149].

The spatial resolution required in structural health monitoring ranges from a few meters to a few cm depending on the application [39], [149], which can be achieved using a distributed SBS measurement such as Brillouin optical time domain analysis (BOTDA). This approach employs optical pump pulses whose duration determines the spatial resolution of the SBS response [50]. However, for a pulse duration shorter than the acoustic lifetime, the SBS spectrum broadens and the gain reduces significantly [69]. Therefore, this approach is limited by the phonon lifetime in optical fibers - approximately $10\,\mathrm{ns}$ - which translates into $1\,\mathrm{m}$ spatial resolution [87]. Several methods were proposed to improve the spatial resolution of the time domain

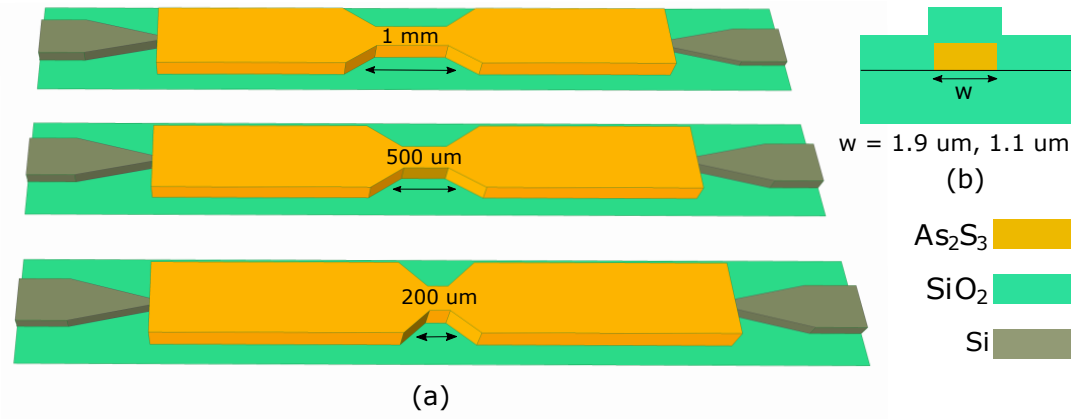

FIGURE 6.7: Schematic of the test waveguides on the silicon-chalcogenide hybrid platform. The length of the test area is reduced from $1\,\mathrm{mm}$ to $200\,\mu\mathrm{m}$. The inset at the top right shows the cross-section of the hybrid waveguide. The width of the waveguide (w) varies between $1.90\,\mu\mathrm{m}$ to $1.10\,\mu\mathrm{m}$ along the test waveguide.

technique including dark pulses [97] and Brillouin echo distributed sensing (BEDS) [39], [48], [92], which improved the spatial resolution to a few cm.

A more recent SBS-based sensing technique, which offers higher spatial resolution is called Brillouin optical correlation domain analysis (BOCDA). This scheme relies on the correlation between the cw pump and probe waves [112]. Different variations of BOCDA include broad-spectrum pump and probe sources based on frequency modulation [111], [249], random phase modulation [51], [237], filtered ASE source [113] and chaotic laser [114]. Spatial resolution of a few mm in optical fiber was reported using this technique [38], [113], which unlike the time domain technique is not limited by the phonon lifetime [112].

The higher spatial resolution offered by BOCDA opens up the opportunity to monitor and characterize smaller and more sensitive structures such as micro-fibers [123] and on-chip photonic waveguides [1]. SBS-response characterization becomes critical in micro- and nano-scale structures, where the geometrical non-uniformities along the waveguide result in a broadening of the SBS spectrum [41] and influence the applications which rely on the narrow-linewidth of the SBS process [6], [17], [18], [32], [33], [80], [81]. In addition, the SBS response in nano-scale waveguides is more sensitive to the complex geometrical features such as tapers, bends and on-chip gratings [234] due to the strong effect of the waveguide boundaries in the sub-wavelength regime [83], [84]. Therefore, identifying the local SBS responses at these critical points gives some insight on the geometry-dependent acousto-optic interactions and provides a feedback for the design and fabrication step in order to improve the quality of the SBS waveguides.

Previous works on the local SBS response characterization in micro-scale waveguides based on BOCDA involve mapping the uniformity of a silica planar lightwave circuit (PLC) [47] and a photonic crystal fiber (PCF) [48] and excitation and detection of surface acoustic waves in micro-fibers [123]. Recently, sub-mm spatial resolution was achieved by employing the BOCDA technique in a chalcogenide photonic waveguide with an improved signal-to-noise ratio (SNR) compared to the optical fiber measurements [1]. The chalcogenide waveguide offers a higher SBS gain due

to the large opto-acoustic overlap, the higher refractive index of the core material and the smaller nonlinear opto-acoustic effective area compared to optical fibers. In addition to these advantages, the use of a phase-sensitive detection technique [112] further improves the spatial resolution and the SNR of the measurement. This experiment as the first demonstration of the sub-mm BOCDA measurement on a chip-scale, opened up the opportunity to study the effect of geometrical variation and design parameters on the overall SBS response of more complex and compact photonic-phononic waveguides with small feature such as on-chip gratings [234]. However, to monitor such small structures, the spatial resolution has to be in the order of the small waveguide features such as spiral bends, tapers and gratings, which is the focus of this work.

Following our initial reports, in this paper, we present a set of new measurements with four-fold improvement in detection capability down to $200\,\mu m$ and a comprehensive study of the geometry-dependent opto-acoustic interactions in those structures. This experiment is demonstrated in a controlled environment in which we tailor the on-chip sensing geometry to confirm the spatial resolution of the BOCDA technique. We designed SBS waveguides with width variations along their length in order to experimentally demonstrate the capability of our distributed SBS measurement system in identifying features which are rather small to be realized by an integrated SBS measurement. We further verified the experimental results with numerical calculations to explain the gain spectrum of the local opto-acoustic interactions along the photonic waveguide. This study opens up opportunities to investigate the local SBS response of more complex structures with very fine features and is a major step forward to a better understanding of the spatial limit of opto-acoustic interactions in sub-wavelength regimes.

Waveguide design and fabrication

We designed a hybrid silicon-chalcogenide chip consisting of several waveguides, each contains a controlled width variation to characterize the local SBS responses within the waveguides and confirm the spatial resolution. A schematic of the test

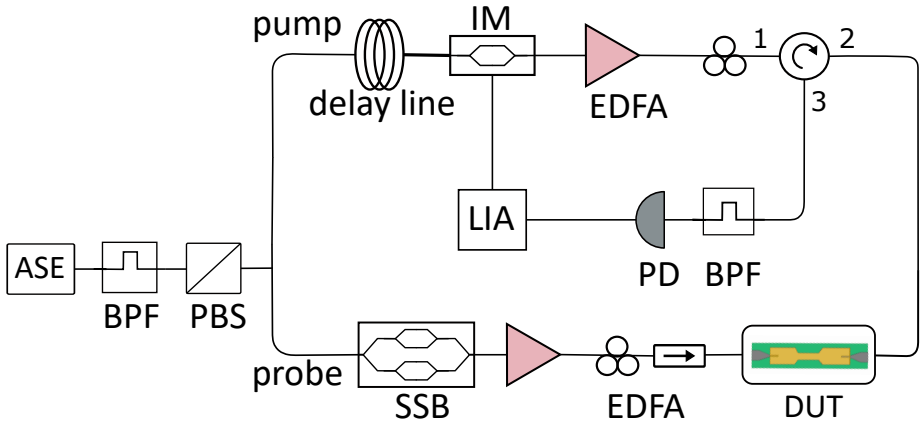

FIGURE 6.8: BOCDA setup based on the ASE of an erbium doped fiber. BPF: band-pass filter, PBS: Polarisation beam splitter, SSB: single side-band modulator, IM: intensity modulator, EDFA: erbium doped fiber amplifier, DUT: device under test PD: photo detector, LIA: lock-in amplifier.

structures on a hybrid platform is shown in figure 6.7 (a). The length of the controlled width varies from $1\,\mathrm{mm}$ to $200\,\mu\mathrm{m}$ for different waveguides. A number of reference waveguides with constant width are also designed to characterize the opto-acoustic responses at specific waveguide cross-sections. A cross-section view of the chalcogenide waveguide used in this work is shown in figure 6.7 (b). The hybrid silicon-chalcogenide waveguide consists of SOI grating couplers to couple the light into and out of the waveguide. The grating couplers selectively couple the fundamental TE mode into the standard single mode silicon nanowire ($450\,\mathrm{nm} \times 220\,\mathrm{nm}$). The silicon nanowires attached to the grating couplers continue for $1\,\mathrm{mm}$ before they taper down to $150\,\mathrm{nm}$ wide tips. A layer of $690\,\mathrm{nm}$ thick chalcogenide (As_2S_3) is then deposited into the area between the two grating couplers covering the silicon tapers but leaving the grating couplers uncovered. The chalcogenide waveguides with the length of $6\,\mathrm{mm}$ are written using the electron beam lithography (EBL) technique, followed by plasma etching and are then covered by a layer of silica cladding to protect the waveguides and provide optimum acoustic confinement.

Experiment

The local SBS response achieved in this measurement is based on BOCDA using the amplified spontaneous emission (ASE) of an erbium doped fiber. This technique was first employed to measure a local hot spot in an optical fiber with $4\,\mathrm{mm}$ spatial resolution [113]. In this technique, the polarized ASE source provides a highly uncorrelated source for the pump and probe waves. The degree of the correlation between the pump and the probe is controlled by the ASE bandwidth. Increasing the ASE bandwidth reduces the correlation between the pump and the probe waves and results in a narrow correlation peak in time. The duration of the correlation peak determines the spatial resolution of the measurement, which can be approximated by: $\frac{1}{2}V_g\Delta t$ with V_g being the group velocity and Δt is inversely related to the ASE bandwidth [113]. As the correlation peak becomes shorter in time, the signal from the local SBS interaction becomes weaker compared to the background noise from the spontaneous scattering at all the other points in the medium (outside the correlation peak). Therefore, the SNR decreases and sets a lower limit on the practical spatial resolution of the BOCDA measurement technique. In addition, for ASE bandwidths larger than the Brillouin frequency shift (BFS), the separation between the back-reflected pump and the amplified probe becomes challenging due to the large spectral overlap [1]. In our setup, we use As_2S_3 strip waveguides with high SBS gain coefficient and a lock-in amplifier (LIA) to improve the SNR and obtain spatial resolutions beyond the limits achieved in the optical fiber measurement.

A schematic of the experimental setup is presented in figure 6.8. It consists of the ASE source whose bandwidth is controlled by a tunable band-pass filter (BPF). It then divides into the counter-propagating pump and probe arms. The probe wave goes through a single side-band modulation using a dual-parallel Mach-Zehnder modulator (DPMZM) with a carrier suppression of 20 dB and a side-band suppression of 15 dB. The pump wave is intensity-modulated with pulse lengths of $500\,\mathrm{ns}$ and a frequency of $100\,\mathrm{kHz}$ and is synchronized with the LIA. The light is coupled in and out of the waveguide using silicon grating couplers with the measured total back-reflection of $-18\,\mathrm{dB}$. A sharp optical filter is added before the photo detector to remove the pump back-reflection as much as possible before sending the measured

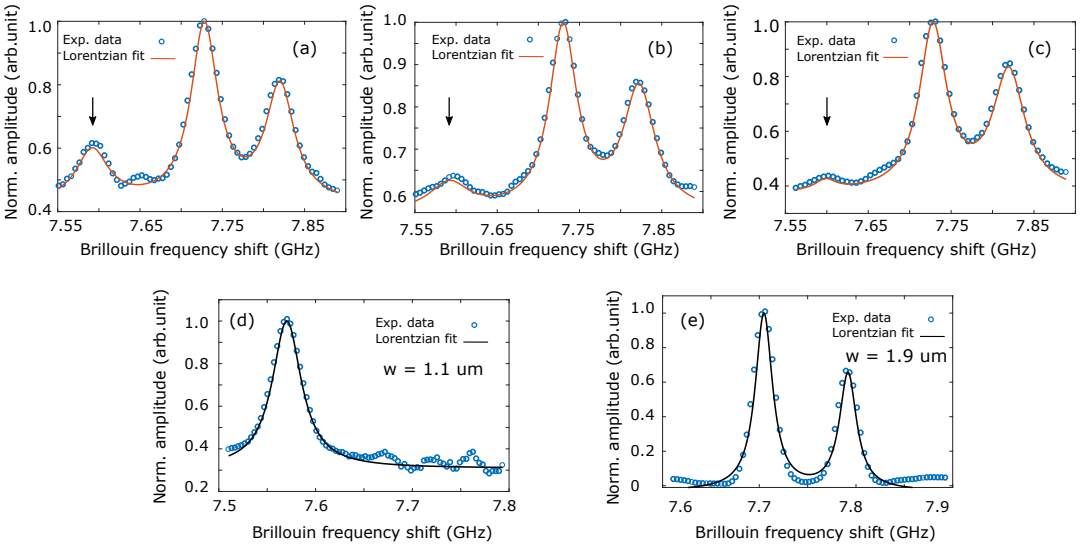

FIGURE 6.9: a) Integrated SBS response of the test waveguides with (a) 1 mm, (b) 500 µm and (c) 200 µm feature size corresponding to the schematic in figure 6.7. The black arrows indicate the disappearance of the peak at lower frequency attributed to the narrow waveguide region from (a) to (c). Integrated SBS response of the reference waveguides with (d) 1.10 µm and (e) 1.90 µm width. In all the plots, the experimental data is shown with blue dots and the Lorentzian fit is shown with a solid line.

signal to the LIA. The essential part of this experiment is cutting the pump back-reflection, because by filtering out the pump back-reflection, part of the SBS signal will also be removed. However, we achieved enough signal even after cutting 90 % of the response to detect a segment of 200 µm of the waveguide.

In order to identify the SBS response of the entire test waveguides, we first performed an integrated SBS measurement by setting the filter bandwidth to 3 GHz, corresponding to 12 mm spatial resolution (twice the length of the waveguide). Figure 6.9 (a)-(c) show the integrated SBS measurement of the test waveguides corresponding to the structures shown in figure 6.7 (a). The waveguide with 1 mm feature size has three peaks in the Brillouin gain spectrum namely at 7.59 GHz, 7.72 GHz and 7.81 GHz. As the feature size reduces from 1 mm to 200 µm, the peak at lower frequency (7.59 GHz) disappears. These measurements show that there is a link between the lower frequency peak and the narrow-width feature in the middle of the test waveguides. To further confirm this measurement, we investigate the integrated SBS response of two reference waveguides with 1.10 µm and 1.90 µm constant width using a cw laser as the pump and the probe source. The result of these measurements are plotted in figure 6.9 (d) and (e). As it is shown in these plots, the 1.10 µm-wide waveguide has a BFS at 7.57 GHz and the 1.90 µm-wide waveguide has a double peak profile at 7.70 GHz and 7.79 GHz, which is in agreement with the measurements shown in figure 6.9 (a) to (c). The slight offset between the BFS observed in the two sets of measurements (with 3 GHz ASE bandwidth and the cw laser) is due to the fact that the center frequency of the two sources were slightly different.

In order to measure the longitudinal feature in the first test waveguide, a distributed SBS measurement was performed by setting the ASE bandwidth to 60 GHz,

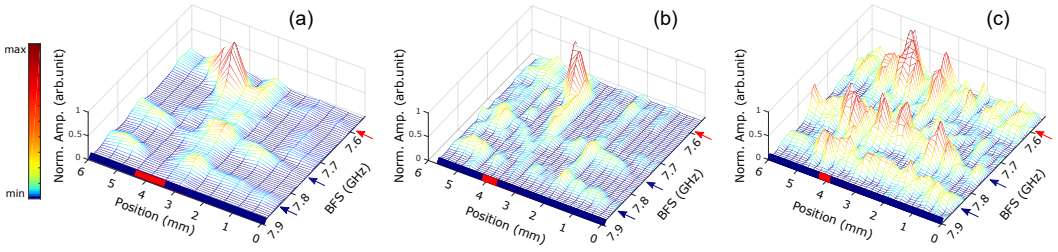

FIGURE 6.10: BOCDA response of the test waveguide with a) 1 mm feature size and 1 mm spatial resolution, b) 500 µm feature size and 750 µm spatial resolution and c) 200 µm feature size and 750 µm spatial resolution. The approximate location of the narrow-width region is shown in red color along the position axis. The blue and red arrows along the BFS axis indicate the BFS in the wide and narrow waveguide regions, respectively. The vertical axis in all plots shows the normalized amplitude (Norm.Amp.).

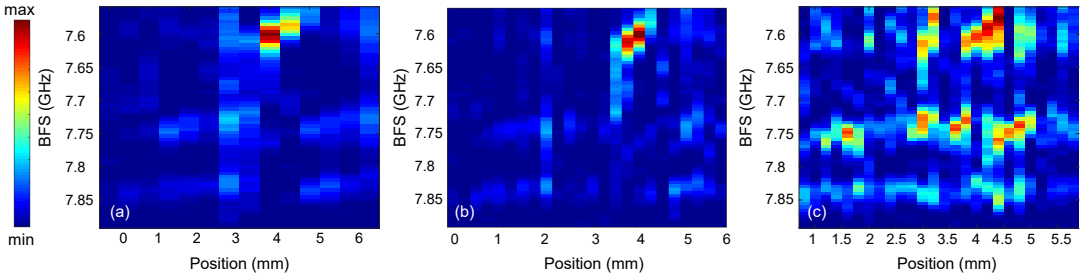

FIGURE 6.11: Normalized power of the Brillouin spectrum at different positions along the waveguide with feature size and step size of a) 1 mm and 500 µm, b) 500 µm and 250 µm, c) 200 µm and 200 µm, respectively.

corresponding to 1 mm spatial resolution in the waveguide. The delay line is set such that the optical length of the pump and the probe arms are equal and then by stepping the delay line with 500 µm steps, the waveguide with 1 mm feature size was scanned. The result of this measurement is shown in figure 6.10 (a), where the BFS peak at 7.59 GHz appears at position 3.5 mm and disappears at 4.5 mm. Outside this region, the Brillouin gain spectrum mainly shows two peaks at 7.72 GHz and 7.81 GHz which indicates that the correlation peak is scanning the wider section of the waveguide. The ASE bandwidth is then increased to 80 GHz, corresponding to a spatial resolution of 750 µm to detect the 500 µm feature in the second test waveguide with step sizes of 250 µm, as presented in figure 6.10 (b). As it is seen in this plot, the BFS peak at 7.59 GHz appears at position 3.75 mm and disappears at position 4.25 mm. Lastly, the waveguide with 200 µm feature was measured using the same ASE bandwidth (80 GHz), however the step size is now reduced to 200 µm. This measurement is shown in figure 6.10 (c), where the 7.59 GHz peak appears between the positions 3.8 mm and 4.2 mm and has the highest amplitude at position 4.0 mm. As it is seen in this figure, the quality of the detected local signals deteriorates in the last measurement due to the lower spatial resolution compared to the feature size and also the lower SNR. Some residual of the 7.59 GHz peak could be observed in traces away from the feature, which is due to the weak SNR and the

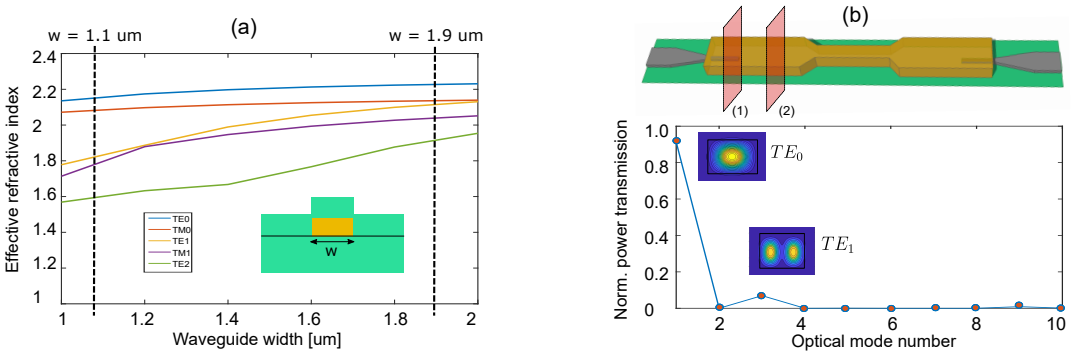

FIGURE 6.12: (a) Schematic of the chalcogenide waveguide cross-section and its dispersion plot, showing the guided optical modes at the two waveguide widths of $1.10\,\mu m$ and $1.90\,\mu m$. (b) Optical mode transition from the silicon taper (plate 1) to the chalcogenide waveguide (plate 2). Bottom: Transmitted optical power from the silicon nanowire to the chalcogenide waveguide through the silicon taper. $90\,\%$ of the optical power is transmitted to the fundamental TE mode and less than $10\,\%$ of the power is in the TE_1 mode.

fact that the signal level is now close to the background noise from the spontaneous Brillouin scattering which happens outside the correlation peak.

In addition, in figure 6.10 (a) and (b), the intensity of the local SBS response at the narrow region waveguide is higher compared to the wide region. This is due to the fact that the SBS gain coefficient per unit length defined as $\frac{g_B}{A_{\text{eff}}}$, with g_B being the SBS gain coefficient, is inversely related to the waveguide's effective opto-acoustic interaction area A_{eff}. Therefore, the SBS gain in the narrower waveguide with approximately four times smaller cross-section, is expected to be stronger than in the wider waveguide. This is confirmed by the normalized Brillouin gain spectrum obtained from the experiment and shown in figure 6.10 (a) to (c), where the peak amplitudes at frequencies $7.72\,\text{GHz}$ and $7.81\,\text{GHz}$ are approximately $25\,\%$ less than the peak amplitude at frequency $7.59\,\text{GHz}$.

Figure 6.11 (a)-(c) provides the BFS vs position for three distributed measurements. As it can be seen in this figure, an experimental spatial resolution of $500\,\mu m$ is clearly achieved. However, when moving to $200\,\mu m$ feature size (figure 6.11 (c)), the measurement becomes noisy and the feature is observed over three traces. In addition, in figure 6.11 (c) the amplitude of the SBS response in the $200\,\mu m$ narrow region is now comparable to that from the wider region, which indicates that the SBS interaction within the $200\,\mu m$ region is very weak. Therefore, the last measurement can be used to locate the $200\,\mu m$ feature, but it does not resolve this feature.

Simulation and analysis

The dependency of the BFS (Ω_B) on material properties and effective refractive index can be approximated by equation 6.2.

$$\Omega_B = \frac{2n_{\text{eff}}V_a}{\lambda_p}, \tag{6.2}$$

where n_{eff} is the effective refractive index, V_a is the acoustic mode velocity and λ_p is the pump wavelength. This relation is valid under the assumption that the waveguide dimensions are much larger than the acoustic wavelength ($w, h \gg \frac{2\pi V_a}{\Omega}$) [42], where w and h stand for the waveguide width and thickness, respectively and Ω is the acoustic angular frequency. This assumption is correct for the optical fibers, however for the sub-wavelength and wavelength-scale waveguides the medium can no longer considered isotropic and the optical field will have components in the direction of propagation which will affect the effective refractive index term [42]. Furthermore, it was demonstrated that in nano-structures other forces such as radiation pressure influence the acoustic mode excitation [250]. In order to include all these effects in our study, we performed a fully vectorial analysis to calculate the BFS in the chalcogenide structures following the approach presented in [84]. However, for our hybrid chalcogenide structures the effect of radiation pressure on the backward SBS gain turns out to be negligible, which is confirmed through numerical calculations. Different waveguide cross-sections accommodate different optical and acoustic modes and therefore the effective opto-acoustic overlap is different from one waveguide geometry to the other. The change in the waveguide cross-section, therefore, manifests in the Brillouin gain spectrum and shifts the BFS, which is what we measure in this experiment.

The chalcogenide waveguide with cross-sections shown in the inset of figure 6.7 (b) supports multiple optical modes as well as acoustic modes. Therefore, careful design considerations are required in order to precisely excite the correct optical mode and comprehensive analysis needs to be done in order to identify the acoustic modes involved in the SBS interaction. The dispersion plot of the chalcogenide waveguide is shown in figure 6.12 (a). The single mode operation of the chalcogenide waveguide is achieved via the adiabatic silicon taper. The silicon tapers are long enough ($100\,\mu\text{m}$) to guarantee a smooth optical mode transition from the silicon nanowire to the chalcogenide waveguide [235]. The fundamental TE mode transition through the adiabatic taper is simulated using a commercial-grade simulator based on the finite-difference time-domain method [223], presented in figure 6.12 (b). As presented in this figure, the majority of the optical power is coupled into the fundamental TE mode of the chalcogenide waveguide and less than $10\,\%$ of the power is transmitted into the higher order TE mode. Therefore, although the waveguide could support multiple optical modes, the silicon tapers were designed to selectively excites only the fundamental TE mode.

The opto-acoustic response is calculated using COMSOL Multiphysics software [251] after ref.[84]. We calculated the overlap between the fundamental optical TE mode with the acoustic modes present in the frequency span between $7.50\,\text{GHz}$ and $7.90\,\text{GHz}$ and reconstructed the Lorentzian Brillouin gain spectrum based on the strength of the opto-acoustic overlap within this spectrum. The simulated normalized Brillouin gain spectrum for the two reference waveguide geometries are shown in figure 6.13. Fabrication variations in thickness and width of $7\,\%$ were allowed in this calculation using a corner analysis [166] to find a reasonable match between the simulation and the experiment. The simulation plots shown in figure 6.13 (b) and (c) represent waveguides with the simulation thickness (h_{sim}) of $707\,\text{nm}$ and the simulation widths (w_{sim}) of $1.02\,\mu\text{m}$ and $1.75\,\mu\text{m}$, respectively. The material properties including stiffness tensor coefficients, density and photoelastic tensor coefficients for this simulation were set after Ref. [252]. Comparing figure 6.13 (b)-(c) with the experimental result shown in figure 6.9 (d)-(e), we find a good agreement between the

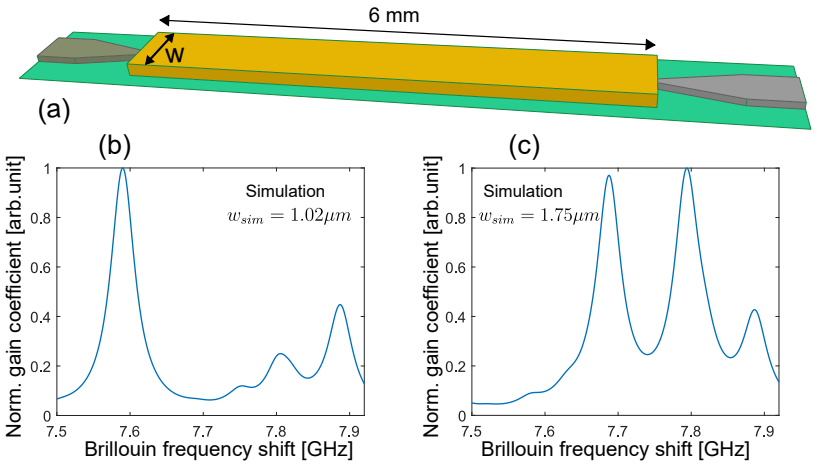

FIGURE 6.13: a) Schematic of a reference waveguide with constant width. Calculated normalized Brillouin gain spectrum for $h_{sim} = 707\,\mathrm{nm}$ thick waveguide with b) $w_{sim} = 1.02\,\mu\mathrm{m}$ and c) $w_{sim} = 1.75\,\mu\mathrm{m}$ width.

experiment and the simulation. This confirms that the shift in the peak of the Brillouin spectrum profile is an effect of the waveguide geometry and the double peak profile observed in the wider waveguide is a result of the existence of two or more higher order acoustic modes which have strong overlap with the optical fundamental TE mode in the vicinity of the BFS.

Discussion

By comparing figure 6.9 (d) and (e) with figure 6.13 (b) and (c), a good agreement between the measured integrated SBS response and the simulation is observed. However, an additional BFS peak at $7.90\,\mathrm{GHz}$ is observed in the simulation but not captured in the experiment. This is most likely due to the fact that the SNR of the measurement was not high enough to detect the rather weak SBS response which is generated by some higher order acoustic modes.

When simulating the optical mode transition from the silicon nanowire to the chalcogenide waveguide, we considered up to $50\,\mathrm{nm}$ vertical offset of the taper tip from the center of the chalcogenide waveguide as well as $20\,\%$ variations of the taper width in order to include the effect of fabrication variations. The effect of the taper misalignment and taper tip width variation on the optical mode transition were negligible and the optical mode transition profiles overlap very closely with the plot shown in figure 6.12 (b), therefore they are not plotted here. In addition, as it is plotted in figure 6.12 (b), approximately $10\,\%$ of the transmitted power from the silicon nanowire is coupled into the TE_1 mode of the $1.90\,\mu\mathrm{m}$-wide chalcogenide waveguide, which could be considered as the origin of the second peak appeared at the lower frequency in the Brillouin gain spectrum. We examined this possibility by calculating the opto-acoustic overlap between the TE_1 mode and the acoustic modes in the waveguide and found out that the frequency splitting between the two peaks in this case is at least $200\,\mathrm{MHz}$, which does not match the experiment. We further studied the contribution of the TM_0 mode in the opto-acoustic overlap to investigate the possibility of mode coupling within the waveguide. The opto-acoustic overlap between the TM_0 mode and the acoustic modes of the waveguide resulted

in a frequency splitting of $180\,\mathrm{MHz}$, which is larger than what we observed in the experiment.

Finally, as it was mentioned earlier, the limiting factor in this experiment was the wide overlap between the back-reflected pump and the amplified probe. Improving fabrication techniques such as the use of tilted grating couplers [253] with very low back reflection can improve the SNR and allows for higher spatial resolution measurement.

Conclusion

In this work, we reported four-fold improvement in detection capability of BOCDA measurement compared to previous works [2]. In addition, we performed numerical simulation to explain the interaction between the optical and acoustic modes at different waveguide cross-sections. This setup provides a platform to test and measure local opto-acoustic responses within the micro- and nano-wires with sub-mm feature size. Moreover, by further increasing the spatial resolution, this technique could provide valuable information regarding the spatial limits of the nonlinear opto-acoustic interaction within the medium.

6.4 Additional analysis

Fabrication tolerances

In addition to the results reported in the publications, we present an analysis on the sensitivity of the acoustic mode and opto-acoustic responses to geometry variations in this section. We use *corner analysis* [166] introduced in chapter 5 to investigate the effect of waveguide width and thickness variations on the overall opto-acoustic response and find the geometry which results in a Brillouin gain spectrum similar to the one we observed in the experiment. We perform the corner analysis in two steps. First, we consider $5\,\%$ variations in width and thickness from the nominal design value as shown in figure 6.14. In this figure the highlighted area shows the set of geometries in which the Brillouin gain spectrum closely matches the experimental result. In order to find a more accurate geometry, we take the highlighted region as new corners and perform a second corner analysis within this area as shown in figure 6.15. The highlighted geometry in this figure is the one that matches the best the experiment. In this region, by fine tuning the width and thickness, we found the optimum values for the thickness and width as $707\,\mathrm{nm}$ and $1.75\,\mu\mathrm{m}$, respectively, which is represented in figure 6.13 (c). For the narrow waveguide region, we assumed the same thickness as the wide waveguide and the width is scaled down compared to the nominal value with the same ratio as the one we obtained for the wide waveguide. This results in the waveguide thickness and width of $707\,\mathrm{nm}$ and $1.02\,\mu\mathrm{m}$, respectively. The simulation result using these values are shown in figure 6.13 (b).

An important conclusion from this simulation is that the acoustic modes are highly sensitive to the geometry of the hybrid waveguide; since the optical mode is kept constant, the change in the opto-acoustic response should be due to the change in the acoustic modes. Figure 6.16 shows the acoustic modes with resonances that

matches to those of Brillouin spectrum peaks. In performing this simulation, the optical mode is set to the fundamental TE mode, because as we mentioned in section 6.1 it is the dominant optical mode in the chalcogenide waveguide.

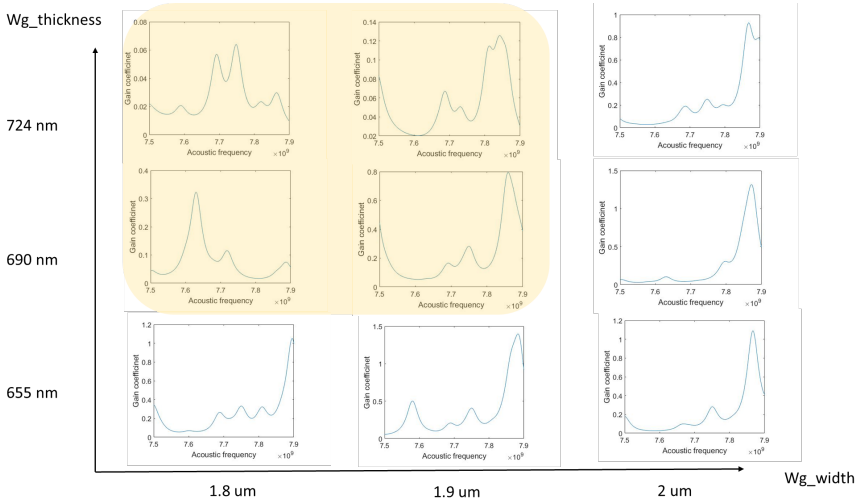

FIGURE 6.14: Corner analysis for the wide waveguide with width and thickness variations of $\pm 5\,\%$.

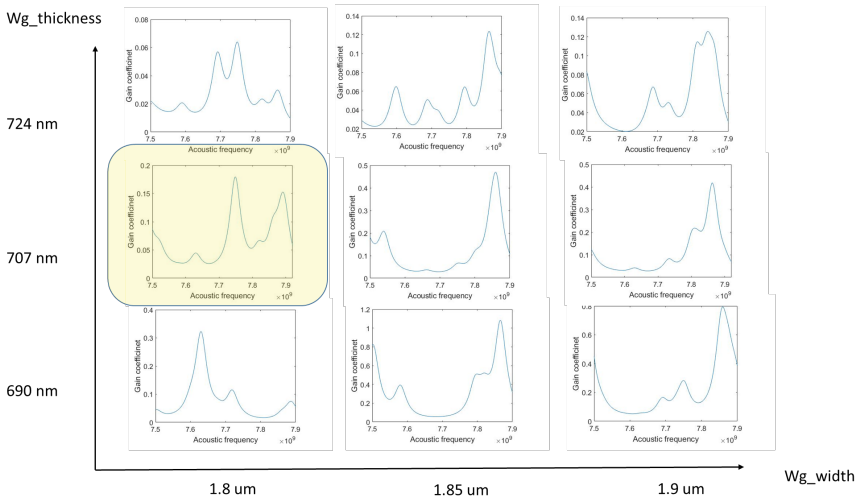

FIGURE 6.15: A finer corner analysis for the wide waveguide with $\pm 2.5\,\%$ variations in width and thickness.

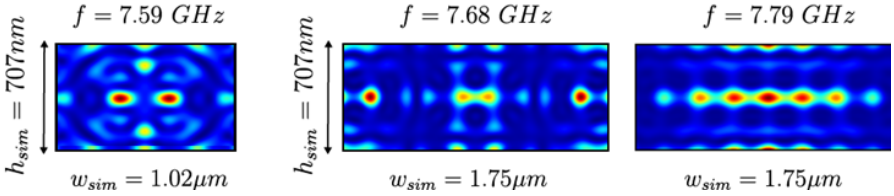

FIGURE 6.16: Normalized power distribution for acoustic modes corresponding to the Brillouin spectrum peaks at each waveguide.

Effect of dispersion on Brillouin frequency shift

In this paragraph, we provide an analysis on the effect of dispersion on the Brillouin response. Since we use broad-spectrum signals (up to $80\,\mathrm{GHz}$) to generate local SBS interaction in the waveguide, the role of dispersion over such wide bandwidth becomes important. The change in BFS as a result of dispersion is studied by taking into the account the material dispersion of As_2S_3 (real dispersion data obtained from the fabrication stage) and plugging it into the derivative of equation 6.2 as follows:

$$\Delta\Omega_B = \frac{2V_a}{{\lambda_p}^2}\left(\frac{dn_{As_2S_3}}{d\lambda_p}\lambda_p - n_{\mathrm{As_2S_3}}\right), \tag{6.3}$$

where $\frac{dn_{As_2S_3}}{d\lambda_p}$ is the material dispersion. From this equation we obtain BFS sensitivity of $5\,\mathrm{MHz/nm}$, which results in $7.6\,\mathrm{MHz}$ BFS change for an $80\,\mathrm{GHz}$ spectrum. This effect results in Brillouin linewidth broadening as we observed in our experiments; for example, in figure 6.9 (d), for an ASE spectrum of $3\,\mathrm{GHz}$, Brillouin linewidth is measured to be $36\,\mathrm{MHz}$. However, for an ASE spectrum of $60\,\mathrm{GHz}$, the Brillouin linewidth is $56\,\mathrm{MHz}$, as shown in figure 6.10 (a). The Brillouin linewidth in both cases are estimated by a Lorentzian profile. It should be noted that for measurements with spectrum as broad as $60\,\mathrm{GHz}$ or larger, SBS occurs over a very short length, and therefore SBS gain is weak, which itself leads to Brillouin linewidth broadening. This explains the additional Brillouin spectrum broadening that we observe in our experimental results.

7 Summary and Outlook

In this thesis, we looked at distributed Brillouin sensing from a different perspective. In contrast to most of the work in this area which deal with optical fibers - as the most fundamental platform for long-range optical distributed sensing - we tailored a particular distributed sensing technique (BOCDA) to monitor and characterize on-chip photonic waveguides with very high spatial resolution. Our main motivation comes from a fundamental curiosity that we share with any other research group who deal with on-chip Brillouin experiments; how is Brillouin gain spectrum in photonic waveguides affected by either design parameters or fabrication inconsistencies. Even though the answer to this question could be approximately given by performing simulations such as corner analysis as described in chapter 6, we presented a definitive answer to this question by performing a local SBS measurement of an on-chip photonic waveguide.

As explained throughout this thesis, geometrical variations along waveguides lead to Brillouin spectral broadening, which in turns affects the quality of the on-chip SBS functionalities. This is of particular importance in the context of photonic integration, where some of the critical integrated on-chip functionalities such as lasers, signal processing and storage devices are relying on the quality of SBS response. The majority of this thesis is focused on designing and examining the local SBS response of silicon-chalcogenide waveguides. These demonstrations serve as examples for characterizing any on-chip waveguides that exhibit backward Brillouin scattering.

In chapter 2, we provided an overview of the field of distributed Brillouin sensing. It was shown that distributed Brillouin measurement was originally developed to serve as a distributed temperature and strain sensor and then gradually evolved in terms of spatial resolution and sensitivity to detect these effects in much shorter lengths with higher sensitivity. This advancement enabled new functionalities such as monitoring the uniformity of a piece of PCF [48] or even silica planar waveguides [47]. We particularly studied Brillouin sensing in micro-scale structures namely micro-fibers, PCFs and on-chip photonic waveguides which set the scene for our contribution: high spatial resolution distributed Brillouin sensing in on-chip waveguides.

In chapter 3, we introduced the mathematical approach necessary to understand and carry out the nonlinear photonic experiments in this work. The first part of this chapter dealt with SPM and TPA, which are used to determine the efficiency of the hybrid silicon-chalcogenide waveguide in terms of third-order nonlinearity. The second part of this chapter explained SBS effect, which is essential for understanding the Brillouin sensing mechanism.

Chapter 4 presented the experimental work toward characterizing the silicon-chalcogenide waveguide against a standard silicon waveguide in terms of nonlinear loss. The experiment in this chapter showed that even though silicon nanowires exhibit a larger Kerr nonlinearity measured by SPM, the silicon-chalcogenide waveguide is advantages because of its negligible nonlinear loss. It was also explained

that introducing chalcogenide into a SOI structure enables SBS in a silicon-based waveguide due to chalcogenide high Brillouin gain coefficient. We then experimentally demonstrated that the hybrid waveguide can exhibit Brillouin gain of $18\,\mathrm{dB}$ by modifying the structure in such a way that both optical and acoustic modes can be confined within the waveguide. Therefore, in this chapter we presented *a) a significant improvement in nonlinear loss*, and *b) a large SBS gain* in the hybrid silicon-chalcogenide waveguide.

Chapter 5 dealt with the on-chip distributed SBS measurement on a chalcogenide waveguide. In this chapter, we explained the principle of BOCDA technique. We showed how the combination of having a high SBS gain medium and an improved detection technique led to the first sub-mm spatial resolution Brillouin measurement. The spatial resolution in this chapter was confirmed by detecting a $1.1\,\mathrm{mm}$ piece of DSF spliced in between two SMF.

In chapter 6, we took advantage of the flexible design process of the hybrid silicon-chalcogenide waveguide to create controlled defects in on-chip waveguides and systematically examine the spatial resolution. In addition to providing a sensing platform, this study aimed to demonstrate on-chip sensing on a silicon-based platform for the first time. The first part of this chapter reported a proof-of-principle experiment where a $2\,\mathrm{mm}$ feature size was successfully detected in the hybrid platform. The second part of this chapter provided a deeper understanding of the nature of optical and acoustic modes interaction in the hybrid waveguide as well as an improvement in the spatial resolution down to $500\,\mu\mathrm{m}$.

For the hybrid silicon-chalcogenide waveguide, one possible future direction is to take advantage of the slot waveguide nonlinearity. Since the effective mode area in this case is very small, the enhancement in nonlinearity is expected to be higher than the cover nonlinearity. A theoretical work on the silicon-chalcogenide slot waveguide is presented in [254]. In this work the waveguide geometry, i.e. slot and rail widths and height, are optimized for maximum SBS interaction. In the optimum condition, SBS gain per unit area (g_B/A_{eff}) is predicted to be $3300\,\frac{1}{\mathrm{W\cdot m}}$, which is 4.5 times larger than the value we reported for the hybrid waveguide with cover nonlinearity in chapter 3. Therefore, if fabricated with enough precision, silicon-chalcogenide slot waveguide is a promising solution to further increasing SBS gain in a silicon-based platform.

In the on-chip distributed sensing experiment, there are several factors that could improve the SNR and consequently the spatial resolution of the system. The spectral profile of the pump and probe waves can be chosen to be Gaussian instead of rectangular. As explained in chapter 5, the auto-correlation function of a Gaussian spectrum is also Gaussian and since this profile does not have any additional side lobes, it provides perfect suppression of SBS response elsewhere except for the correlation peak position in the waveguide. This will reduce the noise that is picked up by the unwanted side-lobes in the sinc correlation profile that we use in the current work. As mentioned in chapter 5, we attempted to use a Gaussian profile, however, there was a trade-off between the profile shape and the extinction ratio of the filter, which made us decide to select the rectangular shape but with a higher extinction ratio.

Another factor that could improve the SNR and therefore the spatial resolution of the measurement is to reduce the pump back-reflection caused by the waveguide facets. In the chalcogenide waveguide, we use lens coupling to couple light in

and out of the waveguide. This means that the light is injected into the waveguide perpendicular to the waveguide facets. In this case, to minimize the back-reflection, anti-reflection coatings were added during the fabrication process. In the hybrid silicon-chalcogenide waveguide, grating couplers were used for coupling light in and out of the waveguide. In this case, one possible approach to reduce the back-reflection from the grating coupler is to use tilted grating couplers [253] with $-40\,\mathrm{dB}$ back-reflection as opposed to $-18\,\mathrm{dB}$ back-reflection that we measured in our waveguide.

A third point to improve the performance of BOCDA setup is to use an even sharper filter at the detection stage for selecting the amplified probe which is widely overlapped with the back-reflected pump, especially for high spatial resolution measurements. The filter we use in our experiment is capable of selecting down to $10\,\mathrm{GHz}$ spectrum before its rectangular profile deteriorates, however an even sharper filter in this case would improve the SNR.

The on-chip distributed Brillouin measurement can bring some benefits to the field of silicon photonic integration. Combined with the advancement in distributed forward Brillouin scattering reported by [134] and [132], BOCDA technique might be utilized to enable high spatial resolution measurement in silicon waveguides. In addition, apart from scanning the waveguide, the high spatial resolution offered by this technique can be used to detect hot spots at critical points on active silicon chips, where certain functionalities such as switching are activated by heat.

A Appendix A

```
1
%THIS IS THE FINAL CODE FOR FOM CALCULATION OF HYBRID 150X220 SILICON-
    CHALCOGENIDE
3 %%NANOWIRE BASED ON AFSHAR'S METHOD- DEVELOPED BY ATIYEH ZARIFI, DECEMBER
    2015%%%%%%%

5 clc; clear all; close all;
load('hybrid_150nm.mat'); % simulation output from Lumerical
7
%%%%%%%%%  Selemier model for As2S3 %%%%%%%
9 % lambda_0=1550e-3;
% lambda = (1500:1:1600) *1e-3;
11 % B1= 4.68 %1.8983;
% C1= 2.64 %0.0225;
13 % % B2=1.922979;
% % C2=0.0225;
15 % % B3=0.8765;
% % C3=0.1225;
17 % % B4=0.11887;
% % C4=0.2025;
19 % % B5=0.95699;
% % C5=750;
21 % ep = 1;
% %n=sqrt( ep + (B1 .* lambda.^2) ./ (lambda.^2 - C1) + (B2 .* lambda.^2)
    ./ (lambda.^2 - C2) + (B3 .* lambda.^2) ./ (lambda.^2 - C3)+ (B4 .*
    lambda.^2) ./ (lambda.^2 - C4)+ (B5 .* lambda.^2) ./ (lambda.^2 - C5));
      % n
23 % n_sqr= ep + (B1 .* lambda.^2) ./ (lambda.^2 - C1) %+ (B2 .* lambda.^2)
    ./ (lambda.^2 - C2) + (B3 .* lambda.^2) ./ (lambda.^2 - C3)+ (B4 .*
    lambda.^2) ./ (lambda.^2 - C4)+ (B5 .* lambda.^2) ./ (lambda.^2 - C5);
% dndl = (n_sqr(3:end)-n_sqr(1:end-2)) ./ (lambda(3:end)-lambda(1:end-2));
25 % dn2dl = (n(3:end)-n(1:end-2)) ./ (lambda(3:end)-lambda(1:end-2));
% ng = n(2:end-1) - lambda(2:end-1).*dn2dl
27 % dispersion_chalc=(n_sqr(51))-(lambda_0/2)*dndl(51)
% n_chalc=sqrt(n_sqr(51));
29
%%% chalc dispersion from sample data %%%%
31 lambda=xlsread('CG_As2S3Cut.csv','A1:A1644');
lambda=lambda*1e-9;
33 n=xlsread('CG_As2S3Cut.csv','B1:B1644');
n_sqr=n.^2;
35 lambda_0=1550e-9;
dndl = (n_sqr(3:end)-n_sqr(1:end-2)) ./ (lambda(3:end)-lambda(1:end-2));
37 dispersion_chalc=(n_sqr(1579))-(lambda_0/2)*dndl(1579)
n_chalc=sqrt(n_sqr(1579));
39 %plot(lambda,n)

41 %%%%%%  Selemier model for SiO2(from "silicon photonics design" by Lukas
      Chrostowski) %%%
lambda_0=1550e-3;
```

```
lambda = (1500:1:1600) *1e-3;
B1=0.69;
C1=0.0684;
B2=0.408;
C2=0.116;
B3=0.897;
C3=9.89;
ep = 1;
n=sqrt( ep + (B1 .* lambda.^2) ./ (lambda.^2 - C1^2) + (B2 .* lambda.^2)
    ./ (lambda.^2 - C2^2)+ (B3 .* lambda.^2) ./ (lambda.^2 - C3^2));
n_sqr=( ep + (B1 .* lambda.^2) ./ (lambda.^2 - C1^2) + (B2 .* lambda.^2)
    ./ (lambda.^2 - C2^2)+ (B3 .* lambda.^2) ./ (lambda.^2 - C3^2));
dndl = (n_sqr(3:end)-n_sqr(1:end-2)) ./ (lambda(3:end)-lambda(1:end-2));
ng = n(2:end-1) - lambda(2:end-1).*dndl

dispersion_sio2=(n_sqr(51))-(lambda_0/2)*dndl(51)    % n_si from Selemier
n_sio2=sqrt(n_sqr(51));

%%%%   silicon LORENTZ FIT  %%%%
lambda = (1200:1:1600) *1e-9;
lambda_0=1550e-9;
c=3e8;
epsilon=7.98737492;      % Permitivity
epsilon_L=3.6880;        % Lorentz linewidth
w0=3.93282466e15;        % Lorentz resonance
delta=1e8;               %Lorentz permitivity
%delta=0;                %Lorentz permitivity
n=sqrt( epsilon + ( epsilon_L * w0^2 ) ./ ( w0^2 - (2*i*delta*2*pi*c./
    lambda) - (2*pi*c./lambda).^2 ));
n_sqr= epsilon + ( epsilon_L * w0^2 ) ./ ( w0^2 - (2*i*delta*2*pi*c./
    lambda) - (2*pi*c./lambda).^2 );
%n_real=real(n_sqr);
dndl = ((n_sqr(3:end))-(n_sqr(1:end-2))) ./ (lambda(3:end)-lambda(1:end-2)
    );
% line of best fit for dndl
% p = polyfit(lambda(2:end-1),dndl,1)
% f = polyval(p,lambda(2:end-1));
% hold on
% plot(lambda(2:end-1),f,'--r')
% plot(lambda(2:end-1),dndl,'--g','LineWidth',2)
dispersion_si= n_sqr(351)-(lambda_0/2)*dndl(351)
n_si=(n(351));
% hold on
% plot(lambda,imag(n))


%%%%% PARAMETERS %%%%%%
n2_si=[6.7e-18 (6.7+0.6)*1e-18 (6.1)*1e-18];
Btpa_si=1.03e-11;
n2_chalc=2.9e-18;
Btpa_chalc=6.2e-15;
n2_sio2=2.6e-20;
Btpa_sio2=0;
%n_air=1;
epsilon_0=8.85e-12;
pi=3.14;
c=3e8;
lambda_0=1550e-9;
x=E_manual.x;     % get simulation geometry from simulation
y=E_manual.y;     % get simulation geometry from simulation
```

```
E=E_manual.E;     % get Electric field matrix from simulation
H=H_manual.H;     % get magnetic field matrix from simulation

%%%%%    Defining non-linear interaction regions   %%%%%

Ex=interp2(Ex,2);
Ey=interp2(Ey,2);
Ez=interp2(Ez,2);
Hx=interp2(Hx,2);
Hy=interp2(Hy,2);
Hz=interp2(Hz,2);

x=linspace(x(1),x(length(x)),length(Ex));
y=linspace(y(1),y(length(y)),length(Ex(1,:)));

dx=(x(1,2)-x(1,1));
dy=(y(1,2)-y(1,1));

xx=find(abs(x)<=0.075e-6);
yy=find(0 <= y & y <= 0.22e-6);
yy1=find(0.22e-6 <= y & y <= 0.7e-6);


Ex_1=Ex(1:xx(1)+2,yy(1):yy1(length(yy1)));
Ex_2=Ex(xx(1):xx(length(xx)),yy1(1):yy1(length(yy1)));  % Cover
    nonlineraity
Ex_4=Ex(xx(1):xx(length(xx)),yy(1):yy(length(yy)));     % Core
    nonlinearity
Ex_3=Ex(xx(length(xx))-2:length(x),yy(1):yy1(length(yy1)));
Ex_5=Ex(1:length(x),1:yy(1));

Ey_1=Ey(1:xx(1)+2,yy(1):yy1(length(yy1)));
Ey_2=Ey(xx(1):xx(length(xx)),yy1(1):yy1(length(yy1)));  %cover
    nonlineraity
Ey_4=Ey(xx(1):xx(length(xx)),yy(1):yy(length(yy)));     % core
    nonlinearity
Ey_3=Ey(xx(length(xx))-2:length(x),yy(1):yy1(length(yy1)));
Ey_5=Ex(1:length(x),1:yy(1));

Ez_1=Ez(1:xx(1)+2,yy(1):yy1(length(yy1)));
Ez_2=Ez(xx(1):xx(length(xx)),yy1(1):yy1(length(yy1)));  %cover
    nonlineraity
Ez_4=Ez(xx(1):xx(length(xx)),yy(1):yy(length(yy)));     %core nonlinearity
Ez_3=Ez(xx(length(xx))-2:length(x),yy(1):yy1(length(yy1)));
Ez_5=Ex(1:length(x),1:yy(1));

%%%%%   RESHAPING THE E_FIELDS      %%%%%

E11 = horzcat(Ex_1,Ey_1,Ez_1);
E22 = horzcat(Ex_2,Ey_2,Ez_2);
E33 = horzcat(Ex_3,Ey_3,Ez_3);
E44 = horzcat(Ex_4,Ey_4,Ez_4);
E55 = horzcat(Ex_5,Ey_5,Ez_5);

%%%% Defining norm for each region %%%%

Norm_E=abs(Ex).^2+abs(Ey).^2+abs(Ez).^2;            % total E_filed
    normalization
Norm_E1=abs(Ex_1).^2+abs(Ey_1).^2+abs(Ez_1).^2;     % E_filed
    normalization for A1
```

```
Norm_E2=abs(Ex_2).^2+abs(Ey_2).^2+abs(Ez_2).^2;      % E_filed
    normalization for A2
Norm_E3=abs(Ex_3).^2+abs(Ey_3).^2+abs(Ez_3).^2;      % E_filed
    normalization for A3
Norm_E4=abs(Ex_4).^2+abs(Ey_4).^2+abs(Ez_4).^2;      % E_filed
    normalization for A4 -core
Norm_E5=abs(Ex_5).^2+abs(Ey_5).^2+abs(Ez_5).^2;      % E_filed
    normalization for A4 -core

%%%%%% GROUP VELOCITY %%%%%%%%

W=real(Ex.*conj(Hy)-Ey.*conj(Hx)) % z-component of cross product of E and
    H fields
W_1=(sum(sum(W))*dx*dy);

W_21= (epsilon_0)*sum(sum(dispersion_si*(Norm_E4)))*dx*dy;
W_22= (epsilon_0)*sum(sum(dispersion_chalc*(Norm_E1)))*dx*dy;
W_23= (epsilon_0)*sum(sum(dispersion_chalc*(Norm_E2)))*dx*dy;
W_24= (epsilon_0)*sum(sum(dispersion_chalc*(Norm_E3)))*dx*dy;
W_25= (epsilon_0)*sum(sum(dispersion_sio2*(Norm_E3)))*dx*dy;


k1=W_21/W_1;
k2=W_22/W_1;
k3=W_23/W_1;
k4=W_24/W_1;
k5=W_25/W_1;

vg_inv=(k1+k2+k3+k4+k5);
vg=1/vg_inv

%%% plots %%%%

% figure(1)
% zmin = floor(min(Ex(:)));
% zmax = ceil(max(real(Ex(:))));
% zinc = (zmax - zmin) / 20;
% zlevs = zmin:zinc:zmax;
% contourf(abs(Ex'),zlevs)

figure(2)
title('E_field Intensity');
zmin = floor(min(Norm_E(:)));
zmax = ceil(max(Norm_E(:)));
zinc = (zmax - zmin) / 20;
zlevs = zmin:zinc:zmax;
contourf(abs(Norm_E)',zlevs)

% figure(3)
% title('E_field Intensity');
% zmin = floor(min(Norm_E3(:)));
% zmax = ceil(max(Norm_E3(:)));
% zinc = (zmax - zmin) / 20;
% zlevs = zmin:zinc:zmax;
% contourf(abs(Norm_E3)',zlevs)
%
% figure(4)
% title('E_field Intensity');
% zmin = floor(min(Norm_E5(:)));
% zmax = ceil(max(Norm_E5(:)));
```

```
% zinc = (zmax - zmin) / 20;
% zlevs = zmin:zinc:zmax;
% contourf(abs(Norm_E5)',zlevs)


%%% effective Kerr nonlinearity %%%


N4= (sum(sum(dispersion_si*(n2_si(3)-i*(Btpa_si*lambda_0/(4*pi)))*(Norm_E4
    ).^2)))*dx*dy;
N3= (sum(sum(dispersion_chalc*(n2_chalc-i*(Btpa_chalc*lambda_0/(4*pi)))*(
    Norm_E3).^2)))*dx*dy;
N2= (sum(sum(dispersion_chalc*(n2_chalc-i*(Btpa_chalc*lambda_0/(4*pi)))*(
    Norm_E2).^2)))*dx*dy;
N1= (sum(sum(dispersion_chalc*(n2_chalc-i*(Btpa_chalc*lambda_0/(4*pi)))*(
    Norm_E1).^2)))*dx*dy;
N5= (sum(sum(dispersion_chalc*(n2_sio2-i*(Btpa_sio2*lambda_0/(4*pi)))*(
    Norm_E5).^2)))*dx*dy;

N=(n_chalc)^2*(N1+N2+N3+N4+N5);

D1= sum(sum((dispersion_si^2)*Norm_E4.^2))*dx*dy;
D2= sum(sum((dispersion_chalc^2)*Norm_E1.^2))*dx*dy;
D3= sum(sum((dispersion_chalc^2)*Norm_E2.^2))*dx*dy;
D4= sum(sum((dispersion_chalc^2)*Norm_E3.^2))*dx*dy;
D5= sum(sum((dispersion_sio2^2)*Norm_E5.^2))*dx*dy;


n2_eff_inv= D1/N+D2/N+D3/N+D4/N+D5/N;
n2_eff=(1/n2_eff_inv)
Btpa_eff=imag(n2_eff)*4*pi/lambda_0


%%%%% Aeff %%%%%

N1= sum(sum((dispersion_chalc)*(Norm_E1)))*dx*dy;
N2= sum(sum((dispersion_chalc)*(Norm_E2)))*dx*dy;
N3= sum(sum((dispersion_chalc)*(Norm_E3)))*dx*dy;
N4= sum(sum((dispersion_si)*Norm_E4))*dx*dy;
N5= sum(sum((dispersion_sio2)*Norm_E5))*dx*dy;

N=(N1+N2+N3+N4+N5)^2;


D1= sum(sum((dispersion_si^2)*Norm_E4.^2))*dx*dy;
D2= sum(sum((dispersion_chalc^2)*Norm_E1.^2))*dx*dy;
D3= sum(sum((dispersion_chalc^2)*Norm_E2.^2))*dx*dy;
D4= sum(sum((dispersion_chalc^2)*Norm_E3.^2))*dx*dy;
D5= sum(sum((dispersion_sio2^2)*Norm_E5.^2))*dx*dy;


Aeff_inv= (D1/N)+(D2/N)+(D3/N)+(D4/N)+(D5/N);
Aeff=(1/Aeff_inv)

%%%%% nonlinear factor Re(Gamma)%%%%

Gamma_eff= (2*pi/lambda_0)*(c/(n_chalc)/vg)^2*(n2_eff/Aeff)

FOM=-(real(Gamma_eff)/(4*pi*imag(Gamma_eff)))
```

../Appendices/code.m

Bibliography

[1] A. Zarifi, B. Stiller, M. Merklein, N. Li, K. Vu, D.-Y. Choi, P. Ma, S. J. Madden, and B. J. Eggleton, "Highly localized distributed Brillouin scattering response in a photonic integrated circuit," *APL Photonics*, vol. 3, no. 3, p. 036 101, 2018. DOI: 10.1063/1.5000108.

[2] A. Zarifi, B. Stiller, M. Merklein, Y. Liu, B. Morrison, A. Casas-Bedoya, G. Ren, T. G. Nguyen, K. Vu, D.-Y. Choi, A. Mitchell, S. J. Madden, and B. J. Eggleton, "Brillouin spectroscopy of a hybrid silicon-chalcogenide waveguide with geometrical variations," *Optics Letters*, vol. 43, no. 15, p. 3493, 2018. DOI: 10.1364/OL.43.003493.

[3] A. Zarifi, B. Stiller, M. Merklein, Y. Liu, B. Morrison, A. Casas-Bedoya, G. Ren, T. G. Nguyen, K. Vu, D.-Y. Choi, A. Mitchell, S. J. Madden, and B. J. Eggleton, "On-chip correlation-based Brillouin sensing: design, experiment, and simulation," *Journal of the Optical Society of America B*, vol. 36, no. 1, p. 146, 2019. DOI: 10.1364/JOSAB.36.000146.

[4] A. Zarifi, B. Stiller, M. Merklein, and B. Eggleton, "High Resolution Brillouin Sensing of Micro-Scale Structures," *Applied Sciences*, vol. 8, no. 12, p. 2572, 2018. DOI: 10.3390/app8122572.

[5] A. Zarifi, A. Casas Bedoya, B. Morrison, Y. Zhang, G. Ren, T. Nguyen, S. Madden, K. Vu, A. Mitchell, C. Wolff, D. Marpaung, and B. J Eggleton, "Nonlinear Loss Engineering in a Silicon-Chalcogenide Hybrid Optical Waveguide," in *Photonics and Fiber Technology 2016 (ACOFT, BGPP, NP)*, vol. 10, 2016, NM4A.6. DOI: 10.1364/NP.2016.NM4A.6.

[6] B. Morrison, A. Casas-Bedoya, G. Ren, K. Vu, Y. Liu, A. Zarifi, T. G. Nguyen, D.-Y. Choi, D. Marpaung, S. J. Madden, A. Mitchell, and B. J. Eggleton, "Compact Brillouin devices through hybrid integration on silicon," *Optica*, vol. 4, no. 8, p. 847, 2017. DOI: 10.1364/OPTICA.4.000847.

[7] C. Sun, M. T. Wade, Y. Lee, J. S. Orcutt, L. Alloatti, M. S. Georgas, A. S. Waterman, J. M. Shainline, R. R. Avizienis, S. Lin, B. R. Moss, R. Kumar, F. Pavanello, A. H. Atabaki, H. M. Cook, A. J. Ou, J. C. Leu, Y.-H. Chen, K. Asanović, R. J. Ram, M. A. Popović, and V. M. Stojanović, "Single-chip microprocessor that communicates directly using light," *Nature*, vol. 528, no. 7583, pp. 534–538, 2015. DOI: 10.1038/nature16454.

[8] G. Reed, G. Mashanovich, F. Gardes, and D. Thomson, "Silicon optical modulators," *Nature Photonics*, vol. 4, no. 8, pp. 518–526, 2010. DOI: 10.1038/nphoton.2010.179.

[9] G. P. Agrawal, *Fiber-optic communication systems*. 2012.

[10] G. P. Agrawal, *Nonlinear Fiber Optics*. 2012.

[11] J. Li, H. Lee, and K. J. Vahala, "Microwave synthesizer using an on-chip Brillouin oscillator," *Nature Communications*, vol. 4, no. 1, p. 2097, 2013. DOI: 10.1038/ncomms3097.

[12] M. Merklein, B. Stiller, I. V. Kabakova, U. S. Mutugala, K. Vu, S. J. Madden, B. J. Eggleton, and R. Slavík, "Widely tunable, low phase noise microwave source based on a photonic chip," *Optics Letters*, vol. 41, no. 20, p. 4633, 2016. DOI: 10.1364/OL.41.004633.

[13] J. K. Ranka, R. S. Windeler, and A. J. Stentz, "Visible continuum generation in air–silica microstructure optical fibers with anomalous dispersion at 800 nm," *Optics Letters*, vol. 25, no. 1, p. 25, 2000. DOI: 10.1364/OL.25.000025.

[14] J. M. Dudley, G. Genty, and S. Coen, "Supercontinuum generation in photonic crystal fiber," *Reviews of Modern Physics*, vol. 78, no. 4, pp. 1135–1184, 2006. DOI: 10.1103/RevModPhys.78.1135.

[15] A. L. Gaeta, "Nonlinear propagation and continuum generation in microstructured optical fibers," *Optics Letters*, vol. 27, no. 11, p. 924, 2002. DOI: 10.1364/OL.27.000924.

[16] M. A. Foster and A. L. Gaeta, "Ultra-low threshold supercontinuum generation in sub-wavelength waveguides," *Optics Express*, vol. 12, no. 14, p. 3137, 2004. DOI: 10.1364/OPEX.12.003137.

[17] D. Marpaung, B. Morrison, M. Pagani, R. Pant, D.-Y. Choi, B. Luther-Davies, S. J. Madden, and B. J. Eggleton, "Low-power, chip-based stimulated Brillouin scattering microwave photonic filter with ultrahigh selectivity," *Optica*, vol. 2, no. 2, p. 76, 2015. DOI: 10.1364/OPTICA.2.000076.

[18] J. Sancho, N. Primerov, S. Chin, Y. Antman, A. Zadok, S. Sales, and L. Thévenaz, "Tunable and reconfigurable multi-tap microwave photonic filter based on dynamic Brillouin gratings in fibers," *Optics Express*, vol. 20, no. 6, p. 6157, 2012. DOI: 10.1364/OE.20.006157.

[19] A. Choudhary, B. Morrison, I. Aryanfar, S. Shahnia, M. Pagani, Y. Liu, K. Vu, S. Madden, D. Marpaung, and B. J. Eggleton, "Advanced Integrated Microwave Signal Processing With Giant On-Chip Brillouin Gain," *Journal of Lightwave Technology*, vol. 35, no. 4, pp. 846–854, 2017. DOI: 10.1109/JLT.2016.2613558.

[20] R. Salem, M. A. Foster, A. C. Turner, D. F. Geraghty, M. Lipson, and A. L. Gaeta, "All-optical regeneration on a silicon chip," *Optics express*, vol. 15, no. 12, pp. 7802–7809, 2007.

[21] P. V. Mamyshev, "All-optical data regeneration based on self-phase modulation effect," in *24th European Conference on Optical Communication.*, vol. 1, 1998, pp. 475–476.

[22] L. Thévenaz, "Slow and fast light in optical fibres," *Nature Photonics*, vol. 2, no. 8, pp. 474–481, 2008. DOI: 10.1038/nphoton.2008.147.

[23] M. Merklein, B. Stiller, K. Vu, S. J. Madden, and B. J. Eggleton, "A chip-integrated coherent photonic-phononic memory," *Nature Communications*, vol. 8, no. 1, pp. 1–7, 2017. DOI: 10.1038/s41467-017-00717-y.

[24] Z. Zhu, D. J. Gauthier, and R. W. Boyd, "Stored Light in an Optical Fiber via Stimulated Brillouin Scattering," *Science*, vol. 318, no. 5857, pp. 1748–1750, 2007. DOI: 10.1126/science.1149066.

[25] S Blair and K Zheng, "Intensity-tunable group delay using stimulated Raman scattering in silicon slow-light waveguides," *Optics Express*, vol. 14, no. 3, pp. 1064–1069, 2006.

[26] M Merklein, B Stiller, and B. J. Eggleton, "Brillouin-based light storage and delay techniques," *Journal of Optics*, vol. 20, no. 8, p. 083 003, 2018. DOI: 10.1088/2040-8986/aad081.

[27] D. J. Moss, R. Morandotti, A. L. Gaeta, and M. Lipson, "New CMOS-compatible platforms based on silicon nitride and Hydex for nonlinear optics," *Nature Photonics*, vol. 7, no. 8, pp. 597–607, 2013. DOI: 10.1038/nphoton.2013.183.

[28] J. Leuthold, C. Koos, and W. Freude, "Nonlinear silicon photonics," *Nature Photonics*, vol. 4, no. 8, pp. 535–544, 2010. DOI: 10.1038/nphoton.2010.185.

[29] W. Zhang, S. Serna, N. Dubreuil, and E. Cassan, "Nonlinear optimization of slot Si waveguides: TPA minimization with FOM_TPA up to 4.25," *Optics Letters*, vol. 40, no. 7, p. 1212, 2015. DOI: 10.1364/OL.40.001212.

[30] C. Koos, P. Vorreau, T. Vallaitis, P. Dumon, W. Bogaerts, R. Baets, B. Esembeson, I. Biaggio, T. Michinobu, F. Diederich, W. Freude, and J. Leuthold, "All-optical high-speed signal processing with silicon–organic hybrid slot waveguides," *Nature Photonics*, vol. 3, no. 4, pp. 216–219, 2009. DOI: 10.1038/nphoton.2009.25.

[31] C. Koos, L. Jacome, C. Poulton, J. Leuthold, and W. Freude, "Nonlinear silicon-on-insulator waveguides for all-optical signal processing," *Optics Express*, vol. 15, no. 10, p. 5976, 2007. DOI: 10.1364/OE.15.005976.

[32] H. Lee, T. Chen, J. Li, K. Y. Yang, S. Jeon, O. Painter, and K. J. Vahala, "Chemically etched ultrahigh-Q wedge-resonator on a silicon chip," *Nature Photonics*, vol. 6, no. 6, pp. 369–373, 2012. DOI: 10.1038/nphoton.2012.109.

[33] I. V. Kabakova, R. Pant, D.-y. Choi, S. Debbarma, B. Luther-Davies, S. J. Madden, and B. J. Eggleton, "Narrow linewidth Brillouin laser based on chalcogenide photonic chip," *Optics Letters*, vol. 38, no. 17, p. 3208, 2013. DOI: 10.1364/OL.38.003208.

[34] J. C. Yong, L. Thévenaz, and B. Y. Kim, "Brillouin fiber laser pumped by a DFB laser diode," *Journal of Lightwave Technology*, vol. 21, no. 2, pp. 546–554, 2003. DOI: 10.1109/JLT.2003.808768.

[35] D. Marpaung, B. Morrison, R. Pant, and B. J. Eggleton, "Frequency agile microwave photonic notch filter with anomalously high stopband rejection," *Optics Letters*, vol. 38, no. 21, p. 4300, 2013. DOI: 10.1364/OL.38.004300.

[36] T. F. S. Büttner, M. Merklein, I. V. Kabakova, D. D. Hudson, D.-Y. Choi, B. Luther-Davies, S. J. Madden, and B. J. Eggleton, "Phase-locked, chip-based, cascaded stimulated Brillouin scattering," *Optica*, vol. 1, no. 5, p. 311, 2014. DOI: 10.1364/OPTICA.1.000311.

[37] D. Braje, L. Hollberg, and S. Diddams, "Brillouin-Enhanced Hyperparametric Generation of an Optical Frequency Comb in a Monolithic Highly Nonlinear Fiber Cavity Pumped by a cw Laser," *Physical Review Letters*, vol. 102, no. 19, p. 193 902, 2009. DOI: 10.1103/PhysRevLett.102.193902.

[38] K.-Y. Song, Z. He, and K. Hotate, "Distributed strain measurement with millimeter-order spatial resolution based on Brillouin optical correlation domain analysis," *Optics Letters*, vol. 31, no. 17, p. 2526, 2006. DOI: 10.1364/OL.31.002526.

[39] L. Thévenaz, "Brillouin distributed time-domain sensing in optical fibers: state of the art and perspectives," *Frontiers of Optoelectronics in China*, vol. 3, no. 1, pp. 13–21, 2010. DOI: 10.1007/s12200-009-0086-9.

[40] K. Hotate, "Fiber distributed Brillouin sensing with optical correlation domain techniques," *Optical Fiber Technology*, vol. 19, no. 6, pp. 700–719, 2013. DOI: 10.1016/j.yofte.2013.08.008.

[41] C. Wolff, R. V. Laer, M. J. Steel, B. J. Eggleton, and C. G. Poulton, "Brillouin resonance broadening due to structural variations in nanoscale waveguides," *New Journal of Physics*, vol. 18, no. 2, p. 025 006, 2016. DOI: 10.1088/1367-2630/18/2/025006.

[42] C. G. Poulton, R. Pant, and B. J. Eggleton, "Acoustic confinement and Stimulated Brillouin Scattering in integrated optical waveguides," *Journal of the Optical Society of America B*, no. c, pp. 1–8, 2013.

[43] B. J. Eggleton, C. G. Poulton, and R. Pant, "Inducing and harnessing stimulated Brillouin scattering in photonic integrated circuits," *Advances in Optics and Photonics*, vol. 5, no. 4, p. 536, 2013. DOI: 10.1364/AOP.5.000536.

[44] R. Van Laer, B. Kuyken, D. Van Thourhout, and R. Baets, "Interaction between light and highly confined hypersound in a silicon photonic nanowire," *Nature Photonics*, vol. 9, no. 3, pp. 199–203, 2015. DOI: 10.1038/nphoton.2015.11.

[45] E. A. Kittlaus, H. Shin, and P. T. Rakich, "Large Brillouin amplification in silicon," *Nature Photonics*, vol. 10, no. 7, pp. 463–467, 2016. DOI: 10.1038/nphoton.2016.112.

[46] Y. Bao and G. Chen, "Temperature-dependent strain and temperature sensitivities of fused silica single mode fiber sensors with pulse pre-pump Brillouin optical time domain analysis," *Measurement Science and Technology*, vol. 27, no. 6, p. 065 101, 2016. DOI: 10.1088/0957-0233/27/6/065101.

[47] K. Hotate, R. Watanabe, Z. He, and M. Kishi, "Measurement of Brillouin frequency shift distribution in PLC by Brillouin optical correlation domain analysis," in *OFS2012 22nd International Conference on Optical Fiber Sensors*, vol. 8421, 2012, 8421CE–8421CE–4. DOI: 10.1117/12.2012653.

[48] B. Stiller, S. M. Foaleng, J.-C. Beugnot, M. W. Lee, M. Delqué, G. Bouwmans, A. Kudlinski, L. Thévenaz, H. Maillotte, and T. Sylvestre, "Photonic crystal fiber mapping using Brillouin echoes distributed sensing," *Optics Express*, vol. 18, no. 19, p. 20 136, 2010. DOI: 10.1364/OE.18.020136.

[49] D. Chow, J. C. Tchahame Nougnihi, A. Denisov, J.-C. Beugnot, T. Sylvestre, L. Li, R. Ahmad, M. Rochette, K. H. Tow, M. A. Soto, and L. Thévenaz, "Mapping the Uniformity of Optical Microwires Using Phase-Correlation Brillouin Distributed Measurements," in *Frontiers in Optics 2015*, 2015, FW4F.4. DOI: 10.1364/FIO.2015.FW4F.4.

[50] T. Kurashima, T. Horiguchi, and M. Tateda, "Distributed-temperature sensing using stimulated Brillouin scattering in optical silica fibers," *Optics Letters*, vol. 15, no. 18, p. 1038, 1990. DOI: 10.1364/OL.15.001038.

[51] A. Zadok, Y. Antman, N. Primerov, A. Denisov, J. Sancho, and L. Thevenaz, "Random-access distributed fiber sensing," *Laser & Photonics Reviews*, vol. 6, no. 5, pp. L1–L5, 2012. DOI: 10.1002/lpor.201200013.

[52] O. Florez, P. F. Jarschel, Y. A. V. Espinel, C. M. B. Cordeiro, T. P. Mayer Alegre, G. S. Wiederhecker, and P. Dainese, "Brillouin scattering self-cancellation," *Nature Communications*, vol. 7, p. 11 759, 2016. DOI: 10.1038/ncomms11759.

[53] R. W. Boyd, *Nonlinear optics*. 2003.

[54] L. Brillouin, "Diffusion de la lumière et des rayons X par un corps transparent homogène-Influence de l'agitation thermique," in *Annales de physique*, vol. 9, 1922, pp. 88–122.

[55] L. Mandelstam, "Light Scattering by Inhomogeneous Media," *Zh. Russ. Fiz-Khim.*, vol. 58, 1926.

[56] T. H. Maiman, "Stimulated Optical Radiation in Ruby," *Nature*, vol. 187, pp. 493–494, 1960.

[57] R. Y. Chiao and B. P. Stoicheff, "Brillouin scattering in liquids excited by the He–Ne maser," *JOSA*, vol. 54, no. 10, pp. 1286–1287, 1964.

[58] E. Garmire and C. H. Townes, "Stimulated Brillouin Scattering in LIQUIDS1," *Applied Physics Letters*, vol. 5, no. 4, pp. 84–86, 1964.

[59] R. G. Brewer and K. E. Rieckhoff, "Stimulated Brillouin scattering in liquids," *Physical Review Letters*, vol. 13, no. 11, p. 334, 1964.

[60] E. E. Hagenlocker and W. G. Rado, "Stimulated Brillouin and Raman scattering in gases," *Applied Physics Letters*, vol. 7, no. 9, pp. 236–238, 1965.

[61] C. L. Tang, "Saturation and spectral characteristics of the Stokes emission in the stimulated Brillouin process," *Journal of Applied Physics*, vol. 37, no. 8, pp. 2945–2955, 1966.

[62] E. P. Ippen and R. H. Stolen, "Stimulated Brillouin scattering in optical fibers," *Applied Physics Letters*, vol. 21, no. 11, pp. 539–541, 1972. DOI: 10.1063/1.1654249.

[63] R. G. Smith, "Optical power handling capacity of low loss optical fibers as determined by stimulated Raman and Brillouin scattering," *Applied Optics*, vol. 11, no. 11, pp. 2489–2494, 1972.

[64] R. W. Boyd, K. Rzaewski, and P. Narum, "Noise initiation of stimulated Brillouin scattering," *Physical Review A*, vol. 42, no. 9, p. 5514, 1990.

[65] N. Olsson and J. Van Der Ziel, "Characteristics of a semiconductor laser pumped brillouin amplifier with electronically controlled bandwidth," *Journal of Lightwave Technology*, vol. 5, no. 1, pp. 147–153, 1987. DOI: 10.1109/JLT.1987.1075405.

[66] E. Lichtman, R. Waarts, and A. Friesem, "Stimulated Brillouin scattering excited by a modulated pump wave in single-mode fibers," *Journal of Lightwave Technology*, vol. 7, no. 1, pp. 171–174, 1989. DOI: 10.1109/50.17750.

[67] A. L. Gaeta and R. W. Boyd, "Stimulated Brillouin scattering in the presence of external feedback," *International Journal of Nonlinear Optical Physics*, vol. 1, no. 03, pp. 581–594, 1992.

[68] D Culverhouse, F Farahi, C. Pannell, and D. Jackson, "Stimulated Brillouin scattering: a means to realise tunable microwave generator or distributed temperature sensor," *Electronics Letters*, vol. 25, no. 14, p. 915, 1989. DOI: 10.1049/el:19890613.

[69] X. Bao, D. J. Webb, and D. A. Jackson, "32-km distributed temperature sensor based on Brillouin loss in an optical fiber," *Optics Letters*, vol. 18, no. 18, p. 1561, 1993. DOI: 10.1364/OL.18.001561.

[70] M. Niklès, L. Thévenaz, and P. A. Robert, "Simple distributed fiber sensor based on Brillouin gain spectrum analysis," *Optics Letters*, vol. 21, no. 10, p. 758, 1996. DOI: 10.1364/OL.21.000758.

[71] M. S. Kang, A. Nazarkin, A. Brenn, and P. S. J. Russell, "Tightly trapped acoustic phonons in photonic crystal fibres as highly nonlinear artificial Raman oscillators," *Nature Physics*, vol. 5, no. 4, pp. 276–280, 2009. DOI: 10.1038/nphys1217.

[72] J.-C. Beugnot, S. Lebrun, G. Pauliat, H. Maillotte, V. Laude, and T. Sylvestre, "Brillouin light scattering from surface acoustic waves in a subwavelength-diameter optical fibre," *Nature Communications*, vol. 5, no. 1, p. 5242, 2014. DOI: 10.1038/ncomms6242.

[73] J. C. Tchahame, J.-C. Beugnot, K. P. Huy, V. Laude, A. Kudlinski, and T. Sylvestre, "Surface Brillouin scattering in photonic crystal fibers," *Optics Letters*, vol. 41, no. 14, p. 3269, 2016. DOI: 10.1364/OL.41.003269.

[74] R. Pant, C. G. Poulton, D.-Y. Choi, H. Mcfarlane, S. Hile, E. Li, L. Thevenaz, B. Luther-Davies, S. J. Madden, and B. J. Eggleton, "On-chip stimulated Brillouin scattering," *Optics Express*, vol. 19, no. 9, p. 8285, 2011. DOI: 10.1364/OE.19.008285.

[75] P. Dainese, P. S. J. Russell, N. Joly, J. C. Knight, G. S. Wiederhecker, H. L. Fragnito, V. Laude, and A. Khelif, "Stimulated Brillouin scattering from multi-GHz-guided acoustic phonons in nanostructured photonic crystal fibres," *Nature Physics*, vol. 2, no. 6, pp. 388–392, 2006. DOI: 10.1038/nphys315.

[76] P. Lu, L. Men, K. Sooley, and Q. Chen, "Tapered fiber Mach–Zehnder interferometer for simultaneous measurement of refractive index and temperature," *Applied Physics Letters*, vol. 94, no. 13, p. 131 110, 2009. DOI: 10.1063/1.3115029.

[77] T. Ritari, J. Tuominen, and H. Ludvigsen, "Gas sensing using air-guiding photonic bandgap fibers," *Optics Express*, vol. 12, no. 17, p. 4080, 2004. DOI: 10.1364/OPEX.12.004080.

[78] D. K. C. Wu, B. T. Kuhlmey, and B. J. Eggleton, "Ultrasensitive photonic crystal fiber refractive index sensor," *Optics Letters*, vol. 34, no. 3, p. 322, 2009. DOI: 10.1364/OL.34.000322.

[79] I. Dicaire, A. De Rossi, S. Combrié, and L. Thévenaz, "Probing molecular absorption under slow-light propagation using a photonic crystal waveguide," *Optics Letters*, vol. 37, no. 23, p. 4934, 2012. DOI: 10.1364/OL.37.004934.

[80] W. Loh, A. A. S. Green, F. N. Baynes, D. C. Cole, F. J. Quinlan, H. Lee, K. J. Vahala, S. B. Papp, and S. A. Diddams, "Dual-microcavity narrow-linewidth Brillouin laser," *Optica*, vol. 2, no. 3, p. 225, 2015. DOI: 10.1364/OPTICA.2.000225.

[81] N. T. Otterstrom, R. O. Behunin, E. A. Kittlaus, Z. Wang, and P. T. Rakich, "A silicon Brillouin laser," *Science*, vol. 360, no. 6393, pp. 1113–1116, 2018. DOI: 10.1126/science.aar6113.

[82] C.-H. Dong, Z. Shen, C.-L. Zou, Y.-L. Zhang, W. Fu, and G.-C. Guo, "Brillouin-scattering-induced transparency and non-reciprocal light storage," *Nature Communications*, vol. 6, no. 1, p. 6193, 2015. DOI: 10.1038/ncomms7193.

[83] W. Qiu, P. Rakich, H Shin, and H Dong, "Stimulated Brillouin scattering in nanoscale silicon step-index waveguides: a general framework of selection rules and calculating SBS gain," *Optics . . .*, vol. 5865, no. 2006, pp. 2764–2777, 2013. DOI: 10.1364/OE.21.031402.

[84] C. Wolff, M. J. Steel, B. J. Eggleton, and C. G. Poulton, "Stimulated Brillouin scattering in integrated photonic waveguides: Forces, scattering mechanisms, and coupled-mode analysis," *Physical Review A*, vol. 92, no. 1, p. 013 836, 2015. DOI: 10.1103/PhysRevA.92.013836.

[85] P. Barclay, K. Srinivasan, and O. Painter, "Evanescent coupling from optical fiber tapers to photonic crystal waveguides and resonators," in *Postconference Digest Quantum Electronics and Laser Science, 2003. QELS.*, vol. 88, 2003, 2 pp. DOI: 10.1109/QELS.2003.238447.

[86] B. Stiller, M. Delqué, J.-C. Beugnot, M. W. Lee, G. Mélin, H. Maillotte, V. Laude, and T. Sylvestre, "Frequency-selective excitation of guided acoustic modes in a photonic crystal fiber," *Optics Express*, vol. 19, no. 8, p. 7689, 2011. DOI: 10.1364/OE.19.007689.

[87] A Fellay, L. Thévenaz, M Facchini, M. Niklès, and P Robert, "Distributed sensing using stimulated Brillouin scattering : towards ultimate resolution.," in *12th International Conference on Optical Fiber Sensors*, vol. 16, 1997, OWD3. DOI: 10.1364/OFS.1997.OWD3.

[88] T. Horiguchi and M. Tateda, "Optical-fiber-attenuation investigation using stimulated Brillouin scattering between a pulse and a continuous wave," *Optics Letters*, vol. 14, no. 8, p. 408, 1989. DOI: 10.1364/OL.14.000408.

[89] T. Horiguchi and M. Tateda, "BOTDA-nondestructive measurement of single-mode optical fiber attenuation characteristics using Brillouin interaction: theory," *Journal of Lightwave Technology*, vol. 7, no. 8, pp. 1170–1176, 1989. DOI: 10.1109/50.32378.

[90] T. Horiguchi, T. Kurashima, and M. Tateda, "A Technique to Measure Distributed Strain in Optical Fibers," *IEEE photonics technology letters*, vol. 2, no. 5, pp. 352–354, 1990. DOI: 10.1109/68.54703.

[91] K. Shimizu, T. Horiguchi, Y. Koyamada, and T. Kurashima, "Coherent self-heterodyne detection of spontaneously Brillouin-scattered light waves in a single-mode fiber," *Optics Letters*, vol. 18, no. 3, p. 185, 1993. DOI: 10.1364/OL.18.000185.

[92] S. M. Foaleng, M. Tur, J.-C. Beugnot, and L. Thevenaz, "High Spatial and Spectral Resolution Long-Range Sensing Using Brillouin Echoes," *Journal of Lightwave Technology*, vol. 28, no. 20, pp. 2993–3003, 2010. DOI: 10.1109/JLT.2010.2073443.

[93] J.-C. Beugnot, M. Tur, S. F. Mafang, and L. Thévenaz, "Distributed Brillouin sensing with sub-meter spatial resolution: modeling and processing," *Optics Express*, vol. 19, no. 8, p. 7381, 2011. DOI: 10.1364/OE.19.007381.

[94] M. A. Soto, G. Bolognini, and F. Di Pasquale, "Analysis of pulse modulation format in coded BOTDA sensors," *Optics Express*, vol. 18, no. 14, p. 14 878, 2010. DOI: 10.1364/OE.18.014878.

[95] X. Bao, A. Brown, M. DeMerchant, and J. Smith, "Characterization of the Brillouin-loss spectrum of single-mode fibers by use of very short (<10-ns) pulses," *Optics Letters*, vol. 24, no. 8, p. 510, 1999. DOI: 10.1364/OL.24.000510.

[96] L. Zou, X. Bao, Y. Wan, and L. Chen, "Coherent probe-pump-based Brillouin sensor for centimeter-crack detection," *Optics Letters*, vol. 30, no. 4, p. 370, 2005. DOI: 10.1364/OL.30.000370.

[97] A. W. Brown, B. G. Colpitts, and K. Brown, "Dark-Pulse Brillouin Optical Time-Domain Sensor With 20-mm Spatial Resolution," *Journal of Lightwave Technology*, vol. 25, no. 1, pp. 381–386, 2007. DOI: 10.1109/JLT.2006.886672.

[98] L. Thévenaz and S. Foaleng Mafang, "Distributed fiber sensing using Brillouin echoes," in *Proceedings of SPIE*, vol. 7004, 2008, 70043N. DOI: 10.1117/12.786283.

[99] Y. Bao, W. Meng, Y. Chen, G. Chen, and K. H. Khayat, "Measuring mortar shrinkage and cracking by pulse pre-pump Brillouin optical time domain analysis with a single optical fiber," *Materials Letters*, vol. 145, pp. 344–346, 2015. DOI: 10.1016/j.matlet.2015.01.140.

[100] K. Kishida and C. H. Li, "Pulse pre-pump-BOTDA technology for new generation of distributed strain measuring system," *Structural health monitoring and intelligent infrastructure*, vol. 1, pp. 471–477, 2005.

[101] Y. Bao and G. Chen, "High-temperature measurement with Brillouin optical time domain analysis of an annealed fused-silica single-mode fiber," *Optics Letters*, vol. 41, no. 14, p. 3177, 2016. DOI: 10.1364/OL.41.003177.

[102] D. Garus, T. Gogolla, K. Krebber, and F. Schliep, "Distributed sensing technique based on Brillouin optical-fiber frequency-domain analysis," *Optics Letters*, vol. 21, no. 17, p. 1402, 1996. DOI: 10.1364/OL.21.001402.

[103] R. Bernini, A. Minardo, and L. Zeni, "Distributed Sensing at Centimeter-Scale Spatial Resolution by BOFDA: Measurements and Signal Processing," *IEEE Photonics Journal*, vol. 4, no. 1, pp. 48–56, 2012. DOI: 10.1109/JPHOT.2011.2179024.

[104] K. Y. Song, K. Hotate, W. Zou, and Z. He, "Applications of Brillouin Dynamic Grating to Distributed Fiber Sensors," *Journal of Lightwave Technology*, vol. 35, no. 16, pp. 3268–3280, 2017. DOI: 10.1109/JLT.2016.2617313.

[105] K. Y. Song, W. Zou, Z. He, and K. Hotate, "All-optical dynamic grating generation based on Brillouin scattering in polarization-maintaining fiber," *Optics Letters*, vol. 33, no. 9, p. 926, 2008. DOI: 10.1364/OL.33.000926.

[106] K. Y. Song, "Operation of Brillouin dynamic grating in single-mode optical fibers.," *Optics letters*, vol. 36, no. 23, pp. 4686–8, 2011. DOI: 10.1364/OL.36.004686.

[107] R. Pant, E. Li, C. G. Poulton, D.-Y. Choi, S. Madden, B. Luther-Davies, and B. J. Eggleton, "Observation of Brillouin dynamic grating in a photonic chip," *Optics Letters*, vol. 38, no. 3, p. 305, 2013. DOI: 10.1364/OL.38.000305.

[108] S. Li, M.-J. Li, and R. S. Vodhanel, "All-optical Brillouin dynamic grating generation in few-mode optical fiber," *Optics Letters*, vol. 37, no. 22, p. 4660, 2012. DOI: 10.1364/OL.37.004660.

[109] W. Zou, Z. He, K.-Y. Song, and K. Hotate, "Correlation-based distributed measurement of a dynamic grating spectrum generated in stimulated Brillouin scattering in a polarization-maintaining optical fiber," *Optics Letters*, vol. 34, no. 7, p. 1126, 2009. DOI: 10.1364/OL.34.001126.

[110] C. Sanghoon, N. Primerov, and L. Thevenaz, "Sub-Centimeter Spatial Resolution in Distributed Fiber Sensing Based on Dynamic Brillouin Grating in Optical Fibers," *IEEE Sensors Journal*, vol. 12, no. 1, pp. 189–194, 2012. DOI: 10.1109/JSEN.2011.2126568.

[111] T. Hasegawa and K. Hotate, "<title>Measurement of Brillouin gain spectrum distribution along an optical fiber by direct frequency modulation of a laser diode</title>," in *Photonics East'99*, vol. 3860, 1999, pp. 306–316. DOI: 10.1117/12.372976.

[112] K. Hotate and T. Hasegawa, "Measurement of Brillouin Gain Spectrum Distribution along an Optical Fiber Using a Correlation-Based Technique—Proposal, Experiment and Simulation—," *Ieice Trans. Electron.*, vol. E83-C, no. 3, pp. 405–412, 2000. DOI: 10.1.1.29.7344.

[113] R. Cohen, Y. London, Y. Antman, and A. Zadok, "Brillouin optical correlation domain analysis with 4 millimeter resolution based on amplified spontaneous emission," *Optics Express*, vol. 22, no. 10, p. 12 070, 2014. DOI: 10.1364/OE.22.012070.

[114] J. Zhang, M. Zhang, M. Zhang, Y. Liu, C. Feng, Y. Wang, and Y. Wang, "Chaotic Brillouin optical correlation-domain analysis," *Optics Letters*, vol. 43, no. 8, p. 1722, 2018. DOI: 10.1364/OL.43.001722.

[115] K. Hotate and S. Ong, "Distributed dynamic strain measurement using a correlation-based Brillouin sensing system," *IEEE Photonics Technology Letters*, vol. 15, no. 2, pp. 272–274, 2003. DOI: 10.1109/LPT.2002.806107.

[116] J. Zhang, C. Feng, M. Zhang, Y. Liu, C. Wu, and Y. Wang, "Brillouin optical correlation domain analysis based on chaotic laser with suppressed time delay signature," *Optics Express*, vol. 26, no. 6, p. 6962, 2018. DOI: 10.1364/OE.26.006962.

[117] K.-Y. Song and K. Hotate, "Enlargement of measurement range in a Brillouin optical correlation domain analysis system using double lock-in amplifiers and a single-sideband modulator," *IEEE Photonics Technology Letters*, vol. 18, no. 3, pp. 499–501, 2006. DOI: 10.1109/LPT.2005.863624.

[118] Y. Antman, L. Yaron, T. Langer, M. Tur, N. Levanon, and A. Zadok, "Experimental demonstration of localized Brillouin gratings with low off-peak reflectivity established by perfect Golomb codes," *Optics Letters*, vol. 38, no. 22, p. 4701, 2013. DOI: 10.1364/OL.38.004701.

[119] D. Elooz, Y. Antman, N. Levanon, and A. Zadok, "High-resolution long-reach distributed Brillouin sensing based on combined time-domain and correlation-domain analysis," *Optics Express*, vol. 22, no. 6, p. 6453, 2014. DOI: 10.1364/OE.22.006453.

[120] K. Hotate, H. A. Rai, and K. Y. Song, "Range-Enlargement of Simplified Brillouin Optical Correlation Domain Analysis Based on a Temporal Gating Scheme," *SICE Journal of Control, Measurement, and System Integration*, vol. 1, no. 4, pp. 271–274, 2008. DOI: https://doi.org/10.9746/jcmsi.1.271.

[121] A. Denisov, M. A. Soto, and L. Thévenaz, "Time gated phase-correlation distributed Brillouin fibre sensor," in *Spie 8794*, vol. 8794, 2013, p. 87943I. DOI: 10.1117/12.2026169.

[122] J. H. Jeong, K. Lee, K. Y. Song, J.-M. Jeong, and S. B. Lee, "Differential measurement for Brillouin optical correlation domain analysis," *Optics Express*, vol. 20, no. 10, p. 11 091, 2012. DOI: 10.1364/OE.20.011091.

[123] D. M. Chow, J.-C. Beugnot, A. Godet, K. P. Huy, M. A. Soto, and L. Thévenaz, "Local activation of surface and hybrid acoustic waves in optical microwires," *Optics Letters*, vol. 43, no. 7, p. 1487, 2018. DOI: 10.1364/OL.43.001487.

[124] K. Hotate and Zuyuan He, "Synthesis of optical-coherence function and its applications in distributed and multiplexed optical sensing," *Journal of Lightwave Technology*, vol. 24, no. 7, pp. 2541–2557, 2006. DOI: 10.1109/JLT.2006.874645.

[125] K. Hotate, K. Abe, and K. Y. Song, "Suppression of Signal Fluctuation in Brillouin Optical Correlation Domain Analysis System Using Polarization Diversity Scheme," *IEEE Photonics Technology Letters*, vol. 18, no. 24, pp. 2653–2655, 2006. DOI: 10.1109/LPT.2006.887369.

[126] A. Brown, B. Colpitts, and K. Brown, "Distributed sensor based on dark-pulse Brillouin scattering," *IEEE Photonics Technology Letters*, vol. 17, no. 7, pp. 1501–1503, 2005. DOI: 10.1109/LPT.2005.848400.

[127] S. W. James and R. P. Tatam, "Optical fibre long-period grating sensors: characteristics and application," *Measurement science and technology*, vol. 14, no. 5, R49, 2003.

[128] Z. L. Ran, Y. J. Rao, W. J. Liu, X Liao, and K. S. Chiang, "Laser-micromachined Fabry-Perot optical fiber tip sensor for high-resolution temperature-independent measurement of refractive index," *Optics express*, vol. 16, no. 3, pp. 2252–2263, 2008.

[129] E. Preter, R. A. Katims, V. Artel, C. N. Sukenik, D. Donlagic, and A. Zadok, "Monitoring and analysis of pendant droplets evaporation using bare and monolayer-coated optical fiber facets," *Optical Materials Express*, vol. 4, no. 5, pp. 903–915, 2014.

[130] E. Preter, B. Preloznik, V. Artel, C. N. Sukenik, D. Donlagic, and A. Zadok, "Monitoring the evaporation of fluids from fiber-optic micro-cell cavities," *Sensors*, vol. 13, no. 11, pp. 15 261–15 273, 2013.

[131] T. G. Euser, J. S. Y. Chen, M Scharrer, P. S. J. Russell, N. J. Farrer, and P. J. Sadler, "Quantitative broadband chemical sensing in air-suspended solid-core fibers," *Journal of Applied Physics*, vol. 103, no. 10, p. 103 108, 2008.

[132] D. M. Chow, Z. Yang, M. A. Soto, and L. Thévenaz, "Distributed forward Brillouin sensor based on local light phase recovery," *Nature Communications*, vol. 9, no. 1, p. 2990, 2018. DOI: 10.1038/s41467-018-05410-2.

[133] Y. Antman, A. Clain, Y. London, and A. Zadok, "Optomechanical sensing of liquids outside standard fibers using forward stimulated Brillouin scattering," *Optica*, vol. 3, no. 5, p. 510, 2016. DOI: 10.1364/OPTICA.3.000510.

[134] G. Bashan, H. H. Diamandi, Y. London, E. Preter, and A. Zadok, "Optomechanical time-domain reflectometry," *Nature Communications*, vol. 9, no. 1, p. 2991, 2018. DOI: 10.1038/s41467-018-05404-0.

[135] E. A. Kittlaus, P. Kharel, N. T. Otterstrom, Z. Wang, and P. T. Rakich, "RF-Photonic Filters via On-Chip Photonic–Phononic Emit–Receive Operations," *Journal of Lightwave Technology*, vol. 36, no. 13, pp. 2803–2809, 2018. DOI: 10.1109/JLT.2018.2809589.

[136] A. Godet, A. Ndao, T. Sylvestre, V. Pecheur, S. Lebrun, G. Pauliat, J.-C. Beugnot, and K. Phan Huy, "Brillouin spectroscopy of optical microfibers and nanofibers," *Optica*, vol. 4, no. 10, p. 1232, 2017. DOI: 10.1364/OPTICA.4.001232.

[137] P. F. Jarschel, L. S. Magalhaes, I. Aldaya, O. Florez, and P. Dainese, "Fiber taper diameter characterization using forward Brillouin scattering," *Optics Letters*, vol. 43, no. 5, p. 995, 2018. DOI: 10.1364/OL.43.000995.

[138] J.-C. Beugnot, T. Sylvestre, H. Maillotte, G. Mélin, and V. Laude, "Guided acoustic wave Brillouin scattering in photonic crystal fibers," *Optics Letters*, vol. 32, no. 1, p. 17, 2007. DOI: 10.1364/OL.32.000017.

[139] J.-C. Beugnot, T. Sylvestre, D. Alasia, H. Maillotte, V. Laude, A. Monteville, L. Provino, N. Traynor, S. F. Mafang, and L. Thévenaz, "Complete experimental characterization of stimulated Brillouin scattering in photonic crystal fiber," *Optics Express*, vol. 15, no. 23, p. 15 517, 2007. DOI: 10.1364/OE.15.015517.

[140] Q. Lin, O. J. Painter, and G. P. Agrawal, "Nonlinear optical phenomena in silicon waveguides: modeling and applications," *Optics Express*, vol. 15, no. 25, p. 16 604, 2007. DOI: 10.1364/OE.15.016604.

[141] L. Yin and G. P. Agrawal, "Impact of two-photon absorption on self-phase modulation in silicon waveguides," *Optics Letters*, vol. 32, no. 14, p. 2031, 2007. DOI: 10.1364/OL.32.002031.

[142] A. C. Turner-Foster, M. a. Foster, J. S. Levy, C. B. Poitras, R. Salem, A. L. Gaeta, and M. Lipson, "Ultrashort free-carrier lifetime in low-loss silicon nanowaveguides," *Optics Express*, vol. 18, no. 4, p. 3582, 2010. DOI: 10.1364/OE.18.003582.

[143] O. Boyraz, T. Indukuri, and B. Jalali, "Self-phase-modulation induced spectral broadening in silicon waveguides.," *Optics express*, vol. 12, no. 5, pp. 829–834, 2004. DOI: 10.1364/OPEX.12.000829.

[144] Y. Zhang, C. Husko, J. Schröder, and B. J. Eggleton, "Pulse evolution and phase-sensitive amplification in silicon waveguides," *Optics Letters*, vol. 39, no. 18, p. 5329, 2014. DOI: 10.1364/OL.39.005329.

[145] D. Dimitropoulos, R. Jhaveri, R. Claps, J. C. S. Woo, and B. Jalali, "Lifetime of photogenerated carriers in silicon-on-insulator rib waveguides," *Applied Physics Letters*, vol. 86, no. 7, p. 071 115, 2005. DOI: 10.1063/1.1866635.

[146] W. Zou, Z. He, and K. Hotate, "Investigation of Strain- and Temperature-Dependences of Brillouin Frequency Shifts in GeO_2-Doped Optical Fibers," *Journal of Lightwave Technology*, vol. 26, no. 13, pp. 1854–1861, 2008. DOI: 10.1109/JLT.2007.912052.

[147] T. Horiguchi, K. Shimizu, T. Kurashima, M. Tateda, and Y. Koyamada, "Development of a distributed sensing technique using Brillouin scattering," *Journal of Lightwave Technology*, vol. 13, no. 7, pp. 1296–1302, 1995. DOI: 10.1109/50.400684.

[148] M. Nikles, L. Thevenaz, and P. Robert, "Brillouin gain spectrum characterization in single-mode optical fibers," *Journal of Lightwave Technology*, vol. 15, no. 10, pp. 1842–1851, 1997. DOI: 10.1109/50.633570.

[149] L. Thévenaz, "Monitoring of large structure using distributed Brillouin fibre sensing," in *13th International Conference on Optical Fiber Sensors*, vol. 374642, 1999, p. 145. DOI: 10.1117/12.2302136.

[150] Yongqian Li, Fucai Zhang, and T. Yoshino, "Wide-range temperature dependence of Brillouin shift in a dispersion-shifted fiber and its annealing effect," *Journal of Lightwave Technology*, vol. 21, no. 7, pp. 1663–1667, 2003. DOI: 10.1109/JLT.2003.814929.

[151] L. Zou, X. Bao, S. Afshar V., and L. Chen, "Dependence of the Brillouin frequency shift on strain and temperature in a photonic crystal fiber," *Optics Letters*, vol. 29, no. 13, p. 1485, 2004. DOI: 10.1364/OL.29.001485.

[152] R. M. Shelby, M. D. Levenson, and P. W. Bayer, "Guided acoustic-wave Brillouin scattering," *Physical Review B*, vol. 31, no. 8, pp. 5244–5252, 1985. DOI: 10.1103/PhysRevB.31.5244.

[153] K. Shiraki and M. Ohashi, "Sound velocity measurement based on guided acoustic-wave Brillouin scattering," *IEEE Photonics Technology Letters*, vol. 4, no. 10, pp. 1177–1180, 1992. DOI: 10.1109/68.163771.

[154] Y. Tanaka and K. Ogusu, "Tensile-strain coefficient of resonance frequency of depolarized guided acoustic-wave Brillouin scattering," *IEEE Photonics Technology Letters*, vol. 11, no. 7, pp. 865–867, 1999. DOI: 10.1109/68.769734.

[155] N. Hayashi, K. Suzuki, S. Y. Set, and S. Yamashita, "Temperature coefficient of sideband frequency produced by polarized guided acoustic-wave Brillouin scattering in highly nonlinear fibers," *Applied Physics Express*, vol. 10, no. 9, p. 092 501, 2017. DOI: 10.7567/APEX.10.092501.

[156] E. Carry, J.-C. Beugnot, B. Stiller, M. W. Lee, H. Maillotte, and T. Sylvestre, "Temperature coefficient of the high-frequency guided acoustic mode in a photonic crystal fiber," *Applied Optics*, vol. 50, no. 35, p. 6543, 2011. DOI: 10.1364/AO.50.006543.

[157] R. Cohen, "Noise-based Brillouin optical correlation domain analysis with mm resolution," PhD thesis, 2014.

[158] A. Byrnes, R. Pant, E. Li, D.-Y. Choi, C. G. Poulton, S. Fan, S. Madden, B. Luther-Davies, and B. J. Eggleton, "Photonic chip based tunable and reconfigurable narrowband microwave photonic filter using stimulated Brillouin scattering," *Optics Express*, vol. 20, no. 17, p. 18 836, 2012. DOI: 10.1364/OE.20.018836.

[159] R. Pant, A. Byrnes, C. G. Poulton, E. Li, D.-Y. Choi, S. Madden, B. Luther-Davies, and B. J. Eggleton, "Photonic-chip-based tunable slow and fast light via stimulated Brillouin scattering," *Optics Letters*, vol. 37, no. 5, p. 969, 2012. DOI: 10.1364/OL.37.000969.

[160] X. Bao and L. Chen, "Recent Progress in Brillouin Scattering Based Fiber Sensors," *Sensors*, vol. 11, no. 4, pp. 4152–4187, 2011. DOI: 10.3390/s110404152.

[161] A. Motil, A. Bergman, and M. Tur, "[INVITED] State of the art of Brillouin fiber-optic distributed sensing," *Optics & Laser Technology*, vol. 78, pp. 81–103, 2016. DOI: 10.1016/j.optlastec.2015.09.013.

[162] J. W. Goodman, *Statistical optics*. 2015.

[163] P. W. Milonni and J. H. Eberly, *Laser Physics*. 2010, p. 844. DOI: 10.1002/9780470409718.

[164] K. Kulpa, *Signal processing in noise waveform radar*. 2013.

[165] S. K. Turitsyn, S. A. Babin, D. V. Churkin, I. D. Vatnik, M. Nikulin, and E. V. Podivilov, "Random distributed feedback fibre lasers," *Physics Reports*, vol. 542, no. 2, pp. 133–193, 2014. DOI: 10.1016/j.physrep.2014.02.011.

[166] L. Chrostowski and M. Hochberg, *Silicon Photonics Design*. 2015. DOI: 10.1017/CBO9781316084168.

[167] A. Liu, R. Jones, L. Liao, D. Samara-Rubio, D. Rubin, O. Cohen, R. Nicolaescu, and M. Paniccia, "A high-speed silicon optical modulator based on a metal–oxide–semiconductor capacitor," *Nature*, vol. 427, no. 6975, p. 615, 2004.

[168] P. Dong, L. Chen, and Y.-k. Chen, "High-speed low-voltage single-drive push-pull silicon Mach-Zehnder modulators," *Optics express*, vol. 20, no. 6, pp. 6163–6169, 2012.

[169] D. J. Thomson, F. Y. Gardes, J.-M. Fedeli, S. Zlatanovic, Y. Hu, B. P. P. Kuo, E. Myslivets, N. Alic, S. Radic, and G. Z. Mashanovich, "50-Gb/s silicon optical modulator," *IEEE Photonics Technology Letters*, vol. 24, no. 4, pp. 234–236, 2012.

[170] T. Baehr-Jones, B. Penkov, J. Huang, P. Sullivan, J. Davies, J. Takayesu, J. Luo, T.-D. Kim, L. Dalton, A. Jen, M. Hochberg, and A. Scherer, "Nonlinear polymer-clad silicon slot waveguide modulator with a half wave voltage of 0.25V," *Applied Physics Letters*, vol. 92, no. 16, p. 163 303, 2008. DOI: 10.1063/1.2909656.

[171] Q. Xu, B. Schmidt, S. Pradhan, and M. Lipson, "Micrometre-scale silicon electro-optic modulator," *nature*, vol. 435, no. 7040, p. 325, 2005.

[172] Y. Hu, X. Xiao, H. Xu, X. Li, K. Xiong, Z. Li, T. Chu, Y. Yu, and J. Yu, "High-speed silicon modulator based on cascaded microring resonators," *Optics express*, vol. 20, no. 14, pp. 15 079–15 085, 2012.

[173] G. Li, X. Zheng, J. Yao, H. Thacker, I. Shubin, Y. Luo, K. Raj, J. E. Cunningham, and A. V. Krishnamoorthy, "25Gb/s 1V-driving CMOS ring modulator with integrated thermal tuning," *Optics Express*, vol. 19, no. 21, pp. 20 435–20 443, 2011.

[174] W. D. Sacher, W. M. J. Green, S. Assefa, T. Barwicz, H. Pan, S. M. Shank, Y. A. Vlasov, and J. K. S. Poon, "Breaking the cavity linewidth limit of resonant optical modulators," *arXiv preprint arXiv:1206.5337*, 2012.

[175] Y. Tang, H.-W. Chen, S. Jain, J. D. Peters, U. Westergren, and J. E. Bowers, "50 Gb/s hybrid silicon traveling-wave electroabsorption modulator," *Optics express*, vol. 19, no. 7, pp. 5811–5816, 2011.

[176] Y.-H. Kuo, Y. K. Lee, Y. Ge, S. Ren, J. E. Roth, T. I. Kamins, D. A. B. Miller, and J. S. Harris, "Strong quantum-confined Stark effect in germanium quantum-well structures on silicon," *Nature*, vol. 437, no. 7063, p. 1334, 2005.

[177] M. Liu, X. Yin, E. Ulin-Avila, B. Geng, T. Zentgraf, L. Ju, F. Wang, and X. Zhang, "A graphene-based broadband optical modulator," *Nature*, vol. 474, no. 7349, p. 64, 2011.

[178] R Ding, T Baehr-Jones, Y Liu, R Bojko, J Witzens, S. Huang, J Luo, S Benight, P Sullivan, and J. M. Fedeli, "Demonstration of a low V π L modulator with GHz bandwidth based on electro-optic polymer-clad silicon slot waveguides," *Optics Express*, vol. 18, no. 15, pp. 15 618–15 623, 2010.

[179] J.-M. Brosi, C. Koos, L. C. Andreani, M. Waldow, J. Leuthold, and W. Freude, "High-speed low-voltage electro-optic modulator with a polymer-infiltrated silicon photonic crystal waveguide," *Optics Express*, vol. 16, no. 6, pp. 4177–4191, 2008.

[180] J. Wang and S. Lee, "Ge-photodetectors for Si-based optoelectronic integration," *Sensors*, vol. 11, no. 1, pp. 696–718, 2011.

[181] H. Park, A. W. Fang, R. Jones, O. Cohen, O. Raday, M. N. Sysak, M. J. Paniccia, and J. E. Bowers, "A hybrid AlGaInAs-silicon evanescent waveguide photodetector," *Optics express*, vol. 15, no. 10, pp. 6044–6052, 2007.

[182] A. W. Fang, H. Park, O. Cohen, R. Jones, M. J. Paniccia, and J. E. Bowers, "Electrically pumped hybrid AlGaInAs-silicon evanescent laser," *Optics express*, vol. 14, no. 20, pp. 9203–9210, 2006.

[183] B. B. Bakir, A Descos, N Olivier, D Bordel, P Grosse, E Augendre, L Fulbert, and J. M. Fedeli, "Electrically driven hybrid Si/III-V Fabry-Pérot lasers based on adiabatic mode transformers," *Optics express*, vol. 19, no. 11, pp. 10 317–10 325, 2011.

[184] H. Liu, T. Wang, Q. Jiang, R. Hogg, F. Tutu, F. Pozzi, and A. Seeds, "Long-wavelength InAs/GaAs quantum-dot laser diode monolithically grown on Ge substrate," *Nature Photonics*, vol. 5, no. 7, p. 416, 2011.

[185] A. Spott, E. J. Stanton, N. Volet, J. D. Peters, J. R. Meyer, and J. E. Bowers, "Heterogeneous integration for mid-infrared silicon photonics," *IEEE Journal of Selected Topics in Quantum Electronics*, vol. 23, no. 6, pp. 1–10, 2017.

[186] L. Chen, K. Preston, S. Manipatruni, and M. Lipson, "Integrated GHz silicon photonic interconnect with micrometer-scale modulators and detectors.," *Optics express*, vol. 17, no. 17, pp. 15 248–56, 2009. DOI: 10.1364/OE.17.015248.

[187] M. Georgas, B. R. Moss, C. Sun, J. Shainline, J. S. Orcutt, M. Wade, Y. H. Chen, K. Nammari, J. C. Leu, A. Srinivasan, R. J. Ram, M. A. Popovic, and V. Stojanovic, "A monolithically-integrated optical transmitter and receiver in a zero-change 45nm SOI process," *IEEE Symposium on VLSI Circuits, Digest of Technical Papers*, pp. 14–15, 2014. DOI: 10.1109/VLSIC.2014.6858378.

[188] J. Hu, X. Sun, A. Agarwal, and L. C. Kimerling, "Design guidelines for optical resonator biochemical sensors," *Journal of the Optical Society of America B*, vol. 26, no. 5, pp. 1032–1041, 2009. DOI: 10.1364/JOSAB.26.001032.

[189] M. Iqbal, M. A. Gleeson, B. Spaugh, F. Tybor, W. G. Gunn, M. Hochberg, T. Baehr-Jones, R. C. Bailey, and L. C. Gunn, "Label-free biosensor arrays based on silicon ring resonators and high-speed optical scanning instrumentation," *IEEE Journal of Selected Topics in Quantum Electronics*, vol. 16, no. 3, pp. 654–661, 2010.

[190] R. B. Wehrspohn, S. L. Schweizer, J. Schilling, T. Geppert, C. Jamois, R. Glatthaar, P. Hahn, A. Feisst, and A. Lambrecht, "Application of photonic crystals for gas detection and sensing," *Photonic Crystals: Advances in Design, Fabrication, and Characterization*, p. 238, 2006.

[191] J. K. Doylend, M. J. R. Heck, J. T. Bovington, J. D. Peters, L. A. Coldren, and J. E. Bowers, "Two-dimensional free-space beam steering with an optical phased array on silicon-on-insulator," *Optics express*, vol. 19, no. 22, pp. 21 595–21 604, 2011.

[192] R. E. Camacho-Aguilera, Y. Cai, N. Patel, J. T. Bessette, M. Romagnoli, L. C. Kimerling, and J. Michel, "An electrically pumped germanium laser," *Optics express*, vol. 20, no. 10, pp. 11 316–11 320, 2012.

[193] L. Yin, Q. Lin, and G. P. Agrawal, "Soliton fission and supercontinuum generation in silicon waveguides," *Optics Letters*, vol. 32, no. 4, p. 391, 2007. DOI: 10.1364/OL.32.000391.

[194] I.-W. Hsieh, X. Chen, X. Liu, J. I. Dadap, N. C. Panoiu, C.-Y. Chou, F. Xia, W. M. Green, Y. A. Vlasov, and R. M. Osgood, "Supercontinuum generation in silicon photonic wires," *Optics Express*, vol. 15, no. 23, p. 15 242, 2007. DOI: 10.1364/OE.15.015242.

[195] O. Boyraz and B. Jalali, "Demonstration of a silicon Raman laser," *Optics Express*, vol. 12, no. 21, p. 5269, 2004. DOI: 10.1364/OPEX.12.005269.

[196] H. Rong, S. Xu, Y.-H. Kuo, V. Sih, O. Cohen, O. Raday, and M. Paniccia, "Low-threshold continuous-wave Raman silicon laser," *Nature Photonics*, vol. 1, no. 4, pp. 232–237, 2007. DOI: 10.1038/nphoton.2007.29.

[197] Y. Okawachi, M. Foster, J. Sharping, A. Gaeta, Q. Xu, and M. Lipson, "All-optical slow-light on a photonic chip," *Optics Express*, vol. 14, no. 6, p. 2317, 2006. DOI: 10.1364/OE.14.002317.

[198] X. Liu, R. M. Osgood, Y. A. Vlasov, and W. M. J. Green, "Mid-infrared optical parametric amplifier using silicon nanophotonic waveguides," *Nature Photonics*, vol. 4, no. 8, pp. 557–560, 2010. DOI: 10.1038/nphoton.2010.119.

[199] M. A. Foster, A. C. Turner, R. Salem, M. Lipson, and A. L. Gaeta, "Broad-band continuous-wave parametric wavelength conversion in silicon nanowaveguides," *Optics Express*, vol. 15, no. 20, p. 12 949, 2007. DOI: 10.1364/OE.15.012949.

[200] T. Vallaitis, R. Bonk, J. Guetlein, D. Hillerkuss, J. Li, W. Freude, J. Leuthold, C. Koos, M. L. Scimeca, I. Biaggio, F. Diederich, B. Breiten, P. Dumon, and R. Baets, "All-Optical Wavelength Conversion of 56 Gbit/s NRZ- DQPSK Signals in Silicon-Organic Hybrid Strip Waveguides," in *Optical Fiber Communication Conference*, vol. 20, 2010, OTuN1. DOI: 10.1364/OFC.2010.OTuN1.

[201] T. Vallaitis, C. Koos, B. Esembeson, I. Biaggio, T. Michinobu, F. Diederich, P. Dumon, R. Baets, W. Freude, and J. Leuthold, "Highly nonlinear silicon photonics slot waveguides without free carrier absorption related speed-limitations," in *2008 34th European Conference on Optical Communication*, vol. 4, 2008, pp. 1–2. DOI: 10.1109/ECOC.2008.4729411.

[202] Y.-h. Kuo, H. Rong, V. Sih, S. Xu, M. Paniccia, and O. Cohen, "Demonstration of wavelength conversion at 40 Gb/s data rate in silicon waveguides," *Optics Express*, vol. 14, no. 24, p. 11 721, 2006. DOI: 10.1364/OE.14.011721.

[203] H. Rong, A. Liu, R. Jones, O. Cohen, D. Hak, R. Nicolaescu, A. Fang, and M. Paniccia, "An all-silicon Raman laser," *Nature*, vol. 433, no. 7023, pp. 292–294, 2005. DOI: 10.1038/nature03273.

[204] A. Gajda, L. Zimmermann, M. Jazayerifar, G. Winzer, H. Tian, R. Elschner, T. Richter, C. Schubert, B. Tillack, and K. Petermann, "Highly efficient CW parametric conversion at 1550 nm in SOI waveguides by reverse biased p-i-n junction," *Optics Express*, vol. 20, no. 12, p. 13 100, 2012. DOI: 10.1364/OE.20.013100.

[205] R. Jones, H. Rong, A. Liu, A. W. Fang, M. J. Paniccia, D. Hak, and O. Cohen, "Net continuous wave optical gain in a low loss silicon-on-insulator waveguide by stimulated Raman scattering," *Optics Express*, vol. 13, no. 2, p. 519, 2005. DOI: 10.1364/OPEX.13.000519.

[206] P. A. Anderson, B. S. Schmidt, and M. Lipson, "High confinement in silicon slot waveguides with sharp bends," *Optics Express*, vol. 14, no. 20, p. 9197, 2006. DOI: 10.1364/OE.14.009197.

[207] L. An, H. Liu, Q. Sun, N. Huang, and Z. Wang, "Wavelength conversion in highly nonlinear silicon–organic hybrid slot waveguides," *Applied Optics*, vol. 53, no. 22, p. 4886, 2014. DOI: 10.1364/AO.53.004886.

[208] Y. Huang, P. P. Shum, F. Luan, and M. Tang, "Low loss and wide linear amplification range integrated Raman amplifier based on silicon-chalcogenide slot waveguide," *16th Opto-Electronics and Communications Conference, OECC 2011*, pp. 519–520, 2011.

[209] L. Zhang, Y. Yue, Y. Xiao-Li, J. Wang, R. G. Beausoleil, and A. E. Willner, "Flat and low dispersion in highly nonlinear slot waveguides," *Optics Express*, vol. 18, no. 12, p. 13 187, 2010. DOI: 10.1364/OE.18.013187.

[210] J. Matres, C. Lacava, G. C. Ballesteros, P. Minzioni, I. Cristiani, J. M. Fédéli, J. Martí, and C. J. Oton, "Low TPA and free-carrier effects in silicon nanocrystal-based horizontal slot waveguides," *Optics Express*, vol. 20, no. 21, p. 23 838, 2012. DOI: 10.1364/OE.20.023838.

[211] Q. Liu, S. Gao, Z. Li, Y. Xie, and S. He, "Dispersion engineering of a silicon-nanocrystal-based slot waveguide for broadband wavelength conversion," *Applied Optics*, vol. 50, no. 9, p. 1260, 2011. DOI: 10.1364/AO.50.001260.

[212] S. Mas, J. Caraquitena, J. V. Galán, P. Sanchis, and J. Martí, "Tailoring the dispersion behavior of silicon nanophotonic slot waveguides," *Optics Express*, vol. 18, no. 20, p. 20 839, 2010. DOI: 10.1364/OE.18.020839.

[213] J. S. Levy, A. Gondarenko, M. A. Foster, A. C. Turner-Foster, A. L. Gaeta, and M. Lipson, "CMOS-compatible multiple-wavelength oscillator for on-chip optical interconnects," *Nature Photonics*, vol. 4, no. 1, pp. 37–40, 2010. DOI: 10.1038/nphoton.2009.259.

[214] A. D. Bristow, N. Rotenberg, and H. M. van Driel, "Two-photon absorption and Kerr coefficients of silicon for 850–2200nm," *Applied Physics Letters*, vol. 90, no. 19, p. 191 104, 2007. DOI: 10.1063/1.2737359.

[215] X. Gai, Y. Yu, B. Kuyken, P. Ma, S. J. Madden, J. Van Campenhout, P. Verheyen, G. Roelkens, R. Baets, and B. Luther-Davies, "Nonlinear absorption and refraction in crystalline silicon in the mid-infrared," *Laser & Photonics Reviews*, vol. 7, no. 6, pp. 1054–1064, 2013. DOI: 10.1002/lpor.201300103.

[216] M. Pagani, D. Marpaung, D.-Y. Choi, S. J. Madden, B. Luther-Davies, and B. J. Eggleton, "Tunable wideband microwave photonic phase shifter using on-chip stimulated Brillouin scattering.," *Optics express*, vol. 22, no. 23, pp. 28 810–8, 2014. DOI: 10.1364/OE.22.028810.

[217] M. Merklein, A. Casas-Bedoya, D. Marpaung, T. F. S. Buttner, M. Pagani, B. Morrison, I. V. Kabakova, and B. J. Eggleton, "Stimulated Brillouin Scattering in Photonic Integrated Circuits: Novel Applications and Devices," *IEEE Journal of Selected Topics in Quantum Electronics*, vol. 22, no. 2, pp. 336–346, 2016. DOI: 10.1109/JSTQE.2016.2523521.

[218] A. Zarifi, A. Casas Bedoya, B. Morrison, Y. Zhang, G. Ren, T. Nguyen, S. Madden, K. Vu, A. Mitchell, C. Wolff, D. Marpaung, and B. J Eggleton, "Nonlinear Loss Engineering in a Silicon-Chalcogenide Hybrid Optical Waveguide," in *Photonics and Fiber Technology 2016 (ACOFT, BGPP, NP)*, 2016, NM4A.6. DOI: 10.1364/NP.2016.NM4A.6.

[219] S. Afshar V., T. M. Monro, and C. M. de Sterke, "Understanding the contribution of mode area and slow light to the effective Kerr nonlinearity of waveguides," *Optics Express*, vol. 21, no. 15, p. 18 558, 2013. DOI: 10.1364/OE.21.018558.

[220] S. Afshar V., M. A. Lohe, T. Lee, T. M. Monro, and N. G. R. Broderick, "Efficient third and one-third harmonic generation in nonlinear waveguides," *Optics Letters*, vol. 38, no. 3, p. 329, 2013. DOI: 10.1364/OL.38.000329.

[221] R. Osgood, N. Panoiu, J. Dadap, X Liu, X Chen, I. Hsieh, E Dulkeith, W. Green, and Y. Vlasov, "Engineering nonlinearities in nanoscale optical systems: physics and applications in dispersion-engineered silicon nanophotonic wires," vol. 235, pp. 162–235, 2009. DOI: 10.1364/AOP.1.000162.

[222] S. Afshar V. and T. M. Monro, "A full vectorial model for pulse propagation in emerging waveguides with subwavelength structures part I: Kerr nonlinearity," *Optics Express*, vol. 17, no. 4, pp. 2298–2318, 2009. DOI: 10.1364/OE.17.002298.

[223] *Lumerical Software*.

[224] P. W. Nolte, C. Bohley, and J. Schilling, "Tuning of zero group velocity dispersion in infiltrated vertical silicon slot waveguides.," *Optics express*, vol. 21, no. 2, pp. 1741–50, 2013. DOI: 10.1364/OE.21.001741.

[225] T. Fujisawa and M. Koshiba, "All-optical logic gates based on nonlinear slot-waveguide couplers," *Journal of the Optical Society of America B*, vol. 23, no. 4, p. 684, 2006. DOI: 10.1364/JOSAB.23.000684.

[226] C. A. Barrios, "High-performance all-optical silicon microswitch," *Electronics Letters*, vol. 40, no. 14, pp. 862–863, 2004.

[227] T. Vallaitis, S. Bogatscher, L. Alloatti, P. Dumon, R. Baets, M. L. Scimeca, I. Biaggio, F. Diederich, C. Koos, W. Freude, and J. Leuthold, "Optical properties of highly nonlinear silicon-organic hybrid (SOH) waveguide geometries," *Optics Express*, vol. 17, no. 20, p. 17 357, 2009. DOI: 10.1364/OE.17.017357.

[228] A. Martinez, J. Blasco, P. Sanchis, J. V. Galan, J. Garcia-Ruperez, E. Jordana, P. Gautier, Y. Lebour, S. Hernandez, R. Spano, R. Guider, N. Daldosso, B. Garrido, J. M. Fedeli, L. Pavesi, and J. Marti, "Ultrafast All-Optical Switching in a Silicon-Nanocrystal-Based Silicon Slot Waveguide at Telecom Wavelengths," *Nano Letters*, vol. 10, no. 4, pp. 1506–1511, 2010. DOI: 10.1021/nl9041017.

[229] N. Levanon and E. Mozeson, *Radar Signals*. 2004. DOI: 10.1002/0471663085.

[230] A. Kobyakov, M. Sauer, and D. Chowdhury, "Stimulated Brillouin scattering in optical fibers," *Adv. Opt. Photon.*, vol. 2, no. 1, pp. 1–59, 2010. DOI: 10.1364/AOP.2.000001.

[231] C. A. Galindez-Jamioy and J. M. López-Higuera, "Brillouin Distributed Fiber Sensors: An Overview and Applications," *Journal of Sensors*, vol. 2012, pp. 1–17, 2012. DOI: 10.1155/2012/204121.

[232] K. Y. Song and K. Hotate, "Distributed Fiber Strain Sensor With 1-kHz Sampling Rate Based on Brillouin Optical Correlation Domain Analysis," *IEEE Photonics Technology Letters*, vol. 19, no. 23, pp. 1928–1930, 2007. DOI: 10.1109/LPT.2007.908772.

[233] H. Shin, J. A. Cox, R. Jarecki, A. Starbuck, Z. Wang, and P. T. Rakich, "Control of coherent information via on-chip photonic–phononic emitter–receivers," *Nature Communications*, vol. 6, no. 1, p. 6427, 2015. DOI: 10.1038/ncomms7427.

[234] M. Merklein, I. V. Kabakova, T. F. S. Büttner, D.-y. Choi, B. Luther-Davies, S. J. Madden, and B. J. Eggleton, "Enhancing and inhibiting stimulated Brillouin scattering in photonic integrated circuits," *Nature Communications*, vol. 6, no. 1, p. 6396, 2015. DOI: 10.1038/ncomms7396.

[235] A. Casas-Bedoya, B. Morrison, G. Ren, K. Vu, A. Zarifi, T. Nguyen, D. Choi, D. Marpaung, S. Madden, A. Mitchell, and B. J. Eggleton, "Net Brillouin gain of 18.5 dB in a hybrid silicon chip," in *Frontiers in Optics 2016*, 2016, FF2B.8. DOI: 10.1364/FIO.2016.FF2B.8.

[236] B. Stiller, A. Kudlinski, M. W. Lee, G. Bouwmans, M. Delque, J.-C. Beugnot, H. Maillotte, and T. Sylvestre, "SBS Mitigation in a Microstructured Optical Fiber by Periodically Varying the Core Diameter," *IEEE Photonics Technology Letters*, vol. 24, no. 8, pp. 667–669, 2012. DOI: 10.1109/LPT.2012.2186286.

[237] Y. Antman, L. Yaron, T. Langer, M. Tur, N. Levanon, and A. Zadok, "Experimental demonstration of localized Brillouin gratings with low off-peak reflectivity established by perfect Golomb codes," *Optics Letters*, vol. 38, no. 22, p. 4701, 2013. DOI: 10.1364/OL.38.004701.

[238] R. Cohen, Y. London, Y. Antman, and A. Zadok, "Few millimeter-resolution Brillouin optical correlation domain analysis using amplified-spontaneous-emission pump and signal waves," in *Proc. of SPIE*, vol. 9157, 2014, 91576B. DOI: 10.1117/12.2059362.

[239] G. Agrawal, "Nonlinear effects in Silicon Waveguides," *Internal Presentation*, 2007.

[240] S. J. Madden, D.-Y. Choi, D. a. Bulla, a. V. Rode, B Luther-Davies, V. G. Ta'eed, M. D. Pelusi, and B. J. Eggleton, "Long, low loss etched As_2S_3 chalcogenide waveguides for all-optical signal regeneration.," *Optics express*, vol. 15, no. 22, pp. 14 414–14 421, 2007. DOI: 10.1364/OE.15.014414.

[241] *FINISAR*.

[242] *Yenista Optics-XTM50*.

[243] *AlnairLabs*.

[244] M. Santagiustina, S. Chin, N. Primerov, L. Ursini, and L. Thévenaz, "All-optical signal processing using dynamic Brillouin gratings," *Scientific Reports*, vol. 3, no. 1, p. 1594, 2013. DOI: 10.1038/srep01594.

[245] C. Galland, N. Sangouard, N. Piro, N. Gisin, and T. J. Kippenberg, "Heralded single-phonon preparation, storage, and readout in cavity optomechanics," *Physical Review Letters*, vol. 112, no. 14, pp. 1–6, 2014. DOI: 10.1103/PhysRevLett.112.143602.

[246] K. Fang, M. H. Matheny, X. Luan, and O. Painter, "Optical transduction and routing of microwave phonons in cavity-optomechanical circuits," *Nature Photonics*, no. June, 2016. DOI: 10.1038/nphoton.2016.107.

[247] X.-H. Jia, H.-Q. Chang, K. Lin, C. Xu, and J.-G. Wu, "Frequency-comb-based BOTDA sensors for high-spatial-resolution/long-distance sensing," *Optics Express*, vol. 25, no. 6, p. 6997, 2017. DOI: 10.1364/OE.25.006997.

[248] M. S. Kang, A. Brenn, G. S. Wiederhecker, and P. S. Russell, "Optical excitation and characterization of gigahertz acoustic resonances in optical fiber tapers," *Applied Physics Letters*, vol. 93, no. 13, p. 131 110, 2008. DOI: 10.1063/1.2995863.

[249] K.-Y. Song and K. Hotate, "Brillouin Optical Correlation Domain Analysis in Linear Configuration," *IEEE PHOTONICS TECHNOLOGY LETTERS*, vol. 20, no. 24, pp. 2150–2152, 2008.

[250] P. T. Rakich, C. Reinke, R. Camacho, P. Davids, and Z. Wang, "Giant Enhancement of Stimulated Brillouin Scattering in the Subwavelength Limit," *Physical Review X*, vol. 2, no. 1, p. 011 008, 2012. DOI: 10.1103/PhysRevX.2.011008.

[251] *COMSOLMultiphysics v. 5.2*.

[252] M. J. A. Smith, B. T. Kuhlmey, C. M. de Sterke, C. Wolff, M. Lapine, and C. G. Poulton, "Metamaterial control of stimulated Brillouin scattering," *Optics Letters*, vol. 41, no. 10, p. 2338, 2016. DOI: 10.1364/OL.41.002338.

[253] Y. Li, L. Li, B. Tian, G. Roelkens, and R. G. Baets, "Reflectionless Tilted Grating Couplers With Improved Coupling Efficiency Based on a Silicon Overlay," *IEEE Photonics Technology Letters*, vol. 25, no. 13, pp. 1195–1198, 2013. DOI: 10.1109/LPT.2013.2261484.

[254] S. R. Mirnaziry, C. Wolff, M. J. Steel, B. J. Eggleton, and C. G. Poulton, "Stimulated Brillouin scattering in silicon/chalcogenide slot waveguides," *Optics Express*, vol. 24, no. 5, p. 4786, 2016. DOI: 10.1364/OE.24.004786.